Gravitational lensing of SNLS Supernovae

Taia Kronborg

September 3, 2009

Acknowledgements

Abstract

Type Ia supernovae have become an essential tool of modern observational cosmology. By studying the distance-redshift relation of a large number of supernovae, the nature of dark energy can be unveiled. Distances to Type Ia SNe are however affected by gravitational lensing which can induce systematic effects in the measurement of cosmology. The majority of the supernovae is slightly demagnified whereas a small fraction is significantly magnified due to the mass distribution along the line of sight. This causes naturally an additional dispersion in the observed magnitudes. There are two different ways to estimate the magnification of a supernova. A first method consists in comparing the supernova luminosity, which is measured to about 15% precision, to the mean SN luminosity at the same redshift. Another estimate can be obtained from predicting the magnification induced by the foreground matter density modeled from the measurements of the luminosity of the galaxies with an initial prior on the mass-luminosity relation of the galaxies. A correlation between these 2 estimates will make it possible to tune the initially used mass-luminosity relation resulting in an independent measurement of the dark matter clustering based on the luminosity of SNe Ia. Evidently, this measurement depends crucially on the detection of this correlation also referred to as the lensing signal. This thesis is dedicated to the measurement of the lensing signal in the SNLS 3-year sample.

Les supernovae de Type Ia sont devenues un outil essentiel dans la cosmologie observationnelle moderne. En étudiant la relation distance-redshift d'un grand nombre de supernovae, la nature de l'énergie noire peut être contrainte. Les distances au SNe de Type Ia sont néanmoins affectées par l'effet de lentilles gravitationnelles qui pourrait induire des effets systématiques dans les mesures de cosmologie. La plupart des supernovae sont faiblement demagnifiées et une petite fraction sont magnifiées de manière importante du fait de la distribution de masse dans la ligne de visée. Ceci induit naturellement une dispersion supplementaire dans les magnitudes observées. Il existe 2 façons d'estimer l'amplification des SNe Ia. Une première méthode consiste à comparer la luminosité de la supernova, qui est mesuré avec une précision typique de 15% , à la moyenne des luminosités de SNe au même redshift. Une autre estimation peut être obtenue en prédisant l'amplification induit par la densité de matière en avant-plan modelée en se basant sur les mesures de la luminosité des galaxies avec un à priori initial sur la relation de masse-luminosité des galaxies. La corrélation entre ces 2 estimateurs permet d'accorder la relation de masse-luminosité utilisée initialement pour obtenir une mesure indépendante fondée sur la luminosité des SNe Ia. Bien évidemment, cette mesure nécessite dans un premier temps la détection de cette corrélation et cette thèse a été dédiée à la mesure de la corrélation dans l'échantillon de SNLS 3 ans.

Contents

Introduction

In science, the most important revolutions are often initiated by small disagreements.

Copernicus suggested in the 16th century that the earth is not the center of the universe. This was based on variations in the movements of the planets which was at that time considered negligible.

In 1919, Arthur Eddington went on an important solar eclipse expedition to provide the first proof in favor of the theory of General Relativity by Einstein. He measured the very small deflection of light induced by the sun's gravitational field and found it to be twice the expected value from a newtonian point of vue. GR has completely changed our perspective of the universe and is one of the fundamental corner stones of modern cosmology.

One of the most important revolutions within the last decade was initiated in 1998 with the discovery of the accelerating expansion of the universe. A small deviation from the expected luminosity of distant Type Ia supernovae led physicists to conclude their ignorance with respect to the constitution of $\sim 70\%$ of the universe. The universe would be filled with a new substance of still undetermined nature which is responsible for the acceleration of the universe, now referred to as Dark Energy.

Type Ia supernovae have uniform light curves and a small dispersion among their peak brightness and as a consequence they can be used to measure distances precisely. By studying the distance-redshift relation of a large number of supernovae, precise constraints on cosmology can be obtained.

This thesis investigates gravitational lensing of Type Ia supernovae. Gravitational lensing will magnify or demagnify the supernovae due to mass inhomogeneities along the line of sight and as a consequence they will appear to be closer or more distant than they really are. This may have a noticeable effect on the derived cosmology which needs to be quantified.

With the advent of large supernova surveys it becomes now possible to use the magnification of SNe to probe the foreground Dark Matter density distribution. The method is as follows. There are two different ways to estimate the magnification of a supernova. A first method consists in comparing the supernova luminosity, which is measured to about 15% precision, to the mean SN luminosity at the same redshift. Another estimate can be obtained from predicting the magnification induced by the foreground matter density modeled from the measurements of the luminosity of the galaxies with an initial prior on the mass-luminosity relation of the galaxies We expect there to be a correlation between these two estimates and if such a correlation is found it is then possible to probe the Dark Matter clustering of the foreground galaxies.

This realization relies on one crucial step which is the detection of this correlation, also referred to as the lensing signal. This thesis has primarily been dedicated to the detection of the lensing signal in the SNLS third year sample.

The first part of this thesis is devoted to the theoretical and observational background of the subject. In the first chapter, a review on modern cosmology is presented including the important cosmological probes and the latest results. The basics of Type Ia supernova and their use in cosmology is viewed in chapter 2 whereas the theory of gravitational lensing is presented in chapter 3.

The second part consists of developing the idea of using the gravitational magnification of Type Ia supernovae as a new probe for Dark Matter clustering. This is done in chapter 4 which also includes a review of standard methods to obtain mass-luminosity relations for galaxies.

The last part of the thesis discusses the analysis of the SNLS 3-year data set and the results. In chapter 5 a detailed description of the analysis is given and in chapter 6 the results and prospects for the analysis are presented. Chapter 7 concludes the thesis.

Chapter 1

Cosmology

Cosmology is the study of the world in which we live, an important and exciting subject to study. We try, using scientific methods to understand the origin, the evolution and the fate of the universe.

During the last few decades there has been an explosion of development in the scientific field of cosmology. The technical progress has been enormous and the volume and accuracy of the data from observational cosmology has improved considerably. The paradox, however, is the more we learn about the universe the less we seem to understand. Let me illuminate this statement by looking at some of the rewarding observational results in cosmology within the past decade:

1. The value of the total density parameter , Ω_{tot} can be determined by using the anisotropy of the CMB (Cosmic Microwave Background radiation) fluctuations (see section 1.4.1) combined with a measurement of the Hubble constant, H_0. The results show that the value of the density parameter of our universe is very near one, $\Omega_{tot} = 1$ (Spergel *et al.*, 2003, 2007; Dunkley *et al.*, 2009; Komatsu *et al.*, 2009) which is in favor of an inflation scenario.

2. Only a few minutes after the Big Bang, nuclei heavier than H-1 start to form. This is referred to as the Big Bang nucleosynthesis (BBN) or primordial nucleosynthesis. The phase only lasts for about 17 minutes before the universe cools sufficiently for nuclear fusion to stop. BBN is responsible for the production of light elements such as deuterium, helium, and lithium in the universe and the theory gives precise predictions of the primordial abundances of these light elements which can be tested by observations (Coc *et al.*, 2004; Pettini *et al.*, 2008). By combining the observed abundances with the CMB data one can conclude that the fraction of baryonic matter, $\Omega_B \approx 0.045$ (Komatsu *et al.*, 2009). These observations take into account all the existing baryonic matter in the universe. Knowing the value of the total density parameter Ω_{tot} one might say that our universe is mostly non-baryonic.

3. Observations of the dynamic aspect of large structures such as galaxy rotation, cluster velocity dispersion, galaxy formation and gravitational lensing studies show that there exists a non luminous matter, called Dark Matter, probably consisting of massive particles with very weak interactions which can collapse and form halos at galactic scales (Rubin & Ford, 1970; Roberts & Rots, 1973; Zwicky, 1933).

4. Observations of Type Ia supernovae indicate that there exists another component, Dark Energy, with a negative pressure driving the acceleration of the universe (Perlmutter *et al.*, 1999; Riess

et al., 1998; Astier *et al.*, 2006; Wood-Vasey *et al.*, 2007). By far the simplest choice to account for a Dark Energy with a negative pressure is to "reintroduce" what was referred to by Einstein himself as the greatest blunder: the cosmological constant.

5. Recent observations of the CMB , BAO and weak lensing (Komatsu *et al.*, 2009; Eisenstein *et al.*, 2005; Percival *et al.*, 2007) have pinned down the value of the density parameter of all matter to $\Omega_M \approx 0.27$

6. In summary, by combining the former cited observations, BAO (Baryonic Acoustic Oscillation), Supernovae and CMB we conclude that they all favor the standard cosmological model where about 4% of the matter is baryonic and "well-known", 23% consists of dark matter we know little about and which still lacks direct detection, and finally the most important component of our universe is the "newly" discovered dark energy ($\sim$ 70%) which we know hardly anything about. Our universe is indeed dark and mysterious.

Let us first review some basics of modern cosmology and the framework they are developped in.

1.1 Homogeneity and isotropy

Recent observations of the CMB and large galaxy surveys have made it possible to state that the universe is spatially homogeneous and isotropic on large scales ($> 70h^{-1}$Mpc). Isotropy means that the universe looks the same in all directions. Observational evidence for this hypothesis comes for example from the CMB which shows a remarkably isotropic temperature down to the level of 10^{-5}K over the whole sky once the dipole has been subtracted. One can also look at the structure formation of the universe at late times and find that over large scales the universe is isotropic (see fig 1.1)

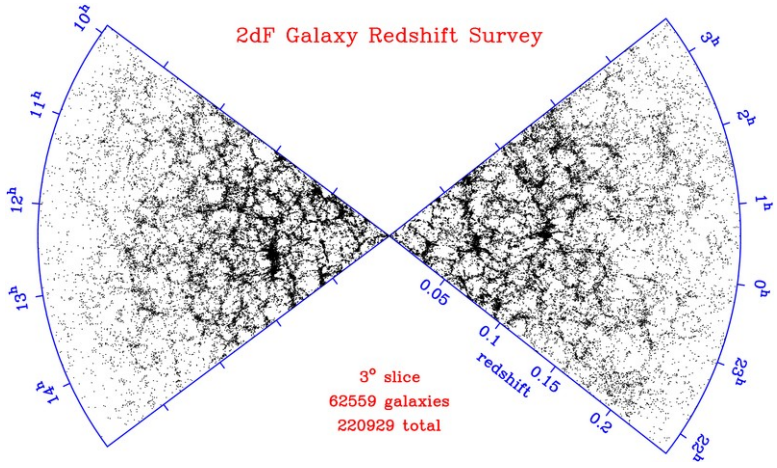

Figure 1.1: A 3 degree slice of the universe for z< 0.25 from the 2dF galaxy survey. The image is taken from Colless *et al.* (2003) and is a part of the final data release (2003). Our galaxy is situated in the intersection of the two slices of the observed sky. Even though structures are present on small scales, the universe overall is homogeneous on large scales

Homogeneity means that the universe looks the same at every point. To examine homogeneity one could invoke the Copernican principle that we do not live in a special place in the universe and thus since the universe is isotropic in our local universe it should be isotropic in every point in the universe and this implies homogeneity. The homogeneous universe is also observationally well supported by large galaxy surveys like the SDSS which has shown that our universe is homogeneous on scales larger than $60 - 70h^{-1}$Mpc (Colless *et al.*, 2003; Yadav *et al.*, 2005).

These two facts highly simplify our way of modeling the universe and it can be approximated as a homogeneous and isotropic three-dimensional space which may expand or in principle contract as a function of time. A simple and unique metric, for-filling these properties is the Robertson-Walker (RW) metric.

$$ds^2 = dt^2 - a^2(t)\left[\frac{dr^2}{1-kr^2} + r^2\left(d\theta^2 + \sin^2\theta d\phi^2\right)\right] \tag{1.1}$$

where $a(t)$ is the time dependent scale factor and k geometrically describes the curvature of the spatial section. $k = +1$ describes a positively curved space, $k = 0$ a flat space and $k = -1$ a negatively curved space.

1.2 Friedmann's equations

In 1916, Einstein published his general theory of relativity which revolutionized the theory of gravitation in modern physics making it one of the corner stones of modern cosmology (Einstein, 1916). The Einstein equations including a cosmological constant can be written as

$$R_{\mu\nu} - \frac{1}{2}Rg_{\mu\nu} - \Lambda g_{\mu\nu} = 8\pi G T_{\mu\nu} \tag{1.2}$$

where $R_{\mu\nu}$ is the Ricci tensor, R is the Ricci scalar defined as the trace of the Ricci tensor, Λ is the cosmological constant, G is a gravitational constant, $T_{\mu\nu}$ is the energy-momentum tensor and finally $g_{\mu\nu}$ is the metric. As said in the previous section, the RW metric is a consequence of the homogeneity and isotropy of the universe and we can now solve the Einstein equations for this particular metric. For simplicity and consistency with current observations related to the universe, the energy momentum tensor takes the form of a perfect fluid with an isotropic pressure. Vanishing of the covariant divergence of the energy-momentum tensor leads to the energy conservation equation

$$\dot{\rho} + 3\left(\frac{\dot{a}}{a}\right)(\rho + p) = 0 \tag{1.3}$$

where ρ is the energy density of the fluid and p is the pressure of the fluid. Solving the Einstein equations using this simple description of matter leads to 2 equations. The first equation is known as the Friedmann equation

$$H^2 = \left(\frac{\dot{a}}{a}\right)^2 = \frac{8\pi G}{3}\rho + \frac{\Lambda}{3} - \frac{k}{a^2} \tag{1.4}$$

where $H = \frac{\dot{a}}{a}$ is the Hubble parameter where the current value, H_0 is called the Hubble constant. The Hubble parameter relates the recession velocity between moderately distant galaxies and our own, and their distance to us through a linear law

$$v \simeq Hd \tag{1.5}$$

as discovered by E. Hubble in 1929 (Hubble, 1929), where v is the velocity and d the is the comoving proper distance. This law was one of the great discoveries in the last century and it showed that rather than being static which was the common belief at that time, the universe is expanding. The second equation is the acceleration equation

$$\frac{\ddot{a}}{a} = -\frac{4\pi G}{3}(\rho + 3p) \tag{1.6}$$

The Friedmann equation reveals the astonishing fact that there is a direct and simple connection between the density of the universe and its global geometry.

1.3 Definition of redshift

In the following it will be useful to define the redshift of an object, z.

When a galaxy moves away or towards us, the lines in its spectrum are shifted to longer or shorter wavelengths leading to a relative redshift or blueshift respectively. This effect can be interpreted as a Doppler effect when the relative velocity of the galaxy, v is much smaller than the speed of light. In this case, the redshift is defined as

$$\frac{\lambda_0}{\lambda} - 1 = \frac{v}{c} = z \tag{1.7}$$

where λ is the emitted wavelength and λ_0 is the observed wavelength .

Within the cosmological frame, the photons propagating through space are stretched due to the expansion of the universe, leading to an increase in wavelength. This increase is related to the scale factor in the following way

$$\frac{\lambda_0}{\lambda} = z + 1 = \frac{a_0}{a} \tag{1.8}$$

where a_0 is the present value of the scale factor. In practice, the redshift of an object can be determined by recognizing the redshifted wavelengths of the different spectral features and compare them to laboratory measurements of the wavelengths.

1.4 The cosmological parameters

The Friedmann equation can be used to define a critical density for which $k = 0$:

$$\rho_c = \frac{3H^2}{8\pi G} \tag{1.9}$$

when effectively accounting for Λ as another energy since $\rho_\Lambda = \frac{\Lambda}{8\pi G}$. The total density parameter of the universe can then be defined with respect to the critical density

$$\Omega_{tot} = \frac{\rho}{\rho_c} \tag{1.10}$$

This relates the density parameter to the local geometry

$$\Omega_{tot} > 1 \quad \Rightarrow k = +1 \tag{1.11}$$

$$\Omega_{tot} = 1 \quad \Rightarrow k = 0 \tag{1.12}$$

$$\Omega_{tot} < 1 \quad \Rightarrow k = -1 \tag{1.13}$$

It is convenient to relate the density parameter of each component in the universe to the critical density as

$$\Omega_i = \frac{\rho_i}{\rho_c} \tag{1.14}$$

where $\sum_i \Omega_i = \Omega_{tot}$.

Before solving the Friedmann equation for cosmological purposes we need to state how the pressure and the energy density are connected to each other. The common approximation within the perfect fluid is that of an equation of state parameter, w relating the energy density and the pressure

$$p = w\rho \tag{1.15}$$

The equation of state parameter can either be a constant or be dependent on redshift.

Using the energy-conservation equation (eq.1.3) and a constant equation of state parameter leads to the following evolution of the energy density parameter with the scale parameter $a(t)$.

$$\rho(a) \propto \frac{1}{a(t)^{3(1+w)}} \tag{1.16}$$

Shortly after the Big Bang our universe was dominated by radiation where $w = 1/3$ and the energy density of radiation will scale as $a(t)^{-4}$. For a universe dominated by dust or pressureless matter, the equation of state parameter is $w = 0$ leading to an energy density of dust which scales as $a(t)^{-3}$. Choosing $w = -1$ which corresponds to the cosmological constant leads to a constant energy density, ρ_Λ.

It is more convenient to put the Friedmann equation in a form that contains present-day expansion rate and density parameters.

Taking into account the fact that our universe is presently dominated by two components (matter and dark energy) leads us to the following expression for $H(z)$

$$H^2(z) = H_0^2 \left[\Omega_m(1+z)^3 + \Omega_{de}(1+z)^{3(1+w)} + (1-\Omega_{tot})(1+z)^2\right] \tag{1.17}$$

where Ω_m and Ω_{de} are the density parameters of matter and dark energy respectively.

1.5 The present universe

In this section we will concentrate on the actual universe in which we live and discuss some properties. A very remarkable fact is that the universe is highly dominated by dark components (dark matter and dark energy).

Most striking among them is the dominant source of Dark Energy, which may be a vacuum energy (cosmological constant), a dynamic field, or something even more dramatic.

Dark Matter

Less than 5% of the energy density of the universe comes from baryonic and in principle visible matter but it has long been known that an invisible and undetected matter exists. The first observer to point out the importance of the hidden matter was the Swiss physicist Fritz Zwicky in 1933 . By applying the virial theorem to clusters he noticed that some of the galaxies should in theory escape from the cluster if

no other mass than the visible mass was present in the cluster (Zwicky, 1933). He resolved the problem by introducing a hidden mass (and he even suggested the idea of using gravitational lensing as proof).

Rotation curves of spiral galaxies were studied in the 1970s (Rubin & Ford, 1970; Roberts & Rots, 1973) giving rise to the evidence that also galaxies contained a large fraction of dark matter.

Today, the distribution of dark matter has been studied intensively using tools like the dynamics of galaxies and clusters, gravitational lensing and temperature distribution of hot gas. Also cosmological probes such as the CMB, BAO, Type Ia Supernovae give compelling evidence of dark matter and all observations agree on the existence of a large fraction of dark matter in the universe.

The crucial question that remains unsolved to date is what dark matter is made of. One must not forget that primordial nucleosynthesis together with the CMB and the BAO (see section 1.4.1 and 1.4.2) set stringent constraints on the fraction of matter of baryonic origin in the universe and one must turn physics beyond the standard model of particle physics to seek an explanation. Of course there is always the possibility that general relativity fails to describe gravity at galaxy and cluster scales but if we put this possibility aside we need to search for new particles. The simplest assumptions concerning dark matter particles is that they do not interact significantly with other matter and that their velocity is negligible compared to the speed of light, leading to the description of cold dark matter where possible candidates include the lightest supersymmetric particle, axions, sterile neutrinos, Kalusa Klein particles and primordial black holes amongst others. The statement of no significant interaction with other matter makes these particles invisible through standard electromagnetic observations and thus dark. Simulations of a Cold Dark Matter (CDM) dominated universe predict galaxy distributions compatible with the observational universe. Note however that problems at galactic scales persist (i.e. inner density slope of Dark Matter profiles and dwarf galaxies).

Dark Energy

As said previously, Dark Energy discovered using type Ia supernovae was one of the biggest cosmological surprises of the last century, however, the exact nature of Dark Energy is still undetermined. The Dark Energy is generally described by a perfect fluid with the equation of state, $p = w\rho$, where w is the equation of state parameter.

If general relativity is correct then the found accelerating expansion requires a Dark Energy density with negative pressure. This can be seen directly from the acceleration equation (eq. 1.6). Using equation 1.15 leads to the following conclusion

$$\frac{\ddot{a}}{a} \propto -\rho(1 + 3w) \tag{1.18}$$

For the acceleration of the universe to be positive, $\frac{\ddot{a}}{a} > 0$, we must require that $w < -1/3$ and thus the pressure must be negative.

The simplest Dark Energy model to explain the cosmic acceleration is the cosmological constant where $w = -1$. The cosmological constant can be considered as a vacuum energy which could be well described by quantum fluctuations in quantum mechanics, although this interpretation carries numerous conceptual problems. Existing quantum field theories predict a huge cosmological constant, more than 100 orders of magnitude too large compared to the observed value. To obtain the observed value the huge vacuum energy almost needs to be cancelled out. It is difficult to understand such fine-tuning.

Another problem to be raised is the puzzle of cosmic coincidence where one asks the question why the cosmic acceleration began when it did. In the early universe the cosmological constant was not the dominant component that it is now and will be in the future, thus the possibility to actually measure the

cosmological constant depends strongly on the cosmic epoch of the observations . We would probably not have been able to measure it in the past and it will be a lot easier in the future. The fact that the contribution of the cosmological constant is comparable to that of matter exactly in our epoch may seem suspicious.

With these difficult concepts of sometimes more philosophical grounds, the cosmological constant theory has been questioned. However, these problems can be partly solved if one thinks of the dark energy as a dynamic field like quintessence which is a time-evolving scalar field with negative pressure sufficient to drive the accelerating expansion. This is in contrast to the cosmological constant which is constant in the entire universe and for all times.

Various models of dynamic fields have emerged to explain dark energy but it is very difficult to set stringent observational constraints and thus rule out some of the models.

Today, one of the most important goals in cosmology is to determine whether the equation of state parameter w is constant or evolving and in the latter case, how it evolves with time. To investigate this, a simple and linear parameterization of w is used.

$$w = w_0 + w'(a - a_0) \tag{1.19}$$

where w_0 is the present value and w' is the first derivative showing the evolution of the equation of state parameter.

1.6 Distance measurements

A definition of different distance measurements will be useful in the following

The angular diameter distance

Let us consider the actual size of an object, x, and the angular size, θ, this object subtends on the sky. The angular diameter distance, d_A, is then defined as

$$d_A = \frac{x}{\theta} \tag{1.20}$$

The luminosity distance

The luminosity distance d_L, of an object is related through the flux-luminosity relation.

$$F = \frac{L}{4\pi d_L^2} \tag{1.21}$$

where F is the received flux of the object and L is its intrinsic luminosity.

Both d_A and d_L depend on the underlying cosmology of the universe and can be expressed in terms of the radial coordinate in the Robertson-Walker metric, χ.

$$d_A = a_0 \frac{r(\chi)}{(1+z)} \tag{1.22}$$

$$d_L = a_0 r(\chi)(1+z) \tag{1.23}$$

where

$$= \sin\chi \qquad \Omega_T > 1 \tag{1.24}$$

$$r = \chi \qquad \Omega_T = 1 \tag{1.25}$$

$$= \sinh\chi \qquad \Omega_T < 1 \tag{1.26}$$

and χ, the radial coordinate in the Robertson-Walker metric can be expressed as follows

$$\chi = \frac{1}{a_0}\int_0^z \frac{dz'}{H(z')} \tag{1.27}$$

1.7 The magnitude system

In astronomy, the magnitude system is frequently used to describe the brightness of an object. This is a logarithmic scale where the apparent magnitude of an object, m, is defined as the flux ratio of the flux of the object, f, measured in a given observational filter and the flux of a reference object (Vega star for example), f_0, in the same filter.

$$m = -2.5\log_{10}\frac{f}{f_0} \tag{1.28}$$

The absolute magnitude of an object is a measure of the intrinsic brightness of the object and is defined as the apparent magnitude the object would have if it were 10pc away from the observer.

1.8 Cosmological probes

Cosmology has for a long time been a theoretical field due to the lack of observations, but with the increasing amount of data and technical progress we are now in the era of observational cosmology. 4 powerful measurements have been proven excellent cosmological probes.

1.8.1 CMB (Cosmic Microwave Background radiation)

Less than one second after the Big Bang the universe was filled with a hot and dense plasma of photons, electrons and baryons all in interaction. As the universe expanded, the temperature of the plasma dropped below the critical value of 2967 K for electrons and protons to combine and form neutral hydrogen. This decoupling of matter and radiation is referred to as the recombination period and took place at z$\sim$ 1100 and made the universe transparent to radiation. As the universe continued to expand and cool down, so did the cosmic radiation and today the CMB radiation is very cold, only 2.725° above absolute zero which makes it observable primarily in the microwave range. Although the CMB is invisible to the naked eye it fills the entire universe and is detectable in all directions. The CMB (and by extension, also the early universe) is astonishingly featureless, the temperature is uniform to better than one part in a hundred thousand. Observing the CMB means looking back at the surface of last scattering as the CMB has travelled across the universe rather unimpeded since then. This implies that any ”features” imprinted in this surface of last scatter will remain imprinted in the CMB. In addition the CMB spectrum is affected by various processes as it propagates towards us like the integrated Sachs-Wolf effect, the re-ionization, the Sunyaev-Zel'dovich effect and gravitational lensing.

The CMB was first discovered by chance in 1965 by Robert Woodrow Wilson and Arnia Penzias. The existence of a cosmic radiation background had already been predicted in the 40s and 50s (Alpher & Herman, 1948; Alpher *et al.*, 1953) and the construction of a radiometer with the goal of a detection of such radiation was already enhanced when Penzias and Wilson found an excess temperature of a radio antenna which they could not account for (Penzias & Wilson, 1965). The radiation was that of thermal black body radiation.

The CMB contains a great deal of information about the properties of our universe which can be measured in no other way and a lot of effort has gone into measuring these properties since its discovery.

Anisotropy, Acoustic peaks and Cosmological parameters

Even though the temperature of the CMB is extremely uniform all over the sky there are small temperature fluctuations associated with fluctuations of the matter density in the early universe. The anisotropy of the CMB was first detected by the COBE (COsmic Background Explorer) satellite in 1992 but with a poor angular resolution. With the WMAP (Wilkinson Microwave Anisotropy Probe) satellite launched in 2001 the temperature fluctuations have been mapped with much higher resolution and accuracy (see fig 1.2). The new information contained in these small fluctuations improves our understanding on several key questions in cosmology.

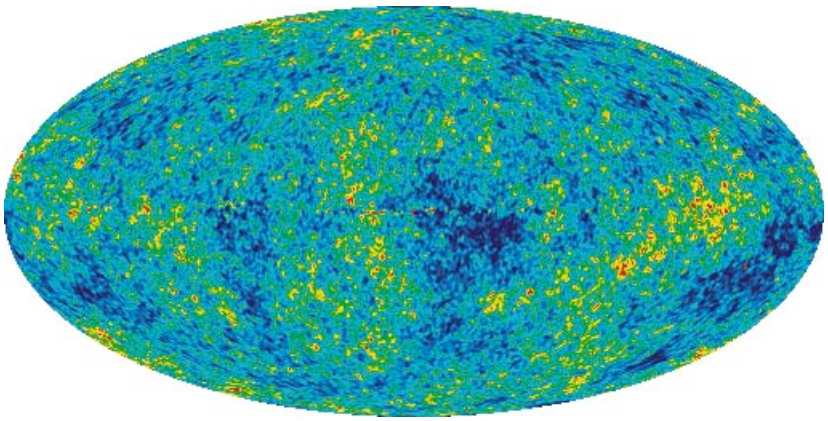

Figure 1.2: The cosmic microwave temperature fluctuations from the 5-year WMAP data seen over the full sky. The average temperature is 2.725 Kelvin, and the colors represent temperature fluctuations. Red regions are warmer and blue regions are colder with a relative difference of about 0.0002 degrees. Credit: Hinshaw *et al.* (2009).

There is general agreement that the observed anisotropy in the CMB grew from the gravitational pull of small fluctuations present in the early universe. These perturbations, mainly dominated by dark matter gave rise to acoustic oscillations in the photon-baryon fluid due to a competition between the photons and the baryons. The gravitational attraction between baryons makes them tend to collapse and form denser halos which will compress the photon-baryon fluid whereas the photon pressure provides an opposite restoring force. This will result in oscillations giving rise to sound waves propagating in the fluid. At the time of recombination, the oscillation phases were frozen in the CMB and projected on the sky carrying an imprint which is strongly dependent on the cosmological parameters.

The information that we can extract from the CMB lies in the angular correlations. In particular, the angular scale correlation provides the ”travel length” (sound horizon) at recombination. The CMB

anisotropy is in practice decomposed on spherical harmonics

$$\delta T(\theta, \phi) = \sum_{lm} a_{lm} Y_{lm}(\theta, \phi) \tag{1.29}$$

where the two angles, θ and ϕ specify the position in the sky. The standard measure of the CMB anisotropy is generally described by the angular power spectrum at each l , conventionally written as

$$(\delta T)^2 = \frac{l(l+1)}{2\pi} C_l \tag{1.30}$$

where $C_l =< |a_{lm}|^2 >$ is an average over m.

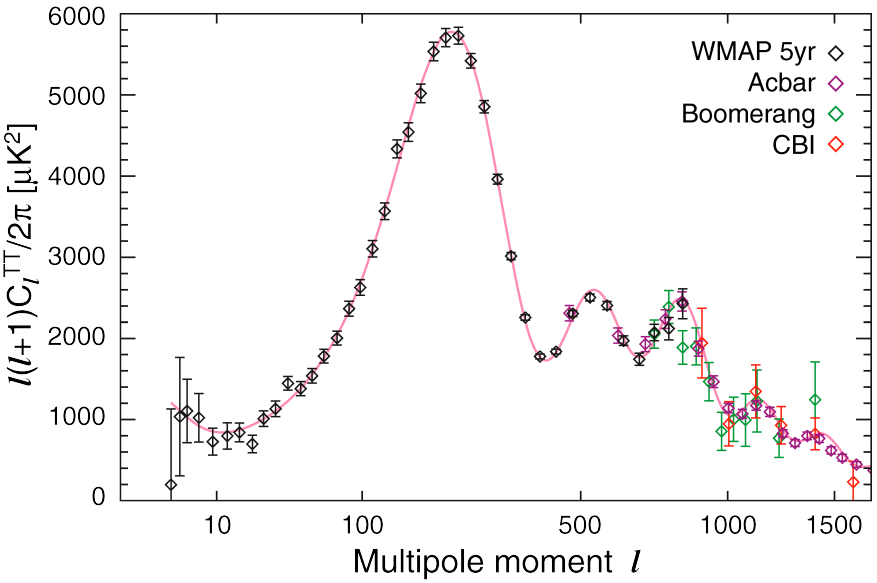

Figure 1.3: This figure illustrates the angular size of the observed temperature fluctuations. The large first peak corresponds to the maximum angular correlation in the CMB map. Credit: Nolta *et al.* (2009)

In figure 1.3 the angular power spectrum from the WMAP5 release (Nolta *et al.*, 2009) is shown. The first and dominating peak shows a maximum power at $l \sim 220$ which corresponds to an angular size of about 1 degree. From the location of this peak, information about the overall geometry of the universe can be extracted. (Note that the angular power spectrum consists of several peaks when expressed in spherical harmonics, but in direct space (a simple 2 point correlation function) it will present just 1 peak in analogue to the Baryon Acoustic Oscillations (see next section)).

The method is the following. The preferred angular size corresponds to the size of the sound horizon at recombination divided by the angular diameter distance from the observer to recombination. The size of the sound horizon can be determined using the speed of the sound waves and the time elapsed from the Big Bang to recombination. Both the size of the sound horizon and the angular diameter distance are dependent on the underlying cosmology and combining the CMB with a measurement of H_0 and/or other cosmological probes such as the BAO and the Type Ia supernovae provides excellent constraints on the geometry of the universe. The spatial curvature of the universe has thus been probed to be very close to 0 (we live in a flat universe) (Komatsu *et al.*, 2009).

The angular power spectrum depends on the underlying cosmology and can be used to probe several cosmological parameters or different combinations of them. Using the CMB anisotropies one can probe the fraction of baryonic matter in the universe since this fraction will influence the balance between pressure and gravity in the baryon-photon fluid leading to an effect of increasing the amplitude of the oscillations as well as causing an alternation in the odd and even peak heights in the CMB spectrum.

Another striking feature in the CMB is the polarization of the radiation at the level of a few microkelvins. 2 different types of polarization exist, the E-modes and the B-modes. Polarization arises naturally due to Thomson scattering in the primordial plasma. The anisotropy needed in the plasma for polarization to occur could arise from different types of perturbations. The E-modes may be due to both scalar and tensor perturbations, but the B-mode is only due to tensor perturbations giving rise to a potential detection of primordial gravitational waves. The E-mode was first detected in 2002 by DASI and the TE (Temperature E-mode) correlation was measured by the WMAP in 2003. Detecting the B-modes will be extremely difficult since the signal is very small, they are believed to have an amplitude of at most 0.1 μK. The newly launched Planck mission is expected to measure the temperature anisotropies to cosmic variance up to $l = 2000$, to yield accurate measurements of E-modes, and to detect the small scale B-modes due to gravitational lensing of E-modes.

The latest cosmological results from the WMAP will be summarized in section 1.5 after an overview of the other cosmological probes.

1.8.2 Baryonic Acoustic Oscillations

As explained above, acoustic oscillations in the primordial plasma occur as a consequence of the competition between gravitational attraction amongst the baryons and the pressure from the photons. Said in other words, the initial perturbations create a pressure imbalance in the baryon-photon gas and the way of stabilizing these imbalances is by creating sound waves. These oscillations leave their imprint in the CMB but the same features are predicted to create an imprint on baryonic structures at every stage of the evolution of the universe. These imprints are called Baryon Acoustic Oscillations (BAO).

After the discovery of the CMB, predictions affirmed that the same features should exist in the galaxy distribution. These features occur on very large scales, $\sim$ 150 Mpc at z=0. Together with the fact that they are small ($\sim$ a few %) poses a tremendous challenge to observations demanding surveys that cover large volumes of the universe. Thus at the time of prediction it was not possible to pursue a detection and the BAO were first detected in 2005 by the SDSS team (3.4σ detection) (Eisenstein *et al.*, 2005) and rapidly after confirmed by the 2dF Galaxy Redshift Survey team (Cole *et al.*, 2005; Percival *et al.*, 2009).

In the early universe the major components of the universe, i.e., dark matter, baryons, photons, neutrinos, behaved as one strongly-coupled single fluid. To explain the origin of the baryon acoustic oscillations further, we shall here consider one of the over dense initial perturbations present in the early universe[1]. We will look at the mass profile of the perturbation as a function of radius from the center of the initial perturbation and see how it evolves with redshift (time) (see fig 1.8.2a). The neutrinos immediately start to free stream away from the perturbation since they do not interact with any of the components in the fluid and are too fast to be gravitationally bound (see fig. 1.8.2b). The cold dark matter only responds to gravity and stays in the center of the perturbation. At this time (before the recombination period), the photons and the gas (electrons and nuclei) are bound together in one single

[1]This explanation is based on the detailed description of the BAO made by Daniel Eisenstein which can be found on http://cmb.as.arizona.edu/~eisenste/acousticpeak/acoustic_physics.html

fluid with an enormous pressure. Pressure imbalances in this gas give rise to the creation of spherical sound waves resulting in the perturbation of the gas and the photons being carried out to a spherical shell (see 1.8.2b). Arrives the period of recombination where the photons decouple from the gas and start free streaming like the neutrinos (see fig. 1.8.2c) At this point, the pressure in the gas is released and the gas perturbation wave is frozen in. We are now left with an initial concentration of dark matter in the center of the perturbation and a peak of gas concentration further out (see fig. 1.8.2d). The dark matter and the neutral gas gravitationally attract each other and as time goes by, the perturbations begin to mix giving rise to the characteristic peak in the density spectrum (see fig. 1.8.2e). The acoustic peak decreases in contrast because there is much more dark matter than gas (see fig. 1.8.2f). In conclusion, galaxies form in regions with initial over densities and there should be an enhanced concentration of galaxies in the regions 150 Mpc (the distance between two galaxies is approximately 1 Mpc/h) away from these initial densities of the order of 1%. By studying the two point correlation function between galaxies of large volumes of the universe it is possible to probe the baryon acoustic oscillations.

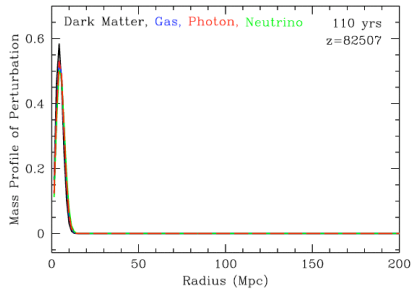

(a) the initial perturbation with all the components centered in the center of the perturbation

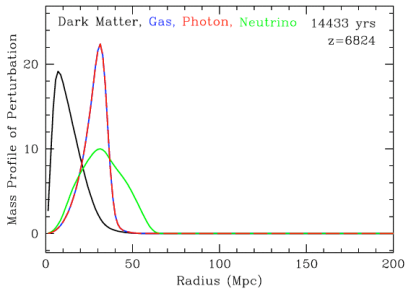

(b) The neutrinos are streaming away from the perturbation and the pressure of the photon-baryon gas gives rise to a sound wave moving the perturbation of the gas away from the center

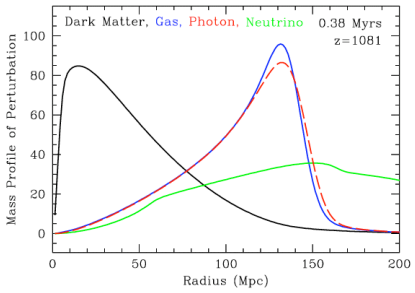

(c) The photons decouple from the matter and begin to free stream away from the perturbation.

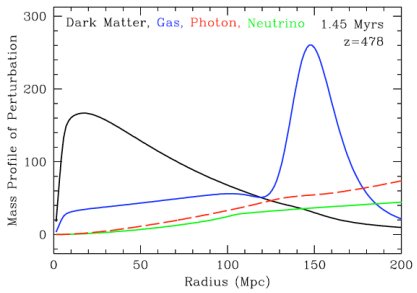

(d) The photons and neutrinos are gone and what is left is dark matter centered on the initial perturbation and a peak containing the gas around 150 Mpc away from the center

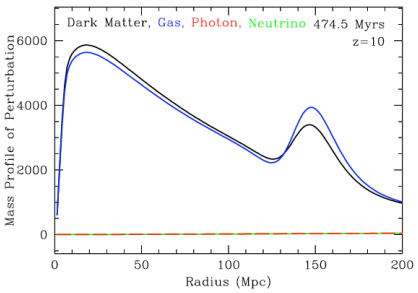

(e) The dark matter and the gas are gravitationally attracted to each other and start to mix.

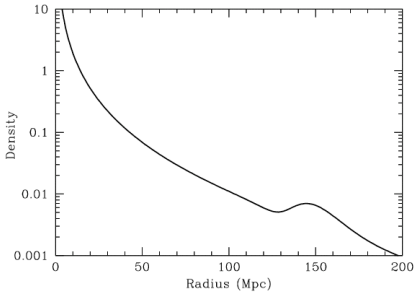

(f)

Figure 1.4: Educative figures on how to understand the BAO. The illustrations have been made by Daniel Eisenstein using the code CMBfast with the cosmology $\Omega_M = 0.3$, $\Omega_b = 0.049$, $h = 0.7$ and massless neutrinos.

Cosmology with BAO

The BAO is a recently detected and very powerful cosmological probe.

By measuring the correlation function for the large scale structures and compare it to theoretical predictions with a fixed baryon density parameter (derived by CMB and nucleo-synthesis) it is possible to probe the matter density in the universe since this is correlated with the shape and position of the observed acoustic peak. Eisenstein *et al.* (2005) first detected the baryon acoustic oscillation peak at the 3.4 σ level (see fig. 1.5). This plot shows the resulting correlation function for 46,748 galaxies out

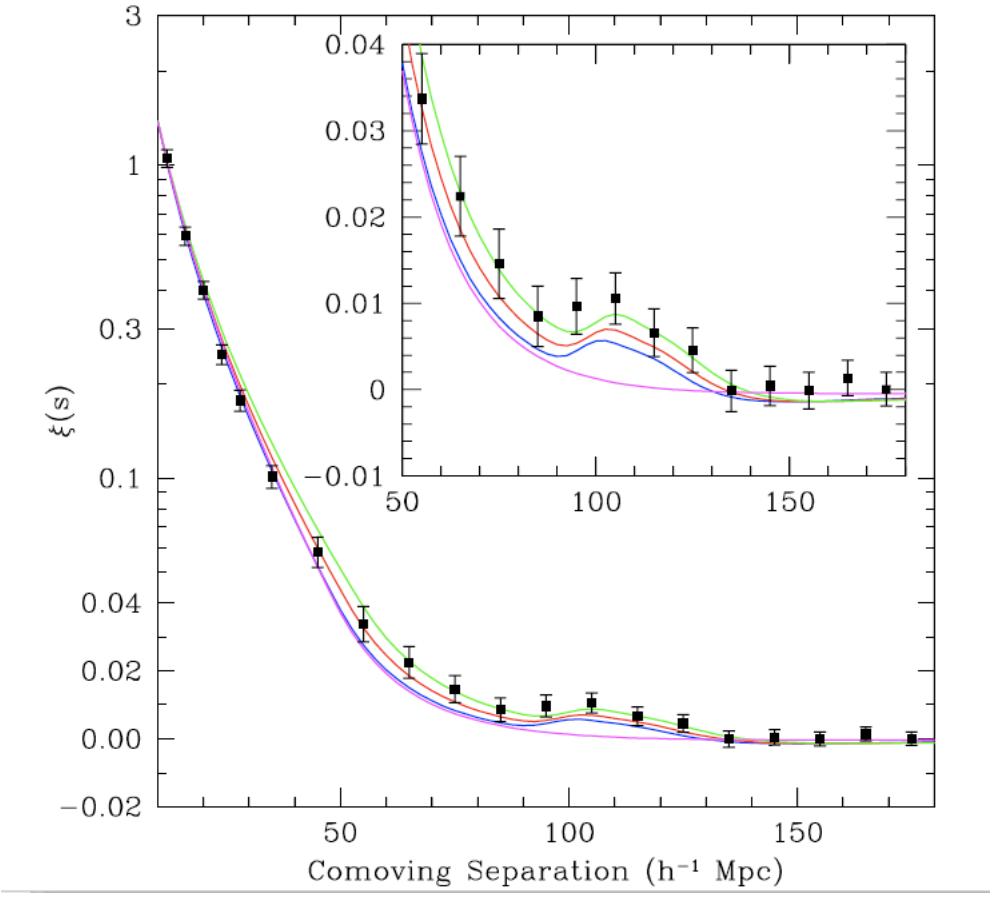

Figure 1.5: The two point correlation function for 46,748 galaxies out to a redshift of z = 0.47 covering 3816 square degrees of the sky measured by the SDSS team. The black dots are the data and the lines correspond to different models with different fractions of matter. The magenta line corresponds to a pure CDM universe. The small bump in the plot is the signature of BAO and is present at the characteristic scale $\sim 100h^{-1}$Mpc. Note that for a pure CDM universe, the BAO signature is not present. Credit: Eisenstein *et al.* (2005)

to a redshift of z = 0.47 covering 3816 square degrees of the sky. The black dots are the data and the lines correspond to different models with different fractions of matter. The magenta line corresponds to a pure CDM universe which is without the acoustic peak.

BAO can also be used to probe dark energy since the acoustic peak provides a standard ruler to

measure relative distances, hence providing a constraint to the evolution of the expansion rate of the universe. The idea is that, as in the CMB, the acoustic waves create a characteristic scale, the sound horizon which is the co-moving distance that the sound wave can travel between the big bang and recombination. The CMB provides a constraint on this distance divided by the angular diameter distance at recombination (z$\sim$ 1100) and measurements of the BAO results in the same constraints but at different redshifts. One can use BAO alone to yield ratios of angular distances at "low" redshifts (a cosmological test essentially similar to the Hubble diagram of supernovae), or add the CMB measurements at high redshift. At the moment the BAO have only been measured for 2 mean redshifts of 0.2 and 0.35, but in the future one should be able to see the BAO in different shells of redshift interval providing us with a very promising standard ruler for measuring ratios of angular diameter distances which gives rise to a probe of the expansion rate of the universe.

1.8.3 Cosmic shear

Gravitational lensing provides many of the spectacular events in the universe. Large galaxy clusters or very dense galaxies can produce highly distorted arcs or multiple images of background galaxies (see fig 1.6). However, such visual drama is rare and for most lines of sight in the universe the gravitational lensing effect is present but only in the weak lensing regime. Weak lensing creates a distortion in the shape of background galaxies stretching them into elliptical shapes tangentially around the lensing foreground mass, an effect known as the shear (see fig. 1.7).

Figure 1.6: An image of the galaxy cluster Abel 2218 from the Hubble telescope where arcs and multiple images are present. Credits: NASA, Andrew Fruchter and the ERO team.

Unfortunately galaxies are not usually spherical and present an intrinsic ellipticity much greater than the ellipticity induced by gravitational lensing meaning that the weak lensing shear cannot be detected on a galaxy to galaxy basis. However in an isotropic universe, galaxy orientations due to intrinsic

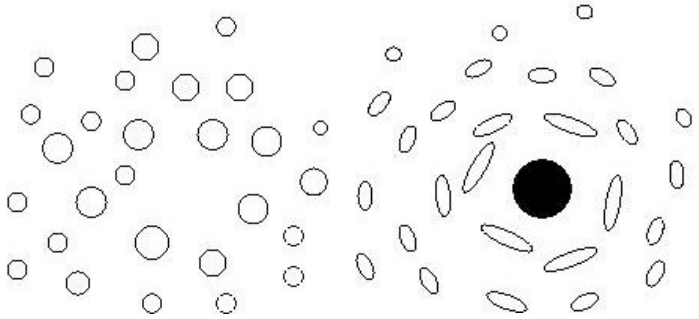

(a) Random intrinsic spherical galaxies

(b) The same galaxies distorted by a foreground mass concentration

Figure 1.7: A grossly exaggerated image of the weak lensing effect of a foreground mass density on background galaxies

properties are random and must average out over a large sample of galaxies. Any coherent alignment of large galaxy samples must thus arise from the effect of weak lensing by foreground structures[2]. Measuring the effect of weak lensing over great patches of the sky can thus provide direct information about the mass fluctuations in the universe.

The cosmic shear refers to the weak lensing effect induced by large scale structures which is very small but detectable today. The utilization of this effect involves computing the shear correlation function which is the mean product of the shear at two points as a function of the distance between those points. These shear correlation functions can be related to the matter power spectrum and the redshift distribution of the sources. The shear correlation functions are sensitive to both the geometry of the universe and the growth of structures.

The detection of the weak lensing of background galaxies requires large samples of galaxies and even though it has been known to exist for some time it has not been technically possible to observe the weak lensing signal until recently. The first detection of the coherent distortion of faint galaxies was made in 2000 by several groups (Wittman *et al.*, 2000; Van Waerbeke *et al.*, 2000; Bacon *et al.*, 2000; Kaiser *et al.*, 2000) proving that the statistics of shear is promising for fundamental cosmology.

Another interesting feature of weak lensing and one of the reasons why it is also so powerful is tomography. Providing we know the redshift distribution of the source galaxies it is possible to measure the weak lensing signal as a function of redshift. This is a big advantage over CMB where the only probed redshift is that of the recombination, $z \sim 1100$, and thus CMB data alone is not very sensitive to the evolution of dark energy. Weak lensing tomography gives the possibility of probing the time history of the expansion of the universe and the growth of structure which again is highly sensitive to dark energy.

1.8.4 Type Ia Supernovae

The last but not least of the common cosmology probes is type Ia Supernovae. Type Ia SNe will be explained thoroughly in the next chapter so here I will just give a brief summary of how to use these extraordinary objects as cosmological tools. Type Ia SNe are very bright and spectacular stellar

[2]Note that intrinsic alignment among galaxies do exist and is one of the systematic uncertainties in weak lensing

explosions with the unique property of having a nearly uniform intrinsic luminosity (absolute magnitude M~-19). Furthermore, the intrinsic luminosity variations are correlated with observables independent from the observed luminosity (see chapter 2). This makes them one of the best standardizable candles of our times. For a standard candle one can define the distance modulus, μ which is related to the luminosity distance , d_L by

$$\mu = m - M = -5 \log_{10} \left(\frac{10pc}{d_L} \right) \tag{1.31}$$

where m is an apparent magnitude and M is the absolute magnitude.

Taking a glance at section 1.6 and equation 1.17, it is easy to see that the luminosity distance is closely related to the cosmological parameters and it is possible by calculating the luminosity distance for standard candles to constrain these parameters.

Type Ia Supernova and Dark energy

One of the great stories of cosmology was the discovery that our universe is not matter-dominated today and we need a new form of energy, dark energy to explain several observations. Type Ia SNe provided the most convincing evidence of the existence of such energy.

In the late 90s two independent groups started the search for a statistically large number of high-z (z~ 0.5) type Ia SNe; The High-Z Supernova Team (Schmidt *et al.*, 1998; Riess *et al.*, 1998; Garnavich *et al.*, 1998; Riess *et al.*, 2000; Tonry *et al.*, 2003; Barris *et al.*, 2004; Clocchiatti *et al.*, 2006) and the Supernova Cosmology Project (Perlmutter *et al.*, 1995, 1997a, 1998, 1999; Knop *et al.*, 2003). The idea was to determine the luminosity distances and thus measure the cosmological parameters. Expecting a matter-dominated universe they were amazed to find that the data are much better suited to a universe dominated by a cosmological constant.

Type Ia Supernovae are used to measure the expansion history of the universe. If the universe is matter-dominated (which was the common belief before the discovery of 1998) the gravitational forces would cause a slowing down in the expansion of the universe leading to the fact that distant supernovae should move away faster than nearby supernovae. But the results showed that the distant supernovae moved slower than believed and as a result, the universe is expanding faster and faster and thus our universe is accelerating. To obtain such an acceleration it is necessary to introduce a dominant form of energy that acts as a repellant force giving rise to the dark energy with the property of having a negative pressure.

Since 1998, other supernovae surveys such as the SNLS[3] and the ESSENCE[4] have confirmed this discovery and put stringent constraints on the cosmological parameters (Astier *et al.*, 2006; Wood-Vasey *et al.*, 2007).

1.9 Current state and the future

Each cosmological probe can constrain a particular set of cosmological parameters, even often a combination of parameters. It is very important to conduct analysis combining all these already powerful probes since this can lead to a breaking of degeneracies which are particular to each probe leading to extremely well determined constraints on cosmology (see an example fig 1.8).

[3]http://www.cfht.hawaii.edu/SNLS/

[4]http://www.ctio.noao.edu/wproject/

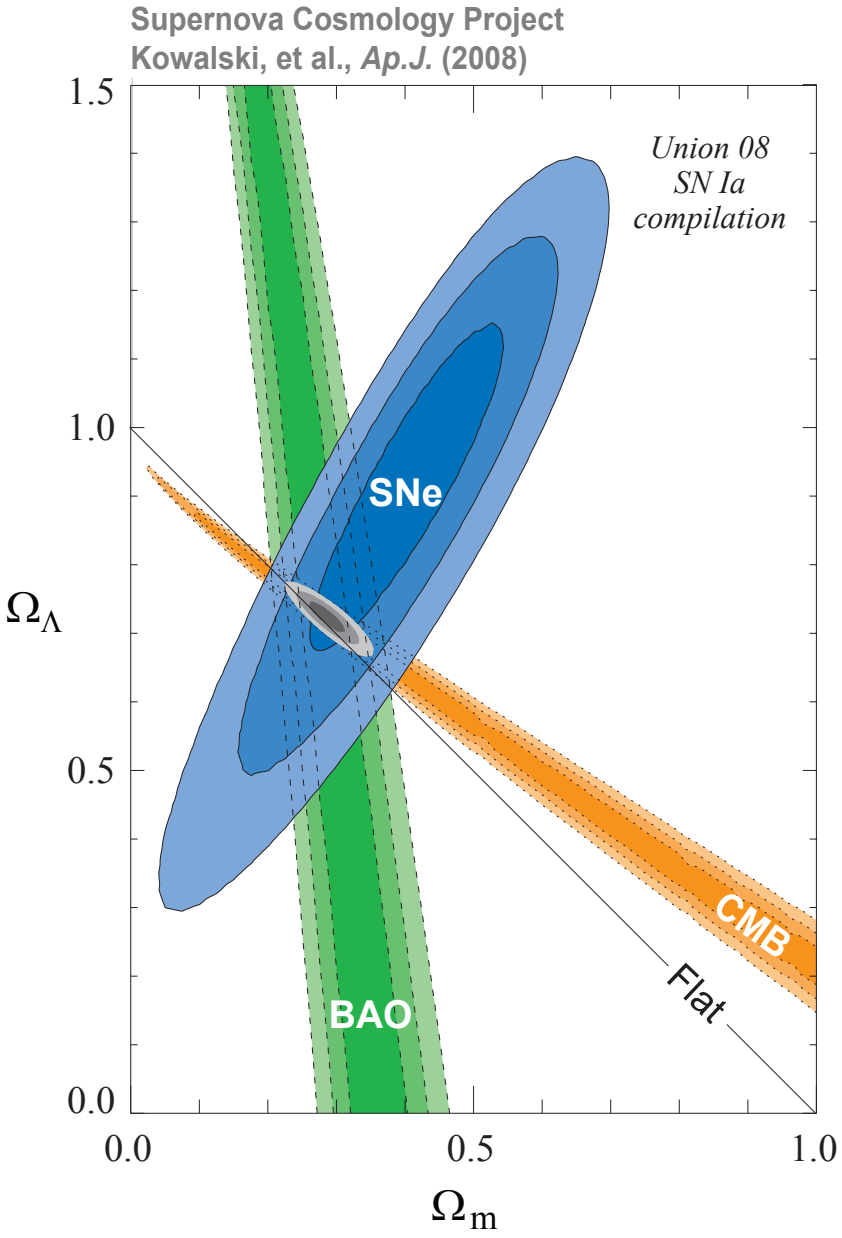

Figure 1.8: Confidence contours (68%, 95% and 97.3%) for a fit to an (Ω_M, Ω_Λ) cosmology obtained by combining different cosmological probes: Type Ia SNe, CMB and clusters. Credit: Kowalski *et al.* (2008)

The efficiency is maximized when the different probes are complementary which means that the degeneracies on the cosmological parameters are orthogonal. This is for instance the case when combining CMB data with distance measurements from type Ia supernovae in the $(\Omega_m, \Omega_\Lambda)$ plane.

For the moment, all data are consistent with the simple flat ΛCDM-model which includes the cosmological constant (Λ) and cold dark matter (CDM). This model is also referred to as the concordance model and depends on 6 free parameters.

- H_0, the Hubble constant which determines the present expansion rate of the universe.
- Ω_b, the baryon density in the universe
- Ω_m, the total matter density in the universe
- τ, the optical depth to reionization.
- A_s, the amplitude of the primordial spectra
- n_s, the scalar index of the primordial fluctuations. This parameter gives a measurement of how the fluctuations change with scale.

Other parameters that can be derived are for example the critical density ρ_c, the dark energy density Ω_Λ, the amplitude of mass fluctuations σ_8 and the age of the universe t_0.

Combining all the cosmological probes gives us the well known picture, the universe is flat and consists of a fairly small fraction of baryonic matter ($\Omega_b \approx 0.044$), a larger fraction of dark matter ($\Omega_{dm} \approx 0.23$) and the dominant component today, some form of dark energy makes up for the rest.

A brief summary of the cosmological results from WMAP-5 combined with Type Ia SNe and BAO (Komatsu *et al.*, 2009)

- We live in a spatially flat universe. In the case of a ΛCDM cosmology, the curvature density parameter, Ω_k, is compatible with 0, $\Omega_k = -0.0050^{+0.0061}_{-0.0060}$.
- Ω_b (baryons) = 0.0456± 0.0015 and Ω_{dm} (cold dark matter) = 0.228 ± 0.013 for a flat ΛCDM cosmology.
- When fitting for a dark energy with a constant equation of state, w, in a flat universe $w = -0.992^{+0.061}_{-0.062}$ whereas allowing a non-zero curvature results in $w = -1.006^{+0.067}_{-0.068}$. In the case of a time-dependant equation of state, the present day value of w, w_0 is constrained to $w_0 = -1.06 \pm 0.14$ for a spatially flat universe. The derivative of the equation of state parameter, w', is set to $w' = 0.36 \pm 0.62$
- Our universe is observed as being nearly flat and the fluctuations observed by WMAP seems to be nearly Gaussian (Komatsu, 2003) and adiabatic (Spergel & Zaldarriaga, 1997; Spergel *et al.*, 2003; Peiris *et al.*, 2003). One way of explaining these observational facts is to invoke inflation (Starobinskii, 1979; Guth, 1981; Linde, 1982; Albrecht & Steinhardt, 1982). We currently believe that during a fraction of a second after the Big Bang, the universe underwent an exponential expansion which is referred to as the period of inflation leading to a nearly flat universe with the curvature density parameter, Ω_k, of the order of the quantum fluctuations, 10^{-5}. There is no direct evidence of inflation ever happening and a huge variety of inflation models exists. By using the

polarization data from the WMAP5 it has been possible to exclude a large set of inflation models based on the measurement of the spectral index of initial scalar fluctuations, n_s, and the ratio of the amplitude of tensor fluctuations to scalar fluctuations r.

- The WMAP5 data has placed limits on the total mass of effective neutrinos and the effective number of neutrino-like species still relativistic at recombination. Neutrinos have been established to have a non-zero mass by neutrino oscillation experiments (Davis *et al.*, 1969; Ahmed *et al.*, 2004; Hirata *et al.*, 1992; Araki *et al.*, 2005; Ahn *et al.*, 2003) and tight limits have been set on the squared mass differences between the neutrino mass eigenstates. Cosmology can also provide useful limits on neutrino masses (Hannestad & Raffelt, 2006; Ichikawa *et al.*, 2005; Goobar *et al.*, 2006; Seljak *et al.*, 2006). CMB alone cannot set very stringent limits on the total mass of neutrinos, but combined with distance estimators such as Sne Ia and BAO and sometimes also the shape of the galaxy power spectra, important limits can be derived.

  Combining WMAP5 with Sne and BAO yields the following limit on the sum of the neutrino masses: $\sum m < 0.67$ eV (95% CL) for $w = -1$. The effective number of neutrinos at recombination is derived as $N_{eff} = 4.4 \pm 1.5$ which is consistent with the standard value of 3.

- All in all, the latest results are all in agreement with the previous results and this favors the simplest ΛCDM model. Variations from this model like non-Gaussianity and non-adiabiticity have been tested and no convincing deviations have been found.

Today is a very exciting period for cosmology. Due to the rapid technical improvements over the last decade we can now glimpse the possibility of testing several theories with solid observational results which a mere 20 years ago would have been impossible. New big projects to improve these already excellent cosmological probes will make it possible to study the evolution of the universe in detail and hopefully the puzzle of dark matter and dark energy will seem clearer.

Among the new projects it is worth mentioning the Planck satellite which has recently been launched expecting to harvest new and exciting information about the CMB. The new upcoming ground based 8.4-meter telescope, LSST[5] (Large Synoptic Survey Telescope) will be a wide-field deep survey covering more than 20,000 square degrees. LSST will include both weak lensing measurements, baryonic acoustic oscillation determination and distance measurements with type Ia supernovae. Two new satellite project JDEM[6] (Joint Dark Energy Mission) and EUCLID[7] are being conceived at this moment with the aim of putting tight constraints on the evolution of dark energy.

Thus, the era of observational cosmology is in its very promising beginning

[5]http://www.lsst.org/lsst

[6]http://jdem.gsfc.nasa.gov/

[7]http://sci.esa.int/science-e/www/area/index.cfm?fareaid=102

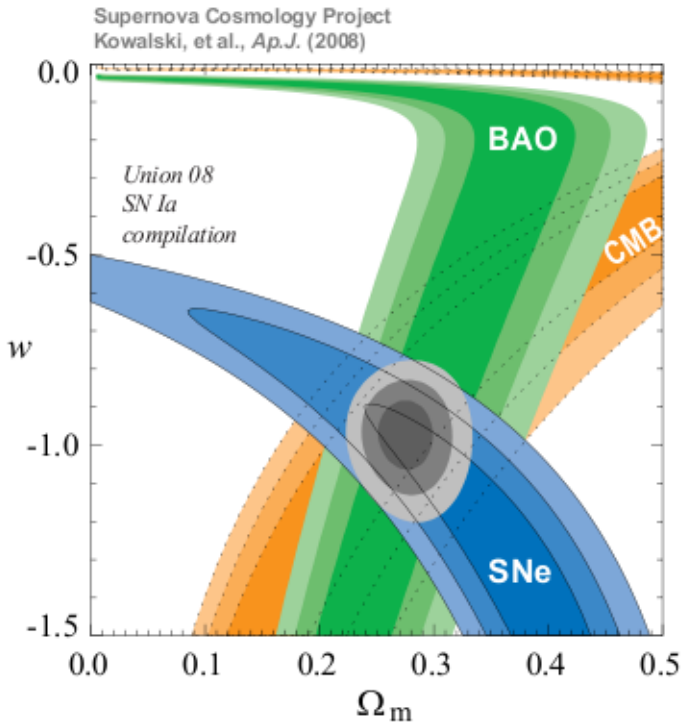

Figure 1.9: Fit to a flat (Ω_M,w) cosmology for SNeIa, BAO and CMB combined. The plot shows the contours at 68%, 95% and 99.7% confidence levels. Credit: Kowalski *et al.* (2008)

Chapter 2

Type Ia Supernovae

A supernova is the result of a huge stellar explosion ending the life of a star. It can be as bright as an entire galaxy for a few weeks making it visible over extremely large distances. In chapter 1 we saw that Type Ia supernovae are excellent distance estimators and highly used as cosmological probe. They show uniform light curves (the flux evolution of the supernova in different bands) and a small dispersion among their peak absolute magnitude. Together with the fact that they are extremely luminous makes them good standardizable candles. In this chapter, Type Ia supernova and their use in cosmology will be presented.

2.1 Observational facts

Spectroscopic classification

Supernovae come in two main observational categories. This classification consists mainly of spectral features of the supernova at maximum light (Filippenko, 1997; Turatto, 2003). Those who exhibit hydrogen in their spectra are classified as Type II and those who lack hydrogen are classified as Type I (see fig. 2.1). Within these two types there are different subtypes. Type II supernovae are subdivided into IIL and P where the hydrogen line is dominant and IIb where the helium line is dominant. Among the Type I supernovae we distinguish between Ia which are characterized by prominent absorption lines near λ 6150Å attributed to Si II, Ib which lack the Si feature but instead show strong He I lines, and Ic which presents no He lines. For a complete and detailed version of the classification scheme see Filippenko (1997).

In Figure 2.2 the spectrum of a typical Type Ia supernova near maximum light is shown. Several absorption features are present in this spectrum such as MgII and FeII and of course the SiII (6150) line, which is the signature of Type Ia SNe. The matter ejected from the explosion travels at high velocities, approximately 10,000-20,000 kms^{-1}, which results in a relative blueshift due to the line of sight speed towards the observer and a broadening of the absorption lines du to the isotropic exlosion.

Light curves of Type Ia supernovae

Photometric supernova surveys measure the light curves of the supernova which consists of the integrated signal in each filter (optical and near-infrared) for different spaced observations in time (during $\sim 60 - 90$ days for type Ia SNe). The majority of Type Ia SNe have characteristic and very similar light

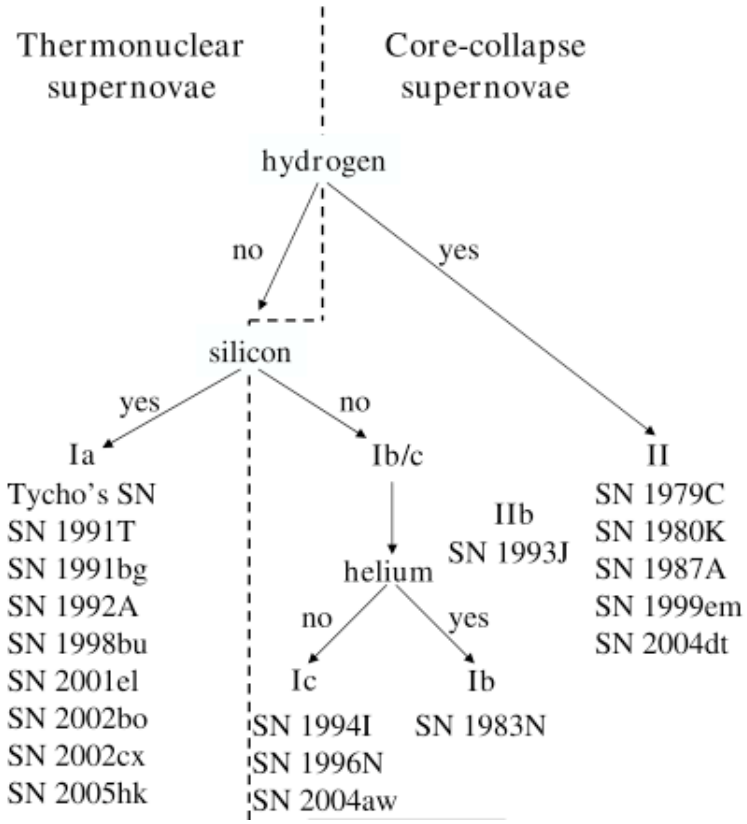

Figure 2.1: An overview of the classification scheme for SNe. Credit: Leibundgut (2008)

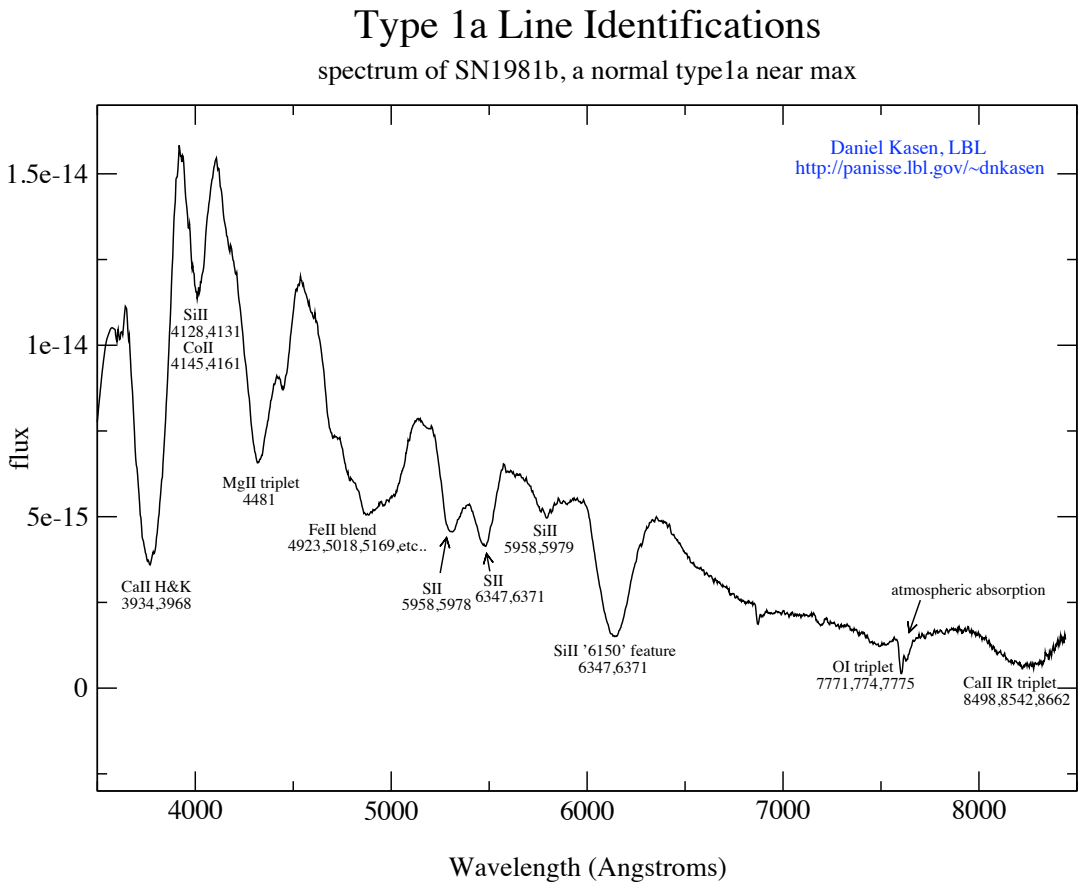

Figure 2.2: A typical SN Ia spectrum near maximum light showing the different absorption features. Credit: Daniel Kasen, LBL.

curves lasting for several months. Typical light curves in the standard Johnson-Cousins (UBVRI) filters for a Type Ia supernova are shown in fig 2.3. By convention, the origin of the timescale corresponds to maximum luminosity in the B-band. The shape of the light curve depends on the filter in which the supernova has been observed. In general, the light curves are bell-shaped but in the R-band we observe a typical shoulder and in the I-band a second maximum. A thorough discussion on the shapes of Type Ia SNe lightcurves can be found in Kasen *et al.* (2007); Woosley *et al.* (2007); Kasen *et al.* (2008)

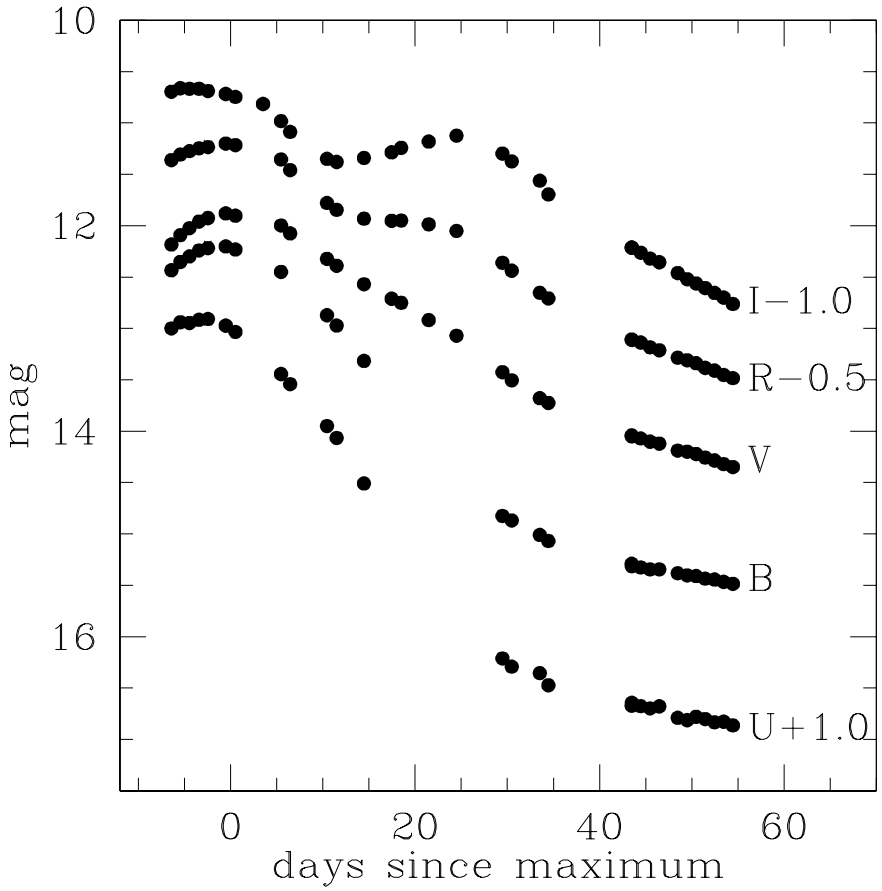

Figure 2.3: Typical SN Ia lightcurves in the UBVRI bands. Credit: Guide (2005)

Even though Type Ia SNe are quite homogeneous they still present variations in the peak brightness of the order of σ = 0.5mag. This is not sufficiently precise to use them as distance indicators. Fortunately, the shape of Type Ia SNe light curves and the color of the SNe are related to their intrinsic peak luminosity.

Using measurements of nearby SNeIa where the functional form of the luminosity-distance relationship is relatively insensitive to the underlying cosmology, Phillips (1993) showed that the intrinsic luminosity of a supernova correlates with the detailed shape of the overall light curve. Slowly declining supernovae are brighter than fast declining supernovae and as a result, the light curve is stretched as a function of maximum peak brightness, also called the width-luminosity relation. In the same spirit, the SNe also present a correlation between the color of the supernova and its maximum peak brightness, the brighter-bluer relation, expressing the fact that blue supernovae are brighter than red ones. Using

these two correlations results in a significant decrease in the peak brightness dispersion ($\sigma \sim 0.15$mag) making type Ia supernova excellent standard candles.

Remark on K-correction and filters

A small comment concerning the K-correction and filters will be useful in the following:

In astronomy, the flux of an object is measured through different instrumental filters or bandpasses and as a consequence we will only see a fraction of the spectrum redshifted into the observer frame. This is illustrated in fig. 2.4.

To be able to convert the observed flux of an object to rest-frame flux a correction is needed, the K-correction. If we wish to know the absolute magnitude M_Q in the emitted-frame bandpass Q for a source observed to have and apparent magnitude of m_R (observed through the bandpass R) we would have to apply the k-correction, K_{QR}

$$m_R = M_Q + \mu + K_{QR} \tag{2.1}$$

where μ is the distance modulus defined in eq. 1.31. The K-correction is a function of the spectral energy density of the object, the different bandpass and the redshift of course and is defined as

$$K_{QR} = -2.5 \log_{10} \left[\frac{1}{(1+z)} \times \frac{\int S(\lambda/(1+z)) T_R(\lambda) d\lambda}{\int S(\lambda) T_Q(\lambda) d\lambda} \times \frac{\int S_0(\lambda) T_Q(\lambda) d\lambda}{\int S_0(\lambda) T_R(\lambda) d\lambda} \right] \tag{2.2}$$

where $S(\lambda)$ is the spectrum of the object, $S_0(\lambda)$ is the spectrum a reference object and $T(\lambda)$ is the transmission of the bandpass. For an overview of the K-correction see (Hogg *et al.*, 2002).

With respect to filters, the Landolt Johnson-Kron-Cousins-UBVRI filter system has been traditionally used and is a standard in astronomy. As a result, the supernova restframe emission is traditionally characterized in this standard filter system. In this chapter I will mainly display supernova properties using these standard filters. However, the observational filters may be different due to other filter sets being optimal for the telescope and the science performed at the telescope. To be able to connect the filter sets, another correction is needed, traditionally known as the S-correction (Stritzinger *et al.*, 2002).

Note however, as we will see in chapter 5, that within the SNLS collaboration (Astier *et al.*, 2006), the K and S corrections are not used as described above. The SNLS use a modeling of the SN spectral sequence integrated in the observed filters which is directly compared to the observations.

2.2 Theoretical model

All supernovae are the stellar explosion of massive stars, but Type Ia supernovae are believed to be related to a quite special mechanism, which gives rise to such uniform objects. The most commonly accepted model of type Ia SNe is that of an explosion of a carbon and oxygen white dwarf in a binary system which accumulates material from a nearby companion star.

Figure 2.5 illustrates one plausible, though not yet confirmed, progenitor system of a Type Ia Supernova. The system starts with the existence of a binary system composed of 2 stars, one more massive than the other which gives rise to a faster evolution leading to it becoming a red giant earlier than the other. This eventually leads to the collapse of the red giant and it becomes a white dwarf. A white dwarf is a very compact star mainly composed of carbon and oxygen. Since there is no more nuclear processes in the white dwarf, the only thing that supports the dwarf against self-gravity and collapse is the electron degeneracy pressure.

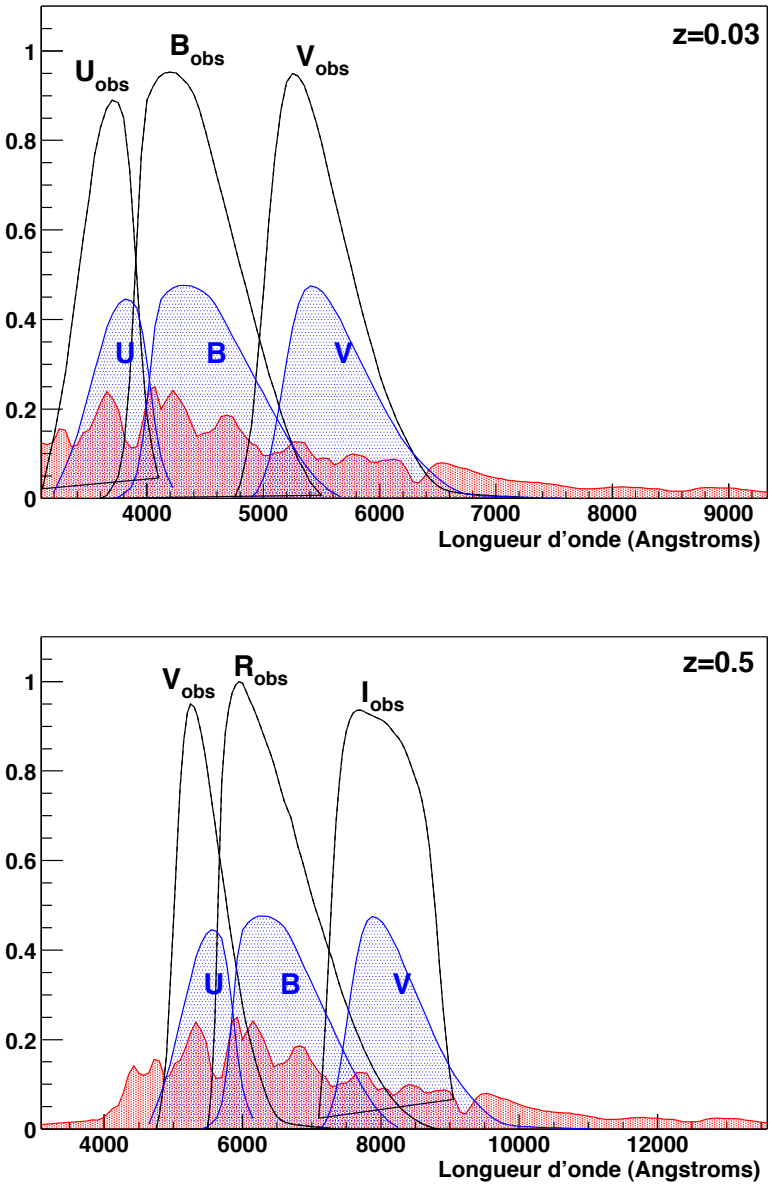

Figure 2.4: The spectrum of a supernova at z=0.03 (top panel) and z= 0.5 (bottom panel). In blue, rest-frame bands. In black observational bands. The rest-frame B-band emission of the SN which can be measured with the B-band for a nearby SN but must be measured in the R-band for a redshifted SN. Credit: Guide (2005)

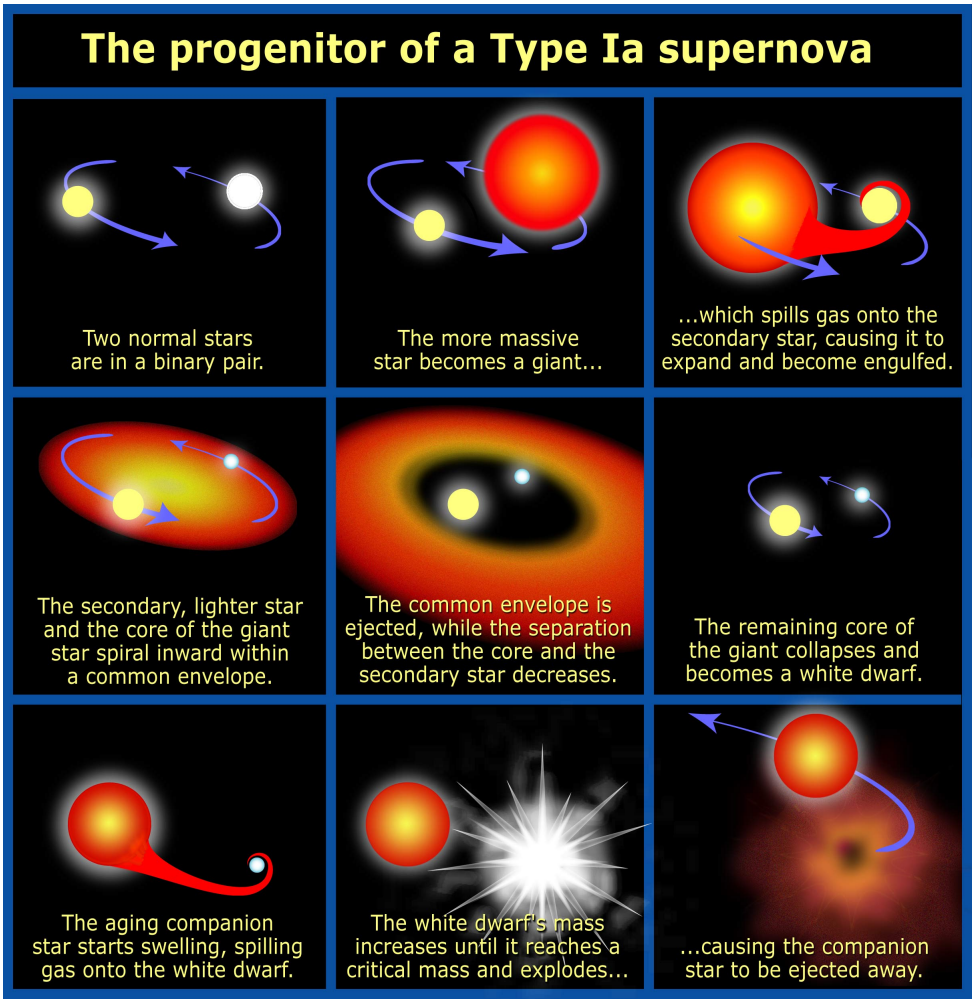

Figure 2.5: The progenitor of a Type Ia Supernova (Illustration credit: NASA, ESA, and A. Field (STScI))

In the new binary system , the companion of the white dwarf continues its evolution and becomes a red giant. The white dwarf now starts accumulating material from the red giant, but there is a limit to how much mass the white dwarf can accumulate before it explodes. This is referred to as the Chandrasekhar limit. The white dwarf may now approach this Chandrasekhar limit (the critical mass about $1.44 M_{\odot}$) which triggers a thermonuclear runaway explosion, giving rise to a spectacular event up to 9 billion times more luminous than the sun at maximum luminosity. A type Ia supernova is born.

Note that we cannot actually see the explosion but rather the light produced from the thermalization of gamma rays powered by radio-active decays from ^{56}Ni through ^{56}Co to ^{56}Fe (Colgate & McKee, 1969; Clayton, 1974; Kuchner *et al.*, 1994), hence the nickel mass is related to the observed luminosity at peak light. (For a review on different SNe Ia explosion models see Hillebrandt & Niemeyer (2000)).

This special scenario explains why all type Ia supernovae are so much alike given the varied range of stars they start from since the Chandrasekhar limit is a nearly-universal quantity. The slow approach to a sudden explosion at a characteristic mass erases most of the original differences among the progenitor stars and makes the light curves and the spectra of all type Ia supernovae remarkably uniform. However, there is still a scatter of approximately 40% in the observed peak brightness, which can probably be traced back to differences in the composition of the white dwarf or an anisotropic explosion seen from different angles (Kasen *et al.*, 2009).

2.3 Estimation of distances with SNe Ia

In cosmology, Type Ia SNe are used as distance estimators (see section 1.4.4) (Tonry *et al.*, 2003; Knop *et al.*, 2003; Astier *et al.*, 2006; Riess *et al.*, 2004; Wood-Vasey *et al.*, 2007; Riess *et al.*, 2007; Kowalski *et al.*, 2008). The distance estimates are obtained from a modeling of the observed light curves. Typically, the supernova observations are performed with a limited set of filters and a limited cadence of observations. To be able to interpolate between the spaced observations a modeling of the supernova emission is needed.

2.3.1 Distance modulus

Conventionally most people define a distance modulus, μ, as the rest-frame B-band magnitude (m_B) of the supernova minus its absolute magnitude in the same band, (M_B) which is related to the luminosity distance ($m - M = -5 \log_{10}\left(\frac{10pc}{d_L}\right)$) . Linear corrections as a function of a shape parameter and a rest-frame color are also applied to finally yield the following distance estimator

$$\mu = m_B - M_B + \alpha \times shape - \beta \times color \tag{2.3}$$

where *shape* and *color* are parameters related to the overall shape of the lightcurve and color and α and β are nuisance parameters related to the shape and the color respectively. m_B, *shape* and *color* differ from one supernova to another whereas the parameters M_B, α and β are the same for all SNe.

Although cosmology analyses based on SNe all perform linear corrections based on a shape and a color parameter the significance and value of these parameters may differ. The shape parameter may be a stretch parameter ($s - 1$) where, s, is indeed a stretch factor around maximum peak in the rest-frame B-band (Perlmutter *et al.*, 1997b; Guy *et al.*, 2005). The lightcurve fitter MLCS and MLCSK2 (Riess *et al.*, 1996; Jha *et al.*, 2007) use a shape parameter directly related to a luminosity offset Δ whereas

for the lightcurve fitter SALT2 (Guy *et al.*, 2007) the shape parameter is the coefficient x_1 of a linear combination of an average spectrum and the first principal component.

The exact definition and interpretation of the color parameter have been widely discussed and differ significantly from one analysis to another. It can be interpreted as extinction of the supernovae due to dust or intrinsic color differences or both. The SNLS collaboration has chosen to define one single color parameter without any attempt to separate the contribution from dust absorption and intrinsic color. Other analyses, such as the MLCS2k2 (Jha *et al.*, 2007) light curve fitter used in the ESSENCE (Wood-Vasey *et al.*, 2007) and the GOODS (Riess *et al.*, 2004, 2007) survey use a color term interpreted as extinction by dust and as a result β (from eq. 2.3) is fixed to R_B from the Cardelli *et al.* (1989) Milky Way extinction law. Currently, the interpretation of the color term is still under open debate (Tripp, 1998; Riess *et al.*, 2004; Guy *et al.*, 2005, 2007; Conley *et al.*, 2007; Riess *et al.*, 2007; Wood-Vasey *et al.*, 2007; Jha *et al.*, 2007; Conley *et al.*, 2008). Note however that all attempts to fit β find it smaller than R_B.

It is worth pointing out that recent effort has been made concerning the best choice of parameters to standardize SNe Ia and thus minimize the residuals to the Hubble diagram (Bailey *et al.*, 2009). This method is based on spectral flux ratios which at the moment provide among the lowest scatter Hubble diagrams ever published.

It should also be noted that whereas correction factors need to be applied in the optical to make SNe Ia standard candles they may be close to standard candles in the near-infrared (Krisciunas *et al.*, 2004). A very small scatter in the peak luminosity has been found without any luminosity indicators.

In conclusion, to date all Type Ia SNe surveys include linear corrections in their distance modulus based on a shape and a color parameter whose exact definition and interpretation may vary from one analysis to another. However, the goal of supernova cosmology is to obtain a distance estimator free of redshift dependent biases.

2.3.2 Light curve fitting

To obtain the set of parameters for each SN that are needed for the distance estimates, i.e m_B, *shape* and *color*, a modeling of the light curves to be able to extrapolate between observations in different bands is needed. For this purpose, a model of the spectral sequence of the SN is required. It has been proven extremely difficult to predict the observed sequence based on different physical models of the supernova progenitors and as a result, empirical methods of modeling are used in the light curve fitting today (SALT (Guy *et al.*, 2005), SALT2 (Guy *et al.*, 2007), SIFTO (Conley *et al.*, 2007), MLCS2k2 (Jha *et al.*, 2007)).

Traditionally, standard light curve templates based on the measurements of nearby SNe Ia (Goldhaber *et al.*, 2001) are defined and K-corrections as a function of phase, redshift and color (Nugent *et al.*, 2002) are applied to the data so as to compare the observational measurements with the "standard" light curve templates. Recently, improved methods taking into account the K-corrections by directly comparing the integrated spectral templates in the model of the instrumental response with the measurements and thus not correcting the data points have been developed (SALT, SALT2, SIFTO).

2.4 Hubble diagram

The distance-redshift relation, also referred to as the Hubble diagram is an extremely useful tool in cosmology. The Hubble diagram expresses distances in the universe as a function of redshift.

In practice it is the distance modulus (see eq. 2.3) as a function of redshift which is illustrated in the Hubble diagram. The Hubble diagram and the residuals to the best fit cosmology using the Union sample of all the available data sets is displayed in figure 2.6. Using previously showed cosmological models (see chapter 1) one can compare the theoretical luminosity distances for different cosmological parameters to the current data and thus constrain the cosmological parameters. After the construction of the Hubble diagram using the derived distance modulus (see eq. 2.3), the cosmological parameters are found by minimizing the residuals in the Hubble diagram. So far, the latest SNe Ia results are consistent with a value of $w = -1$ within the uncertainties which are of the order of 13% statistical and 13% systematic for ESSENCE (Wood-Vasey *et al.*, 2007), 9% statistical and 5% systematic for SNLS (Astier *et al.*, 2006) and 6% statistical and 6% systematic for the Union sample (Kowalski *et al.*, 2008), hence supporting the cosmological constant model.

2.5 Systematic uncertainties

With the strong increase in the number of discovered Type Ia supernovae the statistical and systematic uncertainties are currently at the same level, and hence just increasing the number of supernovae will not improve the cosmological results any longer. To perform precision cosmology we must be able to decrease the systematic uncertainties first.

Cosmology with Type Ia supernovae is based on flux ratios or equivalently luminosity distance ratios squared, of nearby and high-z supernovae

$$\frac{f(z_1, T_{rest})}{f(z_2, T_{rest})} = \left(\frac{d_L(z_2)}{d_L(z_1)}\right)^2 \tag{2.4}$$

where T_{rest} is the transmission of the filter in the rest frame band.

The flux of the supernova in its restframe is related to observations as follows

$$f(z, T_{rest}) = 10^{-0.4(m(T_{obs}) - m_{ref}(T_{obs}))} \times \frac{\int S_{SN}(\lambda) T_{rest}(\lambda) d\lambda}{\int S_{SN}(\lambda) T_{obs}(\lambda(1+z)) d\lambda} \int S_{ref}(\lambda) T_{obs}(\lambda) d\lambda \tag{2.5}$$

where $m(T_{obs})$ is the observed magnitude of the supernova, $m_{ref}(T_{obs})$ is the magnitude of a reference object, S_{SN} is the spectrum of the SN and S_{ref} is that of the reference object. This equation gives great understanding of the possible systematic uncertainties influencing the cosmological results. The first part of the equation is related to the observed magnitudes of the supernova and the reference object. This is defined by the photometry and the calibration and is thus highly sensitive to uncertainties in these areas. The second part takes into account the K-correction relating the observed magnitudes to a rest frame magnitude using an empirical method to model the supernova emission. The accuracy of the modeling of the filter transmission will also influence this part. The last piece of the equation is related to the choice of a reference object and the uncertainty associated with the spectrum of this object.

In addition, other external sources of systematic uncertainties such as a selection bias, evolution of the SN with redshift, possible contamination by other supernova types to the type Ia sample, extinction by dust in the host galaxy in relation to the choice of the color law as explained previously and gravitational lensing due to foreground mass densities must also be accounted for.

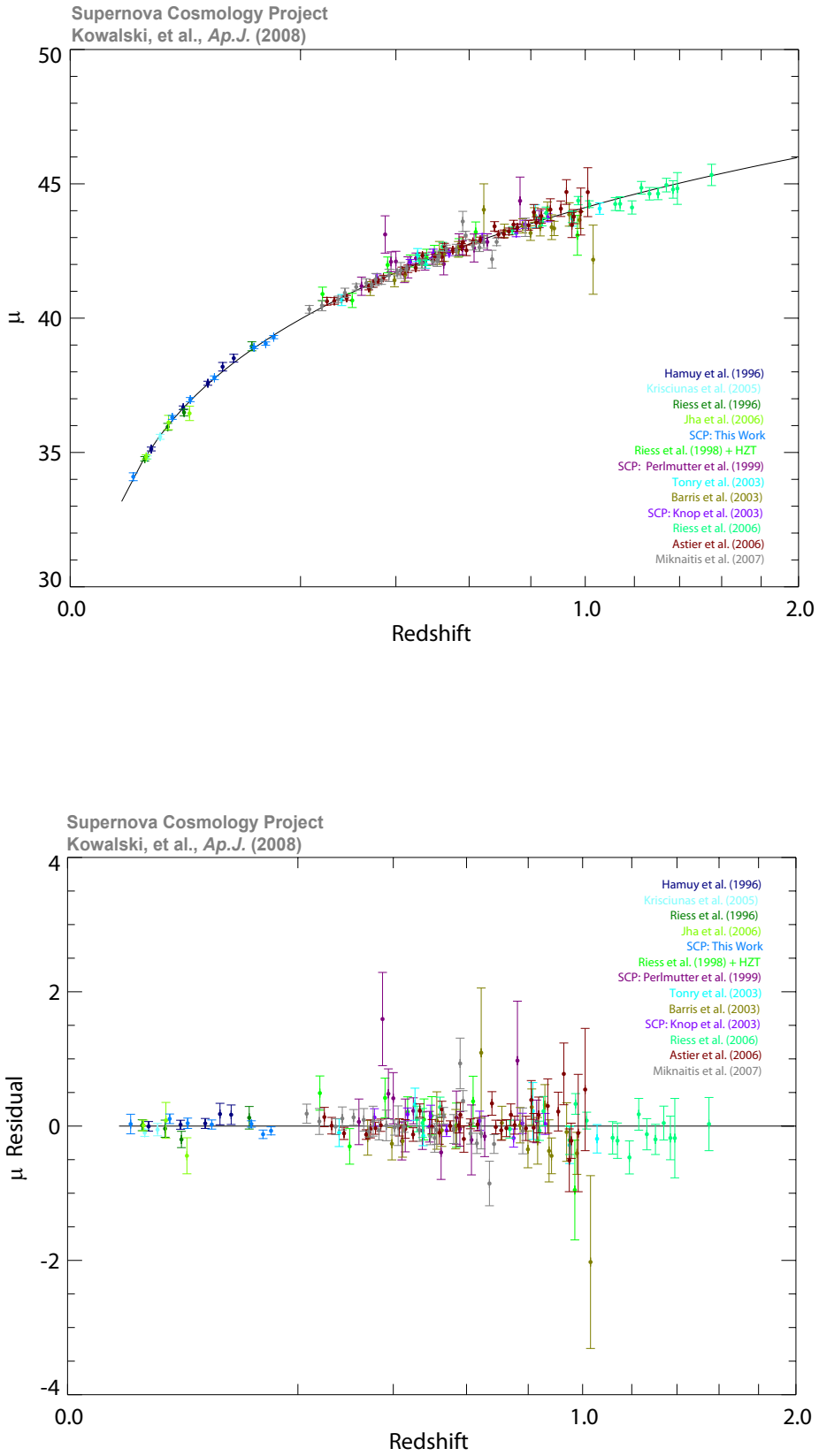

Figure 2.6: The Hubble diagram of the Union sample in the top panel and the residuals to the Hubble diagram in the bottom panel. Credit: Kowalski *et al.* (2008).

In this section I will give a brief description of some of these important systematics in todays supernova surveys.

2.5.1 Calibration systematics

Calibration is needed to transform the observed instrumental fluxes into physical flux units and is thus a crucial component in all cosmological observations and especially in precision measurements concerning type Ia supernovae. For supernovae surveys, the observations of objects in a large redshift range implies cross calibrating over four orders of magnitude with a relative precision to the order of 0.01 magnitude in todays surveys and even smaller in future surveys. Another critical aspect to take into account is that the observations are made in very different bands and with different telescopes which ultimately need to be transformed into the same magnitude system for comparison.

Here I will briefly explain how calibration in supernova surveys is performed in general and illuminate some of the systematics introduced in this process.

A brief overview of the calibration method

All supernova surveys aim at assigning calibrated magnitudes to both nearby and high-z supernovae expressed in the same photometric system. The calibration is in general carried out in 2 steps.

1. Choosing science field stars (tertiary stars) which are calibrated to standard stars (secondary stars) thus attributing magnitudes to the tertiary stars.

2. Converting magnitudes into physical fluxes using a spectrophotometric standard.

3. Using the calibrated tertiary stars to calibrate the supernovae.

The tertiary stars are observed in the science fields close to the supernovae. Standard stars are stars with known magnitudes given in a particular broadband magnitude system.

Assigning a magnitude to a star with respect to another star with known magnitude is done by measuring the ratio of the fluxes between the stars obtained with the same technique and with the same observational conditions.

$$m_A - m_B = -2.5 \log_{10} \frac{f_A}{f_B} \tag{2.6}$$

where m is the magnitude and f is the instrumental flux of the corresponding star. In this way we first calibrate the tertiary stars to the standard field stars attributing calibrated magnitudes to the tertiary stars. Then the same method is used when calibrating the SNe to the tertiary stars resulting in calibrated magnitudes for the SNe.

This is not the final outcome because for cosmological analysis we consider ratios of fluxes (see equation 2.4). In order to interpret the calibrated observed magnitudes as physical fluxes, we must know the magnitude and spectral energy density (SED) of a reference star. The calibrated flux, f, of an object with magnitude m can then be expressed as

$$f = 10^{-0.4(m-m_{ref})} \times \int S_{ref}(\lambda) T(\lambda) d\lambda \tag{2.7}$$

where m_{ref} is the calibrated magnitude of the reference star, $S_{ref}(\lambda)$ is the SED of the reference star and $T(\lambda)$ is the effective passband of the imager.

In the following, I will emphasize some of the systematics associated with calibration.

Systematic uncertainties involved in the calibration

In order to calibrate the tertiary stars it is necessary to choose a broadband magnitude system with a corresponding photometric catalog of standard stars. The optimal choice would be a standard photometric calibration system with a filter set close to the filters of the survey. This is not always possible and as a result it is necessary to model the transformation from the chosen photometric system in which the standard stars are reported to the observing camera system. This leads to systematic uncertainties. Other systematic uncertainties involved in the calibration of the tertiary stars are the photometry (the measurements of the secondary stars and the tertiary stars must be performed using the same photometry) and the normalization of the exposure time and air mass.

With respect to the choice of the optimal reference star, ideally, this star should be directly observable with the survey telescope although this is hardly ever the case since the standard star is often too bright. As a consequence one must rely on given magnitudes in a specific broadband system and possibly perform corrections to express the reference star magnitudes in the survey camera system introducing additional uncertainties. Uncertainties concerning the SED must also be included.

When calibrating the supernovae by measuring the flux ratio of the supernovae to that of the tertiary stars it is important to measure the flux of the tertiary stars and the supernovae using the exact same photometry. This will include systematic uncertainties.

2.5.2 Selection bias

The selection bias, also called Malmquist bias is a selection effect in observational astronomy for flux limited samples. The effect consists of the preferential selection of brighter objects when operating close to the detection limit. In a flux-limited supernova survey this implies an increase in the average measured supernova brightness in a redshift dependent way and may thus affect the cosmological results. The calculation of the distances is not uniquely dependent on the average luminosity but also on stretch and color which makes the correction due to selection bias a bit more complicated than a simple shift in the average luminosity (Perret, 2009, in preparation for the SNLS collaboration).

Another problem in current surveys is also that the nearby supernova sample combines SNe observed by various surveys giving rise to a sample with very different analysis paths and observational conditions that are not well known. As a result it is currently difficult to evaluate the Malmquist bias. However, new nearby surveys such as SkyMapper[1]amongst others will help making the modeling of this bias easier in the future.

In Astier *et al.* (2006) simulations were conducted so as to evaluate the selection bias for the SNLS sample and the nearby sample. They found that the bias on the distance modulus is about 0.02mag at z=0.8, increasing to 0.05 at z=1 for the SNLS sample and about 0.017mag for the nearby sample.

2.5.3 Possible supernova evolution

One of the questions that arose after the discovery of the acceleration of the universe through observations of Type Ia supernovae was the question of supernova evolution with time. Could it be possible to explain the results including a supernova evolution with time giving rise to intrinsically dimmer supernovae in the past. This has been proven not to be the case (see Leibundgut (2001)), but supernova evolution is still to be considered a source of systematic uncertainties.

[1]http://www.mso.anu.edu.au/~stefan/skymapper/

The idea of an evolution of the chemical composition and the metallicity of the supernova with time is somehow logical due to an observed evolution in the stellar composition. If this was the case, a difference should be of notice comparing spectra of low and high-z supernovae. What may be even more relevant to study is a possible evolution of the SNe as a function of the host galaxies properties such as morphology, star formation rate and metallicity.

Considerable effort has been put into the study of a possible supernova evolution. Astier *et al.* (2006) found no significant evolution of the color or the color-relation of the SNe with redshift nor with the stretch and the brighter-slower relation. When comparing spectroscopic indicators such as equivalent width and ejecta velocities of high and low-z supernovae, no evolution was found (Balland *et al.*, 2006; Blondin *et al.*, 2006; Bronder *et al.*, 2008). When comparing host galaxies a correlation between the stretch of the supernova and the host galaxy morphology has been found (Hamuy *et al.*, 1995, 1996, 2000; Riess *et al.*, 1999; Gallagher *et al.*, 2005). Sullivan *et al.* (2006b) show that the SNe exploding in an environment with high star formation rate have higher stretch and are thus brighter. This shows that to some extent, the SNe properties do depend on their environment. However, this dependency has little impact on cosmology since after corrections for the width-luminosity relation (stretch factor) the supernovae absolute magnitudes are the same.

Another claim of correlation has been made by Gallagher *et al.* (2008) expressing the fact that the residuals to the Hubble diagram may be correlated with the host-galaxy metal abundance. This has been predicted by theoretical models (Timmes *et al.*, 2003). However, the latest results from Sullivan *et al.* (2009) show that observed metallicity evolution can be explained with a redshift-evolving stretch distribution which results in the scenario of the non-evolution of supernova brightness with time.

2.5.4 Color parameterization

As already explained previously, the interpretation of the color parameter in the cosmological analysis can be ambiguous. The color term can be interpreted as extinction due to dust in the host galaxy or an intrinsic supernova color or both. The parameter β related to the color term in the distance modulus (see eq. 1.31) is within the SNLS collaboration fitted simultaneously with the cosmology without any priors on the origin of the color. Other groups like Wood-Vasey *et al.* (2007) and Riess *et al.* (2004, 2007) consider that the observed color excess is solely due to extinction by dust and they force β to be similar to the extinction curve of the milky-way galaxy. They use the Cardelli *et al.* (1989) extinction law and impose $\beta = R_B = 4.1$.

When no preconceived notions are added with respect to β several authors estimate this parameter to $\beta \simeq 2$ (Tripp, 1998; Guy *et al.*, 2005, 2007; Conley *et al.*, 2007, 2008) which is significantly different from 4.1. This implies that either the extinction law in supernova host galaxies is very unusual or an intrinsic supernova color which dominates over the extinction term is present.

Firm proof of intrinsic color term has not been established yet although several facts point in this direction. For instance, the distribution of supernova colors in spiral and elliptical galaxies are the same in spite of the expected higher dust density in spiral galaxies.

Note however that we expect more dust in galaxies at high redshift due to a higher Star Formation Rate in the past and as a consequence a redshift dependent bias may be induced when not correctly considering the dust properties of the SN host galaxy.

2.5.5 Gravitational lensing

The apparent brightness of a given supernova is affected by gravitational lensing due to the mass distribution along the line of sight. This will lead to a slight demagnification of most of the supernovae whereas a very small sample will be highly magnified with respect to a homogeneously distributed universe causing additional dispersion in the Hubble diagram.

Several papers have already showed interest in this subject and several estimations of the effect of gravitational lensing on the cosmological results have been made (Bergström *et al.*, 2000; Holz & Linder, 2005; Gunnarsson *et al.*, 2006; Jönsson *et al.*, 2006, 2008). These investigations show that the impact of gravitational lensing due to mass densities in the supernova line of sight on the cosmological parameters is small for current surveys (SNLS, ESSENCE, GOODS). For future surveys however, where the redshift limit is pushed further out, this effect may become an issue.With regards to the SNLS, Astier *et al.* (2006) showed that the systematic errors induced by gravitational lensing was rather small, a result that was confirmed by Jönsson *et al.* (2008) performing simulations for the final SNLS sample. However, the possibility of detecting a correlation between the observed brightness of the supernova and the magnification, a lensing signal, is shown to be possible within the SNLS sample (Jönsson *et al.*, 2008) and a tentative detection has been made in the GOODS field (Jonsson *et al.*, 2006). A firm detection would lead to a possibility of measuring the dark matter distribution as a function of stellar luminosity. This is the theme of my thesis and will be explained thoroughly in the next chapters.

Chapter 3

Gravitational lensing

The spectacular events of gravitational lensing can be seen in the universe as rings, arcs and multiple images and are merely a geometrical effect of light being bent around massive objects such as galaxy clusters (see fig. 1.6). In general relativity, the presence of matter will curve spacetime and as a consequence, light rays will be deflected leading to extreme events. But these cases of strong lensing are rare and in most cases gravitational lensing causes slight distortions and small magnifications. An important property of gravitational lensing is the fact that it depends solely on the mass distribution of the lens, hence it is a very powerful method to probe the distribution of dark matter in the universe which has been used widely in astronomy/cosmology over the past 20 years.

3.1 Some historical events

The discovery of gravitational lensing is often associated with Albert Einstein and general relativity but it was actually a German physicist, Johann Soldner, who pointed out the effect of deflection of light rays due to the Sun using newtonian physics. About a 100 years later Albert Einstein (Einstein, 1916) used general relativity to point out that the deflection angle resulting from general relativity is actually twice the newtonian prediction. This result was confirmed in 1919 by Arthur Eddington who during a solar eclipse measured the change in position of stars in the vicinity of the sun due to the gravitational solar attraction (Eddington, 1919). He measured a deflection angle comparable to the one predicted by Einstein leading to an immediate acceptance of the theory of General Relativity as a very successful and powerful theory.

The idea of observing multiple images of a source was examined (Chwolson, 1924; Einstein, 1936) but one came to the conclusion that the deflection angle was much too small to be observed for star sized lensing objects and thus would remain a theoretical curiosity. It was only a bit later that Zwicky (Zwicky, 1937) pointed out that considering galaxies instead of stars as lenses would lead to a large enough deflection angle to be observed and thus he gave great potential to gravitational lensing and mass determination. Lensing by galaxies and clusters are one of the major disciplines of gravitational lensing today.

3.2 Theory and the thin screen approximation

To give a thoroughly but simple explanation of gravitational lensing, I will use the thin screen approximation which is valid when the physical size of the lens is small compared to the distance between the source and the lens and between the lens and the observer. In this case the deflection is confined to a point of the light path. The mass distribution of the lens can then be replaced by a mass sheet orthogonal to the line-of-sight, the lens plane (see fig 3.10).

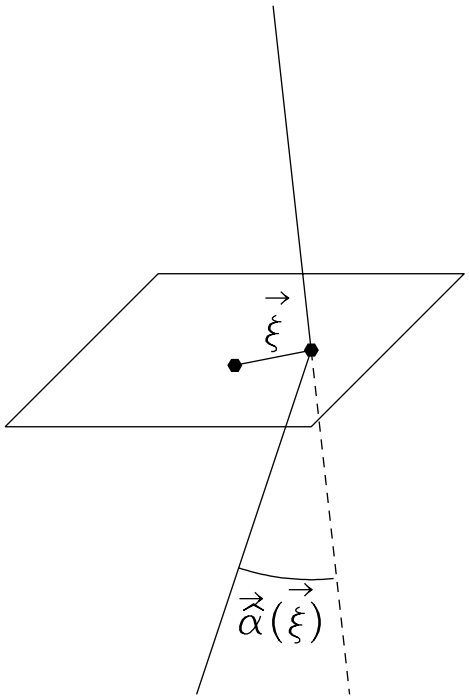

Figure 3.1: A light ray intersecting the lens plane at ξ is deflected by an angle $\vec{\alpha}(\vec{\xi})$. Credit: Narayan & Bartelmann (1996)

The deflection angle, $\vec{\hat{\alpha}}$, which is the angle by which a light ray is curved due to the gravitational field of a massive body is a function of the newtonian potential and can be written

$$\vec{\hat{\alpha}} = \frac{2}{c^2} \int \vec{\nabla}_{\perp} \vec{\psi} dz \tag{3.1}$$

where z is the line-of-sight direction.

The mass sheet can be characterized by its surface mass density with , $\vec{\xi}$, a two-dimensional vector in the lens plane

$$\Sigma(\vec{\xi}) = \int \rho(\vec{\xi}, z) dz \tag{3.2}$$

Space-time can here be characterized by a locally flat Minkowskian metric near the lens plane which is then weakly perturbed by the newtonian potential, $\vec{\psi}$, of the mass density of the lensing object. For this approximation to be valid, the newtonian potential and the peculiar velocity of the lens have to be small $|\psi| << c^2$ and $v << c$. This approximation is valid in almost every case of astrophysical interest.

Using this characterization, the scaled deflection angle can be expressed in terms of the surface mass density

$$\vec{\hat{\alpha}} = \frac{4G}{c^2} \int \frac{(\vec{\xi} - \vec{\xi}') \sum(\vec{\xi}')}{|\vec{\xi} - \vec{\xi}'|^2} d^2\xi' \tag{3.3}$$

3.2.1 The lens equation

The geometry of a typical gravitational lens system is shown in fig.3.2. A source S emits light which is deflected by the angle $\vec{\hat{\alpha}}$ at the lens and reaches the observer O. I is the observed image and the angle between the optic axis and the image is $\vec{\theta}$. The angle between the optic axis and the source position gives $\vec{\beta}$. The distances between the observer and the source are D_s, D_d and D_{ds} respectively. If we now

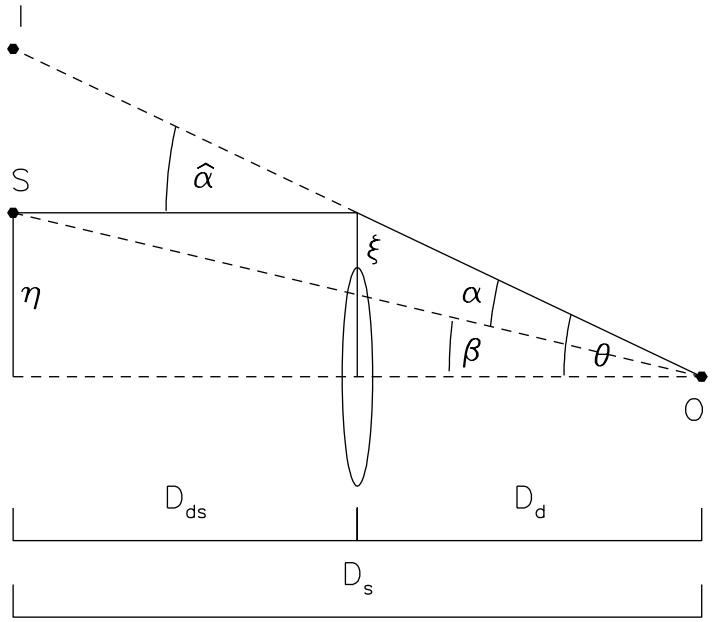

Figure 3.2: The geometry of a typical lens system. The light coming from the source S located at distance η from the optic axis, is passing the lens at distance ξ from the optic axis. The light ray is deflected by an angle $\hat{\alpha}$, and the angular separation of the source and the image as seen by the observer are β and θ, respectively. Also shown is the reduces deflection angle α which is related to the actual deflection angle $\hat{\alpha}$ through equation 3.4. The distances between the observer and the source are D_s, D_d and D_{ds} respectively. Credit: Narayan & Bartelmann (1996)

introduce the reduced deflection angle $\vec{\alpha}$:

$$\vec{\alpha} = \frac{D_{ds}}{D_s}\hat{\vec{\alpha}} \tag{3.4}$$

it leads to a simple equation also called the lens equation, relating the true position of the source and the position seen by the observer, the image.

$$\vec{\beta} = \vec{\theta} - \vec{\alpha}(\vec{\theta}) \tag{3.5}$$

In general this equation is non-linear, giving rise to the possibility of having multiple possible solutions of $\vec{\theta}$ (multiple images), corresponding to a single source position $\vec{\beta}$.

3.2.2 Magnification

Gravitational lensing affects the observed source position, the observed flux and for a finite size background source also the observed source shape. An important property of gravitational lensing though, is that the surface brightness of the source is conserved (because of Liouville's theorem). The relation between the surface brightness $I_s(\vec{\beta})$ in the source plane and the observed surface brightness in the lensing plane can be written

$$I(\vec{\theta}) = I_s(\beta(\theta)) \tag{3.6}$$

As a result, the magnification can be calculated using the lens equation. The magnification is described by the determinant of the magnification tensor, M, which is defined as the inverse of the Jacobian matrix of the lens equation, A.

$$\mu = \det M = \frac{1}{\det A} \tag{3.7}$$

where μ is the magnification and the Jacobian matrix A is written

$$A = \frac{\partial \vec{\beta}}{\partial \vec{\theta}} \tag{3.8}$$

3.3 Spherical symmetric lenses

In general, the mass distribution of dark matter halos can be complicated and it is necessary to use numerical methods to calculate the deflection angle. However, for a few cases with a particularly simple modeling of the mass distribution, analytical expressions can be obtained.

In the simple case of a circularly symmetric lens, light deflections become a one-dimensional problem. The surface mass density can be expressed as

$$\Sigma(\xi) = \int \rho(\xi, z) dz \tag{3.9}$$

where ξ is the distance from the lens center. The deflection angle is then given by

$$\hat{\alpha}(\xi) = \frac{4GM(\xi)}{c^2 \xi} \tag{3.10}$$

where $M(\xi)$ is the mass enclosed within the radius ξ

$$M(\xi) = 2\pi \int_0^{\xi} \Sigma(\xi')\xi' d\xi' \tag{3.11}$$

Using equation (3.10) and (3.4) we find that in the case of a circular symmetric lens with an arbitrary mass profile, the lens equation reads

$$\beta(\theta) = \theta - \frac{D_{ds}}{D_d D_s} \frac{4GM(\theta)}{c^2 \theta} \tag{3.12}$$

where we have set $\xi = D_d\theta$. For a point-like source positioned on the optical axis ($\beta = 0$), the image will be a ring with radius θ_E

$$\theta_E = \left(\frac{4GM(\theta_E)}{c^2} \frac{D_{ds}}{D_d D_s} \right)^{1/2} \tag{3.13}$$

also called the Einstein ring.

The Einstein radius sets the scales in lens systems. It gives roughly the boundary for whether multiple images can occur. In general, for a source located inside the Einstein ring it is possible to have multiple images and for a source located outside the Einstein ring we will only have one image. Moreover, the typical angular separation of multiple images is of the order of $2\theta_E$.

The magnification induced by a symmetric lens can be calculated using eq. 3.7 and yields

$$\mu = \frac{\theta}{\beta} \frac{d\theta}{d\beta} \tag{3.14}$$

3.3.1 A particularly simple model - The Singular Isothermal Sphere (SIS)

One of the simplest models used to describe the density profile of astronomical objects such as galaxies and clusters is the Singular Isothermal Sphere (from now referred to as SIS). This model is based on the assumption of matter behaving like a self-gravitating ideal gas in equilibrium. A mass distribution of such a model has the density profile

$$\rho(r) = \frac{\sigma^2}{2\pi G r^2} \tag{3.15}$$

where σ is the velocity dispersion of the test particles in the halo (stars for a galaxy, galaxies for a cluster) and r is the distance to the center. The SIS is indeed singular (as the name suggests) at the origin ($r = 0$). For the use of the SIS model in gravitational lensing this is not considered a problem since the mass enclosed within a certain radius is finite as we will see in the following. The velocity dispersion is constant across the galaxy. By projecting the mass density along the line of sight one obtains the following description for the surface mass density

$$\Sigma(\xi) = \frac{\sigma^2}{2G\xi} \tag{3.16}$$

The total mass within the radius, ξ is given by

$$M(\xi) = 2\pi \int_0^{\xi} \frac{\sigma^2}{2G} \frac{1}{\xi'} \xi' d\xi' = \frac{\pi\sigma^2}{G} \xi \tag{3.17}$$

Using $\xi = D_d\theta$ leads to a lens equation of the following form

$$\beta(\theta) = \theta - \frac{4\pi\sigma^2}{c^2}\frac{D_{ds}}{D_s} \tag{3.18}$$

For $\beta = 0$, the Einstein radius is given by

$$\theta_E = 4\pi\left(\frac{\sigma}{c}\right)^2 \frac{D_{ds}}{D_s} \tag{3.19}$$

and the magnification can be expressed as

$$\mu(\theta) = \frac{|\theta|}{|\theta| - \theta_E} \tag{3.20}$$

Depending on the impact parameter, lensing by a SIS model can result in either one or two images. Primary images have $\mu \geqslant 1$ and secondary have $\mu < 0$.

The isothermal model has been proven a good fit to elliptical galaxies (Koopmans *et al.*, 2006; Treu *et al.*, 2006; Koopmans *et al.*, 2009) which are among the strongest lensing galaxies.

3.4 Multiple lens-plane method

In general, the magnification of each supernova is induced by the deflections due to all lenses along the line of sight. The mass of each lens can be taken into account using the so-called multiple lens-plane method which is a generalization of the lens equation. Using the thin screen approximation (see previous section) the mass of each galaxy can be projected onto a mass sheet at the respective redshift giving rise to multiple planes in the line of sight. As said in section 3.2, the lens equation in its most general form yields

$$\vec{\beta} = \vec{\theta} - \frac{D_{ds}}{D_s}\vec{\hat{\alpha}}(\vec{\theta}) \tag{3.21}$$

Let N be the number of lens planes, labeled by i where N is the farthest lens (the source would be labelled $N + 1$) and 1 is the closest. In this case, it is possible to obtain the angular position of the light-ray in each plane recursively from the observed angular position

$$\theta_{j+1} = \theta_1 - \sum_{i=1}^{j} \frac{D_{ij}}{D_j}\hat{\alpha}(\theta_i) \tag{3.22}$$

The generalized lens equation yields

$$\beta(\theta_1) = \theta_1 - \sum_{i=1}^{N} \frac{D_{is}}{D_s}\hat{\alpha}_i(\theta_i) \tag{3.23}$$

where $\hat{\alpha}_i$ is the deflection due to the mass projection of the i-th lens.

To calculate the magnification factor one must calculate the Jacobian matrix of the lens equation (see eq. 3.7) which is given by

$$A(\theta_1) = \frac{\partial\beta}{\partial\theta_1} = I - \sum_{i=1}^{N} \frac{D_{is}}{D_s}\frac{\partial\hat{\alpha}_i}{\partial\theta_1} = I - \sum_{i=1}^{N} \frac{D_{is}}{D_s}\frac{\partial\hat{\alpha}_i}{\partial\theta_i}\frac{\partial\theta_i}{\partial\theta_1} \tag{3.24}$$

where I is the identity matrix.

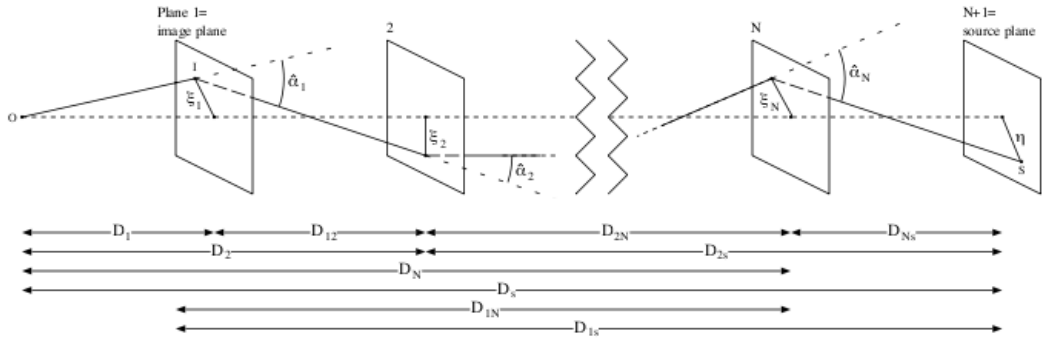

Figure 3.3: Schematic of the multiple lens plane method. Credit: Gunnarsson (2004)

Q-LET

Q-LET (Gunnarsson, 2004) is a publically available FORTRAN 77 code that uses the multiple lens-plane method described previously to enable a quick estimate of the gravitational lensing effects on a source taking into account the multiple deflections that arise when several lenses at different redshifts are situated close to the line of sight. It projects the lens' mass distribution of each lens onto a lens plane and traces the light-ray recursively from the image plane back through all the lens planes to the source plane where the magnification is given. I have used this code to estimate the magnification for the SNLS supernovae.

Q-LET can estimate the magnification modeling the foreground mass distribution as SIS or NFW (Navarro, Frenk and White) (Navarro *et al.*, 1997) profiles. For more information on the NFW profile see section 4.2. It is also possible to choose between a point- or an extended source with elliptical image shape. In relation to my analysis, the foreground galaxies have been modeled as SIS and the supernova is chosen as a point source.

To compute the magnification of each supernova, the angular positions of all the lensing galaxies must be given with respect to the supernova location. Other parameters needed to be able to estimate the magnification is the redshift of each lens plane (galaxy) together with a mass estimate. For the SIS, the velocity dispersion, σ which is related to the magnification (see eq. 3.19 and 3.20) is given. How to derive velocity dispersions for all the galaxies will be thoroughly explained in the next chapter.

When calculating the magnification, the angular distance diameters between the different lenses the source and the observer will intervene and thus it is necessary to specify a cosmology. For the purpose of my analysis, the standard cosmology of $h = 0.7$, $\Omega_M = 0.27$ and $\Omega_\Lambda = 0.73$ has been chosen and all distances are computed using the filled beam approximation meaning that the universe is

homogeneously distributed with the specified cosmology. To estimate the magnification, the lensing galaxies have been put on top of this homogeneous distribution leading to a magnification always greater than one compared to a homogeneously distributed universe.

Note that for multiple images, the secondary image has a negative magnification and thus the earlier statement is only correct concerning the primary images.

Chapter 4

Gravitational magnification of Type Ia SNe: a new probe for Dark Matter clustering

As said previously, Type Ia supernova are one of the best known standard candles and highly used as a cosmological probe to constrain cosmological parameters. Gravitational lensing has the effect of increasing the scatter in the hubble diagram due to mass inhomogeneities along the line of sight. Of course it is important to consider the effect on cosmology due to gravitationally lensed SNeIa, but what might be even more interesting is to invert the problem and use the observed extra scatter in the Hubble diagram as an indirect estimate of the magnification of the SNe leading eventually to the possibility of determining properties of the foreground matter.

There are in principle two ways of estimating the magnification of a Type Ia SN. Using the current best fit cosmological model one can assume that parts of the residuals to the Hubble diagram are due to gravitational lensing, leading to an indirect estimate of the SN magnification. On the other hand, it is possible to estimate the magnification of each event by carefully modeling the foreground galaxies using photometric data together with former derived mass-luminosity relations for galaxies and dark matter halo models. The aim is to search for a correlation between these two estimates and if such a correlation is found it is then possible to tune the initially used mass-luminosity relation in the modeling of the foreground galaxies and thus create an independent measurement of the mass-luminosity ratio for the SNLS galaxies.

This chapter is dedicated to the effect of gravitational lensing on Type Ia SNe and mass-luminosity relations for galaxies. In the first sections we present previous results on the effect of gravitational lensing on SNeIa and prospects for a signal detection (i.e. the correlation between the supernova brightness calculated based on a specific cosmological model and the magnification estimated using photometric data on foreground galaxies) within the SNLS surveys based on simulations. The last section will discuss two different methods on how to obtain a mass-luminosity relation for galaxies, namely by galaxy-galaxy lensing or the empirical Tully-Fisher and Faber-Jackson relations.

4.1 The effect of gravitational lensing on the SNeIa Hubble diagram

A supernova can either be magnified or demagnified with respect to a homogeneous mass density distribution in the universe (see section 5.6). In fact, some of the supernovae will be highly magnified

whereas most of the events will be slightly demagnified and consequently appearing to be closer or more distant respectively than they really are. This will have an effect on the derived cosmology. Note that the effect of gravitational lensing on SNe will increase with z.

It is important to evaluate the significance of a possible lensing bias on the mean and whether correcting for lensing for each SN individually can help decrease the scatter in the Hubble diagram. Another problem with the effect of gravitational lensing is that it could lead to selection biases due to exclusion of outliers in the Hubble diagram which are significantly lensed.

Several groups have already addressed these problems statistically giving rise to an effect which is smaller than the dominant uncertainties in the current surveys (Riess *et al.*, 2004; Holz & Linder, 2005; Astier *et al.*, 2006; Wood-Vasey *et al.*, 2007; Sarkar *et al.*, 2008). Whether correcting for gravitational lensing on an event by event basis has a noticeable effect has also been evaluated by Gunnarsson *et al.* (2006); Jönsson *et al.* (2008) and section 4.2 of this thesis. Fortunately, the conclusion of these investigations has been that for surveys like the SNLS, the effect of gravitational lensing will not bias the cosmological results significantly although much more care needs to be taken in the future when the experiments will be pushed to higher redshifts and higher statistics and other now dominant systematic effects will decrease.

4.2 Signal detectability

This section aims at investigating whether the detection of a lensing signal (correlation between the residuals to the Hubble diagram and the magnification) is possible in the current SNIa surveys.

4.2.1 Previous results

The idea of detecting a lensing signal using supernovae samples is not new, several studies of the lensing signature in supernovae surveys have already been performed, but the claim of a detection remains somewhat ambiguous . The first claim of a detection of the weak lensing signal was made by Williams & Song (2004). They correlated the brightness of high-z supernovae from the High-z Supernova Search Team and the Supernova Cosmology Project with the density of the foreground galaxies. They found that brighter supernovae preferentially lay behind overdense regions. Wang (2005) later confirmed this result using only the measured supernova brightness. He did not use any information on foreground densities. Instead he derived the expected weak lensing signatures of Type Ia SNe by convolving the intrinsic distribution in peak luminosity with magnification distributions of point sources and compared this theoretical distribution to 110 high and low z SNe from the Riess sample (Riess *et al.*, 2004). Later, Ménard & Dalal (2005) performed similar analysis as Williams & Song (2004) but this time more accurate determination of the foreground galaxies was available using SDSS photometry. They chose partly the same supernova sample but no correlation was found. High-z supernovae from the GOODS-field have also been a subject to this kind of study. Jonsson *et al.* (2006) made a tentative detection but found only a trend and no firm results due to low statistics.

All these results show the lack of a firm detection of the lensing signature in supernova samples and currently, the SNLS is one of the most promising surveys for such a detection.

4.2.2 Prospects for the SNLS survey

The first 5 months of this thesis was dedicated to performing simulations estimating the possible impact of gravitational lensing on the cosmological parameters in the SNLS survey and evaluating whether the signature of lensing was detectable. This work led to a collaboration with a Swedish group and particularly Jakob Jonnson who explored the ideas leading to a published article (Jönsson *et al.*, 2008). Here we will briefly summarize this analysis and the results concerning the expectations of the detection of a lensing signal.

The simulations of the SNLS SNeIa including the effect of gravitational lensing

700 type Ia SNe have been simulated based on the properties of SNe observations from (Astier *et al.*, 2006). We assume a constant rate of SNe per co-moving volume leading to a rapid increase in the number of SNe with increasing z.

Every survey has its detection limitations giving rise to a selection bias. At the boundary of the limiting magnitude cut-off, only the most luminous SNe will be detected (the bluest ones with the most stretch) biasing the cosmological results. For simplicity, we assume that the selection bias is driven by the efficiency of spectroscopic identification of Type Ia SNe leading to the introduction of a spectroscopic cut-off, as imposed in realistic models. This spectroscopic cut-off has been tuned to actual observation conditions by the SNLS group (Howell *et al.*, 2005a) (see fig. 4.3). Performing a spectroscopic cut-off implies loosing some of the 700 simulated SNe leading to a mean number of the supernova sample of ~ 500 which is in good agreement with the expected number of SNe for the final SNLS sample.

For each supernova, a random stretch and color have been estimated taking into account the observed brighter-slower and brighter-bluer correlations. This model has been compared to observations in Astier *et al.* (2006) (see fig. 4.2). Using the SNLS data it is possible to estimate the uncertainties of measurements on the stretch, s, color, c, and rest frame magnitude, m_B^*, parameters. The estimations as functions of redshift are the following (see fig(4.1)):

$$\sigma_c = 0.49z^2 - 0.38z + 0.08 \quad for\ z > 0.5 \quad else\ \sigma_c = 0.01 \tag{4.1}$$

$$\sigma_s = 0.066z - 0.014 \quad for\ z > 0.35 \quad else\ \sigma_s = 0.01 \tag{4.2}$$

$$\sigma_{m_B^*} = 0.84z^2 - 1.04z + 0.34 \quad for\ z > 0.8 \quad else\ \sigma_{m_B^*} = 0.05 \tag{4.3}$$

These uncertainties have been taken into account when estimating the measured color and stretch for each supernova.

To estimate the lensing effect of each of the simulated supernovae, the SNOC-package (Supernova Observation Calculator) (Goobar *et al.*, 2002) has been used. This is a Monte-Carlo program where the procedure is to trace light beams backwards in time from the observer to the host galaxy of the supernova taking into account the possible intervening matter in the line of sight. The matter is accounted for by specifying typical matter distributions in spherical cells so that each cell on the light path corresponds to an inhomogeneity in the line of sight. The matter distribution in the cells can be chosen to be point-masses, uniform spheres, SIS (see eq. 3.15) or NFW (Navarro,Frenk and White) (Navarro *et al.*, 1997) predicted by numerical simulations of Cold Dark Matter. This model is amongst the most popular halo models at the moment and presents the following density profile

$$\rho(r) = \frac{\delta_c \rho_c}{(r/r_s)(1 + r/r_s)^2} \tag{4.4}$$

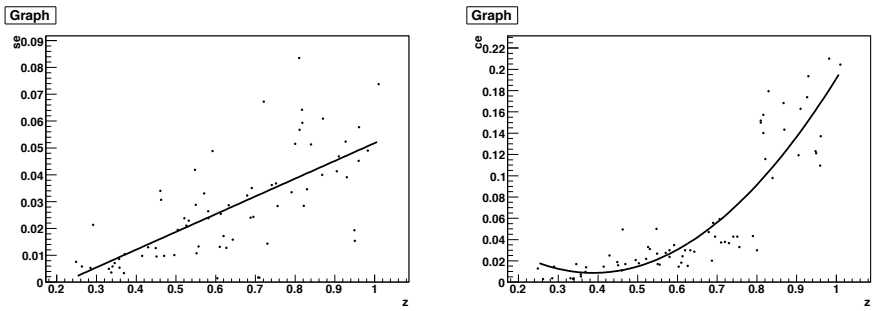

(a) uncertainties on the stretch parameter s vs z

(b) uncertainties on the color parameter c vs z

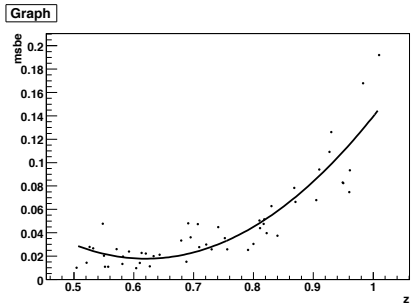

(c) uncertainties on the rest-frame magnitude m_B^* vs z

Figure 4.1: Plots of the uncertainties of the parameters c, s and $m*_B$ vs z.

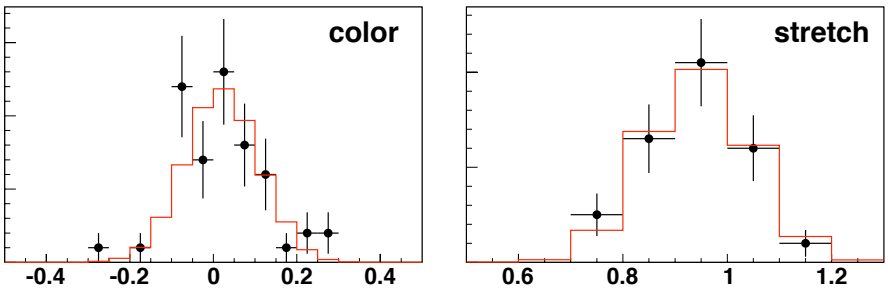

(a) color distribution

(b) stretch distribution

Figure 4.2: Distributions of stretch and color of SNLS SNe (black dots) with a distribution of simulated SNe (red histograms) superimposed. Credit: Astier *et al.* (2006)

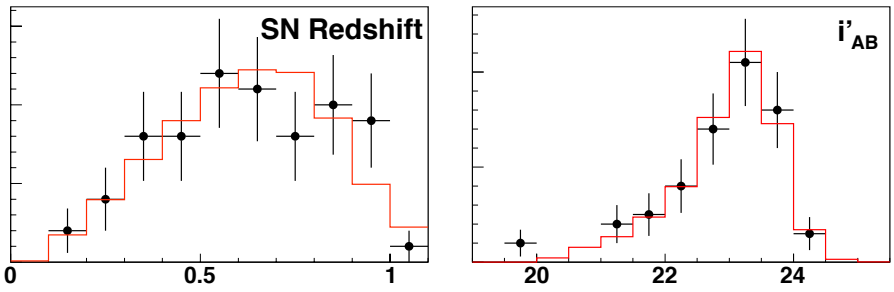

(a) redshift distribution (b) peak i_M magnitude distribution

Figure 4.3: Distributions of redshifts and peak i_M magnitudes of SNLS SNe (black dots) with a distribution of simulated SNe (red histograms) superimposed. Credit: Astier *et al.* (2006)

where δ_c is a characteristic density, ρ_c is the critical density, and $c = r/r_s$ is called the concentration parameter. In this simulation, the NFW profile has been chosen. The main difference in using SNOC instead of Q-LET, which has been used in the rest of the analysis, is that SNOC simulates the foreground mass densities whereas Q-LET requires a mass estimate of each intervening galaxy.

Results on the signal detectability

With regards to cosmology we found that correcting for magnification due to gravitational lensing for the SNLS SNe has a negligible impact. This is in good agreement with Jönsson *et al.* (2006, 2008)

However, investigating whether the correlation between the residuals and the magnification can be detected within the SNLS sample gave very promising results.

To account for the scatter in the magnification we have used results from Jonsson *et al.* (2006) where the magnification together with the magnification error have been estimated for 26 SNe from the GOODS fields leading to the following relation between the magnification error and the magnification

$$\sigma_{-2.5\log_{10}(\mu)} = 0.02 - 0.217 \times (-2.5\log_{10}(\mu)) \tag{4.5}$$

where μ is the magnification factor and $-2.5\log_{10}(\mu)$ expresses the magnification in magnitudes.

For a correlation we assume the simplest possible linear relation, namely residual=magnification and calculate the following χ^2

$$\chi^2_\mu = \sum \frac{(mag - r)^2}{\sigma_r^2 + \sigma_{mag}^2} \tag{4.6}$$

where *mag* is the magnification in magnitudes and r is the residual. The residual uncertainties also include the intrinsic dispersion. This can be compared to the case assuming no correlation where

$$\chi^2_0 = \sum \frac{r^2}{\sigma_r^2} \tag{4.7}$$

Figure 4.4 shows a histogram of 100 realizations of $C = \chi^2_0 - \chi^2_\mu$ for the two samples: with lensing effects (in red) and without lensing effects (in black). We see that the distributions are well defined and well separated and moreover, there is $> 99\%$ chance of detecting the lensing signal with a 3σ significance.

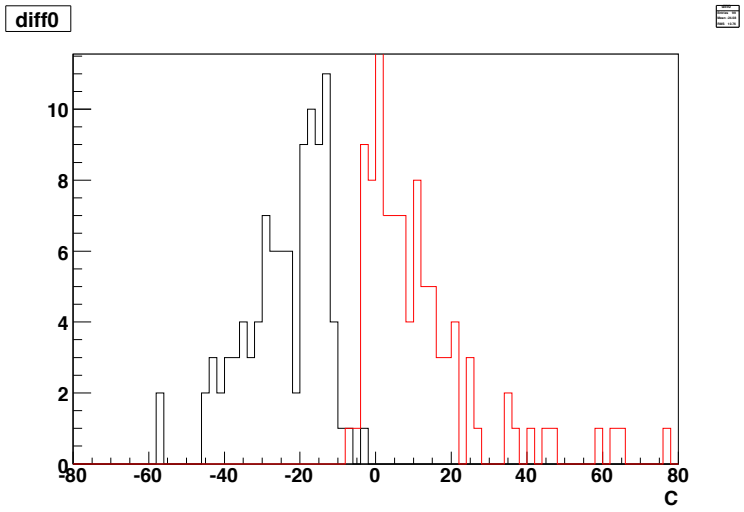

Figure 4.4: Histogram of C for the two samples: with lensing effects (in red) and without lensing effects.

These results were confirmed by Jönsson *et al.* (2008) who found that with respect to the SNLS full sample, the probability of measuring a 3σ correlation between the Hubble diagram residuals and the calculated lensing magnification is $> 95\%$ (see fig 4.5). Moreover, Jönsson *et al.* (2008) also showed that if such a signal is detected it should in principal be possible to set constraints on the normalization of the masses of the lensing galaxy haloes.

4.3 Mass-luminosity relations.

The new idea presented in this thesis consists of using Type Ia SNe magnification to probe the mass-luminosity relation of the foreground mass densities. There are however several other methods to infer the total mass of a galaxy (luminous + dark matter) such as gravitational lensing, measurement of rotational velocities / velocity dispersions and the dynamics of satellite galaxies amongst others.

In this section we will present an overview of two different methods to obtain mass-luminosity relations for galaxies, namely the classical method which is based on the measurements of velocity dispersions / rotation velocities of galaxies giving rise to the empirical Tully-Fisher and Faber-Jackson relations and another newly established method, the weak galaxy-galaxy lensing signature in large surveys. Recent results (Böhm *et al.*, 2004; Mitchell *et al.*, 2005; Kleinheinrich *et al.*, 2004; Hoekstra *et al.*, 2004) which have also been used as input mass-luminosity relations in the analysis (see chapter 5) will be compared.

4.3.1 Weak galaxy-galaxy lensing

The weak lensing signal can be measured out to large projected distances from the lens, and hence provides a unique probe of the gravitational potential on large scales as compared to dynamical measurements which require visible tracers. The galaxy-galaxy lensing signal is manifested by images of background galaxies being distorted by foreground galaxies which can be used to infer important properties of the matter distribution around the foreground galaxies. As already explained in section

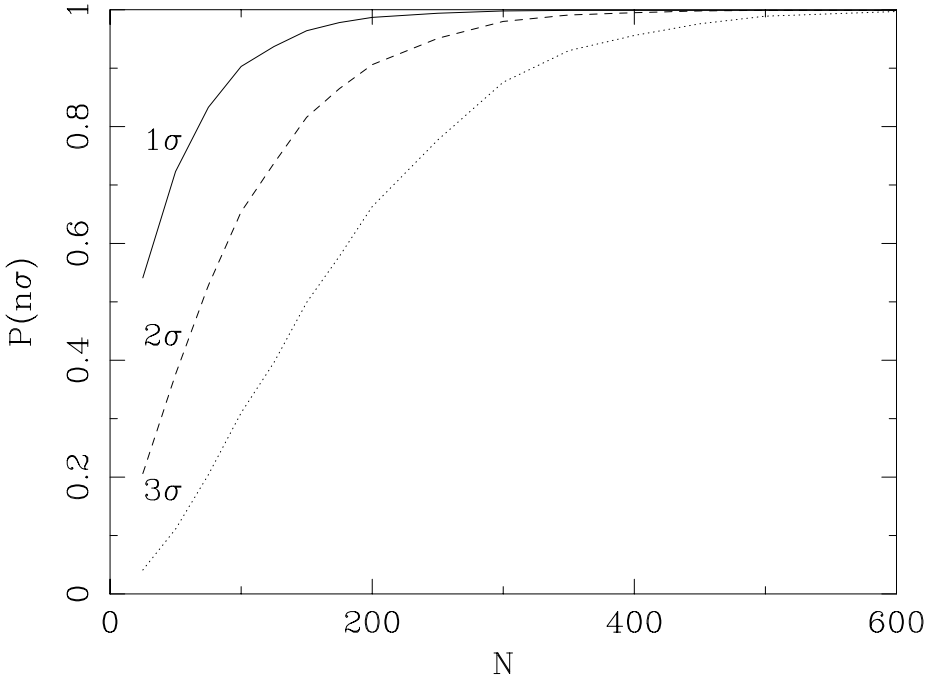

Figure 4.5: The probability of detecting a correlation between the estimated magnification and the residuals to the hubble diagram at different confidence levels, P(n), as a function of the number of supernovae, N. The solid, dashed, and dotted curves shows the probability to detect a correlation at the 1σ, 2σ, and 3σ confidence level, respectively. Credit: Jönsson *et al.* (2008)

1.4.3, one can only study ensemble averaged properties, because the weak lensing signal induced by individual galaxies is too low to be detected.

Theory

The tangential shear, γ_T, which is related to the second partial derivatives of the newtonian potential, ϕ, induce an effect that distorts the sources in an anisotropic way stretching them tangentially around the foreground mass (see fig. 4.6). For an exact definition of the shear see Narayan & Bartelmann (1996). This tangential alignment, or tangential shear can be measured through the ellipticities of the

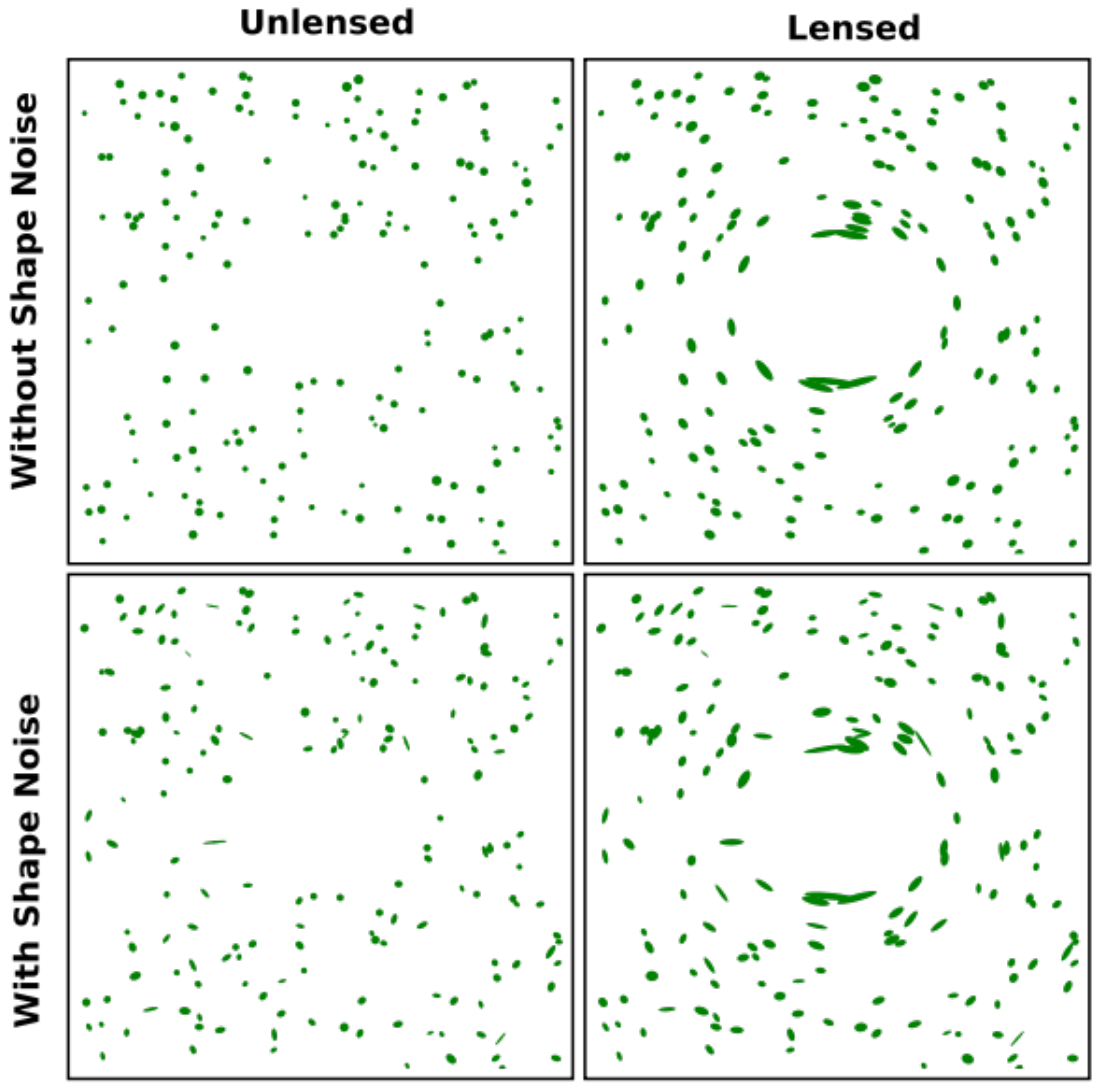

Figure 4.6: The effect of weak lensing due to a foreground mass on a sample of background galaxies. In the upper figures, the intrinsic shape of the galaxies are assumed spherical. In the bottom figures, a more realistic picture with different intrinsic elliptical shapes of the galaxies is presented. In this figure, the distortion is exaggerated with respect to realistic astronomical systems.

background galaxies and their systematic alignment. This gives rise to a mean tangential shear divided into angular bins (see fig. 4.7).

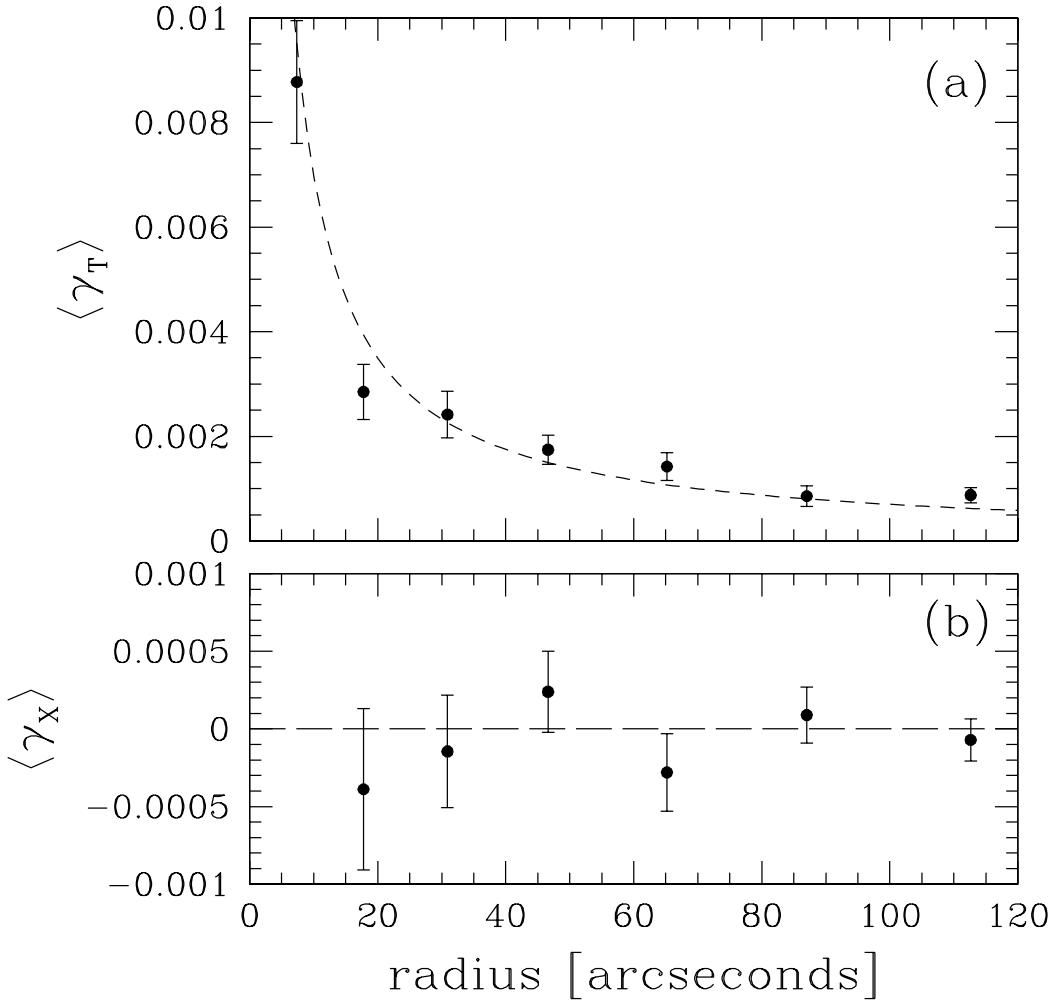

Figure 4.7: The averaged shear as a function of radius out to 2' from the lens with the best fit to a SIS model is shown in the top figure. To check for residual systematics, the sources are rotated by 45° (increasing phase of $\pi/4$) which shows no signal, bottom figure. Credit: Hoekstra *et al.* (2004).

The averaged tangential shear (averaged over several thousands of galaxies) must then be fit with an assumed halo model to be able to extract average physical properties of the haloes such as velocity dispersion and mass.

The SIS (Singular Isothermal Sphere) model has already been presented in section 3.3.1. This a simple model and has been widely used in weak lensing studies (Hoekstra *et al.*, 2004; Kleinheinrich *et al.*, 2004; Parker *et al.*, 2005, 2007). For this model, the tangential shear is proportional to the Einstein radius

$$\gamma_T = \frac{\theta_E}{2\theta} = \frac{2\pi\sigma_v^2}{c^2\theta}\frac{D_{ds}}{D_s} \tag{4.8}$$

Although the SIS model has been used in the analysis (see chapter 5), it is worth pointing out that the NFW-profile (see eq. 4.4) is also highly used in weak lensing. The equations describing the shear for an NFW-model can be found in Bartelmann (1996) and Wright & Brainerd (2000). In the following we will concentrate on results based on SIS models.

It is useful to scale the velocity dispersion of a galaxy with a fiducial luminosity, L_*. Inspired by the Tully-Fisher and Faber-Jackson relations, scaling relations between the velocity dispersion and the luminosity or the virial mass and the luminosity of the following form are adopted.

$$\frac{\sigma}{\sigma_*} = \left(\frac{L}{L_*}\right)^{\alpha} \tag{4.9}$$

$$\frac{M}{M_*} = \left(\frac{L}{L_*}\right)^{\beta} \tag{4.10}$$

where α and β are scale parameters.

Weak lensing results

The COMBO-17 survey (Classifying Objects by Medium-Band Observations in 17 filters) and the RCS (Red Cluster Sequence) survey are two of the main galaxy-galaxy lensing surveys together with the SDSS and the CFHT (Canada-France-Hawaii-Telescope) wide survey. Here, results from the first two surveys are presented.

The COMBO-17 survey is a deep survey providing photometric redshifts and spectral classification of galaxies in 17 different filters (the five broadband filters UBVRI and 12 other medium band filters) for objects down to R=24. The lenses and sources are selected based on their photometric redshifts. Lenses lie in the redshift range $0.2 < z < 0.7$ yielding a mean redshift of $z \sim 0.4$. Results are given for the full sample but the lens sample is also split into two subsamples with blue or red rest-frame colors giving rise to important results as a function of color. It is widely known that elliptical galaxies are more massive than spiral galaxies with respect to the same luminosity and as a result it is important to give mass-luminosity relations for ellipticals and spirals separately. Performing a color cut will help mimic a morphological separation between spirals and ellipticals. Kleinheinrich *et al.* (2004) (from now on K04) have analyzed the data yielding a mass to luminosity relation for the full sample probed out to a maximum radius of $150h^{-1}$ kpc.

$$\sigma = 156^{+18}_{-24}\left(\frac{L}{10^{10}h^{-2}L_{r\odot}}\right)^{0.28^{+0.12}_{-0.09}} km.s^{-1} \tag{4.11}$$

where L is the luminosity of the galaxy in the r-band. The fiducial luminosity, $L^* = 10^{10}h^{-2}L_{r\odot}$ is in this case given in the SDSS r-band. In the following, the results will be of the form from eq. 4.9 and therefore only the values of the parameters σ_* and α will be provided. For this first result this implies $\sigma_* = 156^{+18}_{-24}$km.s^{-1} and $\alpha = 0.28^{+0.12}_{-0.09}$. When splitting their sample they find $\sigma_{*red} = 185^{+24}_{-30}$km.s^{-1} and $\alpha_{red} = 0.28^{+0.15}_{-0.12}$ whereas $\sigma_{*blue} = 130^{+30}_{-36}$km.s^{-1} and $\alpha_{blue} = 0.22^{+0.15}_{-0.15}$. Moreover (Kleinheinrich *et al.*, 2005) show that without photometric/spectroscopic redshifts for the lensing galaxies it is not possible to constrain the scaling parameters. However, galaxy-surveys with high quality multi band photometric data leading to excellent photometric redshift estimates can give tight constraints also on these parameters.

Hoekstra *et al.* (2004) (from now on H04) have used R imaging from the RSC (Red Sequence Cluster) survey which covers 90 deg2 in both R, and SDSS z' band. Photometric redshifts of the galaxies are unknown and as a result the galaxies are split into source and lens galaxies based on their apparent R_C magnitude. The lensing galaxies are defined as having $19.5 < R_C < 21$ and the source galaxies $21.5 < R_C < 24$. For a SIS, the lensing signal depends on the angular diameter distances between the observer the lens and the source and as a consequence in lack of photometric redshifts of the galaxies one needs to adopt a redshift distribution for both lens and source populations. The redshift distribution for the lenses is based on the CNOC2 Field Galaxy Redshift Survey and for the sources, a redshift distribution derived from the Hubble Deep Field is used leading to a mean redshift of z = 0.35 for the lensing galaxies and z = 0.53 for the source galaxies. Color information for the galaxies from the CNOC2 survey is also used to compute rest-frame B-band luminosities. Inspired by the Tully-Fisher and Faber Jackson relations, H04 assumes a scaling parameter, $\alpha = 0.3$ and find for the full sample probed out to $400h^{-1}$ kpc, $\sigma_* = 140 \pm 7\text{km.s}^{-1}$.

Difficulties when comparing weak lensing results

- **Probed radius**
  The observational difference leading to the most prominent effect is the radius within which the signal is probed. Different weak lensing surveys probe the signal on different scales. K04 measures the signal for different values of the maximum radius leading to a decrease in the velocity dispersion with increasing maximum distance together with a systematic increase in the scale parameter, α. For a maximum radius of $150h^{-1}$kpc, K04 finds $\sigma_* = 156^{+18}_{-24}\text{km.s}^{-1}$ and $\alpha = 0.28^{+0.12}_{-0.09}$, for a maximum radius of $250h^{-1}$kpc they find $\sigma_* = 138^{+18}_{-18}\text{km.s}^{-1}$ and $\alpha = 0.31^{+0.12}_{-0.12}$ and for a maximum radius of $400h^{-1}$kpc they find $\sigma_* = 120^{+18}_{-30}\text{km.s}^{-1}$ and $\alpha = 0.40^{+0.21}_{-0.15}$. This results in a difference of more than 20% in the velocity dispersion for the two extreme cases. As a result, when comparing weak lensing results it is important to compare measurements obtained on similar scales.

- **Fiducial luminosity**
  Although very often, the fiducial luminosity is given as $L_* = 10^{10}h^{-2}L_{B\odot}$ in the rest-frame B-band this is not always the case leading to a necessity to perform k-corrections for comparison. This is not always straightforward since a modeling of the galaxy distribution and the filter transmission in question is needed. K04 give the results scaled with $L^* = 10^{10}h^{-2}L_{r\odot}$ in the SDSS r-band. For a conversion to the B-band, they calculate that galaxies in their sample with a fiducial luminosity of $L_* = 10^{10}h^{-2}L_{B\odot}$ in the B-band have a fiducial luminosity of $L_* = 1.1\times10^{10}h^{-2}L_{r\odot}$ in the SDSS r-band.

- **Virial mass/radius**
  Both the SIS and the NFW models are singular for $r = 0$ which turns out not to be a problem for lensing (see section 3.3.1) but the models diverge for large radius and thus, to probe finite halo masses it is necessary to truncate the radius. The finite radius is usually taken to be the virial radius but several definitions exists. The most commonly used virial radius is defined as the radius inside which the mean density is n times the mean density of the universe. Usually n=200 and one often sees M_{200} or r_{200} in the literature. It is also possible to define the virial radius as the radius inside which the mean density is 200 times the critical density of the universe. This will lower the virial radius and thus lower the mass by a factor of 0.62 and 0.79 respectively for

a NFW profile (Kleinheinrich *et al.*, 2004). Other definitions of the virial radius also exists(see an example in Hoekstra *et al.* (2005)).

4.3.2 Faber-Jackson (FJ) and Tully-Fisher (TF) relations

Instead of using the statistical method of galaxy-galaxy lensing based on thousands of galaxies the velocity dispersion can also be inferred by direct measurement and several groups have measured the velocity dispersion of elliptical galaxies or the rotation velocity of spiral galaxies.

Measurement of the rotational velocity / velocity dispersion of galaxies

The measurement of the rotational velocity of spiral galaxies is either based on a modeling of the global profile width of the 21 cm radio line from hydrogen which can be related to the maximum rotational velocity of the galaxy or a relative doppler shift in the spectral emission lines. For a rotating spiral galaxy, the spectrum will be red- and blueshifted along the spectral axis compared to the observed wavelength of the line at the center.

In elliptical galaxies, the absorption lines are broadened due to the motion of the stars and by comparing the spectrum of the galaxy with a fiducial spectral template, the velocity dispersion can be inferred.

A strong correlation between the luminocity of a galaxy and its velocity dispersion / rotation velocity has been found (Poveda, 1961; Fish, 1964; Faber & Jackson, 1976; Tully & Fisher, 1977; Haynes *et al.*, 1999).

For an illustrative example see fig. 4.8 and 4.9. These relations (Faber-Jackson for ellipticals and Tully-Fisher for spirals) are empirical and can be expressed as

$$L \propto \sigma^{\eta} \tag{4.12}$$

$$L \propto V_{max}^{\gamma} \tag{4.13}$$

where L is the luminosity of the galaxy, σ is the velocity dispersion, V_{max} is the maximum rotational velocity and η and γ are the Faber-Jackson and Tully-Fisher indexes respectively.

We should bear in mind that the observed velocity dispersion / rotational velocity based on the detected luminous matter of the galaxy is not necessarily equal to the actual velocity dispersion / rotational velocity induced by the potential of their dark matter halo.

Concerning the rotational curves of spiral galaxies it is important to measure the maximum rotational velocity in the region of constant rotation velocity where the Dark Matter Halo dominates the mass distribution (see fig. 4.10). For example, Böhm *et al.* (2004) use a rotation curve modeling where V_{max} represents the turnover into this region. Note however that not all spiral galaxies have a constant V_{rot} at large radii. Sub luminous galaxies are known to have a rising curve even beyond a characteristic radius whereas very bright galaxies will have a falling curve (Casertano & van Gorkom, 1991; Persic & Salucci, 1991; Persic *et al.*, 1996). This can make it difficult to infer the correct maximum rotational velocity of the Dark Matter halo.

With regards to the velocity dispersion measured in elliptical galaxies, the aperture-corrected central velocity dispersion, which is what is usually referred to in the FJ relations, has been found very nearly equal to the dark matter velocity dispersion when modeling the halo as a SIS (Franx, 1993; Kochanek, 1994).

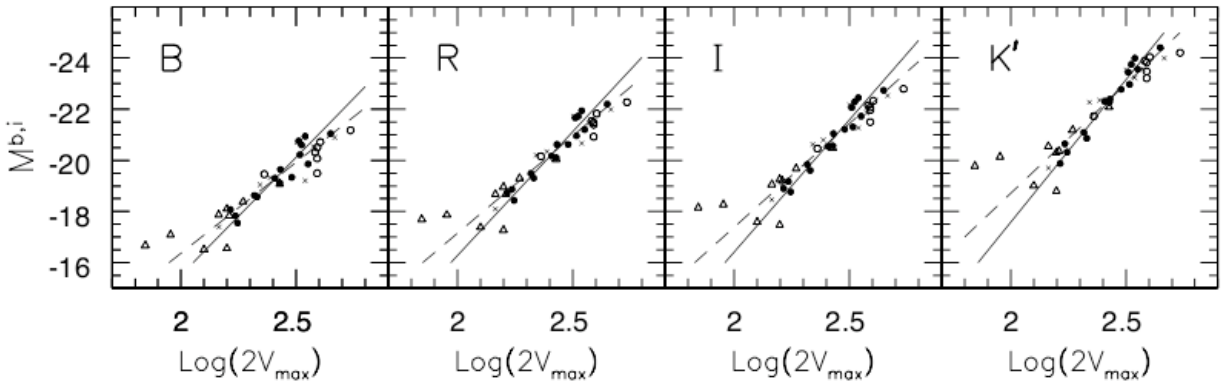

Figure 4.8: The Tully-Fisher relation from Verheijen (2001). The logarithm of the maximum rotational velocity as a function of absolute magnitude in the different bands (BRIK'). The solid line is the best fit to a selected sample of galaxies (filled circles) based on the quality of the rotational curve and the dashed line is the best fit to the full sample.

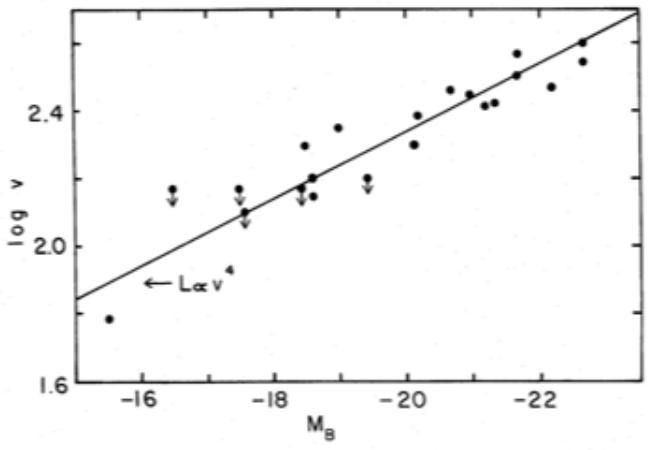

Figure 4.9: The original relation from Faber & Jackson (1976). Velocity dispersions versus absolute magnitude in the B-band. Credit: Faber & Jackson (1976)

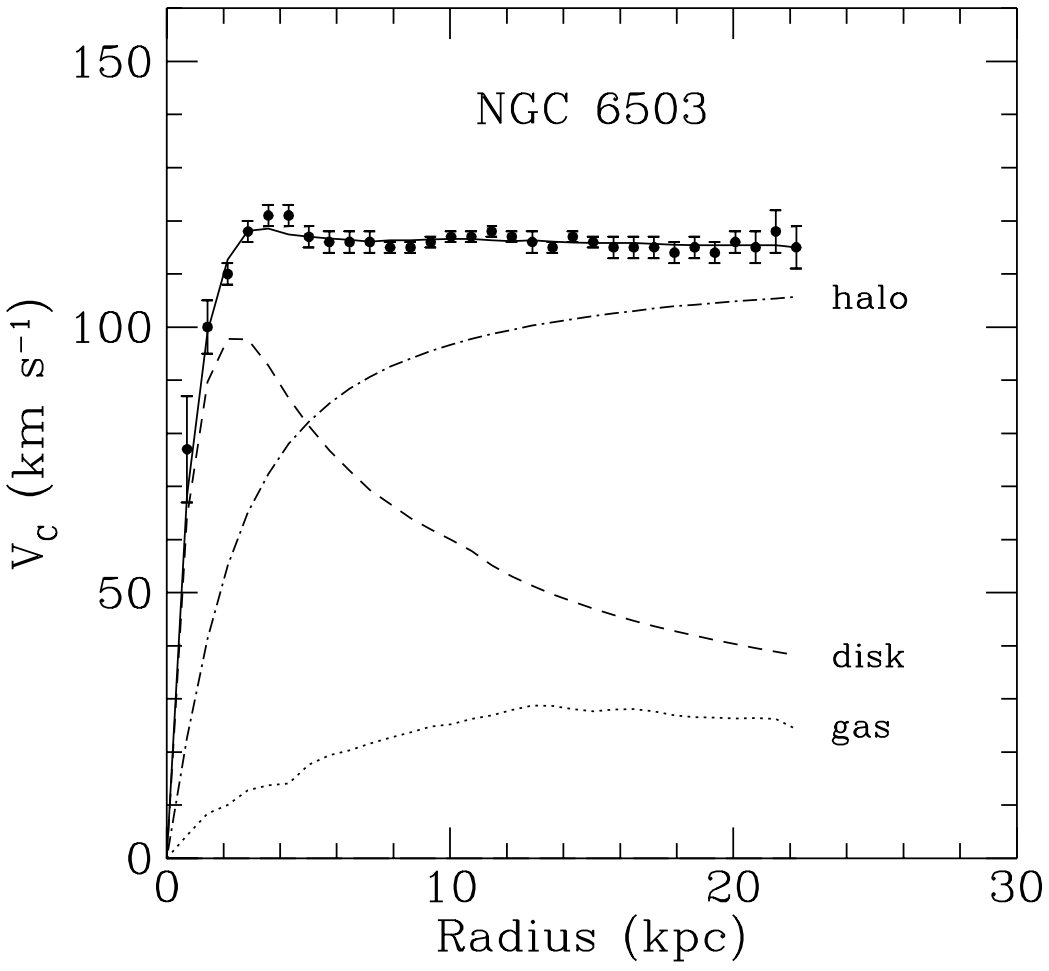

Figure 4.10: The rotational curve of a spiral galaxy with the disk, halo and gas contribution. Credit: Kamionkowski (1998)

In the following it will be useful to relate the rotation velocity to the velocity dispersion of a SIS. Using Newton's law for stars in a circular orbit in a galaxy, the orbital velocity, v_o, can be expressed as

$$v_o(r) = \sqrt{\frac{GM(r)}{r}} \tag{4.14}$$

where $M(r)$ is the mass enclosed within the radius of the orbit r. In the part where the rotational curve flattens out, the mass of the galaxy, $M(r)$ can be derived as

$$M(r) = \frac{V_{max}^2}{G} r \tag{4.15}$$

where V_{max} is the maximum orbital velocity.

For a SIS with the density profile described in eq. 3.15, the total mass inside the radius, r, can be written as

$$M(r) = \frac{2\sigma^2}{G} r \tag{4.16}$$

where σ is the velocity dispersion. By combining eq. 4.15 and 4.16, the maximum rotational velocity can be related to the velocity dispersion of the galaxy via

$$\sigma = \frac{V_{max}}{\sqrt{2}} \tag{4.17}$$

In the following some recent results on the Tully-Fisher and the Faber-Jackson relations will be presented.

Results for the Tully-Fisher relation

The Tully-Fisher relation (hereafter TF) relates the measured rotational velocities of spiral galaxies with their brightness. Several groups (Barden *et al.*, 2003; Milvang-Jensen *et al.*, 2003; Böhm *et al.*, 2004; Bamford *et al.*, 2006; Chiu *et al.*, 2008) have measured the Tully-Fisher relation and its evolution with redshift for different samples. The results are in general quite homogeneous and the observed differences can often be related to different selection effects and/or different assumptions for the nearby TF relation. The TF relation is based on spiral galaxies but the classification of spiral galaxies and the severeness of the morphological cuts can lead to differences in the galaxy sample. The above mentioned TF results all investigate whether there is an evolution in the TF relation with redshift and the given results are valid for z$\lesssim$ 1. To do so, the high-z TF relation needs to be compared with a local one. This can be done using nearby spiral galaxies from the same sample or by using a former derived relation like Pierce & Tully (1992) or Verheijen (2001). The choice may lead to differences.

Böhm *et al.* (2004) (from now on B04) give results which are based on the measurement of the rotation velocity of 77 spiral galaxies in the FORS Deep Field covering a redshift range of $0.1 < z < 1.0$ using the Very Large Telescope in Multi Object Spectroscopy mode. The mean redshift of the galaxies is $z = 0.45$. To anchor the relation at the low redshift end, they have used the nearby Tully-Fisher relation from Pierce & Tully (1992). B04 find the following relation between the maximum rotation velocity, V_{max} and the absolute magnitude of the galaxy in the rest-frame B-band depending on the redshift (see fig. 4.11).

$$\log V_{max} = -0.134\,(M_B + 3.52 + (1.22 \pm 0.56) \cdot z + (0.09 \pm 0.24)) \tag{4.18}$$

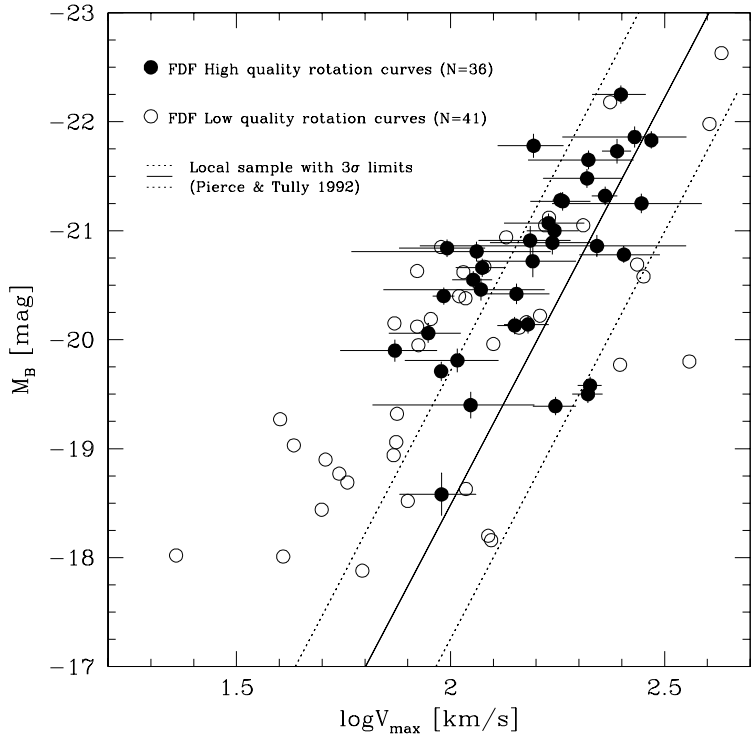

Figure 4.11: The Tully-Fisher relation for the B04 results.

with an observed scatter of

$$\sigma_{M_B} = 0.41 \tag{4.19}$$

The dependency on redshift merely expresses a positive luminosity evolution meaning that a galaxy with the same rotation velocity was brighter in the past. This trend has been found in several other results (Barden *et al.*, 2003; Milvang-Jensen *et al.*, 2003; Bamford *et al.*, 2006; Chiu *et al.*, 2008) and is expected due to the effect of a younger stellar population with a higher fraction of high luminosity stars in the earlier universe compared to the local universe.

Results for the Faber-Jackson relation

For ellipticals, the velocity dispersion can be inferred and related to the brightness of the galaxies used to establish the Faber-Jackson relation (hereafter FJ). One of the largest samples of measured velocity dispersions of elliptical galaxies is based on SDSS (Sloan Digital Sky Survey) data. The SDSS is one of the major imaging (five optical filters, *u'g'r'i'z'*) and spectroscopic redshift surveys covering over 7,500 square degrees of the Northern Hemisphere with obtained spectra from over 800,000 galaxies and 100,000 quasars.

The Faber-Jackson relation has been derived by Mitchell *et al.* (2005) (hereafter M05) for a sample of $\sim$ 30.000 elliptical galaxies from the SDSS. The selection criteria for the sample and the estimate of the velocity dispersion are explained in Bernardi *et al.* (2003a). The selection of early type galaxies is based on both morphological and spectral criteria with only high signal to noise galaxies showing Vaucouleurs surface brightness profiles included in the sample. The observed velocity dispersion has been determined by analyzing the integrated spectrum of the whole galaxy and aperture corrected to a standard effective radius.

M05 find the following relation between the velocity dispersion and the absolute magnitude of the galaxy in the rest-frame r-band depending on redshift.

$$< log(\sigma) >= 2.2 - 0.091(M_r + 20.79 + 0.85z) \tag{4.20}$$

corresponding to a FJ index of $\eta = 4.4$ see eq. 4.12. In figure 4.12, the inferred relation from the SDSS is shown.

The scatter in the FJ relation induces an uncertainty in the estimate of the velocity dispersion which has been given by Sheth *et al.* (2003).

$$\sigma_{\log\sigma} = 0.79(1 + 0.17(M_r + 21.025 + 0.85z)) \tag{4.21}$$

To convert SDSS r-band absolute magnitudes in the AB system to standard B-band Vega absolute magnitudes, a typical color $M_B - M_r$ for ellipticals in the AB system is estimated yielding $M_B - M_r = 1.20$ (Gunnarsson *et al.*, 2006) and an AB to Vega relation $B_{AB} = B_{Vega} - 0.12$ is adopted . Using this conversion and calculating the velocity dispersion for a $L_* = 10^{10}h^{-2}L_{B\odot}$ galaxy and a redshift of z=0.45 leads to $\sigma = 179 \pm 30\mathrm{kms}^{-1}$ and $\alpha = 1/\eta = 0.275$.

4.3.3 Comparison

For a summary and comparison of L^* galaxy fiducial velocity dispersions and the different scale parameters for both weak lensing results (modeling the lenses as SIS) and TF and FJ results see table. 4.1 and fig. 4.13.

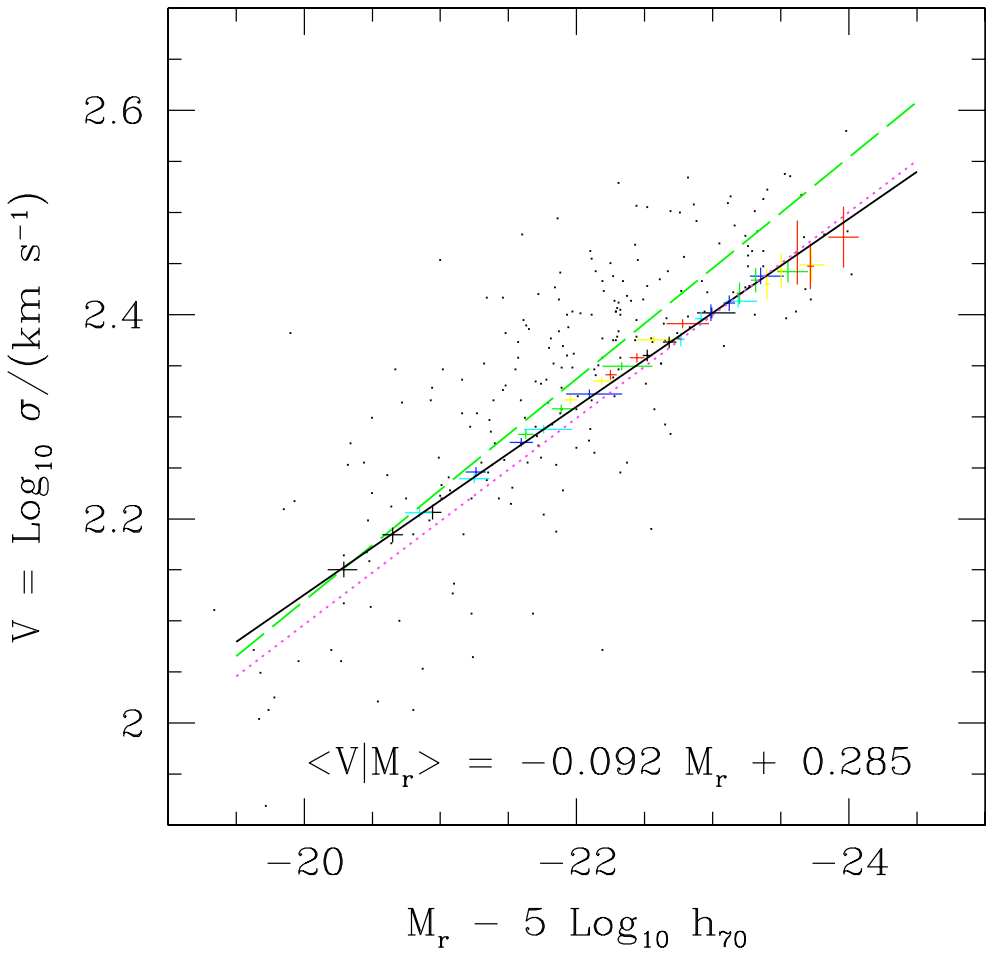

Figure 4.12: Correlation between velocity dispersion and luminosity (Faber-Jackson relation) for the SDSS sample of ~ 30.000 elliptical galaxies. The error-bars refer to the SDSS elliptical galaxy sample. The solid line shows a straight line fit to the data. The dotted line shows the fit from Bernardi *et al.* (2003b) which consists of an earlier sample of the SDSS elliptical galaxies (~ 9.000) rescaled to account for new photometry. A local sample of 236 elliptical galaxies from Prugniel & Simien (1996) is shown in dots and the dashed line shows a fit to their sample. Credit : Mitchell *et al.* (2005)

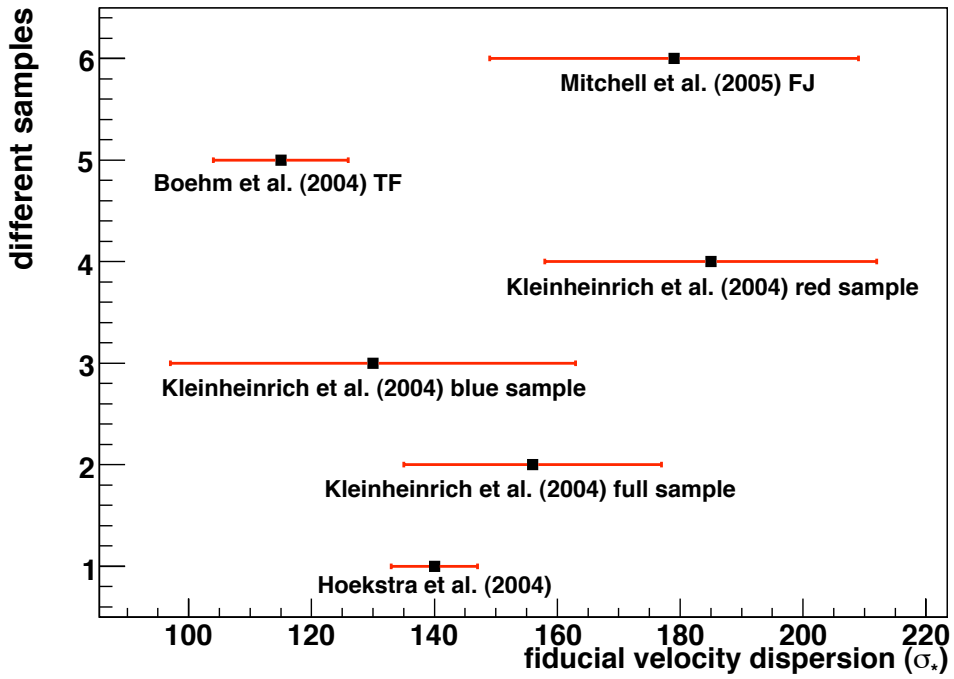

Figure 4.13: The velocity dispersions for a L^* galaxy.

Article	scaling parameter α	σ_* km/s
Hoekstra *et al.* (2004) ($L^* = 10^{10}h^{-2}L_{B\odot}$)	0.3	140 ± 7
Kleinheinrich *et al.* (2004) ($L^* = 10^{10}h^{-2}L_{r\odot}$)		
full sample	$0.28^{+0.12}_{-0.09}$	156^{+18}_{-24}
blue sample	$0.22^{+0.15}_{-0.15}$	130^{+30}_{-36}
red sample	$0.28^{+0.15}_{-0.12}$	185^{+24}_{-30}
Böhm *et al.* (2004) (TF) ($L^* = 10^{10}h^{-2}L_{B\odot}$)	0.33	115 ± 11
Mitchell *et al.* (2005) (FJ) ($L^* = 10^{10}h^{-2}L_{B\odot}$)	0.275	179 ± 30

Table 4.1: L^* galaxy fiducial velocity dispersions.

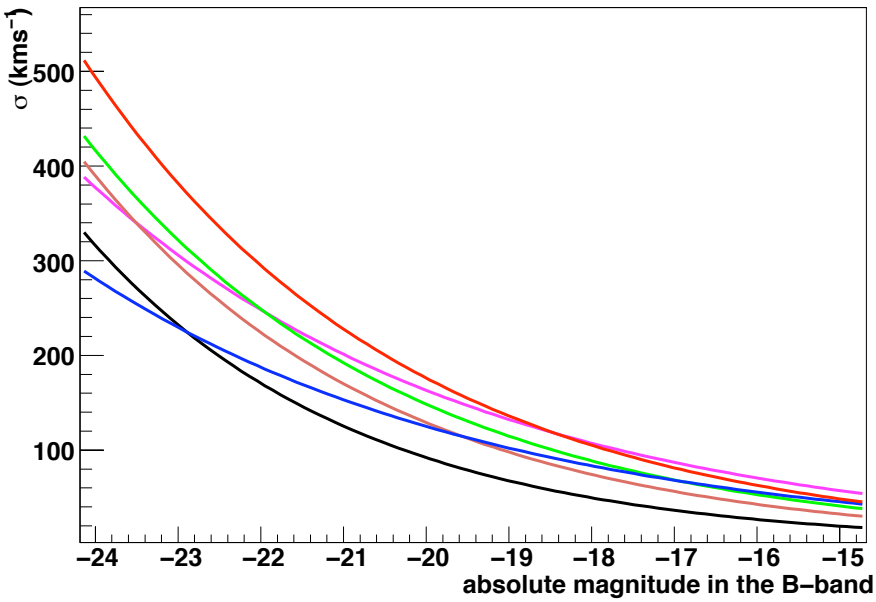

Figure 4.14: The velocity dispersion as a function of absolute magnitude in the B-band for the K04 full sample relation in green, the K04 red sample in red, the K04 blue sample in blue, the H04 relation in brown, the FJ relation in magenta and the TF relation in black. The calculations are done for the redshift $z = 0.4$ for the TF and FJ relations so as to be comparable to the mean lensing redshift of the two other surveys.

Figure 4.14 shows a comparison of the different already presented mass-luminosity relations for the SIS model. The velocity dispersion, σ, is plotted as a function of absolute magnitude in the B-band for the K04 full sample relation, the K04 red sample, the K04 blue sample, the H04 relation, the FJ relation and the TF relation. The calculations are done for the redshift $z = 0.4$ for the TF and FJ relations so as to be comparable to the mean lensing redshift of the two other surveys (COMBO-17 and RCS). When looking at the TF and FJ relations it is worth noticing that the FJ relation has higher velocity dispersions than the TF relation which is expected since for a given B-band luminosity, ellipticals are more massive than spirals. The K04 full sample relation and the H04 relation lie in the middle almost over the whole range which is expected since this is an average value of all the galaxies, however, with a preference for high velocity dispersions in the bright end. It is important to notice that for high luminosity galaxies the difference in mass estimate from these relations can lead to big differences for SNe magnifications.

The separation of the sample into a red and blue sample has led to a relation with low velocity dispersion for the blue sample and one with high velocity dispersions for the red sample. In figure 4.15 the results from the TF and FJ relations together with the red and blue sample results for K04 are shown appart. The relations agree quite well. A preference for high velocity dispersions in the K04 results for bright galaxies ($-23 < M_B < -19$) is seen. The difference in velocity dispersion for spirals and elliptical or blue and red is important since this can lead to a big difference in the estimated magnification. This shows the importance of determining the velocity dispersion based on the color of the galaxy.

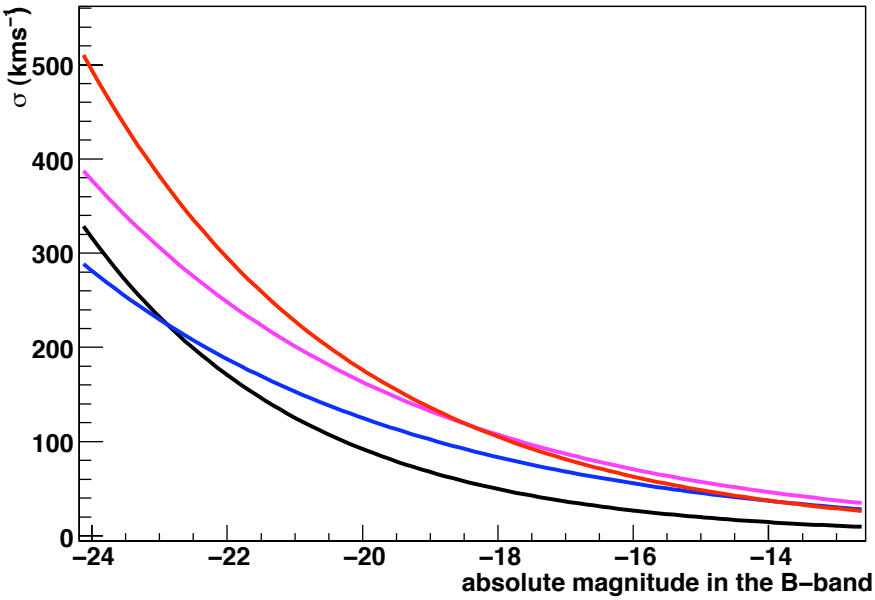

Figure 4.15: The velocity dispersion as a function of absolute magnitude in the B-band for the TF relation in black, the FJ relation in magenta, the K04 blue sample in blue and the K04 red sample in red.

Chapter 5

Measuring the SNLS supernovae magnification

This chapter is dedicated to the analysis of the SNLS 3rd year data sample in order to estimate the magnification of each SNIa that enter the Hubble diagram. We aim at detecting a correlation between the relative brightness of the SN, given by the residual to the Hubble diagram and the estimated magnification due to foreground mass over densities. The residuals have been provided by the SNLS team and here we estimate the magnification using photometric data of foreground galaxies.

Before describing the analysis performed in this thesis we will present an overview of the SNLS 3-year supernova sample including the survey, the detection, identification and photometry of the supernovae and also the 3-year calibration.

5.1 SNLS 3 year dataset

The main goal of the SNLS is to probe the nature of the dark energy by measuring its equation of state parameter and thus be able to distinguish between different dark energy models. The survey aims at using luminosity distance measurements of a large sample of Type Ia SNe ($\sim$ 500) in the redshift range z=0.2-1.1. The SNLS started observing in August 2003, and in October 2008 the last data was taken leading to a total duration of the survey of 5 years and a few extra months. So far, this project has been one of the leading Type Ia SN surveys and has already set tight constraints on the cosmological parameters (Astier *et al.*, 2006).

5.1.1 The survey

The SNLS consisted of an imaging survey detecting and monitoring the light curves of the SNe, and a spectroscopic follow-up confirming the nature of the SN and measuring the redshift. The imaging survey was part of the deep component of the Canada-France-Hawaii Telescope Legacy Survey (CFHTLS) which consisted of a deep survey, a wide survey and a very wide survey. The observations were performed at the CFHT which is a 3.6 meter optical/infrared telescope located at the summit of Mauna Kea (Hawaii), 4200 meter above sea-level (see image 5.1).

As for the deep survey, a total of 202 nights of CFHT time were allocated to image four low Galactic extinction fields (D1, D2, D3, D4) around the sky in 5 different filters (u, g, r, i, z). Characteristics of

Figure 5.1: The CFH Telescope at the summit of Mauna Kea. Credit: CFHT homepage

Field	RA(2000)	Dec (2000)	Other Observations
D1	02:26:00.00	-04:30:00.0	XMM Deep, VIMOS, SWIRE, GALEX
D2	10:00:28.60	+02:12:21.0	Cosmos/ACS, VIMOS, SIRTF, XMM
D3	14:19:28.01	+52:40:41.0	Groth strip, Deep2, ACS
D4	22:15:31.67	-17:44:05.0	XMM Deep

Table 5.1: Characteristics of the four SNLS fields.

the four fields are summarized in table 5.1.

The MegaCam imager (Boulade *et al.*, 2003) (360 Megapixels, 1 deg^2) is located at the prime focus of CFHT (see figure 5.2). The camera consists of 40 CCDs where 36 are currently in use (se figure 5.3). Each CCD includes 2048×4612 pixels of 13.5μm giving rise to a total of 340 million pixels. The pixels subtend 0.185" on a side which allows one to properly sample point sources (an average of 0.8" FWMH and 0.5" for a few nights per year).

The instrument MegaCam embraces 5 different observational filters (u, g, r, i ,z) which are very similar though not identical to the SDSS filters. To be able to correctly measure the flux of the supernova in its referential it is necessary to take into account the ensemble of the observational system (entire instrument + atmosphere) for each filter. As a result, effective filters are constructed considering the transmission of the filter, the transmission of the optical system and the reflectivity of the mirror together with the quantum efficiency of the CCDs. In figure 5.4, the effective passbands for the MegaCam are presented.

The SNLS was designed to improve significantly on the strategy of discovery and photometric

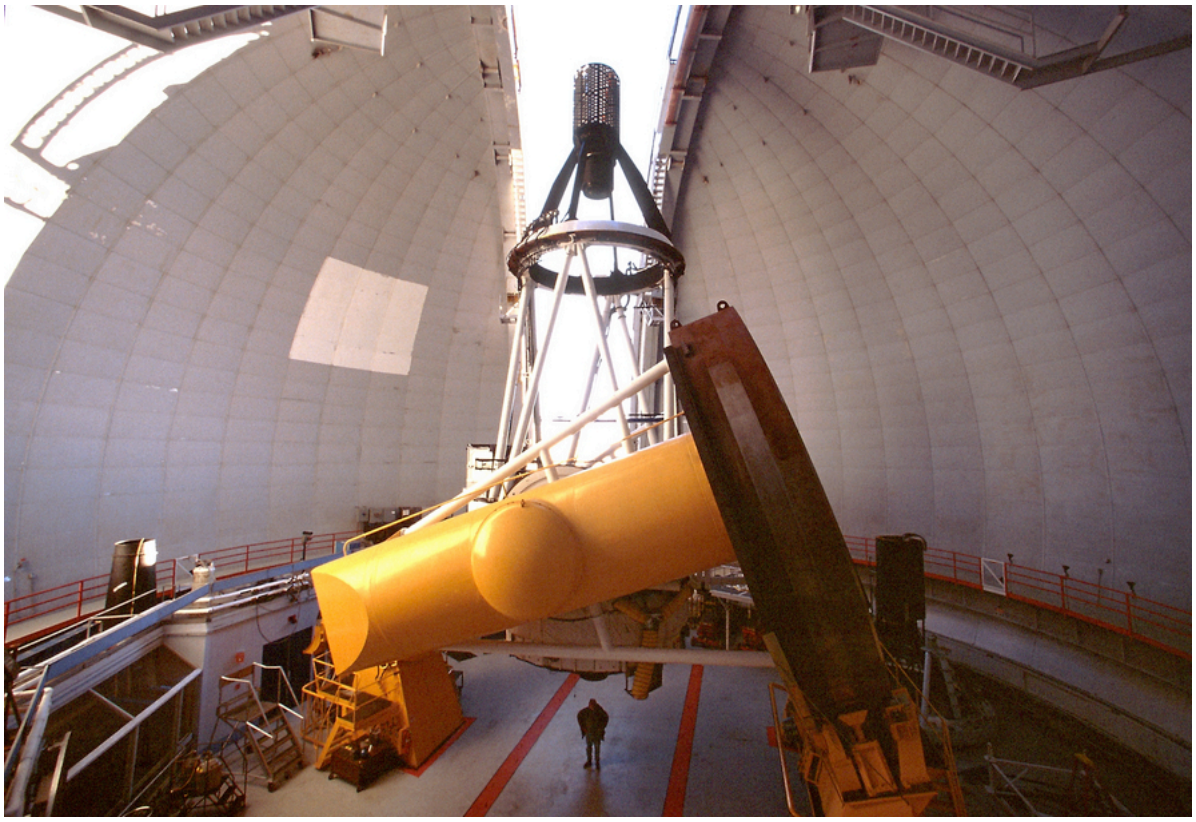

Figure 5.2: The MegaCam imager located at the prime focus at CFHT. Credit: CFHT homepage

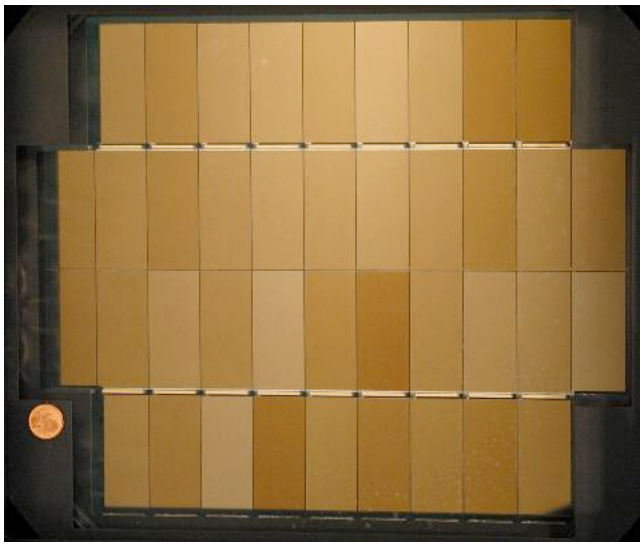

Figure 5.3: The MegaCam camera consists of 40 CCDs, 36 currently in use. Credit: CFHT homepage

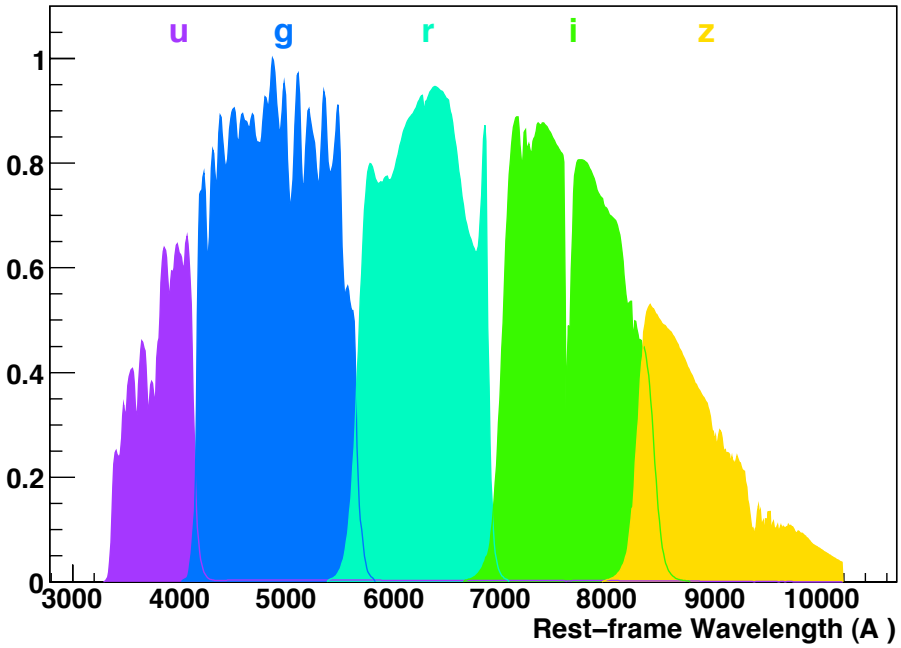

Figure 5.4: MegaCam effective passbands.

follow-up compared to previous surveys. They used the so-called rolling search method which consists of observing the same field every 3-4 days in the filters g, r, i and z if possible for as long as the field remains visible. This has been proven very efficient in detecting and monitoring Type Ia SNe because for every observation of the same field, new SNe are discovered in parallel with monitoring the already detected SNe. In figure 5.5 the advantage of the rolling search method is put forward.

5.1.2 Detection and identification of Type Ia Supernovae

The CFHT staff observed and pre-processed the data using the Elixir reduction pipeline (Magnier & Cuillandre, 2004). The data was reduced building preliminary flat field corrections, bias subtraction, mask and fringe removal (in the i' and z' band) made available to the SNLS collaboration.

New candidates were detected by subtraction of a reference image to the current science image. Two independent real-time analysis pipelines existed, one run by the Canadian team and one run by the French team. These two pipelines were kept separate throughout the survey producing a final merged candidate list for spectroscopy with $\sim 90\%$ of the candidates in common. A photometric ranking was then defined for the spectroscopic follow-up (Sullivan *et al.*, 2006a).

Spectroscopy of the SNe is crucial in order to obtain SN redshifts, and to confirm the type of each SN. Due to the faintness of distant SNe, the spectroscopy has to be performed on 8-10 meter class telescopes, and the organization of the spectroscopical follow-up was one of the major successes of the SNLS project. The merged candidate list was sent for follow-up spectroscopy at the VLT[1], Gemini[2]

[1]http://www.eso.org/projects/vlt/
[2]http://www.gemini.edu/

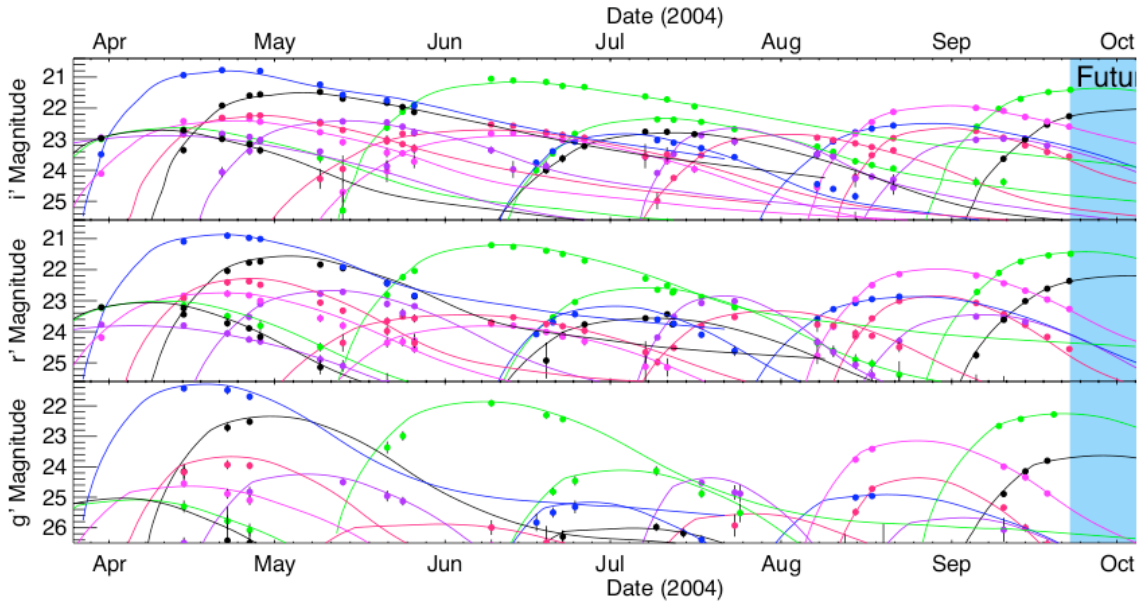

Figure 5.5: The rolling search method. New SNe are discovered simultaneously with adding points to existing light curves. Credit: Sullivan & The Supernova Legacy Survey Collaboration (2005)

and Keck[3]. The rolling search method at the CFHT led to improved efficiency for the follow-up since the light-curve monitoring of the object helps trigger spectroscopy at maximum light. The events are classified as secure SN Ia, probable SN Ia ("SN Ia*") and other. For more information on the exact definitions of classifications, see Howell *et al.* (2005b); Baumont *et al.* (2008); Balland (2009). For cosmological analysis, both secure SN Ia and probable SN Ia have been kept.

During the first year, 91 Type Ia SNe were spectroscopically confirmed and 71 were used for cosmological analysis. The third year data sample has increased considerably giving rise to 233 spectroscopically confirmed Type Ia SNe used in cosmological fits, and with the full data sample, ~ 500 Type Ia SNe are expected to be included in the Hubble diagram.

5.1.3 Photometry of the supernovae

All the images in each field and each passband are resampled to a reference image which is the best quality image (best IQ). For the reference image, a PSF (Point Spread Function) model is derived and a convolution kernel is found for each image so as to be able to connect the reference PSF with the PSF of a given image. The kernels also contain the photometric ratios of the science images and the reference image.

The flux of the SN is then estimated based on differential photometry. A model is constructed containing the host galaxy which is spatially variable but constant in time and the SN which is a time variable point source (described in detail in Fabbro (2001), Raux (2003) and Astier *et al.* (2006)).

[3]http://www.keckobservatory.org/

Consider a pixel, p, of the image, i, the intensity, $D_{i,p}$ in this pixel can then be modeled:

$$D_{i,p} = \Big[(f_i P_{ref} + g) \otimes k_i\Big]_p + b_i \tag{5.1}$$

where f_i is the flux of the SN in the image i, P_{ref} is the PSF of the reference image, k_i is the kernel that relates the reference PSF to the PSF of image i, g is the host galaxy intensity in the reference image and b_i is the local background in image i. In the images before the SN explosion or long after, the SN flux is set to zero.

The photometric fit, a χ^2 minimization procedure, consists of fitting simultaneously the pixels of the host galaxy, the position of the SN and the flux of the SN in each image using the previously derived kernels. The g and r band light curves present low signal to noise at high redshifts and as a result the position is not fitted in those bands, instead the averaged position of the r and i band fits is used.

5.1.4 Calibration

Assigning physical fluxes to SNe is performed using the following sequence (see also section 2.4 where the calibration procedure is sketched).

1. Magnitudes are attributed to field stars (tertiary stars) by measuring the flux ratio of these stars to secondary standard stars with known magnitudes.

2. Physical fluxes of an object can be assigned from the calibrated magnitudes by using the SED of a reference object with known magnitudes.

3. The SNe are in turn calibrated by comparing the photometry of the SNe to that of field stars by measuring the flux ratios using the same photometric method.

The 3-year SNLS calibration is presented in great detail in Regnault *et al.* (2009). Here is a summary of the important features.

Standard photometric calibration system

The 3-year SNLS dataset has been calibrated using the Landolt (1992) standard star catalog which is reported in the Landolt Johnson-Kron-Cousins-UBVRI system. The optimal choice would have been a standard photometric calibration system with a filter set close to the MegaCam filters. This is not the case for the Landolt Johnson-Kron-Cousins-UBVRI filters which differ significantly from the Megacam filters (see fig. 5.6)

However, the sample of nearby SN Ia used to supplement the SNLS dataset and crucial for cosmology is reported in the Landolt system. Important uncertainties are involved concerning the systematic differences between photometric systems and as a result the SNLS collaboration has despite the big differences in filter sets chosen to calibrate the SNe with respect to the Landolt system.

In practice, the Landolt fields are observed every photometric night leading to zero-points for each of those nights in each band. It is important to take into account that the MegaCam passbands are not uniform and vary as a function of the position in the focal plane. As a result corrections which are based on the modeling of the photometric response system have been applied enabling us to propagate the calibration to the whole focal plane. The Landolt-MegaCam color transformations are modeled as piecewise linear functions including a "color break" marking the transition between the linear functions. In figure 5.7 the color-color plots from the SNLS 3-year calibration (Regnault *et al.*, 2009) are shown.

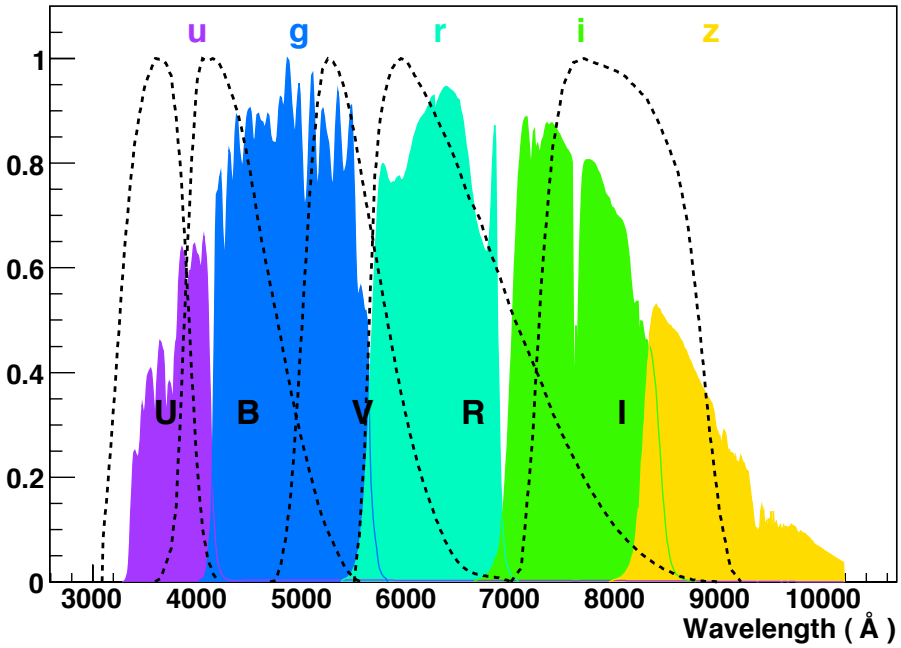

Figure 5.6: The MegaCam filters compared to the Landolt Johnson-Kron-Cousins-UBVRI filters.

The tertiary stars

The catalog of tertiary stars (science field stars) are selected based on their second moments m_{xx}, m_{yy} and m_{xy} (for more information about star selection see section 5.3.2) and are well measured, isolated, non-variable stars.

It is important that the flux of the field stars and the standard stars is measured using the same photometry. For the SNLS, an aperture photometry has been chosen. The data is normalized with respect to the exposure time and the air mass which differ from the two types of observations. The tertiary stars are then calibrated using the night and band zero-points together with the color transformations and photometric corrections. At this stage we have calibrated magnitudes for each tertiary star for observations taken over the 3 year period. An average magnitude for each star, in each band is retained in order to produce the tertiary catalog (Regnault *et al.*, 2009).

The fundamental standard

To be able to transform magnitudes into physical flux measurements one must rely on a fundamental spectrophotometric standard for which we have both magnitudes in the same system as the secondary stars and a high quality spectrum. For the first year calibration Vega was used, but for the 3-year calibration, BD 17 +17 4708 has been used. This star has been observed by Landolt which implies that we have Landolt magnitudes (Landolt & Uomoto, 2007). It has also been observed with the HST STIS (Space Telescope Imaging Spectrographs) and NICMOS (Near Infrared Camera and Multi-Object Spectrometer) instruments which has resulted in a high-quality SED of the star (Bohlin, 2000; Bohlin & Gilliland, 2004; Bohlin, 2007). The absolute flux-scale has been defined based on NLTE models

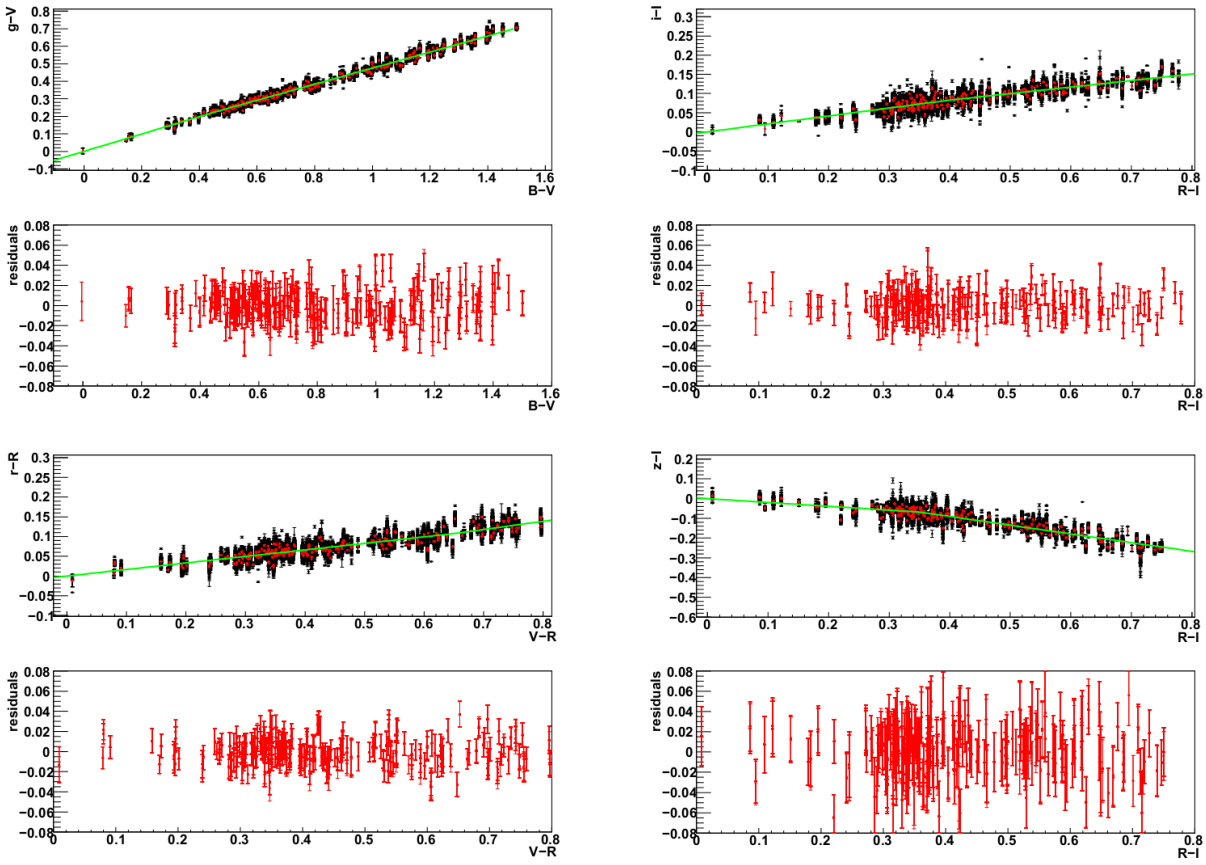

Figure 5.7: The Landolt-MegaCam color-color plots. Credit: Regnault *et al.* (2009)

of hydrogen white-dwarfs (Bohlin, 2000). In addition, BD17 has colors similar to the core of the Landolt stars which reduces the impact of the uncertainties related to color transformations. To assign magnitudes in the SNLS bands of this star measured in the Landolt system we rely on the previously defined Landolt-MegaCam transformation and small corrections of the order of 0.002mag based on stellar models (see Regnault *et al.* (2009)).

Assigning calibrated magnitudes to the SNe

The last step of the calibration is to transfer the calibration of the tertiary stars to the SNe. This consists of measuring the tertiary stars using the exact same photometry as the one used for measuring supernova fluxes. The only difference is that in lack of a host galaxy this component is set to zero in the fit. Then a zero point:

$$ZP = mag + 2.5 \log_{10}(flux) \tag{5.2}$$

where mag is the magnitude of the tertiary star given by the tertiary star catalog, can be assigned to each light curve point.

5.1.5 Third year SN sample

The third year SNLS data sample consists of 233 spectroscopically confirmed Type Ia supernovae in the redshift range 0.2-1.2 after quality cuts.

For the SNLS 3-year sample, two light curve fitters have been used, SALT2 (Guy *et al.*, 2007) and SIFTO (Conley *et al.*, 2008), but for this work we will use results from SALT2. This is an empirical modeling of Type Ia SNe spectro-photometric evolution with time and is built using both light curves and spectra of nearby and distant SNe. This particular light curve fitter uses K-corrections naturally built into the model. The aim of the model is to obtain a best average spectral sequence of Type Ia SN and the main components responsible for the variety of Type Ia SNe taking specifically into account the variability of the large features of Type Ia SNe spectra. In this way, the variability of Type Ia SNe spectra at any given phase can be accounted for at first order. The modeling of the SN rest-frame UV spectral energy distribution is included giving rise to improved distance estimates for high-z SNLS SNe (0.8 <z< 1.1) for which the z-band measurement is poor. The flux of the SN, f, is modeled as

$$f(\lambda, t) = x_0 \times [M_0(\lambda, t) + x_1 M_1(\lambda, t)] \times \exp(c \times CL(\lambda)) \tag{5.3}$$

where t is the phase (time with respect to maximum light in the rest-frame B-band), λ is the wavelength in the rest-frame of the supernova, M_0 is the the average spectral sequence and M_1 describes the main variability of Type Ia SNe. x_0 is the normalization of the SED whereas x_1 is the shape parameter and $CL(\lambda)$ describes the average color correction law together with c, the color parameter. Using the calibrated magnitudes of the supernova in each filter, all observed bands are fitted simultaneously returning the supernova rest-frame B-band magnitude m_B, the shape parameter x_1 and the color parameter c for each SN.

In figure 5.8, the spectrum of one of the supernovae (SN03D1fc) at redshift z=0.332 obtained at the VLT is shown with a raw SALT2 model in green and in red, a best SALT2 fit after a 2^{nd} degree polynomial multiplicative correction that accounts for the λ dependent calibration uncertainty of the spectrum (called re-calibration in SALT2 parlance). The SALT2 fitted light curves of this particular SN are shown in fig 5.9.

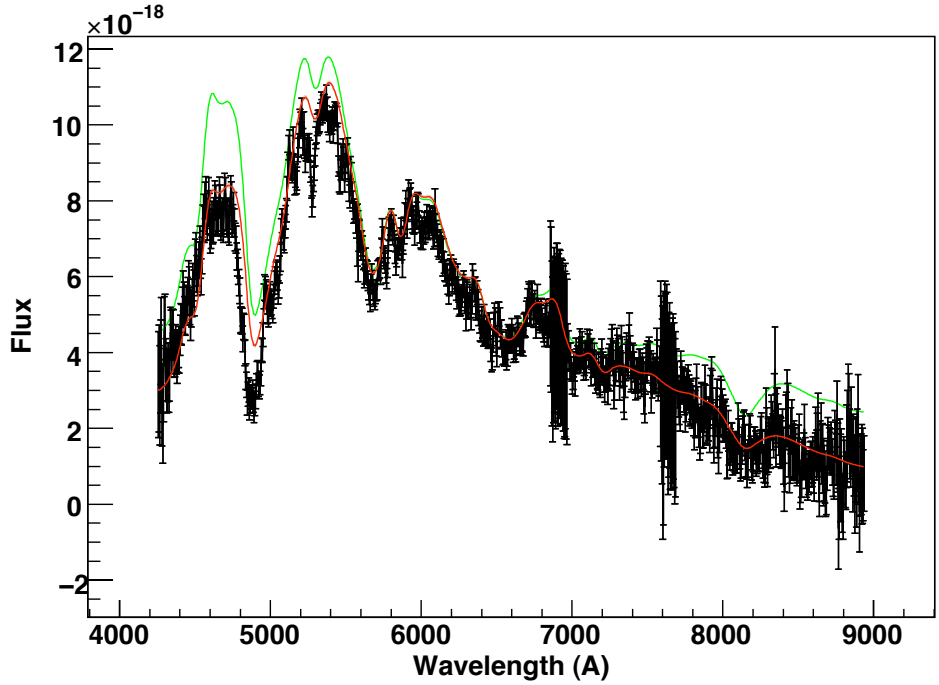

Figure 5.8: The spectrum of SN03D1fc (z=0.332) obtained at VLT. In green: the raw SALT2 model. In red: the best SALT2 fit after re-calibration.

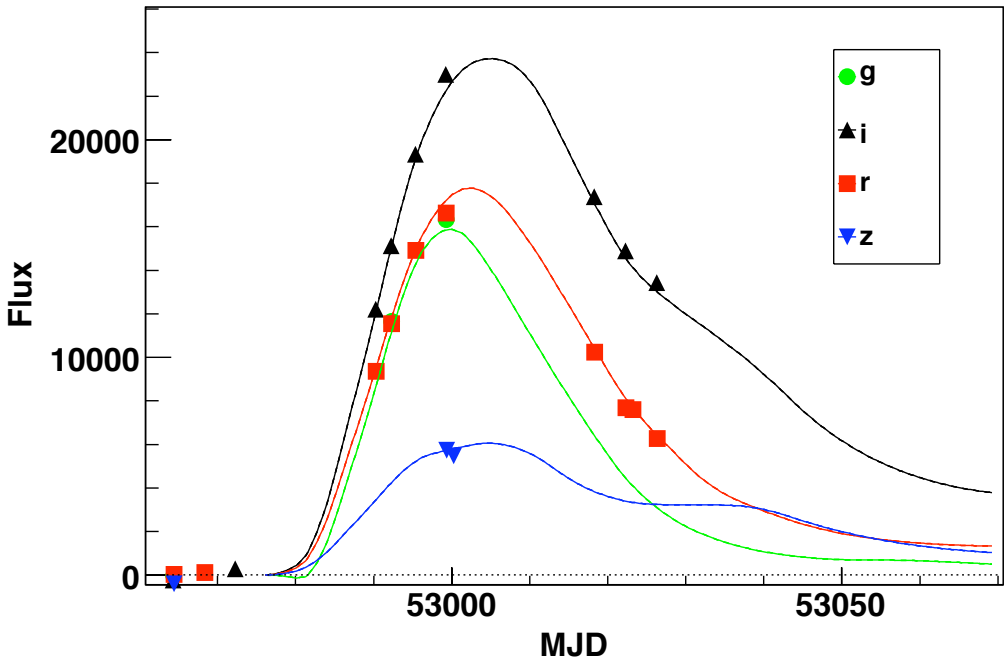

Figure 5.9: Rest-frame griz light curves of SN03D1fc (z=0.332) with SALT2 fits.

The cosmological parameters and the global parameters of the distance modulus such as the average absolute magnitude, M_B together with α and β related to the shape and color parameters respectively (see eq. 2.3) are obtained by performing a χ^2 minimization of the residuals to the Hubble diagram.

$$\chi^2 = \sum_{objects} \frac{(\mu_B - 5\log_{10}(d_L(\theta, z)/10pc))^2}{\sigma^2(\mu_B) + \sigma^2_{int}} \tag{5.4}$$

where d_L is the luminosity distance and θ represents the cosmological parameters that define the fitted model. σ_{int} is the intrinsic dispersion of the SNe and expresses the fact that the observed scatter of the Hubble diagram is larger than expected from measurements and modeling uncertainties. This dispersion accounts for variabilities in the absolute luminosity and an average dispersion due to gravitational lensing and is adjusted to yield a χ^2 value equal to the number of degrees of freedom. The Hubble diagram for the SNLS 3 year sample together with the residuals to the best fit ΛCDM model are presented in figure 5.10.

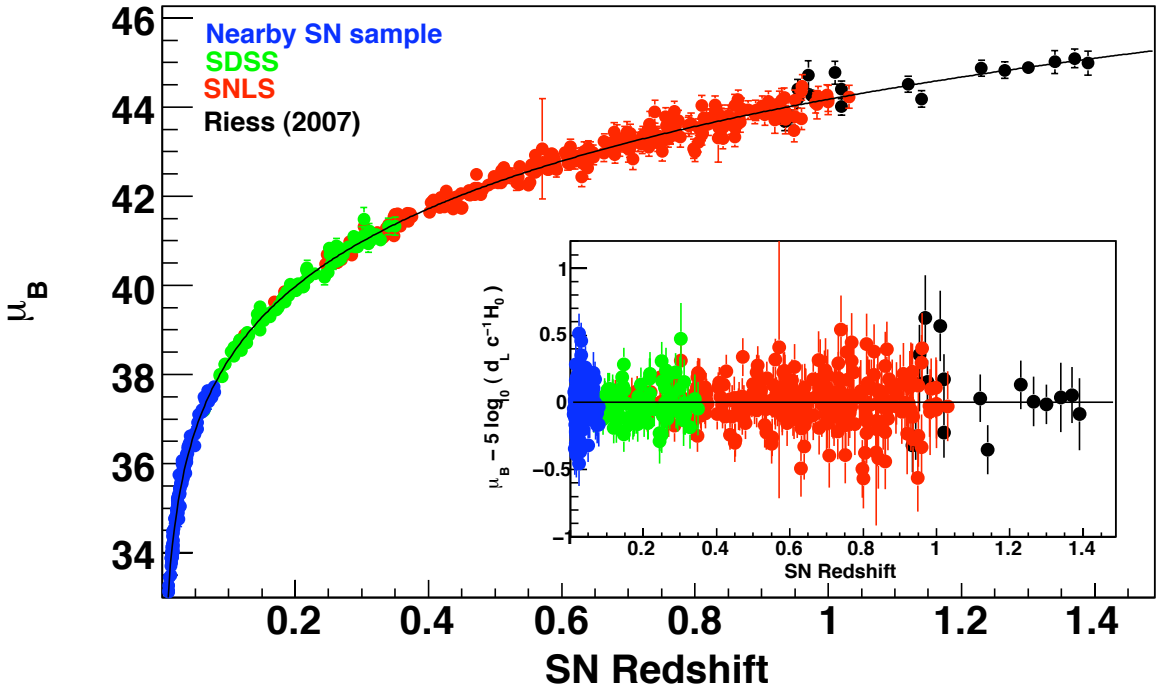

Figure 5.10: The SNLS 3 year Hubble diagram together with the residuals to a ΛCDM model. In blue: Nearby Type Ia SNe sample. In green: SDSS Type Ia SNe (Holtzman *et al.*, 2008). In red: SNLS Type Ia SNe. In black: High-z Type Ia SNe from Riess *et al.* (2007).

5.2 Summary of the analysis chain

The analysis chain for the analysis described in this thesis is the following:

- The first step is to obtain a high quality galaxy catalog with accurate photometric redshift for each galaxy. The galaxy catalogs are built for each field by stacking the images obtained in

the different filters. From these stacked images, the source detection and photometry has been performed using SExtractor (Bertin & Arnouts, 1996), with the detection made in the i-band. These catalogs need to be cleaned from stars and host galaxies of the SNe and certain areas need to be masked out.

- To obtain accurate photometric redshifts and absolute magnitudes in the U, B and V band for each galaxy using the *ugriz* measurements, a new photometric redshift code has been used (Guy& Hardin, *internal note*). This is a template based code where different templates of galaxy spectra are fitted to the actual measurements. The templates have been optimized using galaxies with spectroscopic redshift from the DEEP-2 survey (Davis *et al.*, 2003, 2007). As for the resolution of the code, it has been estimated using galaxies with spectroscopic redshift from the VVDS (Le Fèvre *et al.*, 2004) and has been proven similar to the resolution of the CFHTLS photometric redshifts provided by Ilbert *et al.* (2006).

- The next step is to convert the observed luminosity of each galaxy into a mass estimate using one of the mass-luminosity relations presented in section 4.1. We have chosen to use both mass estimate obtained by TF/FJ relations and galaxy-galaxy lensing. The input mass-luminosity relations are the Böhm *et al.* (2004) results for the TF relation (eq. 4.18) , the Mitchell *et al.* (2005) results for the FJ relation (eq. 4.20) and the Kleinheinrich *et al.* (2004) results for the galaxy-galaxy relation (eq. 4.11). The galaxy haloes are modeled as SIS.

- The last step is to compute the magnification for each SN by selecting galaxies along the line of sight and use the publicly available software Q-LET (see section 3.4), which uses the multiple lens plane algorithm to estimate the magnification factor of the source taking into account all the intervening matter along the line of sight.

5.3 The galaxy catalogs

For this particular analysis, it is essential to obtain a catalog of the field galaxies with an estimate of the redshift and the B, V and U band absolute magnitudes for each galaxy. The B-band absolute luminosity is used for the conversion of luminosity into mass (see chapter 4) whereas the color U-V is needed to separate the galaxy sample into ellipticals and spirals.

5.3.1 Stacking, photometry and extraction

The galaxy catalogs are built on deep image stacks in the u, g, r, i and z filters for each field. These deep image stacks are constructed by selecting 80% of the best quality images including 6241 images in total for the 4 fields. Transmission and seeing cuts (e.g. FWHM $<$ 1.15") are applied. In the u-band, the statistics is low due to a smaller amount of observational time allocated in this band and as a consequence, less stringent cuts are applied on the u images. The selected images are co-added using SWARP v2.10 package[4]. The source detection and photometry is performed using SExtractor V2.4.4 in double image mode. The detection has been made in the i band and is based on approximately 60 hours of imaging. The detection level is set to 2σ so as to maximise the signal detection while minimizing

[4]http://terapix.iap.fr/soft/swarp/

the many spurious detections around stars haloes. We then use the AUTO SExtractor flux, computed in an elliptic aperture to extract the galaxies.

A cut on the signal to noise ratio defined as the ratio of the flux divided by the flux error in the i-band, $S/N > 15$ has also been made so as to optimize the estimate of the effect of gravitational lensing while excluding very small galaxies giving no visible effect. The magnification factors of several randomly picked lines of sight have been calculated for various cuts on the signal to noise. Using a cut at $S/N > 15$ implies loosing on average less than one percent of the lensing signal at z=1.

The different cuts lead to a limiting magnitude *i*, of around 25. In figure 5.3.1, the magnitude distribution in the i-band is shown for the four different fields. For a description of the characteristics of the galaxy catalogs in the four fields, see table. 5.2.

In general, the galaxy catalogs are constructed by seasons which implies excluding the images of the season where the supernova has been detected. Each season lasts for 6 months. This is done so as to minimize the contamination of the SN on the galaxy. In this analysis, however, the seasons have been stacked together so as to obtain the best photometric quality possible for the galaxies. The galaxy in some extent affected by the SN is evidently the host galaxy which is removed in my analysis (see section 5.3.2). There are special cases where the SN is hidden behind a galaxy which is not the host galaxy leading to an impact of the SN on the photometry of the galaxy (see next section). In these cases, the galaxy photometry is performed excluding the images where the SN is present.

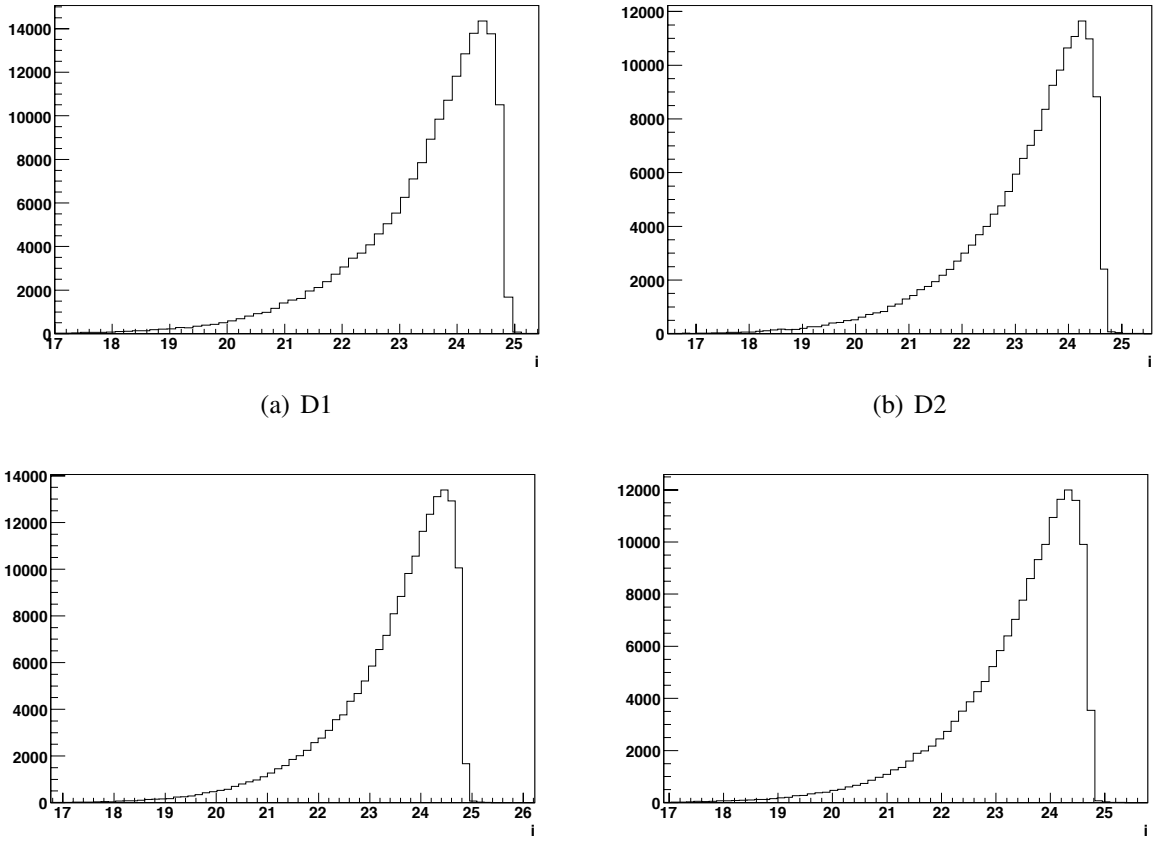

(a) D1

(b) D2

(c) D3

(d) D4

Figure 5.11: The i-band magnitude distributions for the four fields

Field	limiting magnitude in the i-band (S/N> 15)	number of galaxies	number of galaxies per square arc minutes
D1	24.9	181802	51
D2	24.75	163268	45
D3	24.95	181424	50
D4	24.85	163855	46

Table 5.2: Characteristics of the four SNLS field galaxy catalogs.

5.3.2 Classification of stars and SN host galaxies

It is necessary to exclude two categories of objects from the galaxy catalogs: the stars, and the galaxy that hosted the SN.

Identification of stars

Stars can be recognized by their characteristic 2D profile of intensity in the image which defines the PSF. As the PSF varies along the focal plane, stars are distorted in the same way as a function of the location in the focal plane leading to a concentration of objects with the same second moments.

The identification of the stars is hence carried out as follows. The second moments (m_{xx}, m_{yy}, m_{xy}) have been estimated from a 2-D Gaussian fit for all the objects in the catalog giving rise to a measurement of the shape of the object. Stars can then be identified by the locus of objects in the m_{xx}-m_{yy} plane (see fig. 5.12), which will be referred to as the shape parameter. The exact location of the locus is not constant throughout the entire focal plane due to optics (the distortion can be more or less elliptical as a function of the position on the focal plane) and as a result the location of the locus is calculated for different sections of the camera and a 2 dimensional polynomial is fitted so as to obtain the shape parameter of a typical star as a function of the location on the focal plane.

The identification is performed in two steps. A first run selects the location of the locus in each selected section and makes a first adjustment to the polynomial. In this selection mostly stars, but also some galaxies are included. Then the selected objects from the first run are reanalyzed using the newly fitted star shape parameter as a function of the location in the focal plane to discriminate between galaxies and stars.

Identification of the SN host galaxy

To identify the SN host galaxies, it is necessary to use images without the SN, i.e. to further select the images entering the stacks according to their date. For a given SN, we exclude the images taken during the same season, i.e. the 6 consecutive months during which the field is observed. The host galaxy is identified as the closest object to the SN location. For this, a normalized elliptical distance, d, is used so that $d \leq 1$ within the SExtractor "AUTO" photometry aperture:

$$d = \sqrt{(ax^2 + bxy + cy^2)}/KRONfactor \tag{5.5}$$

where $r^2 = ax^2 + bxy + cy^2 = 1$ defines an ellipse with its second order moments equal to those of the galaxy. The non-dimensional number, KRON factor, is then used to scale the ellipse according

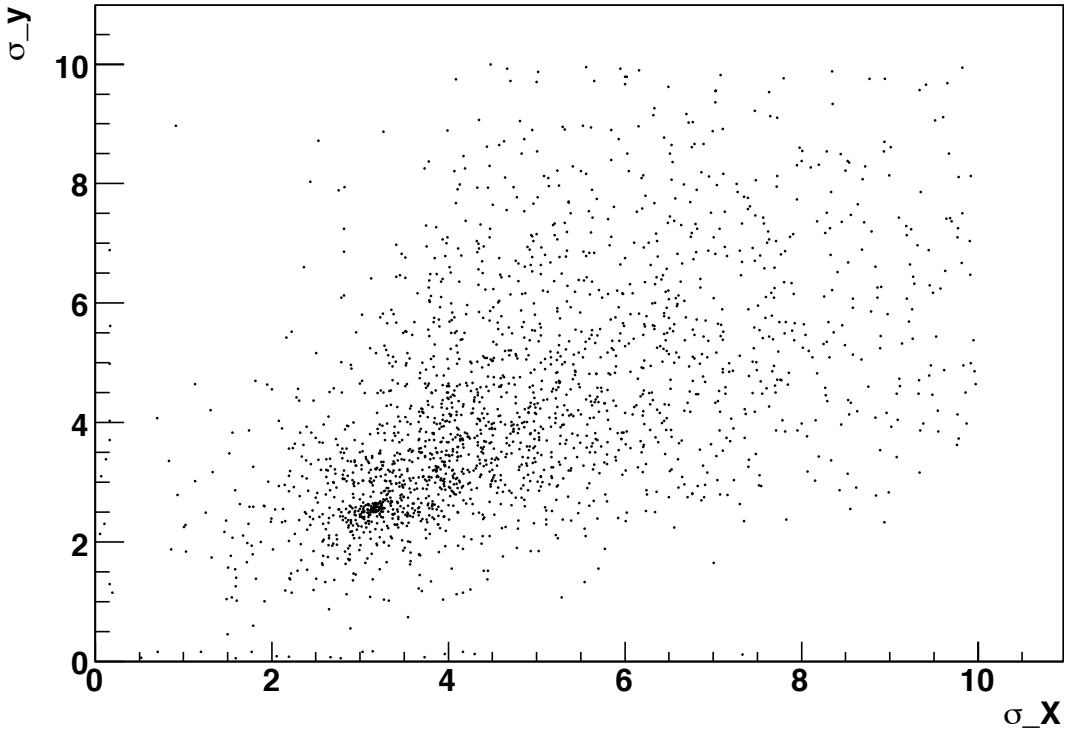

Figure 5.12: The second moments m_{xx} vs m_{yy}. Stars can be identified by the concentration of objects. This shows a section of the centre of the focal plane of 3000x3000 pixels.

to the object light profile[5]. When no object is found within $d > 1.3$ of the SN, we acknowledge the failure in having detected the SN host. When more than one object is detected close to the SN location, we check the correspondence between the galaxies' photometric and the SN spectroscopic redshifts. Dubious cases are flagged as problematic and can lead to exclusion of the SN if the uncertainty in the determination of the host galaxy has a big impact on the magnification of the SN in question. Two SNe from the sample have been excluded in this way.

In the SNLS 3 year sample, 2 cases have been given special care, SN04D2kr and SN05D2bt. These 2 SNe are detected very close to a galaxy where the photometric redshift does not match the spectroscopic redshift. Concerning these two SNe, we are fortunate to have HST imaging from the COSMOS field together with high resolution redshift for one of the galaxies . Figure 5.3.2, and 5.3.2 show the CFHT and the HST images for the SNe in question with a red square for the SN and a red circle in the CFHT image for the disputed host galaxy.

For SN 04D2kr at z=0.744, a smaller and hardly visible galaxy is detected at the location of the SN in the HST image, very close to the large galaxy. The redshift assigned to the large galaxy from CFHT, COSMOS and the SNLS photometric redshift code is z = 0.168, 0.228 and 0.3 respectively implying that the large galaxy in question is not the host galaxy, but a foreground galaxy. The host galaxy is probably the small galaxy detected in the HST image.

Concerning SN 05D2bt at z=0.68, we see that the defined host galaxy in the CFHT image is in fact 2 different galaxies surrounding the SN. Note, in this image the SN has been detected. The largest of the 2 galaxies is a foreground galaxy with the estimated redshift of z = 0.31 and 0.32 from the SNLS photometric redshift code and CFHT respectively.

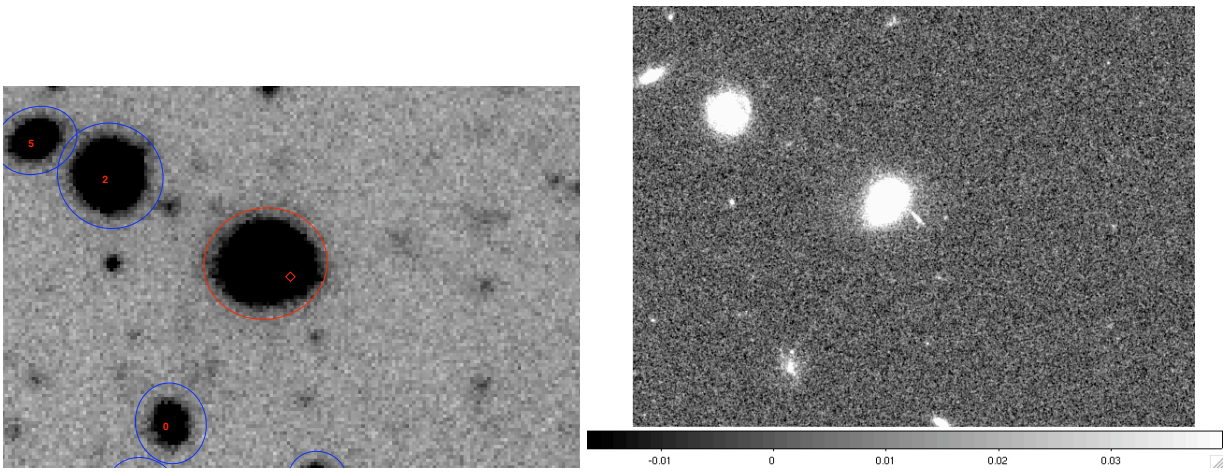

(a) CFHT (b) HST

Figure 5.13: SN04D2kr at z=0.744

5.3.3 Masking areas in the catalogs

Bright stars and edges of the camera field of view give rise to areas in the galaxy catalogs where the photometry is not accurate enough.

[5]The KRON factor is twice the flux-weighted average of the elliptical radius r, for $r \leqslant 6$.

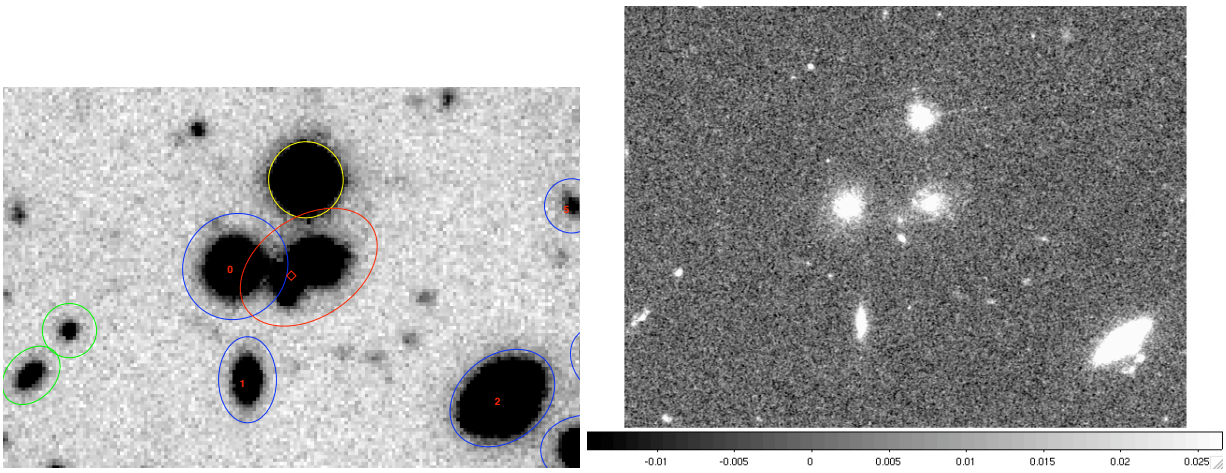

(a) CFHT (b) HST

Figure 5.14: SN05D2bt at z=0.68

Halos around stars due to intern reflections in the optics generate spurious galaxy detections in the catalog for very bright stars, also known as ghosts (see fig. 5.15). Since this is an optic feature depending solely on the design of the telescope, the sizes of the halos are approximately the same (radius of $\sim$ 600 pixels). The strength of the halos is proportional to the flux of the star.

Another problem arises for the brightest stars which consists in pixels reaching their level of saturation and as a consequence electrons will move over to nearby pixels creating bleedings (see fig. 5.16). In these areas, the flux information of an object is lost.

Each star also presents diffraction spikes due to the support rods of the camera. The light is scattered in a preferential direction perpendicular to the rods creating spikes in the image. The size of the spikes is proportional to the flux of the star. Due to this effect, circles with radius varying from 50 to 600 pixels are masked out.

A mask has been constructed based on the flux of the object in the i-band. It is important to take into account the location of the star in the field since due to optic features the halo of the star will be shifted with respect to the center of the star as a function of the distance away from the center of the field, see and example fig. 5.17.

Figure 5.18 shows a cut of the mask in the D1-field, the masked areas are shown in magenta.

5.3.4 Classification of spiral and elliptical galaxies based on colors

The Tully-Fisher and Faber-Jackson relations are derived for spiral galaxies and elliptical galaxies respectively and as a consequence it is necessary to separate the SNLS galaxies into spirals and ellipticals. Morphological classification is not possible using the SNLS data and hence a color cut has been defined. For this purpose it is necessary to obtain photometric redshifts for each galaxy so as to be able to compute rest-frame colors. This is done using a newly developed SNLS photometric redshift code which will be presented in the section 5.4.

In a galaxy color-magnitude diagram the galaxies are separated in a red sequence with mostly elliptical galaxies and a blue cloud with mostly spiral galaxies. To classify the galaxies, the restframe color U-V is computed giving rise to 2 well separated distributions (the red and the blue sequence). In figure 5.19 the restframe color U-V for the SNLS galaxies is shown leading to a color cut at U-V=0.54

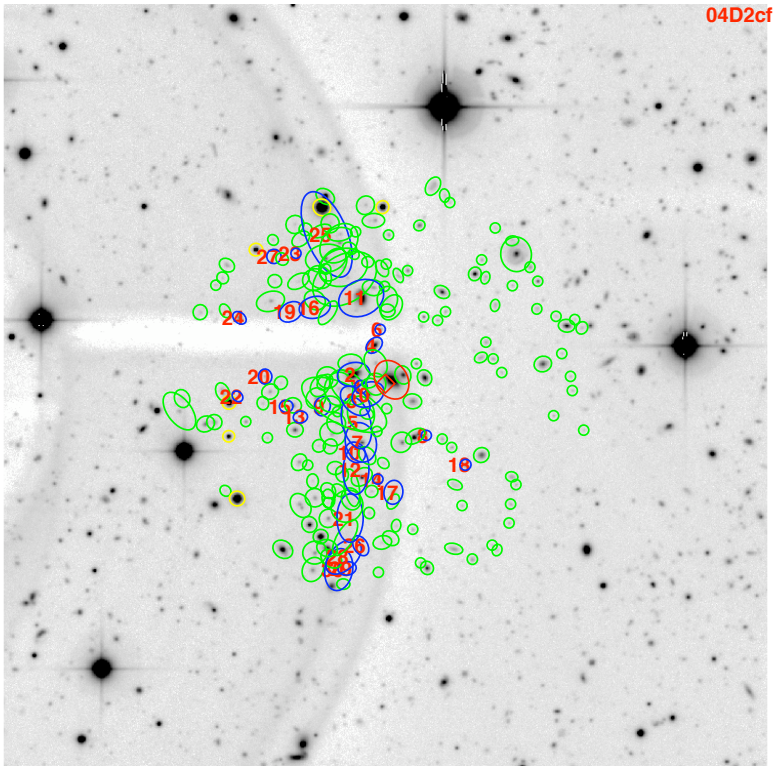

Figure 5.15: Halo around a star creating spurious galaxy detections. Green and blue circles show background and foreground galaxies respectively compared to a given SN in red (SN04D2cf).

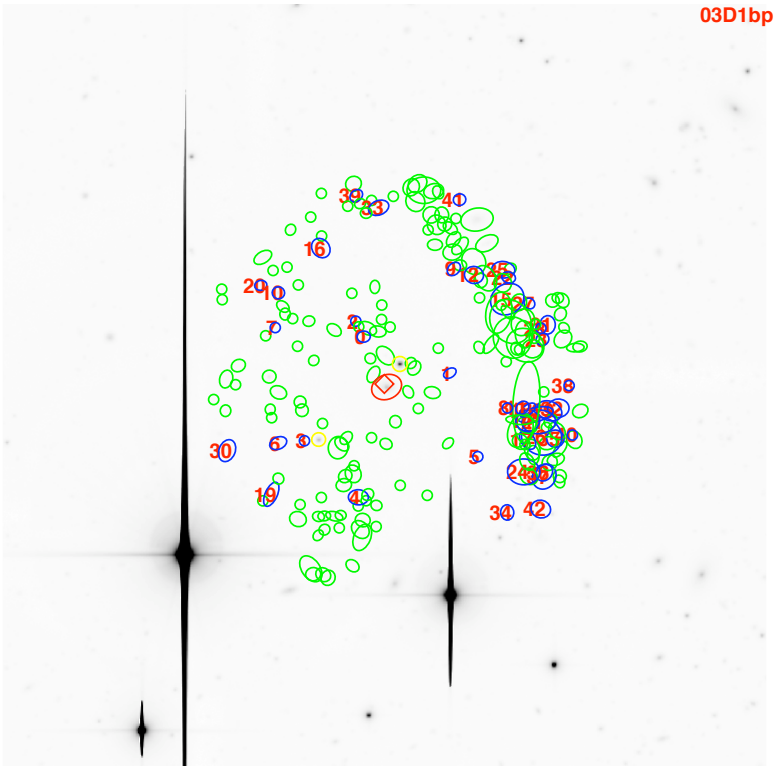

Figure 5.16: Saturated stars in the vicinity of SN03D1bp. Green and blue circles show background and foreground galaxies respectively compared to the SN in red.

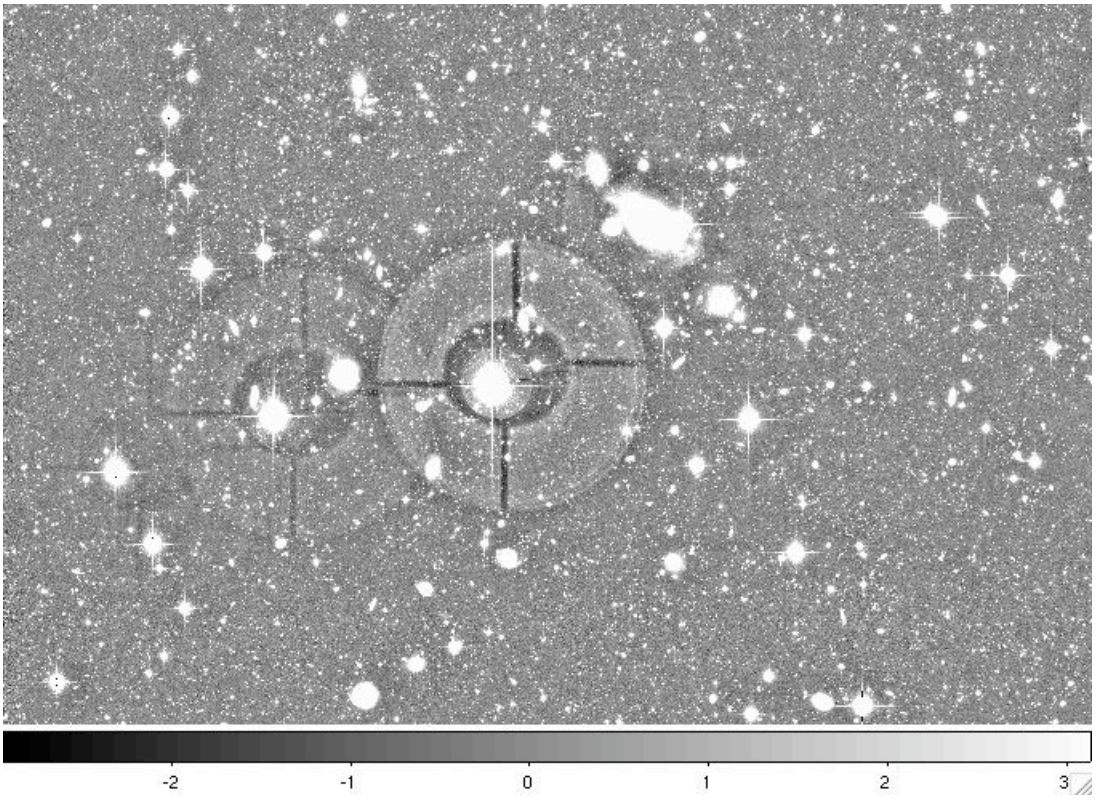

Figure 5.17: The halo of the stars which are shifted with respect to the location in the focal plane.

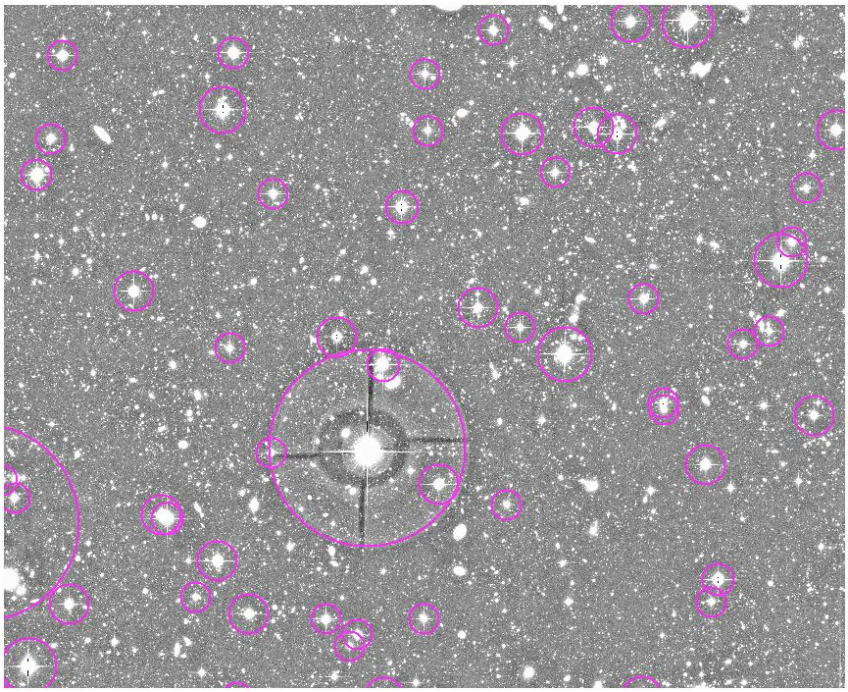

Figure 5.18: A section of the D1 field (5000x4500 pixels) with the masked areas in the magenta circles.

so that for U-V$\geqslant$0.54, the galaxy is classified as an elliptic galaxy and else it is classified as a spiral galaxy.

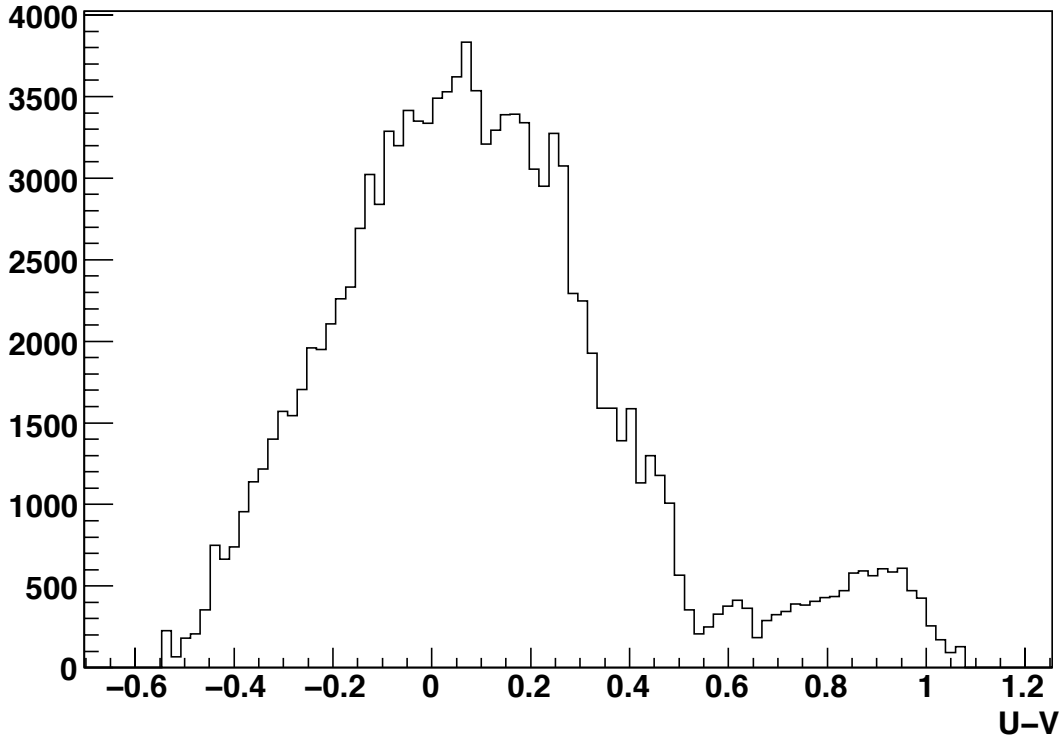

Figure 5.19: Restframe U-V color for the SNLS galaxy catalogs. A cut at U-V=0.54 separates the distribution into red (elliptical) and blue (spiral) galaxies.

5.4 Photometric redshifts

High quality photometric redshifts have been published by Ilbert *et al.* (2006) for the galaxies in the SNLS fields down to $i \cong 24$. But these catalogs do not provide the absolute magnitudes. We also need to be able to propagate easily the uncertainties on the ugriz measurements onto the photo-z and the absolute magnitude estimations. For these reasons, and so as to control the error propagation path, we have chosen to derive the photometric redshifts and the absolute magnitudes using a newly developed photometric redshift code within the SNLS collaboration (Guy& Hardin, *internal note*).

The code is conceived in two steps.

1. The first step is to build a continuous one parameter (a_*) spectral template sequence, $F(a_*, \lambda)$. For each galaxy we will have maximum 5 measurements (*ugriz*) and as a consequence we must have a reduced number of parameters to fit in the code, therefore we require the sequence to be indexed by one parameter. To construct the spectral template sequence we use galaxy spectra derived from a galaxy evolution model which are interpolated to yield a continuous sequence.

2. The next step consists in optimizing the spectral sequence so as to reproduce the observed colors of our data in the best way. The training set comprises a sample of galaxies with known spectroscopic redshift from the DEEP-2 (Davis *et al.*, 2003, 2007) and the performance of the code is tested on a sample of galaxies from the VVDS (Le Fèvre *et al.*, 2004).

5.4.1 The spectral template sequence

The parameter that defines the colors of a galaxy in the best way is the mean age of its stellar population. Elliptical (early type) galaxies will have an old stellar population whereas spiral (late type) galaxies which are still forming a significant fraction of stars will have a much younger stellar population. As a consequence, the one parameter continuous spectral template sequence that we are trying to construct will naturally be indexed by the mean age of the stellar population.

To construct this continuous sequence we first need to obtain a set of initial galaxy spectra. These spectra have been obtained using the galaxy evolution model PEGASE.2 (Fioc & Rocca-Volmerange, 1999). Pegase computes synthetic spectra of galaxies at $N_{\rm step}$ ages ranging from 0 to 20 Gyr. The code is based on a user specified stellar initial mass function (IMF), in our case from Rana & Basu (1992), together with an evolutionary scenario specifying various parameters (initial metallicity, gas infall time scale and star formation relation to the gas content, galactic winds, extinction geometrical model and a history of Star Formation Rate (SFR(t)). Eight scenarios are pre-defined, so as to reproduce at $t \simeq 13\,Gyr$, i.e. at z=0, the colors of local galaxies according to their Hubble type : E, Sa, ..., Sd, Irr, yielding a template library of $8 \times N_{\rm step}$ spectra. They differ essentially by their star formation history.

The mean age of the stellar population is closely related to the colors of the galaxy, early type galaxies are in general redder than late type galaxies. As a matter of fact, both data and the Pegase models follow a continuous sequence when looking in a color-color diagram. For example, in figure 5.20 the $r-i$ vs $i-z$ colors are shown for the different Pegase templates in black dots and data at $0.45 < z_{\rm spectro} < 0.55$ in blue circles. The black solid line shows this continuous sequence. The initial number (20) of galaxy spectra will be chosen so as to populate the entire sequence and have a mean age of the stellar population that corresponds to the colors of each galaxy type. Said in other words, we will choose a limited number of spectra, $F_i(a_i, \lambda)$, labelled by the mean age of the stellar population, a_i, where a_i will be in the range 50Myr$< a_i <$ 13Gyr so as to sweep the entire range of galaxy types. A selection of the initial galaxy spectral templates is presented in figure 5.21.

These initial spectra are then used to construct a continuous sequence by interpolating along the a_* parameter. This results in a one parameter continuous spectral template sequence, $F(a_*, \lambda)$ where a_* is a continuous parameter representing the mean age of the stellar population.

5.4.2 The training of the spectral template sequence

The spectral sequence needs to be optimized so as to describe the data better. The training is based on photometric observations (*ugriz* magnitudes) of 6320 SNLS galaxies with known spectroscopic redshift from the DEEP-2 ($0.1 < z < 1.5$).

Using the spectral template sequence, $F(a_*, \lambda)$, we are able to fit for a_* and calculate the synthetic magnitudes of the fitted template (this process also includes a global flux normalization). In fig. 5.22, the difference between the measured magnitude and the magnitude predicted by the fitted template for the training set is shown. We construct a trained spectral template sequence, $\mathcal{F}$, iteratively by minimizing the magnitude offset (observed magnitudes - predicted magnitudes) in each band. The

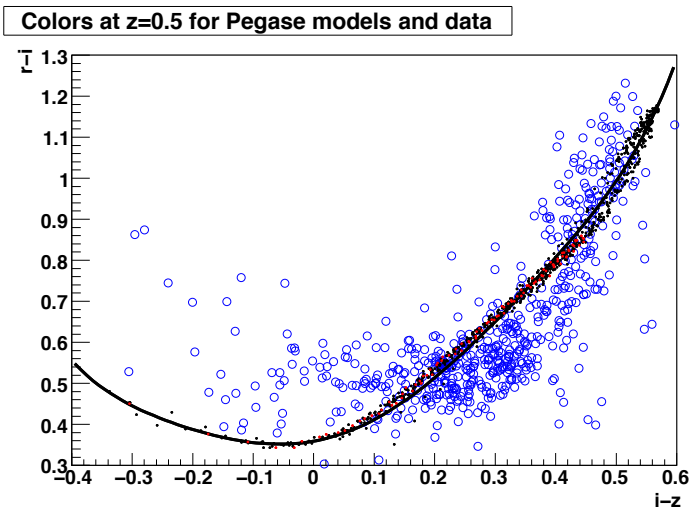

Figure 5.20: The color-color relation r-i vs i-z of the Pegase templates (black), compared with data at $0.45 < z_{\text{spectro}} < 0.55$ (blue). The sequence corresponding to the Pegase Sc templates is indicated in red.

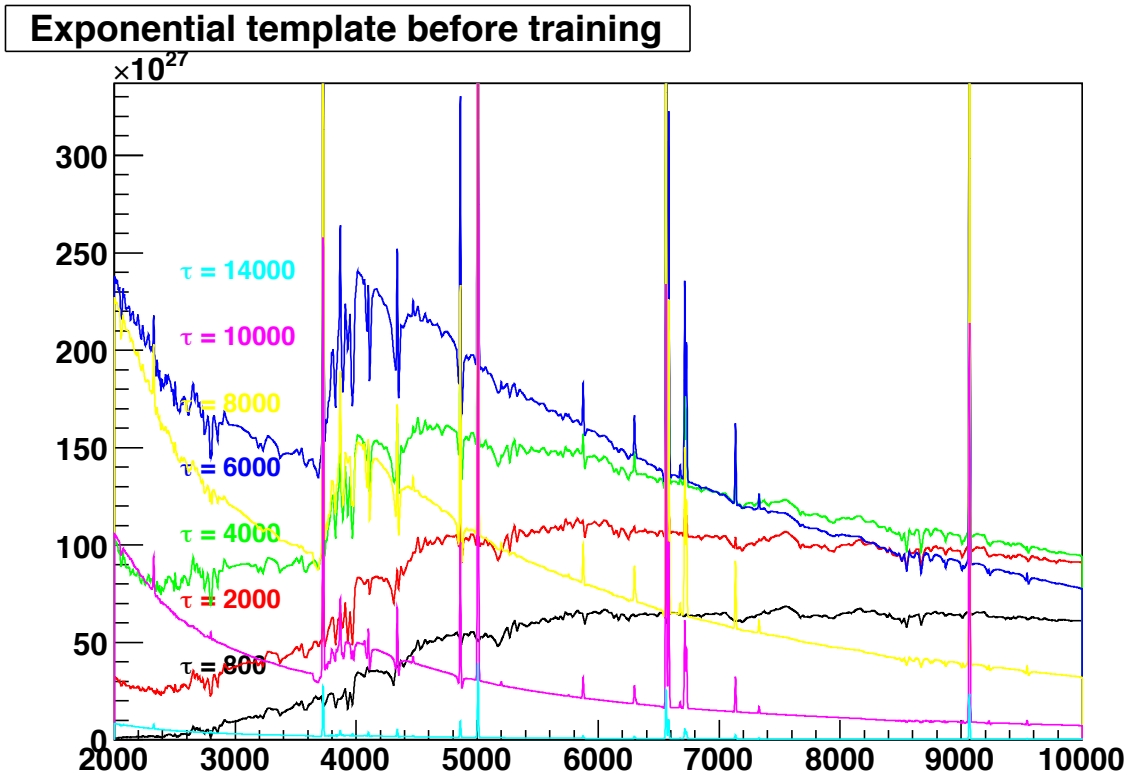

Figure 5.21: The spectral templates : SED for galaxy spectra at different a_*.

	u	g	r	i	z
Δm	-0.0097	0.0027	0	-0.0183	-0.0114

Table 5.3: Computed magnitude offsets in the training process.

trained spectral template sequence is defined as

$$\mathcal{F}(a_*, \lambda) = F(a_*, \lambda) \times f(a_*, \lambda) \tag{5.6}$$

where the correction function, $f(a_*, \lambda)$ is constructed as third order splines with continuous second derivatives[6]. A set of magnitude offsets applied to the data magnitudes is also fitted in this processed (see table 5.3).

The *ugriz* magnitude residuals before and after training are shown in fig. 5.22. With regards to a color-color plot as shown previously we present the $r - i$ vs. $i - z$ plot for $0.45 < z_{\text{spectro}} < 0.55$ (data in blue) compared to the untrained template sequence (black) and the trained template sequence (red) for z=0.5 in fig 5.23.

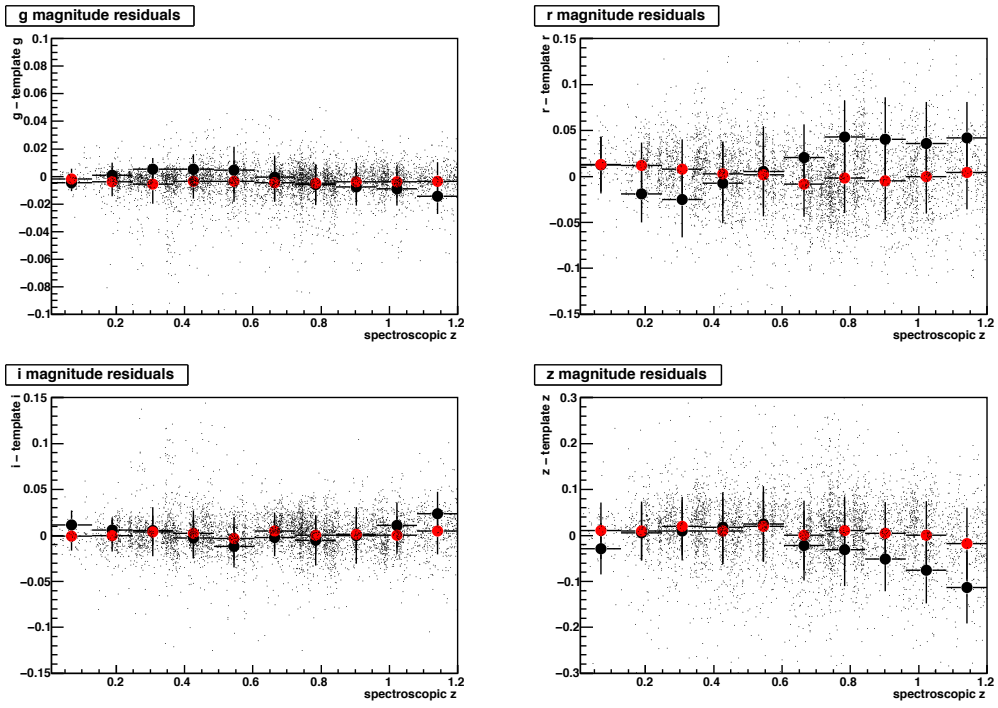

Figure 5.22: The magnitude residual before (black) and after (red) training (the redshift is held fixed at the spectroscopic value during the fit).

[6]The parameter indexing the splines is not directly a_* but a typical SFR timescale

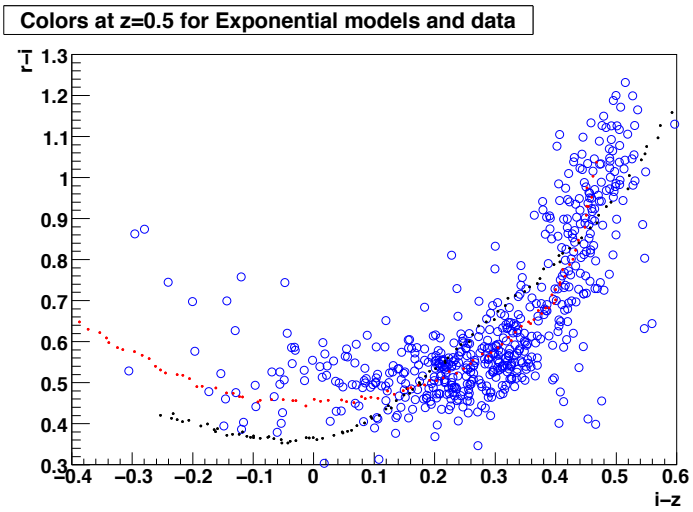

Figure 5.23: The color-color relation r-i vs i-z of the spectral templates, original (black) and trained (red) compared with data at $0.45 < z_{\rm spectro} < 0.55$ (blue).

5.4.3 The photometric redshift fit

Equipped with the trained spectral template sequence, each galaxy in the catalog is fitted to obtain its photometric redshifts by matching the measured *ugriz* magnitude with the synthetic magnitude computed based on the trained spectral template sequence at a given redshift in the same filters through a least square minimization procedure.

The fit is performed in two steps. The first step is to sweep the entire range in redshift (0.0 - 2.0) using an adequate spacing of 0.1, thus keeping the redshift constant for each step. For each constant redshift, a_* and a normalization is fitted giving rise to a minimum χ^2 for each z. The minimum of the χ^2 over the total range in redshift is then selected for a new fit where the normalization, a_* and the redshift are fitted simultaneously. Absolute magnitudes are then computed by integrating the best fit spectrum (based on the best fit a_*) in rest frame U, B and V filters.

Note that we do not fit directly because of local minima in z.

5.4.4 The resolution of the photo-z

The performance of the photometric redshift computation can be evaluated for both the un-trained and trained spectral template sequences using VVDS spectroscopic data available on the D1 field (3595 galaxies at $0.01 < z < 1.5$) (Le Fèvre *et al.*, 2004). The redshift residuals (i.e. Δz=photometric redshift - spectroscopic redshift) as a function of spectroscopic redshift are shown in fig. 5.24 and 5.25. For the un-trained spectra library we see a systematic redshift dependent bias. This tendency disappears when using the trained spectra library.

At $i < 24$, the number of catastrophic failure for which $\Delta z/(1+z) > 0.15$ is of the order of 6.5%. Eliminating catastrophic failures, we obtain a mean and rms for Δz :

$$m_{\Delta z} = 0.0096, \quad \sigma_{\Delta z} = 0.066$$

and for $\Delta z/(1+z)$:

$$m_{\Delta z/(1+z)} = 0.0069, \quad \sigma_{\Delta z/(1+z)} = 0.038$$

This resolution is comparable to the resolution of the photometric redshift for the SNLS galaxies published by Ilbert *et al.* (2006) which yielded a dispersion of $\sigma_{\Delta z/(1+z)} = 0.037$ and a catastrophic error fraction of 3.7% (Note however that priors on redshift and luminosity were considered in Ilbert *et al.* (2006) and not here).

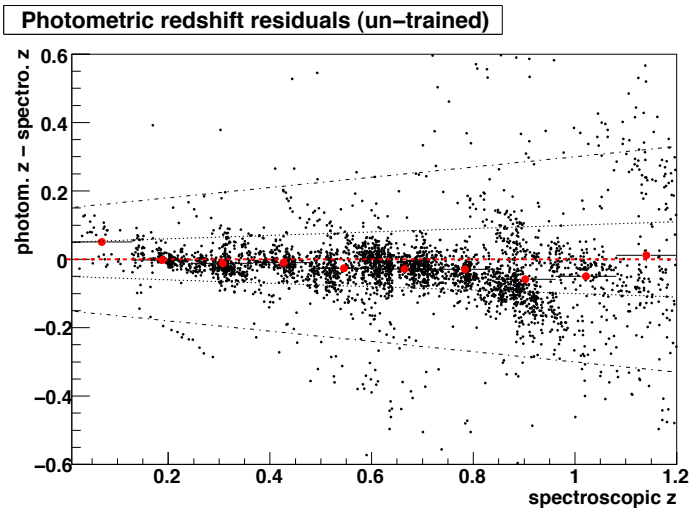

Figure 5.24: Using the un-trained spectral template sequence, the difference of spectroscopic redshift and photometric redshift as a function of spectroscopic redshift for spectroscopic redshifts obtained with the VVDS data set (Le Fèvre *et al.*, 2004).

The uncertainties on the magnification for each SN have been estimated via Monte Carlo simulations (see section 5.7). In the same spirit, we generate here different sets of observed magnitudes according to their uncertainties and fit for the redshift for each set leading to a redshift distribution for each galaxy. It is interesting to compare the uncertainty on the photo-z using MC simulations to the resolution of the SNLS photometric redshift code given by the offset to the spectroscopic redshift. In figure 5.26 we show the rms of the z(photometric-spectroscopic(VVDS)) as a function of photo-z (in dotted black) and compare it to the uncertainty obtained on the photo-z using Monte Carlo simulations (in red). The estimates are in reasonable agreement which validates our method for propagating uncertainties.

5.4.5 High resolution photometric and spectroscopic redshifts

As already explained, for a fraction of the SNLS galaxies we have $\sim$ 12000 spectroscopic redshifts from the VVDS and the DEEP-2. In addition, we have also obtained spectroscopic redshift for $\sim$ 1000 of our galaxies from FORS2 multi slit observations of SNLS SNe. These spectroscopic redshifts have of course been used in the analysis.

The field D2 overlaps with the COSMOS field and it has thus also been possible to obtain high resolution photometric redshifts for a large fraction of the galaxies in the D2 field (Ilbert *et al.*, 2009).

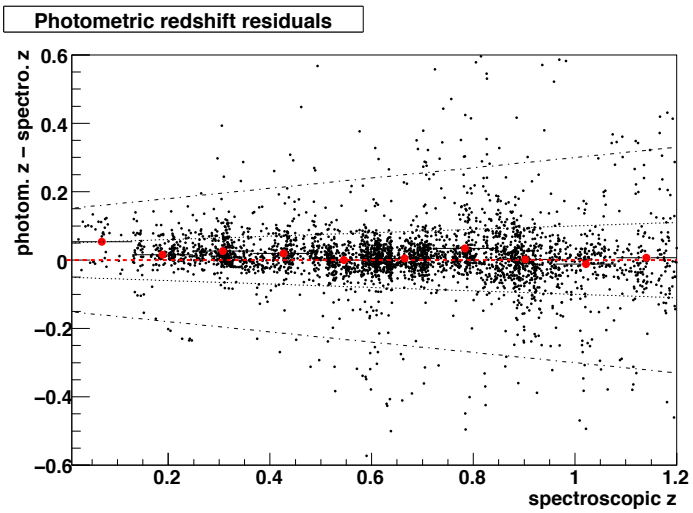

Figure 5.25: Using the trained spectral template sequence, the difference of spectroscopic redshift and photometric redshift as a function of spectroscopic redshift for spectroscopic redshifts obtained with the VVDS data set (Le Fèvre *et al.*, 2004).

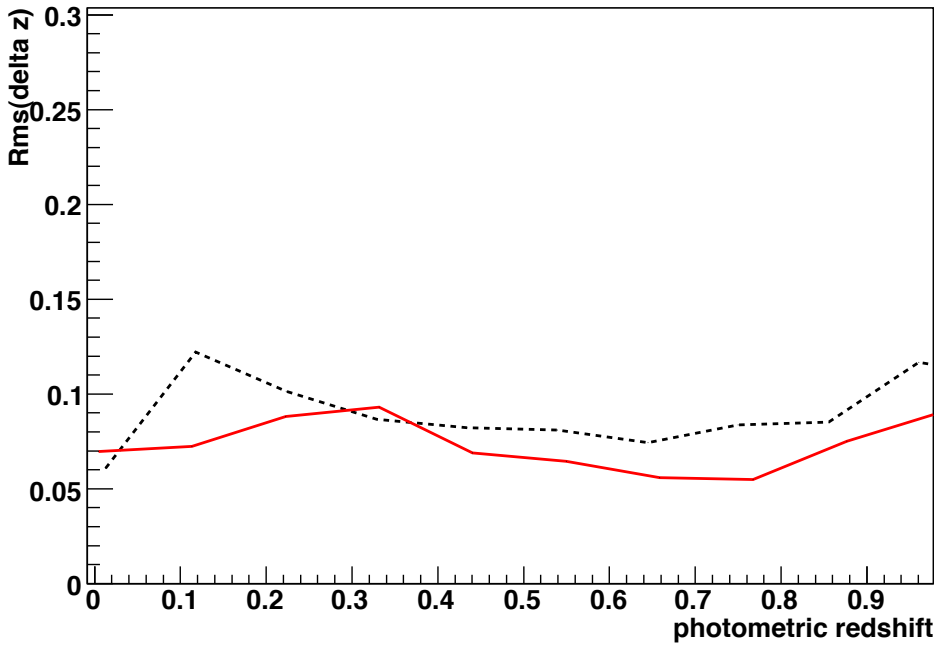

Figure 5.26: The rms of the z(photometric-spectroscopic(VVDS)) as a function of photo-z (in dotted black). The uncertainty obtained on the photo-z using Monte Carlo simulations (in solid red).

5.5 Selection of galaxies along the line of sight

In principle, all galaxies will have a lensing effect on each SN, but for computational reason one must select a reduced sample of galaxies. As to determine the size of the field which is relevant, simulations have been performed. We have calculated the magnification factor for 100 randomly chosen source positions at redshift z=1 as a function of the angular radius centered on the source position within which galaxies are included. SNe at redshift z=1 are among the most distant SNe in the SNLS sample and the effect of lensing is expected to be highest here. This leads to a robust estimate of the size of the field we should consider.

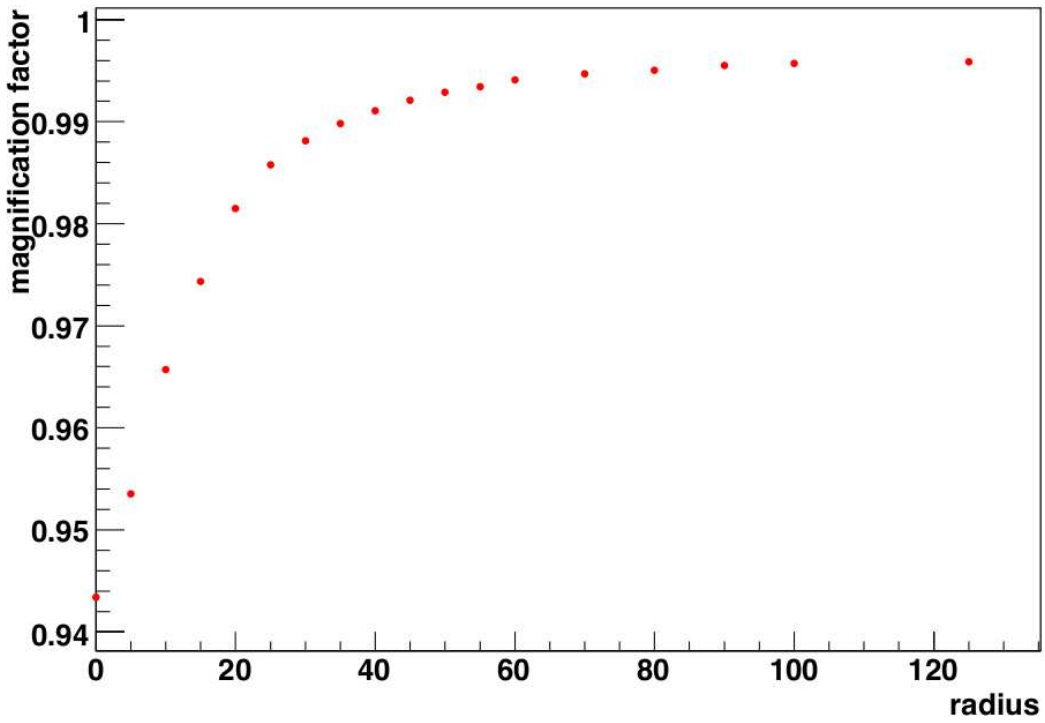

Figure 5.27: The mean magnification factor for a sample of randomly picked source locations at redshift z=1 vs the angular radius centered on the source position within which galaxies are included.

Figure 5.27 shows the mean magnification factor as a function of the angular radius. Including all galaxies within a radius of 60" leads to a loss of the lensing signal of less than 1%. In the following, the selected area will refer to the circled area with a radius of 60 arc seconds centered on the SN.

As explained above, certain areas in the galaxy catalogs are masked and this may have a consequence on the magnification of the supernova. The most conservative choice would be to exclude all

SNe where the selected area overlaps with a masked area but this implies losing about half of the SNe. The effect on the magnification of small spurious galaxy detections or small diffraction spikes in the outskirts of the selected area for SNe is rather small. Due to this reason we have chosen to keep SNe for which the masked area overlap with the outskirts of a selected area. The SN is kept if less than 20" of the outer radius of the selected area overlaps with a masked area.

Other features can also lead to the exclusion of a SN. This could be a non-masked star very close to the line of sight leading to the possibility of excluding an important galaxy hidden behind the star or leading to possible bad photometry for the surrounding galaxies and therefore all SNe are checked through by eye.

Following this procedure we keep 171 SNe out of a total of 233 SNe.

5.6 Normalization of the magnification distribution

Due to the effect of gravitational lensing the observed flux from a SN is not the same as the emitted flux. The observed flux, f_{obs} is given by

$$f_{obs} = \mu f \tag{5.7}$$

where f is the flux that would be observed of the source in a homogeneously distributed universe and μ is the magnification factor. Hence, $\mu > 1$ and $\mu < 1$ describes a magnification and a demagnification with respect to a homogeneous universe. However, because of flux conservation in the universe, the mean magnification due to gravitational lensing of a large number of sources is expected to be unity compared to a homogeneous universe, $< \mu >= 1$.

In the analysis, the magnification factor has been estimated using Q-LET (see section 3.4) in a filled beam scenario which consists of a homogeneously distributed universe with the matter density $\Omega_{matter} = 0.27$, and in addition, the lens galaxies are put on top. This leads to a magnification factor always greater than one relative to a homogeneous universe and as a consequence, the magnification distributions need to be shifted to yield a mean magnification factor of 1.

One must also take into account that due to different cuts and detection limits, fewer galaxies are accounted for at high-z.

To correct for these two effects in the analysis, the calculated magnification distributions have been normalized. Lines-of-sight have been chosen randomly in different redshift intervals in the true galaxy catalogs. 1000 source positions have been picked for each redshift interval which is of 0.1 ranging from z=0.1 to z=1.2 leading to a total of 12000 simulated lines-of-sight per field. The magnification distribution has been calculated for each redshift interval and the normalization factor has been found as a function of redshift. In figure 5.28, the normalization factor as a function of redshift is shown for the 4 different fields and for the 2 different types of input mass-luminosity relations.

A typical magnification distribution is skewed and peaks at a value slightly below 1, which shows that most objects are slightly demagnified. It also presents the characteristic high magnification tail. In figure 5.29 the magnification distribution of 1000 lines-of-sight for sources at z=1 is shown. It is important to sample the high magnification tail so as to obtain a correct normalization. One could ask the question if 1000 lines-of-sight per redshift interval is enough to sample this high magnification tail. The statistical uncertainty of this particular magnification distribution is the rms/ $\sqrt{1000} = 0.003$ and as a result we conclude that 1000 lines-of-sight per redshift interval is sufficient to correctly perform the normalization.

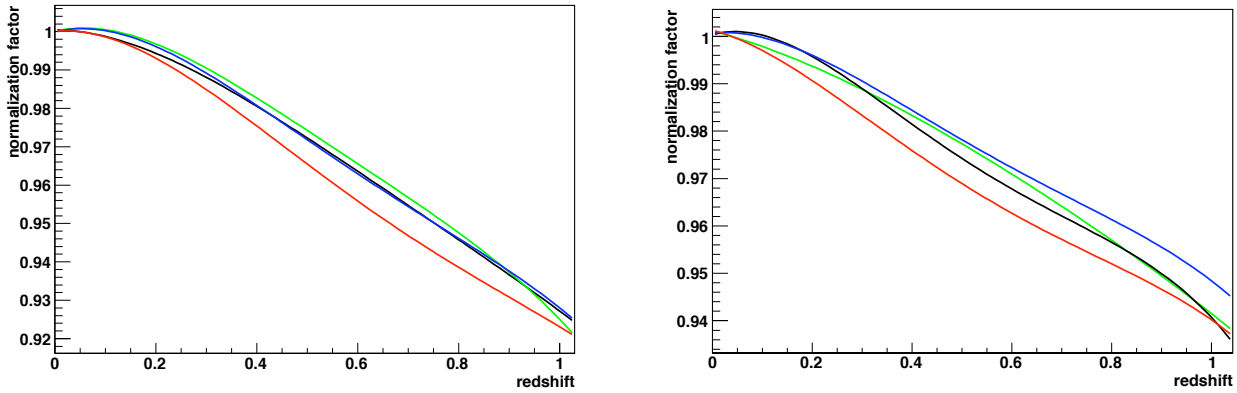

(a) The normalization factor for the galaxy-galaxy lensing K04 relation for the 4 different fields.

(b) The normalization factor for the TF/FJ relations for the 4 different fields.

Figure 5.28: The normalization factor as a function of redshift for the SNLS fields.

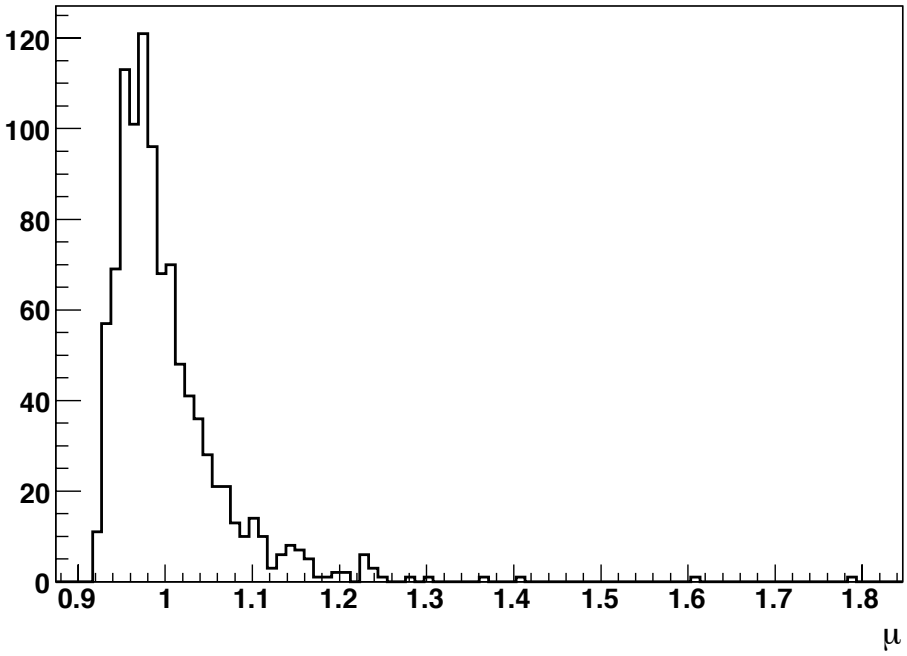

Figure 5.29: The magnification distribution for source positions at z=1 which peaks at a value slightly below one and presents a high magnification tail

5.7 Uncertainties on the magnification of the SNe

To estimate the magnification uncertainty of each SN, Monte Carlo simulations have been used. For each SN, 100 different configurations of the line of sight have been generated by perturbing the Gaussian distributed magnitudes of the foreground galaxies within their uncertainties. Each configuration has then been run through the SNLS photometric redshift code so as to obtain new redshift estimates with corresponding absolute magnitudes. The magnification factor has been calculated for each configuration which in the end gives us a magnification distribution for each SN. The uncertainty on the magnification is taken to be the rms of this distribution.

For the D2 field we have excellent photometric redshifts for a large fraction of the galaxies from the COSMOS catalog (Ilbert *et al.*, 2009), so instead of using the estimated redshifts from the SNLS photometric redshift code we prefer using the COSMOS redshifts and thus the Monte Carlo simulation is somewhat different. In this case we have generated new lines of sight for each SN by drawing Gaussian distributed redshifts using the published redshifts and their uncertainties. These configurations are also run through the SNLS photometric redshift code but this time with the redshift fixed allowing the code to perform K-corrections and obtain absolute magnitudes in the different bands. The uncertainties on the observed magnitudes are also taken into account for each different configuration

The scatter in the mass-luminosity relations has also been taken into account (see equation 4.19 and 4.21 for the TF and FJ relations respectively). For the K04 results (see equation 4.11), the uncertainties are merely statistical and do not represent a physical scatter in galaxy luminosities for a given mass. To account for this, we have chosen to use the scatter obtained for the TF relation also for the K04 relation (eq. 4.19).

In figure 5.30 we show the uncertainties of the magnification as a function of the magnification, both expressed in magnitudes (magnification in magnitudes = $-2.5\log_{10}(\mu)$). This plot has been made using the TF/FJ relations. The solid line is a straight line fit to the data points and yields the following relation

$$\sigma_{-2.5\log_{10}(\mu)} = 0.008 - 0.17 \times (-2.5\log_{10}(\mu)) \tag{5.8}$$

We thus see a relative uncertainty on the magnification of 17%. The most important source of uncertainty comes from the scatter in the mass-luminosity relation. The contribution due to the uncertainties in the redshift is quite small and present a relative error of about 5%. (If we compare these errors to the errors given for the supernovae in the GOODS fields (Jonsson *et al.*, 2006), our analysis presents smaller uncertainties. This is probably due to the fact that they include a scatter due to the choice of halo model (SIS NFW) which is quite large, whereas we only consider the SIS profile in this analysis.

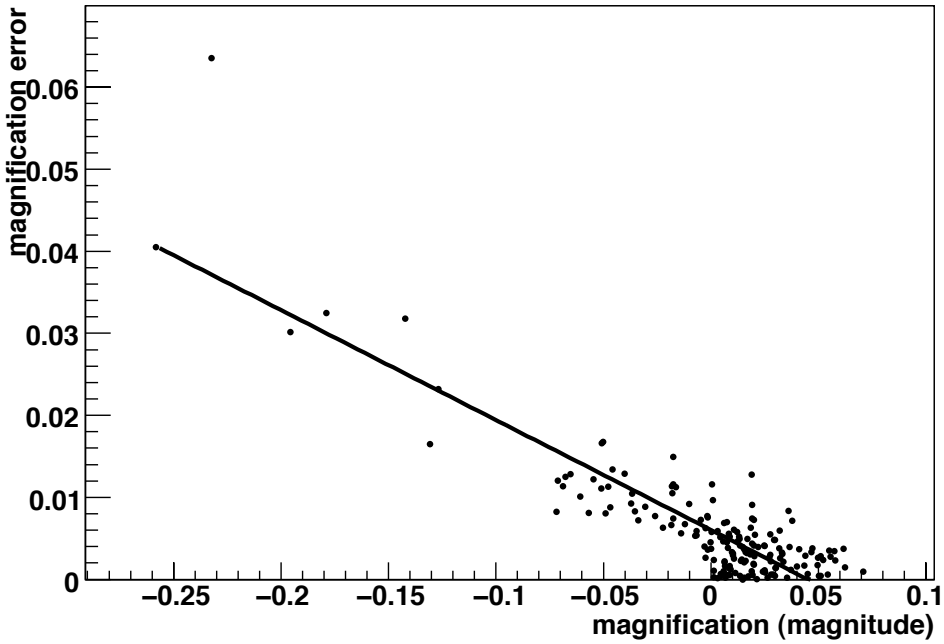

Figure 5.30: The uncertainties on the magnification as a function of the magnification, both expressed in magnitudes. The line shows a straight line fit to the data points.

Chapter 6

Results and prospects

This chapter is dedicated to the results of the analysis of the third year SNLS sample.

6.1 Expectations for a signal detection

Before presenting the results on the analysis of the SNLS third year data sample it is important to keep in mind what the expectations for a signal detection are. In chapter 4 we saw that the prospects of detecting the lensing signal for the full SNLS sample where estimated to be fairly high, > 95% chance of a 3σ detection. The SNLS third year data sample consists of 233 Type Ia supernovae. However, about 25% are masked out (see section 5.3.3) leading to a sample of 171 supernovae included in the analysis.

In figure 4.5 we deduce the chance of detecting a 3σ correlation for this particular sample, which is approximately 55% (see section 4.2.2). These first simulations were based on simulated galaxy catalogs but with the newly extracted galaxy catalogs it is possible to perform detailed Monte Carlo simulations using the true catalogs giving rise to precise predictions on the probability of detecting the lensing signal in the SNLS sample.

6.1.1 Simulations of the SNLS supernova magnification distributions

To simulate the magnification distribution of a sample of supernovae we first calculate magnification distributions of 1000 random source positions in different redshift intervals (interval of 0.1 in the range 0.1-1.2) by calculating the magnification factor for each random position using the true galaxy catalog. A typical magnification distribution is seen in fig. 6.1 for sources at redshift z=1. Note that this magnification distribution is not normalized. In the following, μ^* will be referred to as the non-normalized magnification factor which is always greater than 1. The distribution is skewed and presents the characteristic high magnification tail. Computing a logarithm of the magnification, $\log(\mu^* - 1)$ results in a fairly gaussian distribution of the magnification (see fig. 6.1). The mean of this gaussian distribution together with its variance is then found for each redshift interval leading to a relation between the mean magnification, the variance and the source position redshift. To estimate the magnification of a supernova at a given redshift, a random magnification, $(\log(\mu^* - 1))$, is drawn in a gaussian distribution centered on the mean magnification corresponding to the supernova redshift together with the corresponding standard deviation. The real magnification, μ^*, is then found and normalized.

A simulated data set consists in assigning to each SN a true magnification and a true residual which are equal. Then a scatter in the residuals and the magnification is taken into account leading to a measured magnification and residual for each SN.

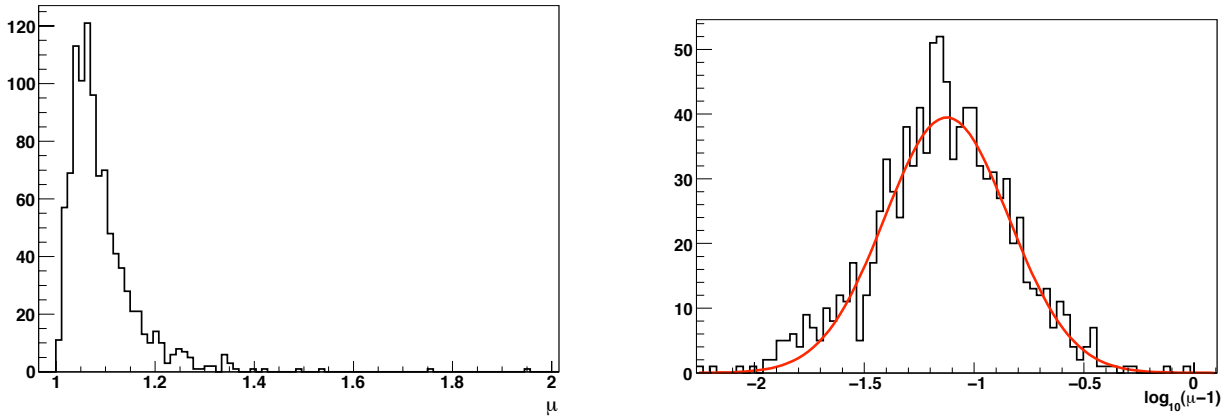

(a) The non-normalized magnification distribution of 1000 random source positions at redshift z=1.

(b) The distribution of $\log(\mu - 1)$ in black and a gaussian distribution in red.

Figure 6.1:

6.1.2 Detection criterion - Weighted correlation coefficient

As a criterion for signal detection we have chosen to compute the weighted correlation coefficient which can be expressed as

$$\rho = \frac{cov(magnification, residual)}{\sqrt{var(magnification)var(residual)}} \tag{6.1}$$

where the weighted covariance of two variables x and y, $cov(x, y)$ can be written

$$cov(x, y) = \frac{\sum wxy}{\sum w} - \bar{x}\bar{y} \tag{6.2}$$

where $\bar{x}$ and $\bar{y}$ are the weighted means.
The variance of the variable x, $var(x)$ can be written as

$$var(x) = \frac{\sum wx^2}{\sum w} - \bar{x}^2 \tag{6.3}$$

In the relations above, w is the weight assigned to each point. It is important to chose the optimal weighting of the data points so as to optimize the chances of a signal detection. Simulations using different weightings have been performed and several features have been taken into account. The supernovae can be weighted according to the scatter in the residuals to the Hubble diagram or/and the scatter in the magnification leading to lower weight for the data points with high uncertainties. They can also be weighted as a function of their redshift since high redshift objects are expected to be more magnified than low redshift objects. Weighting by the uncertainties on the residuals to the Hubble diagram, $w = 1/\sigma^2_{res}$, is found to be the optimal weighting. This results in 35% chance of detecting the

signal with a 3σ significance whereas choosing $w = 1$ or $w = 1/(\sigma^2_{res} + \sigma^2_{mag})$ lowers the chances by 1% and 4% respectively. It seems obvious that weighting by the scatter in the magnification leads to a lower signal detection since the scatter in the magnification is correlated with magnification (see section 5.7) so that highly magnified objects have a high scatter resulting in a lower weight of these objects. The highly magnified objects are expected to drive the correlation and thus giving them less weight results in a lower signal detection. As a consequence, in the following, a weight of $w = 1/\sigma^2_{res}$ has been used.

6.1.3 Signal expectations for the 3-year SNLS sample

As said previously, the 3-year SNLS data sample consists of 171 SNe used for lensing analysis. Both the redshift distribution and the distribution of the residuals to the hubble diagram in this sample (excluding the masked SNe) can be approximated with a gaussian distribution centered on 0.65 with an RMS of 0.2 for the redshift distribution and centered on 0 with an RMS of 0.16 for the distribution of the residuals. (see fig. 6.2).

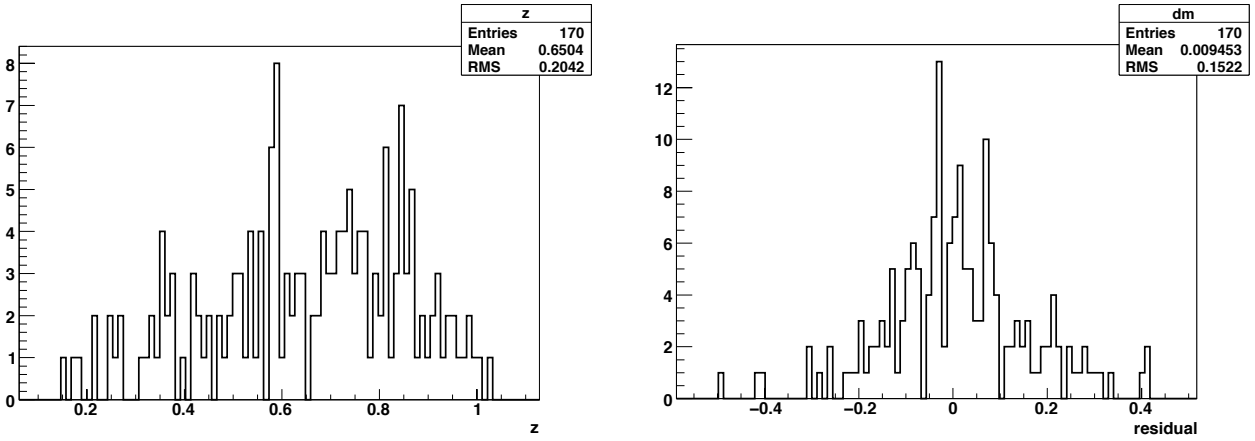

(a) The redshift distribution.

(b) The distribution of the residuals to the hubble diagram.

Figure 6.2: The redshift distribution and the distribution of the residuals to the hubble diagram of the 170 SNe used for the purpose of lensing analysis.

We simulate 10,000 data samples for 171 SNe using the key parameters of the redshift distribution and the distribution of the residuals. The same number of data samples assuming no correlation between the magnification of the SN and its residual to the Hubble diagram are also simulated. We then compute the weighted correlation coefficient for each sample choosing to weight the data points according to $w = 1/\sigma^2_{res}$ (see previous section). In figure 6.3, the distribution of the correlation coefficients for samples (in red) and uncorrelated samples (in black) are presented. We find that the most likely correlation coefficient for the 3-year data sample is $\rho = 0.21$ which corresponds to a significance of the correlation at the 2.5σ level, where σ is the standard deviation of the uncorrelated distribution. The correlation coefficient for a 3σ detection is $\rho = 0.24$. In the SNLS 3-year data sample there is 35% chance of detecting a 3σ correlation.

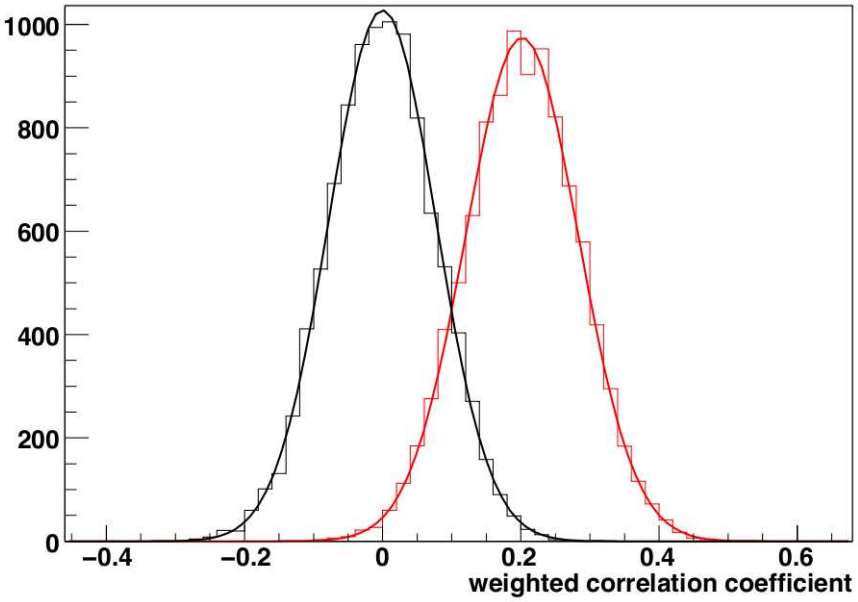

Figure 6.3: The distribution of the weighted correlation coefficient for correlated samples in red and uncorrelated samples in black. There is 50% chance of detecting a correlation of 2.5σ and 35% chance of finding a 3σ signal.

6.2 Magnification of the SNLS 3-year SNe

The magnification distribution of the SNLS 3-year sample is shown in figure 6.4 for the K04 input mass-luminosity relation and in figure 6.5 for the TF and FJ relations.

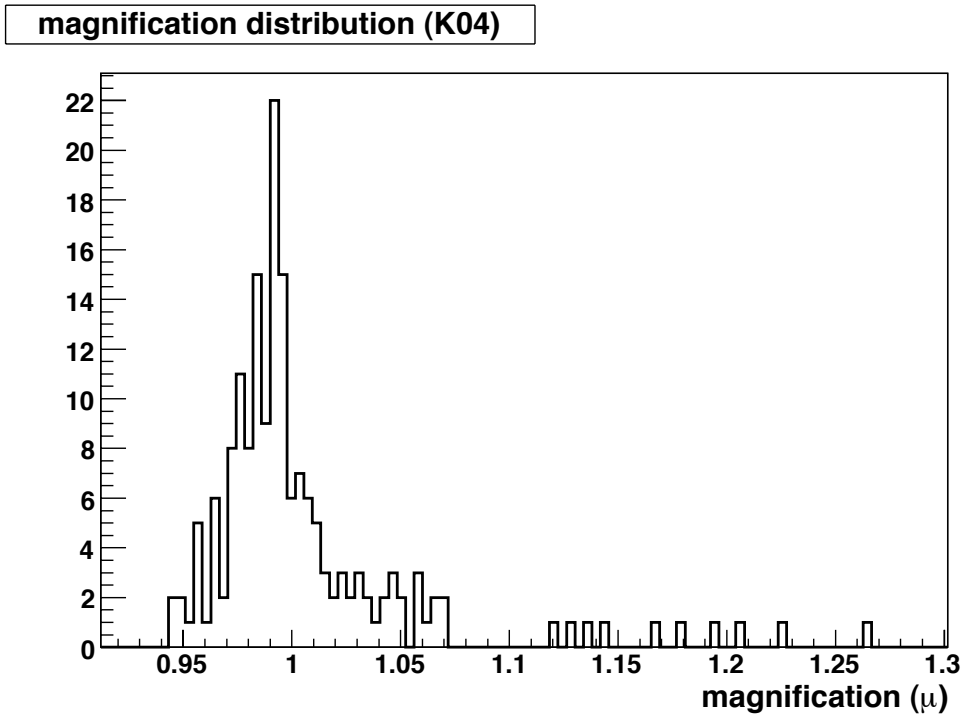

Figure 6.4: The magnification distribution for the K04 input mass-luminosity relation.

The distributions are truly skewed and peaks at values slightly lower than one presenting a long magnification tail. The mean value of the magnification factor is as expected close to one (1.007 ± 0.004 for the K04 results and 0.999 ± 0.004 for the TF/FJ results). In figure 6.6 and 6.7 the magnification factor as a function of redshift is shown for the K04 input mass-luminosity relation and the TF and FJ relations respectively.

As expected, most SNe are demagnified with respect to a homogeneous universe and some are significantly magnified. For an overview of the magnification of each supernova see table 6.1. A 10" radius of the line-of-sight of 8 of the most magnified SNe in the third year data set are shown in fig. 6.8. The supernova and its host are shown in red (square for the supernova and circle for the host). The blue circles display foreground galaxies and the green circled galaxies are background galaxies. Yellow circles are stars or saturated objects which are not included in the calculations. Common for all these magnified SNe is the existence of rather big galaxies with intermediate redshifts (between the supernova and the observer) close to the line-of-sight. For a detailed description of these supernovae and the most important galaxies causing the magnification see table 6.3.

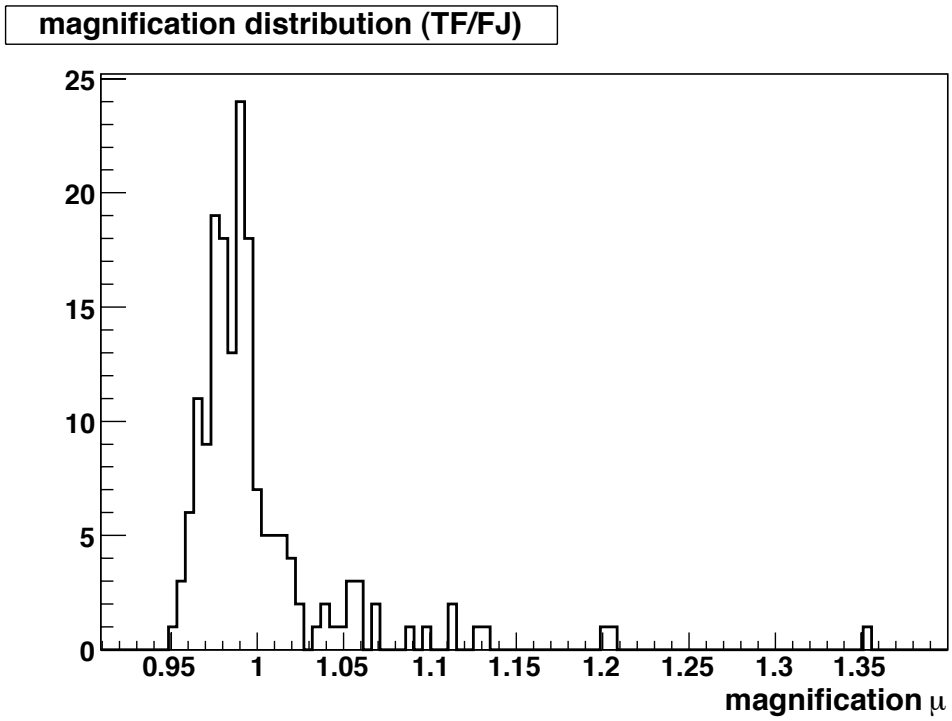

Figure 6.5: The magnification distribution for the TF and FJ input mass-luminosity relations.

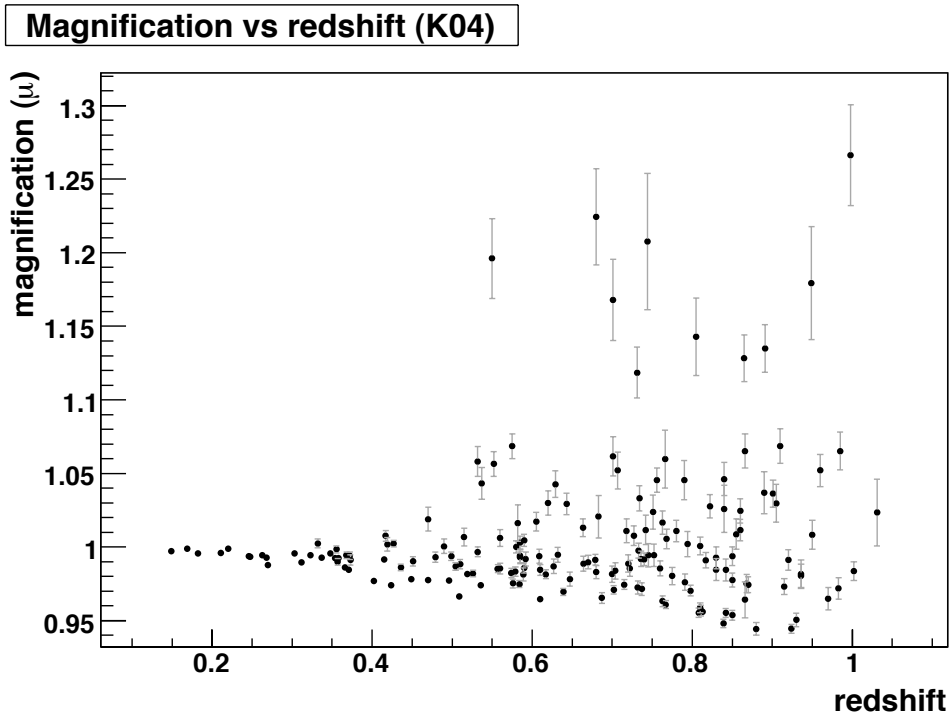

Figure 6.6: The magnification factor as a function of redshift for the K04 input mass-luminosity relation.

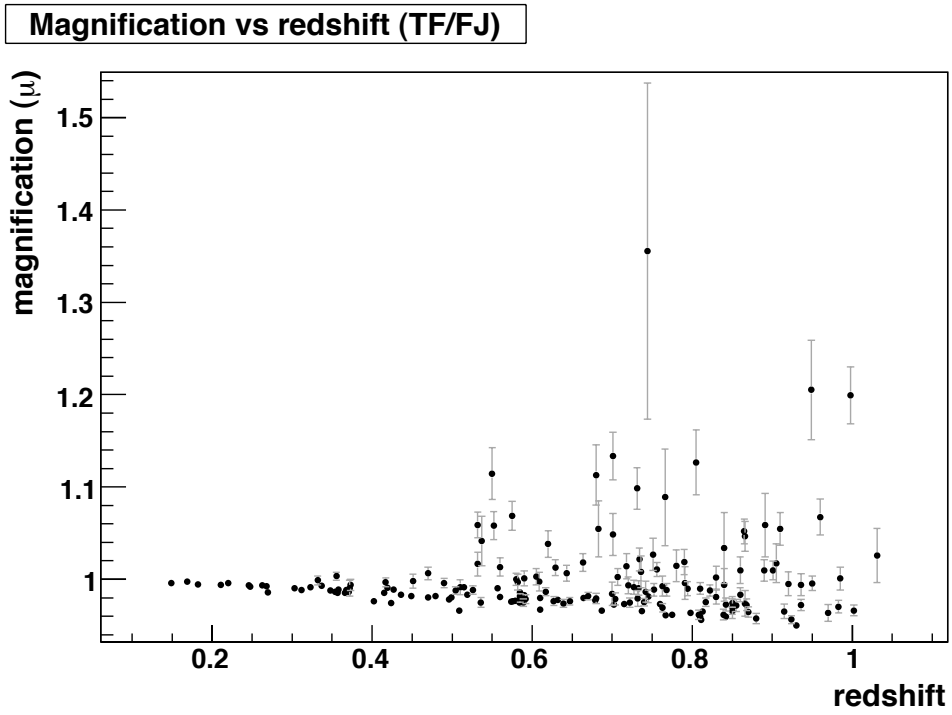

Figure 6.7: The magnification factor as a function of redshift for the TF and FJ input mass-luminosity relations.

6.3 The supernova lensing signal for the SNLS 3-year sample

We are searching for a correlation between the expected supernova brightness calculated from a cosmological model and the estimated magnification of the supernova based on foreground galaxy modeling. In figure 6.9 and 6.10 we show plots of the residuals of the 171 SNe versus the estimated magnification for the K04 input mass-luminosity relation and the TF and FJ relations respectively. The weighted correlation coefficient for this sample is $\rho = 0.12$ using the K04 relation and $\rho = 0.18$ using the TF and FJ relations. To evaluate the significance of the results we calculate the distribution of the weighted correlation coefficient for an uncorrelated sample and compare it with the obtained value for our sample. The uncorrelated sample is obtained by shuffling the values of the real data sample. In figure 6.11 and 6.12 the distributions of the weighted correlation coefficient for the uncorrelated sample are shown in black and the value of the SNLS third year data set is shown in red for the K04 relation and TF/FJ relations respectively.

We find a correlation of 1.6 sigma significance for the K04 relation and 2.3 sigma significance for the TF and FJ relations . Another way of evaluating the result is to calculate the probability of detecting a higher correlation coefficient than $\rho = 0.12(0.18)$ for an uncorrelated sample. We find that there is 5% chance of detecting a correlation coefficient higher than $\rho = 0.12$ and 1% chance of detecting a correlation coefficient higher than $\rho = 0.18$. This leads to a detection of the correlation at the 95% confidence level for the K04 result and at the 99% confidence level for the TF and FJ relations.

The difference of the signal detection for the 2 different input mass-luminosity relations can be expected. The population of lens galaxies are divided into 2 subgroups (spirals and ellipticals) for the TF and FJ relations leading to different mass with respect to the same luminosity whereas the K04 input

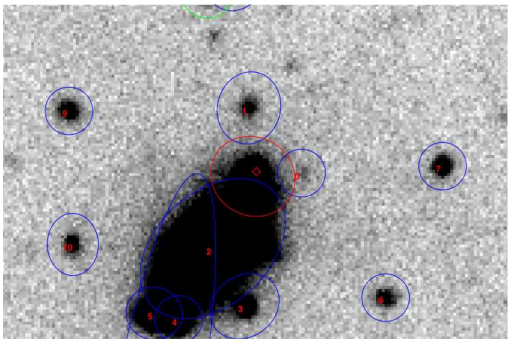

(a) SN03D4cx at z=0.949

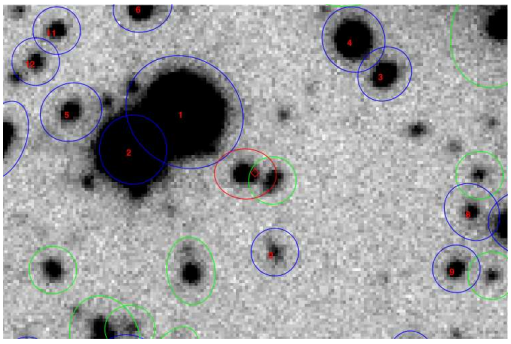

(b) SN04D1iv at z=0.998

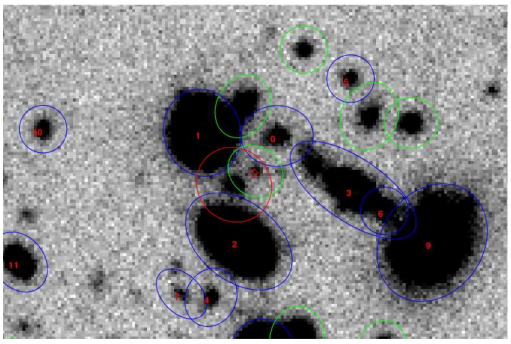

(c) SN04D4bq at z=0.55

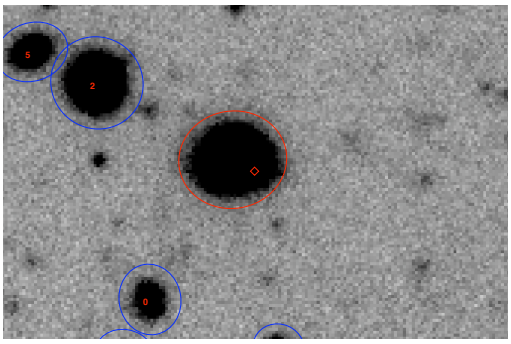

(d) SN04D2kr at z=0.744. Note that the galaxy in red is considered a foreground galaxy and not the host galaxy (see section 5.3.2.)

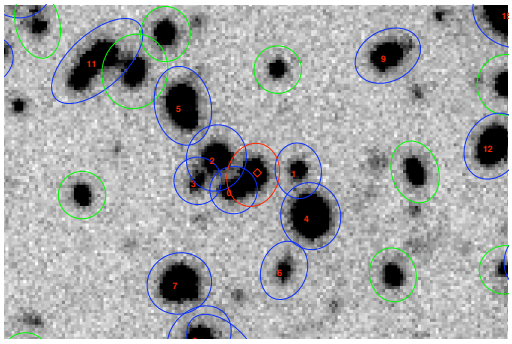

(e) SN05D2by at z=0.91

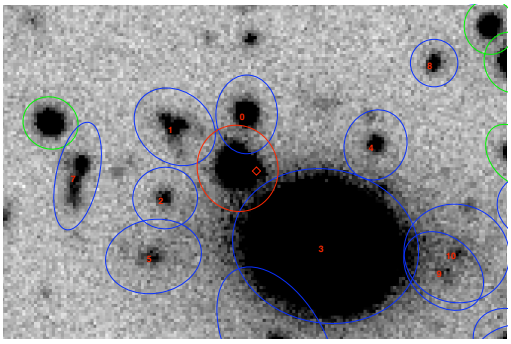

(f) SN05D3cx at z=0.805

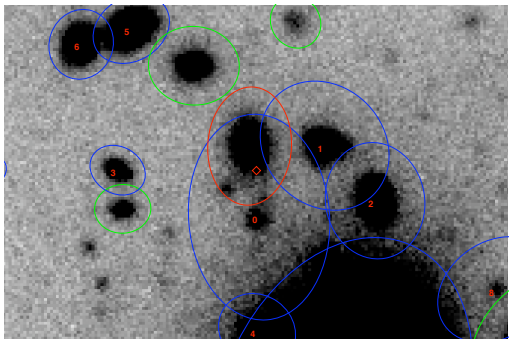

(g) SN05D4cq at z=0.702

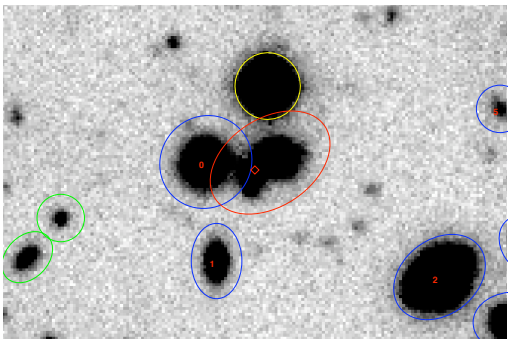

(h) SN05D2bt at z=0.68. Note that the galaxy in red is considered a foreground galaxy and not the host galaxy (see section 5.3.2.)

Figure 6.8: The most magnified supernova in the SNLS 3-year data set. In red: the supernova and the host galaxy. In blue: foreground galaxies. In green: background galaxies. In yellow: stars or saturated objects.

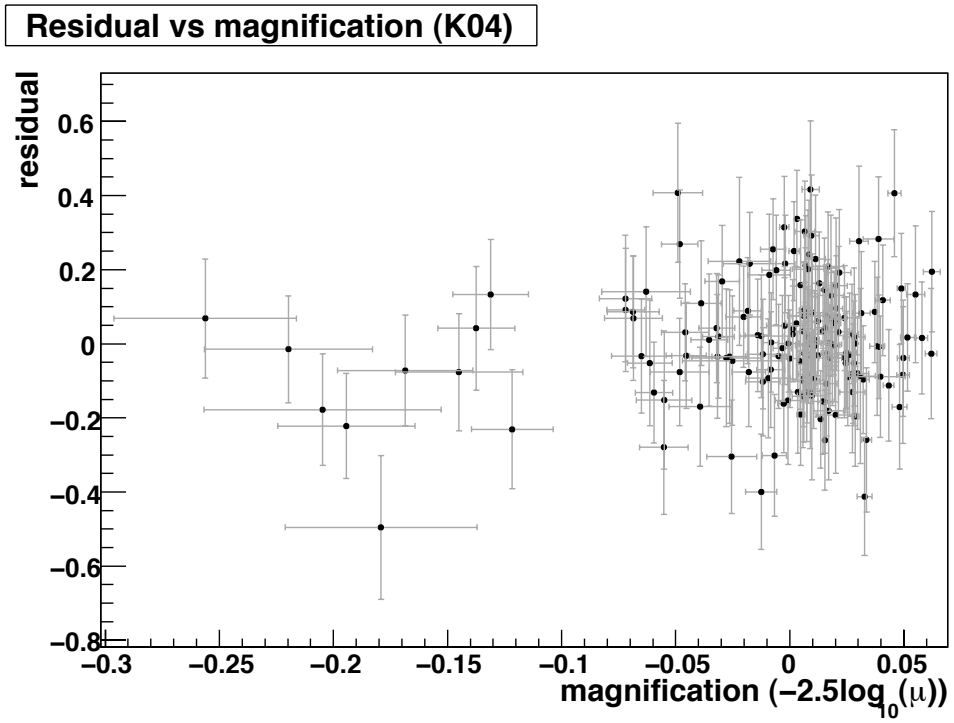

Figure 6.9: The residuals to the Hubble diagram vs the magnification of the SNe expressed in magnitudes for the K04 input mass-luminosity relation.

relation that has been used is an average mass-luminosity for all galaxies. Kleinheinrich *et al.* (2004) also give results when splitting their lens galaxy population into a red and a blue subsample which will be interesting to exploit in the future.

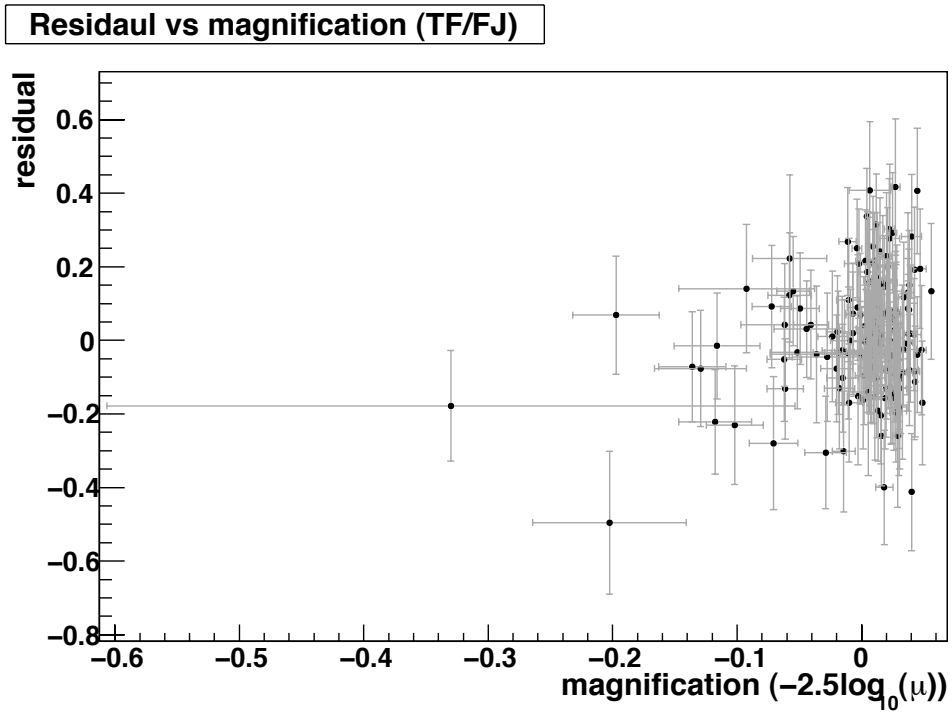

Figure 6.10: The residuals to the Hubble diagram vs the magnification of the SNe expressed in magnitudes for the TF and FJ input mass-luminosity relations.

The most magnified SNe							
		magnification factor μ		Most important lensing galaxies			
SN	z	K04	TF-FJ	z(galaxy)	d (")	σ km/s (K04)	σ km/s (TF-FJ)
04D1iv	0.998	1.267±0.034	1.199±0.031	0.60	7.8	299	295
				0.51	5.8	217	154
04D2kr	0.744	1.208±0.046	1.355±0.182	0.228	1.5	119	150
05D2by	0.891	1.135±0.016	1.059±0.035	0.66	1.8	89	50
				0.68	4.3	151	167
				0.44	2.7	88	54
05D2bt	0.68	1.224±0.33	1.113±0.033	0.31	0.5	99	65
05D3cx	0.805	1.143 ±0.026	1.127±0.035	0.38	6.4	224	243
03D4cx	0.949	1.179±0.038	1.205±0.054	0.45	5.5	246	259
04D4bq	0.55	1.196±0.027	1.114±0.028	0.32	4.4	152	108
				0.38	4.1	190	138
05D4cq	0.702	1.168±0.028	1.133±0.026	0.28	15.7	282	298
				0.43	2.9	106	67

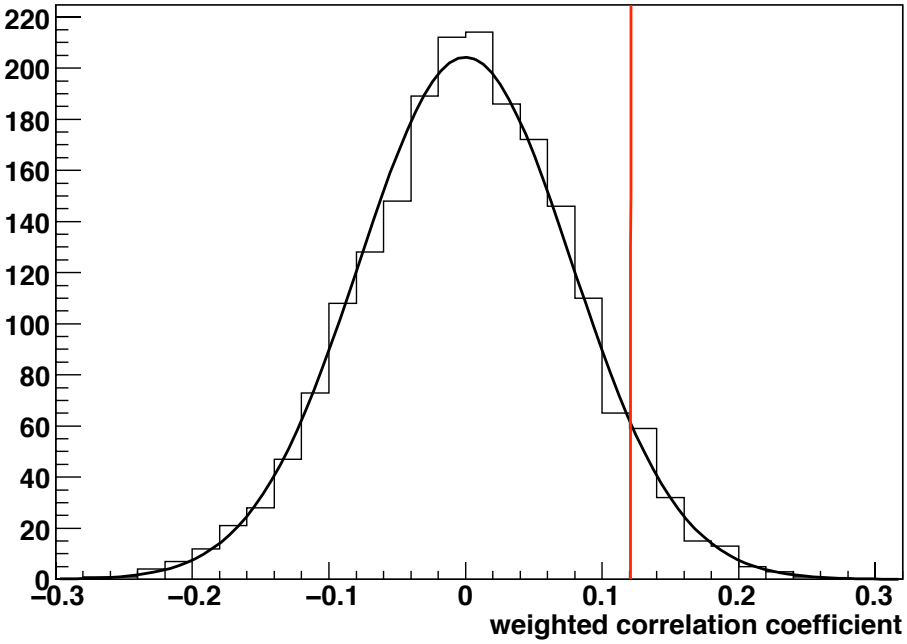

Figure 6.11: The distribution of the weighted correlation coefficients for shuffled samples (a background sample) in black compared to the value obtained with the SNLS 3-year sample in red. Results for the K04 input mass-luminosity relation.

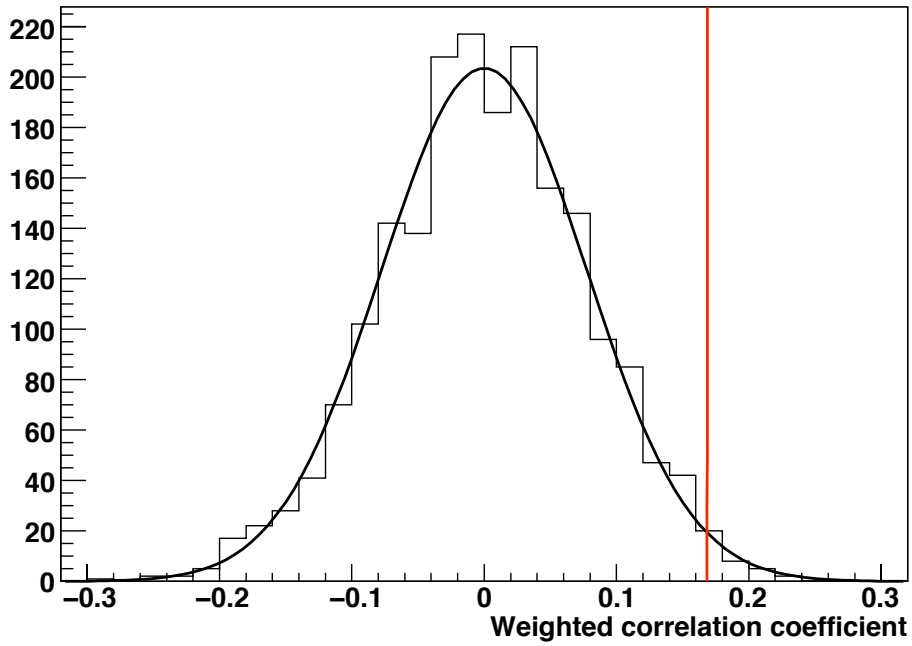

Figure 6.12: The distribution of the weighted correlation coefficients for shuffled samples (a background sample) in black compared to the value obtained with the SNLS 3-year sample in red. Results for the TF and FJ input mass-luminosity relations.

Table 6.1: The magnification of the SNLS SNe from the 3 year sample.

SN	z	magnification factor, μ		SN	z	magnification factor, μ	
		TFFJ	K04			TFFJ	K04
03D1ar	0.408	0.989 ± 0.002	0.996 ± 0.003	03D1au	0.504	0.988 ± 0.004	0.987 ± 0.003
03D1aw	0.582	0.997 ± 0.009	1.016 ± 0.012	03D1ax	0.496	0.978 ± 0.001	0.977 ± 0.001
03D1bk	0.865	1.052 ± 0.013	1.128 ± 0.016	03D1bm	0.575	1.069 ± 0.016	1.069 ± 0.008
03D1cm	0.870	0.964 ± 0.004	0.972 ± 0.005	03D1co	0.679	0.977 ± 0.003	0.991 ± 0.004
03D1dj	0.400	0.986 ± 0.001	0.992 ± 0.002	03D1dt	0.612	1.059 ± 0.022	1.034 ± 0.009
03D1ew	0.868	0.972 ± 0.006	0.975 ± 0.006	03D1fb	0.498	0.996 ± 0.005	1.000 ± 0.005
03D1fc	0.331	0.999 ± 0.005	1.002 ± 0.003	03D1fl	0.688	1.044 ± 0.024	1.144 ± 0.037
03D1fq	0.795	0.990 ± 0.007	1.002 ± 0.009	03D1gt	0.560	1.013 ± 0.010	1.006 ± 0.006
04D1ag	0.557	0.990 ± 0.004	0.985 ± 0.003	04D1ak	0.526	0.988 ± 0.004	0.982 ± 0.002
04D1dc	0.211	0.994 ± 0.000	0.996 ± 0.001	04D1de	0.768	0.988 ± 0.007	1.005 ± 0.007
04D1ff	0.855	0.983 ± 0.008	1.012 ± 0.007	04D1hd	0.368	0.988 ± 0.001	0.994 ± 0.002
04D1hx	0.560	0.981 ± 0.002	0.985 ± 0.004	04D1hy	0.850	0.970 ± 0.012	0.977 ± 0.005
04D1iv	0.998	1.199 ± 0.031	1.266 ± 0.034	04D1jg	0.584	0.975 ± 0.003	0.975 ± 0.002
04D1kj	0.585	0.982 ± 0.002	0.993 ± 0.004	04D1ks	0.798	0.964 ± 0.002	0.970 ± 0.004
04D1oh	0.590	0.983 ± 0.003	0.986 ± 0.004	04D1ow	0.921	0.965 ± 0.008	0.973 ± 0.005
04D1pg	0.515	0.992 ± 0.004	1.007 ± 0.006	04D1pu	0.639	0.974 ± 0.004	0.969 ± 0.002
04D1qd	0.767	0.961 ± 0.001	0.961 ± 0.003	04D1rh	0.436	0.983 ± 0.001	0.986 ± 0.002
04D1rx	0.984	1.001 ± 0.012	1.065 ± 0.013	04D1sa	0.586	0.986 ± 0.003	1.003 ± 0.004
04D1si	0.702	0.973 ± 0.003	0.971 ± 0.003	04D1sk	0.663	1.018 ± 0.010	1.013 ± 0.006
05D1az	0.843	0.959 ± 0.004	0.955 ± 0.003	05D1cb	0.632	0.978 ± 0.004	0.995 ± 0.005
05D1ck	0.617	0.986 ± 0.004	0.981 ± 0.003	05D1cl	0.830	0.981 ± 0.008	0.993 ± 0.008
05D1cs	0.917	0.965 ± 0.005	0.986 ± 0.007	05D1dx	0.580	1.000 ± 0.007	1.000 ± 0.004
05D1ej	0.312	0.988 ± 0.000	0.990 ± 0.001	05D1em	0.866	1.047 ± 0.016	1.065 ± 0.012
05D1eo	0.737	0.966 ± 0.003	0.971 ± 0.004	05D1er	0.860	1.010 ± 0.015	1.025 ± 0.008
05D1hn	0.149	0.996 ± 0.000	0.997 ± 0.000	05D1if	0.763	0.993 ± 0.011	1.017 ± 0.008
05D1ix	0.490	0.996 ± 0.005	1.000 ± 0.005	05D1iy	0.248	0.992 ± 0.000	0.994 ± 0.001
05D1ju	0.707	1.003 ± 0.009	1.052 ± 0.013	05D1kl	0.560	0.994 ± 0.004	1.025 ± 0.007
06D1ab	0.182	0.995 ± 0.000	0.996 ± 0.000	06D1bg	0.760	1.004 ± 0.013	0.995 ± 0.006
06D1bo	0.609	1.023 ± 0.023	1.014 ± 0.009	06D1cm	0.621	0.979 ± 0.003	0.976 ± 0.003
06D1du	0.239	0.994 ± 0.001	0.999 ± 0.002	06D1fd	0.350	1.004 ± 0.005	1.015 ± 0.006
06D1hf	0.340	0.987 ± 0.001	0.990 ± 0.002	06D1hj	0.330	0.988 ± 0.000	0.987 ± 0.001
04D2ac	0.348	0.986 ± 0.001	0.991 ± 0.002	04D2al	0.836	0.993 ± 0.008	1.009 ± 0.008
04D2bt	0.220	0.995 ± 0.000	0.996 ± 0.000	04D2ca	0.835	0.983 ± 0.007	1.010 ± 0.008
04D2cc	0.838	0.978 ± 0.008	0.984 ± 0.005	04D2cw	0.569	1.002 ± 0.009	1.002 ± 0.004
04D2fp	0.415	0.985 ± 0.002	0.991 ± 0.002	04D2fs	0.358	0.985 ± 0.001	0.990 ± 0.002
04D2gp	0.732	0.979 ± 0.009	0.972 ± 0.005	04D2ja	0.741	0.975 ± 0.004	0.992 ± 0.004
04D2kr	0.744	1.355 ± 0.182	1.208 ± 0.046	04D2mc	0.348	0.988 ± 0.001	0.996 ± 0.002
04D2mh	0.587	1.001 ± 0.008	1.005 ± 0.004	04D2mj	0.514	0.980 ± 0.002	0.992 ± 0.003
05D2ab	0.320	0.991 ± 0.002	0.994 ± 0.002	05D2ac	0.479	0.982 ± 0.002	0.993 ± 0.003

SN	z	magnification factor, μ		SN	z	magnification factor, μ	
		TFFJ	K04			TFFJ	K04
05D2ay	0.915	0.995 ± 0.013	0.991 ± 0.007	05D2bt	0.680	1.113 ± 0.033	1.224 ± 0.033
05D2by	0.891	1.059 ± 0.035	1.135 ± 0.016	05D2cb	0.427	0.989 ± 0.003	1.002 ± 0.002
05D2cp	0.731	1.097 ± 0.068	1.059 ± 0.020	05D2ct	0.735	1.022 ± 0.012	1.033 ± 0.009
05D2dm	0.797	0.985 ± 0.012	0.989 ± 0.006	05D2dt	0.574	0.976 ± 0.002	0.982 ± 0.003
05D2dw	0.418	0.997 ± 0.005	1.008 ± 0.004	05D2dy	0.505	0.992 ± 0.008	0.988 ± 0.003
05D2ei	0.365	0.985 ± 0.001	0.986 ± 0.000	05D2fq	0.733	0.991 ± 0.008	0.997 ± 0.005
05D2ja	0.302	0.990 ± 0.001	0.996 ± 0.001	05D2mp	0.354	0.987 ± 0.000	0.992 ± 0.001
05D2nn	0.870	0.965 ± 0.006	0.974 ± 0.005	05D2ob	0.924	0.956 ± 0.004	0.945 ± 0.003
06D2ag	0.310	1.000 ± 0.005	1.008 ± 0.003	06D2bk	0.499	0.980 ± 0.002	0.994 ± 0.003
06D2ca	0.533	0.999 ± 0.011	1.003 ± 0.004	06D2cc	0.532	1.016 ± 0.013	0.997 ± 0.003
06D2ez	0.082	1.001 ± 0.000	1.001 ± 0.000	06D2fb	0.124	1.000 ± 0.001	1.000 ± 0.000
06D2ff	0.345	0.996 ± 0.004	1.002 ± 0.002	06D2ga	0.840	1.034 ± 0.038	1.026 ± 0.016
05D2lz	0.780	1.015 ± 0.017	1.011 ± 0.007	03D3af	0.532	1.059 ± 0.014	1.058 ± 0.010
03D3aw	0.449	0.982 ± 0.000	0.978 ± 0.001	03D3ay	0.371	0.986 ± 0.000	0.985 ± 0.000
03D3ba	0.291	0.991 ± 0.000	0.991 ± 0.000	03D3bb	0.244	0.994 ± 0.000	0.997 ± 0.001
03D3bh	0.249	1.001 ± 0.002	1.002 ± 0.002	03D3bl	0.355	1.003 ± 0.004	0.998 ± 0.002
03D3cc	0.463	1.007 ± 0.006	1.026 ± 0.006	04D3bf	0.156	1.000 ± 0.001	1.004 ± 0.001
04D3co	0.620	1.038 ± 0.015	1.030 ± 0.008	04D3cp	0.830	1.002 ± 0.013	0.985 ± 0.007
04D3dd	1.010	0.966 ± 0.006	0.984 ± 0.006	04D3df	0.470	0.980 ± 0.001	0.978 ± 0.001
04D3do	0.610	0.980 ± 0.003	0.984 ± 0.004	04D3ez	0.263	0.993 ± 0.000	0.994 ± 0.001
04D3fk	0.358	0.989 ± 0.001	0.992 ± 0.001	04D3fq	0.730	0.986 ± 0.011	1.012 ± 0.010
04D3gt	0.451	0.998 ± 0.008	0.990 ± 0.003	04D3gx	0.910	1.055 ± 0.018	1.069 ± 0.012
04D3hn	0.552	1.058 ± 0.015	1.056 ± 0.008	04D3is	0.710	0.974 ± 0.002	0.984 ± 0.006
04D3kr	0.337	0.993 ± 0.002	0.993 ± 0.002	04D3ks	0.752	0.989 ± 0.007	0.994 ± 0.008
04D3lp	0.983	0.970 ± 0.007	0.972 ± 0.007	04D3lu	0.822	0.988 ± 0.006	1.028 ± 0.008
04D3mk	0.813	0.965 ± 0.003	0.956 ± 0.002	04D3ml	0.950	0.996 ± 0.008	1.008 ± 0.010
04D3nc	0.817	0.975 ± 0.005	0.991 ± 0.005	04D3nq	0.220	0.996 ± 0.000	0.999 ± 0.001
04D3nr	0.960	1.067 ± 0.019	1.052 ± 0.011	04D3ny	0.810	0.990 ± 0.006	1.001 ± 0.006
04D3oe	0.756	1.010 ± 0.008	1.045 ± 0.008	05D3ax	0.643	1.007 ± 0.009	1.029 ± 0.007
05D3cf	0.419	0.991 ± 0.002	1.002 ± 0.005	05D3cq	0.890	1.009 ± 0.012	1.037 ± 0.014
05D3cx	0.805	1.127 ± 0.035	1.143 ± 0.026	05D3gv	0.715	0.973 ± 0.003	0.974 ± 0.003
05D3gy	0.840	0.994 ± 0.018	1.046 ± 0.011	05D3hh	0.766	1.089 ± 0.052	1.060 ± 0.020
05D3hq	0.338	0.990 ± 0.001	0.991 ± 0.001	05D3hs	0.664	0.980 ± 0.004	0.989 ± 0.005
05D3ht	0.900	1.010 ± 0.010	1.036 ± 0.009	05D3jb	0.740	0.981 ± 0.007	0.994 ± 0.008
05D3jh	0.718	1.014 ± 0.014	1.011 ± 0.008	05D3jk	0.736	1.008 ± 0.017	0.992 ± 0.005
05D3jq	0.579	0.977 ± 0.002	0.983 ± 0.003	05D3jr	0.370	0.995 ± 0.003	0.993 ± 0.002
05D3kp	0.850	0.966 ± 0.004	0.954 ± 0.003	05D3la	0.936	0.972 ± 0.006	0.982 ± 0.010
05D3lb	0.647	0.976 ± 0.004	0.978 ± 0.005	05D3lq	0.421	1.054 ± 0.013	1.074 ± 0.012
05D3lr	0.609	0.997 ± 0.010	0.994 ± 0.005	05D3mh	0.670	0.982 ± 0.004	0.990 ± 0.005
05D3mn	0.760	0.973 ± 0.004	0.985 ± 0.005	05D3mq	0.246	0.994 ± 0.000	0.994 ± 0.000
05D3mx	0.470	1.006 ± 0.007	1.019 ± 0.008	05D3ne	0.169	0.998 ± 0.000	0.999 ± 0.000
06D3bz	0.727	0.991 ± 0.008	1.008 ± 0.007	06D3cc	0.683	1.055 ± 0.030	1.021 ± 0.015

SN	z	magnification factor, μ		SN	z	magnification factor, μ	
		TFFJ	K04			TFFJ	K04
06D3cn	0.232	0.996 ± 0.001	1.000 ± 0.001	06D3df	0.442	0.983 ± 0.001	0.981 ± 0.003
06D3dl	0.357	0.993 ± 0.002	0.998 ± 0.002	06D3do	0.726	1.008 ± 0.009	1.024 ± 0.009
06D3dt	0.282	0.992 ± 0.000	0.994 ± 0.001	06D3el	0.519	0.983 ± 0.003	0.982 ± 0.002
06D3em	0.680	0.979 ± 0.006	0.983 ± 0.004	06D3en	1.060	1.013 ± 0.019	1.007 ± 0.010
06D3et	0.575	0.976 ± 0.001	0.975 ± 0.003	06D3fp	0.270	0.992 ± 0.000	0.993 ± 0.001
06D3gh	0.720	0.993 ± 0.009	0.989 ± 0.006	03D4au	0.468	1.008 ± 0.008	1.044 ± 0.009
03D4cj	0.270	0.986 ± 0.000	0.988 ± 0.000	03D4cx	0.949	1.205 ± 0.054	1.179 ± 0.038
03D4dh	0.627	0.976 ± 0.005	0.987 ± 0.005	03D4di	0.905	1.017 ± 0.021	1.030 ± 0.013
03D4dy	0.598	0.967 ± 0.002	0.965 ± 0.002	03D4fd	0.790	0.996 ± 0.018	0.976 ± 0.006
03D4gg	0.592	0.979 ± 0.005	0.992 ± 0.005	03D4gl	0.571	0.966 ± 0.003	0.962 ± 0.001
04D4an	0.613	0.972 ± 0.004	0.972 ± 0.004	04D4bk	0.860	0.958 ± 0.006	0.944 ± 0.004
04D4bq	0.550	1.114 ± 0.028	1.196 ± 0.027	04D4dm	0.811	0.956 ± 0.002	0.957 ± 0.004
04D4dw	1.031	1.026 ± 0.029	1.023 ± 0.023	04D4fx	0.629	1.013 ± 0.008	1.043 ± 0.009
04D4gg	0.424	0.974 ± 0.000	0.974 ± 0.001	04D4hf	0.936	0.994 ± 0.012	0.980 ± 0.008
04D4ht	0.217	0.990 ± 0.000	0.992 ± 0.000	04D4ib	0.704	0.979 ± 0.007	0.984 ± 0.006
04D4ic	0.680	0.966 ± 0.004	0.965 ± 0.004	04D4ii	0.866	0.974 ± 0.014	0.964 ± 0.012
04D4im	0.751	1.027 ± 0.017	1.024 ± 0.012	04D4it	0.983	1.055 ± 0.015	1.082 ± 0.014
04D4ju	0.472	0.993 ± 0.006	1.006 ± 0.005	04D4jy	0.930	0.950 ± 0.003	0.950 ± 0.005
05D4ag	0.639	0.964 ± 0.003	0.972 ± 0.004	05D4av	0.543	0.966 ± 0.000	0.966 ± 0.001
05D4be	0.537	1.041 ± 0.027	1.043 ± 0.011	05D4bf	0.590	0.975 ± 0.004	0.981 ± 0.005
05D4bi	0.779	0.962 ± 0.003	0.980 ± 0.006	05D4bj	0.704	1.049 ± 0.023	1.062 ± 0.013
05D4bm	0.377	0.990 ± 0.009	0.994 ± 0.003	05D4cn	0.763	0.969 ± 0.005	0.963 ± 0.004
05D4cq	0.702	1.133 ± 0.026	1.168 ± 0.028	05D4cs	0.790	1.019 ± 0.014	1.045 ± 0.013
05D4dw	0.855	0.972 ± 0.007	1.009 ± 0.010	05D4dx	0.793	0.987 ± 0.010	0.996 ± 0.009
05D4dy	0.810	0.960 ± 0.003	0.959 ± 0.003	05D4ef	0.605	1.003 ± 0.009	1.017 ± 0.006
05D4ej	0.589	0.980 ± 0.005	0.994 ± 0.005	05D4ek	0.537	0.975 ± 0.005	0.974 ± 0.002
05D4em	0.974	0.964 ± 0.009	0.965 ± 0.008	05D4ev	0.719	0.975 ± 0.005	0.986 ± 0.005
05D4ff	0.402	0.976 ± 0.000	0.977 ± 0.001	05D4fg	0.839	0.962 ± 0.006	0.948 ± 0.003
05D4fo	0.398	0.994 ± 0.006	0.991 ± 0.004	05D4gw	0.808	0.962 ± 0.005	0.955 ± 0.003
05D4hn	0.844	0.973 ± 0.007	0.984 ± 0.007	06D4dh	0.303	0.994 ± 0.002	1.000 ± 0.002
06D4dr	0.760	1.065 ± 0.030	1.030 ± 0.010	06D4gs	0.310	0.986 ± 0.001	0.993 ± 0.001
06D4ba	0.700	0.984 ± 0.013	0.982 ± 0.006	06D4bw	0.731	1.098 ± 0.022	1.119 ± 0.017
06D4ce	0.850	0.974 ± 0.005	0.994 ± 0.006				

6.4 Prospects

6.4.1 The SNLS 5-year sample

The natural continuation of this project is to search for the lensing signal using the full SNLS sample (5-year sample) which is expected to consist of about $\sim$ 500 spectroscopically confirmed type Ia SNe and $\sim$ 200 with known spectroscopic redshift of the host galaxy. It may also be possible to include SNe that have been detected in the images but not spectroscopically confirmed, using a photometric identification (Bazin, 2008). Performing simulations for the full SNLS sample (500 SNe with the same redshift distribution as the current sample) we find that there is 80% chance of detecting a 3 σ signal (see fig. 6.13).

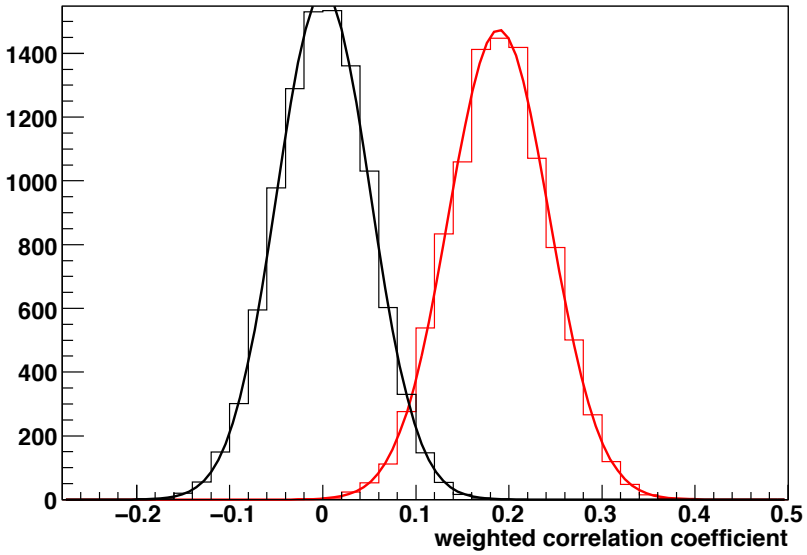

Figure 6.13: The distribution of the weighted correlation coefficient for correlated samples in red and uncorrelated samples in black for 450 supernovae (SNLS full sample). There is 85% chance of detecting a correlation of 3σ

6.4.2 Optimization of the detection of the lensing signal

Another important question to be addressed here is how the uncertainties influence the possibility of detecting the lensing signal. The uncertainties on the magnification have already been discussed in section 5.2.6 and they are quite small (see fig. 5.30) with a mean value of 0.02 magnitudes and the largest uncertainty of the order of 0.1 magnitudes. This is small compared to the uncertainties on the residuals to the Hubble diagram ($0.13 < \sigma_{residual} < 0.24$). For example, assigning a 0.005 uncertainty on the measured magnitudes in the simulations leads to an improvement on the chance of detecting a signal with a 3σ significance of 7% for the current sample and 5% for the full SNLS sample. Hence, improving the magnification estimate has minor influence on the correlation signal.

The chance of detecting a signal will improve significantly due to 3 different features, a bigger supernova sample, higher redshift supernova and a decrease in the scatter in the SN residuals to the Hubble diagram. Increasing the SN sample from 171 to 500 leads to an increase of 50% on the chance of detecting a signal with a 3σ significance. Shifting the redshift distribution towards higher redshifts (example: mean value of 0.8 and an RMS of 0.3) yields an increase of 35% for a sample of 450 supernovae (full SNLS sample). Decreasing the scatter in the residuals to the Hubble diagram from 0.16 to 0.12 leads to an increase of 45% for the full sample.

As a result it is important in the perspective of detecting lensing signals in supernova samples to optimize these features. Unfortunately it is not likely that the scatter in the residuals will decrease significantly in the near future, however, the sample size will be extended and high redshift supernovae will become more frequent throughout the next few years. A significant increase in the number of supernovae will already be achieved with the SNLS full sample.

6.4.3 Future surveys

The SNLS is currently one of the largest Type Ia SNe survey but the next generation of surveys will soon become the leading projects in supernova cosmology.

Several surveys with the goal of detecting nearby SNeIa have already been enhanced. The SkyMapper survey[1] will perform multi-color survey of the southern hemisphere using a 1.35m telescope located at the Mount Stromlo observatory in Australia. They expect to detect approximately 200 nearby SNeIa per year. The PTF[2] (Palomar Transient Factory) situated at the Palomar observatory is expected to harvest $\sim$ 1400 nearby SNeIa per year.

For cosmological purpose it is of great significance to detect higher-z Type Ia SNe. With this goal in mind it is important to mention projects like the Pan-STARRS[3] (Panoramic Survey Telescope And Rapid Response System), a medium deep survey covering 150 deg^2. Pan-STARRS will use 4 different 1.8m telescopes situated at Mauna Kea and Haleakala at Hawaii. They expect to detect approximately 5000 Type Ia Sne per year with a medium redshift of z$\sim$0.5. The Dark Energy Survey[4] (DES) with the goal of investigating the nature of Dark Energy will use a 4 meter telescope at the Cerro Tololo observatory in Chili. Within a period of 5 years they expect to identify $\sim$2000 SNeIa in the redshift range of 0.25 <z< 0.75. The last and most ambitious ground based Type Ia SNe survey is the LSST[5] (Large Synoptic Survey Telescope). LSST is expected to obtain light curves in 6 bands and photometric redshifts of about a million SNe Ia per year in the redshift range of 0.2 <z< 1.2 using a large aperture, wide field survey 8.4m telescope. The survey will cover 20,000 deg^2 of the southern sky revisiting each patch of the sky a 1000 times in 10 years.

As we can see, the statistics of detected and identified Type Ia SNe will explode within the next decade even though only a fraction of the identified SNeIa will be spectroscopically confirmed. It is clear that the new method to obtain mass-luminosity relations for galaxies proposed in this thesis will be very interesting for these surveys, particularly the high redshift surveys.

[1] http://www.mso.anu.edu.au/skymapper/
[2] http://www.astro.caltech.edu/ptf/
[3] http://pan-starrs.ifa.hawaii.edu/public/
[4] https://www.darkenergysurvey.org/
[5] http://www.lsst.org/lsst

Chapter 7

Conclusion

As of today, Type Ia supernovae provide among the most accurate distance estimates. It was precise measurements of these standard candles in 1998 that led to the first direct evidence for the acceleration of the expansion of the universe introducing the mysterious and dominant form of energy in the universe, namely Dark Energy. The current results are consistent with the standard ΛCDM cosmology. At the present time, $\sim$ 500 Type Ia SNe in the redshift range 0 <z< 1.2 have been used for cosmology but within the near future a considerable increase in detected SNeIa is expected to populate the Hubble diagram.

Gravitational lensing has developed into a unique tool to study the Dark Matter distribution in the universe. Lensing is only sensitive to the total mass along the line of sight and takes no notice of its nature allowing one to explore structures which are difficult to detect by other means. In this way, lensing enables us to directly measure how light (galaxies) traces mass.

In this thesis these two powerful measurements have been combined. The idea has been to use Type Ia supernovae to probe the Dark matter clustering by correlating the estimated magnification of the supernova based on a modeling of the foreground mass over densities with the expected brightness increase of the supernova given by the residual to the Hubble diagram.

We have presented the complete analysis on how to estimate the magnification of each supernova. The galaxy catalogs have been made by stacking images obtained in the different filters and the source detection has been performed using SExtractor. Stars and supernova host galaxies have been removed from the catalog and certain areas have been masked due to edges of the camera field of view and bright stars. A newly developed photometric redshift code has been presented providing high resolution redshifts for each galaxy in the catalogs. Results from galaxy-galaxy lensing and the empirical Tully-Fisher and Faber-Jackson relations together with a Dark Matter halo model (SIS) have been used to estimate a total mass of each galaxy necessary in the estimation of the magnification of the supernova. The uncertainties on the magnification have been estimated for each supernova using Monte Carlo simulations.

With respect to the results we found, as expected, most supernovae to be slightly de-magnified and some supernovae to be significantly magnified. We detected a correlation between the supernovae residuals to the Hubble diagram based on the best fit cosmology and the estimated magnification with a significance of 2.3 sigma (99% confidence level) for the current sample (SNLS 3-year). This signal is too weak to obtain a competitive mass-luminosity relation compared to results from galaxy-galaxy lensing and the Faber-Jackson / Tylly-Fisher relations. However, we show in this thesis using Monte Carlo simulations that a signal detection is merely limited by the number of SNe, their redshift dis-

tribution and the scatter in the SN residuals. Reducing the scatter in the estimated magnification by using more precise mass estimates have little impact on the probability of a signal detection. For the full SNLS data set (500 expected spectroscopically confirmed type Ia SNe and 200 with spectroscopic redshift of the host galaxy) there is 80% chance of detecting a lensing signal with a significance of 3 sigma using the same analysis and hence a firm detection of the lensing signal for Type Ia SNe may be within reach shortly.

The idea of using supernova magnification to constrain the total mass density of the foreground galaxies is a new, interesting and highly feasible method. Within the next decade, the number of detected Type Ia supernovae will explode and estimating the magnification of these supernovae will permit us to study the distribution of the dark matter mass around galaxies in great detail.

Bibliography

Ahmed, S. N., Anthony, A. E., Beier, E. W., Bellerive, A., Biller, S. D., Boger, J., Boulay, M. G., Bowler, M. G., Bowles, T. J., Brice, S. J., Bullard, T. V., Chan, Y. D., Chen, M., Chen, X., Cleveland, B. T., Cox, G. A., Dai, X., Dalnoki-Veress, F., Doe, P. J., Dosanjh, R. S., Doucas, G., Dragowsky, M. R., Duba, C. A., Duncan, F. A., Dunford, M., Dunmore, J. A., Earle, E. D., Elliott, S. R., Evans, H. C., Ewan, G. T., Farine, J., Fergani, H., Fleurot, F., Formaggio, J. A., Fowler, M. M., Frame, K., Fulsom, B. G., Gagnon, N., Graham, K., Grant, D. R., Hahn, R. L., Hall, J. C., Hallin, A. L., Hallman, E. D., Hamer, A. S., Handler, W. B., Hargrove, C. K., Harvey, P. J., Hazama, R., Heeger, K. M., Heintzelman, W. J., Heise, J., Helmer, R. L., Hemingway, R. J., Hime, A., Howe, M. A., Jagam, P., Jelley, N. A., Klein, J. R., Kos, M. S., Krumins, A. V., Kutter, T., Kyba, C. C., Labranche, H., Lange, R., Law, J., Lawson, I. T., Lesko, K. T., Leslie, J. R., Levine, I., Luoma, S., MacLellan, R., Majerus, S., Mak, H. B., Maneira, J., Marino, A. D., McCauley, N., McDonald, A. B., McGee, S., McGregor, G., Mifflin, C., Miknaitis, K. K., Miller, G. G., Moffat, B. A., Nally, C. W., Nickel, B. G., Noble, A. J., Norman, E. B., Oblath, N. S., Okada, C. E., Ollerhead, R. W., Orrell, J. L., Oser, S. M., Ouellet, C., Peeters, S. J., Poon, A. W., Robertson, B. C., Robertson, R. G., Rollin, E., Rosendahl, S. S., Rusu, V. L., Schwendener, M. H., Simard, O., Simpson, J. J., Sims, C. J., Sinclair, D., Skensved, P., Smith, M. W., Starinsky, N., Stokstad, R. G., Stonehill, L. C., Tafirout, R., Takeuchi, Y., Tešić, G., Thomson, M., Thorman, M., van Berg, R., van de Water, R. G., Virtue, C. J., Wall, B. L., Waller, D., Waltham, C. E., Tseung, H. W., Wark, D. L., West, N., Wilhelmy, J. B., Wilkerson, J. F., Wilson, J. R., Wouters, J. M., Yeh, M., & Zuber, K. 2004. Measurement of the Total Active (^{8})B Solar Neutrino Flux at the Sudbury Neutrino Observatory with Enhanced Neutral Current Sensitivity. *Physical Review Letters*, **92**(18), 181301–+.

Ahn, M. H., Aoki, S., Bhang, H., Boyd, S., Casper, D., Choi, J. H., Fukuda, S., Fukuda, Y., Gajewski, W., Hara, T., Hasegawa, M., Hasegawa, T., Hayato, Y., Hill, J., Ichikawa, A. K., Ikeda, A., Inagaki, T., Ishida, T., Ishii, T., Ishitsuka, M., Itow, Y., Iwashita, T., Jang, H. I., Jang, J. S., Jeon, E. J., Jung, C. K., Kajita, T., Kameda, J., Kaneyuki, K., Kato, I., Kearns, E., Kibayashi, A., Kielczewska, D., Kobayashi, K., Kim, B. J., Kim, C. O., Kim, J. Y., Kim, S. B., Kobayashi, T., Kohama, M., Koshio, Y., Kropp, W. R., Learned, J. G., Lim, S. H., Lim, I. T., Maesaka, H., Martens, K., Maruyama, T., Matsuno, S., Mauger, C., McGrew, C., Mine, S., Miura, M., Miyano, K., Moriyama, S., Nakahata, M., Nakamura, K., Nakano, I., Nakata, F., Nakaya, T., Nakayama, S., Namba, T., Nishikawa, K., Nishiyama, S., Noda, S., Obayashi, A., Okada, A., Ooyabu, T., Oyama, Y., Pac, M. Y., Park, H., Sakuda, M., Sakurai, N., Sasao, N., Scholberg, K., Sharkey, E., Shiozawa, M., So, H., Sobel, H. W., Stachyra, A., Stone, J. L., Suga, Y., Sulak, L. R., Suzuki, A., Suzuki, Y., Takeuchi, Y., Tamura, N., Toshito, T., Totsuka, Y., Vagins, M. R., Walter, C. W., Wilkes, R. J., Yamada, S., Yamamoto, S., Yanagisawa, C., Yokoyama, H., Yoo, J., Yoshida, M., & Zalipska, J. 2003. Indications of Neutrino Oscillation in a 250km Long-Baseline Experiment. *Physical Review Letters*, **90**(4), 041801–+.

Albrecht, A., & Steinhardt, P. J. 1982. Cosmology for grand unified theories with radiatively induced symmetry breaking. *Physical Review Letters*, **48**(Apr.), 1220–1223.

Alpher, R. A., & Herman, R. 1948. Evolution of the Universe. *Nature*, **162**(Nov.), 774–775.

Alpher, R. A., Follin, J. W., & Herman, R. C. 1953. Physical Conditions in the Initial Stages of the Expanding Universe. *Physical Review*, **92**(Dec.), 1347–1361.

Araki, T., Eguchi, K., Enomoto, S., Furuno, K., Ichimura, K., Ikeda, H., Inoue, K., Ishihara, K., Iwamoto, T., Kawashima, T., Kishimoto, Y., Koga, M., Koseki, Y., Maeda, T., Mitsui, T., Motoki, M., Nakajima, K., Ogawa, H., Owada, K., Ricol, J.-S., Shimizu, I., Shirai, J., Suekane, F., Suzuki, A., Tada, K., Tajima, O., Tamae, K., Tsuda, Y., Watanabe, H., Busenitz, J., Classen, T., Djurcic, Z., Keefer, G., McKinny, K., Mei, D.-M., Piepke, A., Yakushev, E., Berger, B. E., Chan, Y. D., Decowski, M. P., Dwyer, D. A., Freedman, S. J., Fu, Y., Fujikawa, B. K., Goldman, J., Gray, F., Heeger, K. M., Lesko, K. T., Luk, K.-B., Murayama, H., Poon, A. W., Steiner, H. M., Winslow, L. A., Horton-Smith, G. A., Mauger, C., McKeown, R. D., Vogel, P., Lane, C. E., Miletic, T., Gorham, P. W., Guillian, G., Learned, J. G., Maricic, J., Matsuno, S., Pakvasa, S., Dazeley, S., Hatakeyama, S., Rojas, A., Svoboda, R., Dieterle, B. D., Detwiler, J., Gratta, G., Ishii, K., Tolich, N., Uchida, Y., Batygov, M., Bugg, W., Efremenko, Y., Kamyshkov, Y., Kozlov, A., Nakamura, Y., Gould, C. R., Karwowski, H. J., Markoff, D. M., Messimore, J. A., Nakamura, K., Rohm, R. M., Tornow, W., Wendell, R., Young, A. R., Chen, M.-J., Wang, Y.-F., & Piquemal, F. 2005. Measurement of Neutrino Oscillation with KamLAND: Evidence of Spectral Distortion. *Physical Review Letters*, **94**(8), 081801–+.

Astier, P., Guy, J., Regnault, N., Pain, R., Aubourg, E., Balam, D., Basa, S., Carlberg, R. G., Fabbro, S., Fouchez, D., Hook, I. M., Howell, D. A., Lafoux, H., Neill, J. D., Palanque-Delabrouille, N., Perrett, K., Pritchet, C. J., Rich, J., Sullivan, M., Taillet, R., Aldering, G., Antilogus, P., Arsenijevic, V., Balland, C., Baumont, S., Bronder, J., Courtois, H., Ellis, R. S., Filiol, M., Gonçalves, A. C., Goobar, A., Guide, D., Hardin, D., Lusset, V., Lidman, C., McMahon, R., Mouchet, M., Mourao, A., Perlmutter, S., Ripoche, P., Tao, C., & Walton, N. 2006. The Supernova Legacy Survey: measurement of Ω_M, Ω_Λ and w from the first year data set. *Astronomy & Astrophysics*, **447**(Feb.), 31–48.

Bacon, D. J., Refregier, A. R., & Ellis, R. S. 2000. Detection of weak gravitational lensing by large-scale structure. *Monthly Notices of the Royal Astronomical Society*, **318**(Oct.), 625–640.

Bailey, S., Aldering, G., Antilogus, P., Aragon, C., Baltay, C., Bongard, S., Buton, C., Childress, M., Chotard, N., Copin, Y., Gangler, E., Loken, S., Nugent, P., Pain, R., Pecontal, E., Pereira, R., Perlmutter, S., Rabinowitz, D., Rigaudier, G., Runge, K., Scalzo, R., Smadja, G., Swift, H., Tao, C., Thomas, R. C., & Wu, C. 2009. Using Spectral Flux Ratios to Standardize SN Ia Luminosities. *ArXiv e-prints*, May.

Balland, C. 2009. ?

Balland, C., Mouchet, M., Pain, R., Walton, N. A., Amanullah, R., Astier, P., Ellis, R. S., Fabbro, S., Goobar, A., Hardin, D., Hook, I. M., Irwin, M. J., McMahon, R. G., Mendez, J. M., Ruiz-Lapuente, P., Sainton, G., Schahmaneche, K., & Stanishev, V. 2006. Spectroscopy of twelve type Ia supernovae at intermediate redshift. *Astronomy & Astrophysics*, **445**(Jan.), 387–402.

Bamford, S. P., Aragón-Salamanca, A., & Milvang-Jensen, B. 2006. The Tully-Fisher relation of distant field galaxies. *Monthly Notices of the Royal Astronomical Society*, **366**(Feb.), 308–320.

Barden, M., Lehnert, M. D., Tacconi, L., Genzel, R., White, S., & Franceschini, A. 2003. Ha Rotation Curves of z˜1 Galaxies: Unraveling the Evolution of the Tully-Fisher Relation. *ArXiv Astrophysics e-prints*, Feb.

Barris, B. J., Tonry, J. L., Blondin, S., Challis, P., Chornock, R., Clocchiatti, A., Filippenko, A. V., Garnavich, P., Holland, S. T., Jha, S., Kirshner, R. P., Krisciunas, K., Leibundgut, B., Li, W., Matheson, T., Miknaitis, G., Riess, A. G., Schmidt, B. P., Smith, R. C., Sollerman, J., Spyromilio, J., Stubbs, C. W., Suntzeff, N. B., Aussel, H., Chambers, K. C., Connelley, M. S., Donovan, D., Henry, J. P., Kaiser, N., Liu, M. C., Martín, E. L., & Wainscoat, R. J. 2004. Twenty-Three High-Redshift Supernovae from the Institute for Astronomy Deep Survey: Doubling the Supernova Sample at z ¿ 0.7. *Astrophysical Journal*, **602**(Feb.), 571–594.

Bartelmann, M. 1996. Arcs from a universal dark-matter halo profile. *Astronomy & Astrophysics*, **313**(Sept.), 697–702.

Baumont, S., Balland, C., Astier, P., Guy, J., Hardin, D., Howell, D. A., Lidman, C., Mouchet, M., Pain, R., & Regnault, N. 2008. PHotometry Assisted Spectral Extraction (PHASE) and identification of SNLS supernovae. *Astronomy & Astrophysics*, **491**(Nov.), 567–585.

Bazin, G. 2008. *?* Ph.D. thesis, Université Paris 7.

Bergström, L., Goliath, M., Goobar, A., & Mörtsell, E. 2000. Lensing effects in an inhomogeneous universe. *Astronomy & Astrophysics*, **358**(June), 13–29.

Bernardi, M., Sheth, R. K., Annis, J., Burles, S., Eisenstein, D. J., Finkbeiner, D. P., Hogg, D. W., Lupton, R. H., Schlegel, D. J., SubbaRao, M., Bahcall, N. A., Blakeslee, J. P., Brinkmann, J., Castander, F. J., Connolly, A. J., Csabai, I., Doi, M., Fukugita, M., Frieman, J., Heckman, T., Hennessy, G. S., Ivezić, Ž., Knapp, G. R., Lamb, D. Q., McKay, T., Munn, J. A., Nichol, R., Okamura, S., Schneider, D. P., Thakar, A. R., & York, D. G. 2003a. Early-Type Galaxies in the Sloan Digital Sky Survey. I. The Sample. *Astronomical Journal*, **125**(Apr.), 1817–1848.

Bernardi, M., Sheth, R. K., Annis, J., Burles, S., Eisenstein, D. J., Finkbeiner, D. P., Hogg, D. W., Lupton, R. H., Schlegel, D. J., SubbaRao, M., Bahcall, N. A., Blakeslee, J. P., Brinkmann, J., Castander, F. J., Connolly, A. J., Csabai, I., Doi, M., Fukugita, M., Frieman, J., Heckman, T., Hennessy, G. S., Ivezić, Ž., Knapp, G. R., Lamb, D. Q., McKay, T., Munn, J. A., Nichol, R., Okamura, S., Schneider, D. P., Thakar, A. R., & York, D. G. 2003b. Early-type Galaxies in the Sloan Digital Sky Survey. II. Correlations between Observables. *Astronomical Journal*, **125**(Apr.), 1849–1865.

Bertin, E., & Arnouts, S. 1996. SExtractor: Software for source extraction. *Astronomy & Astrophysics Supplement*, **117**(June), 393–404.

Blondin, S., Dessart, L., Leibundgut, B., Branch, D., Höflich, P., Tonry, J. L., Matheson, T., Foley, R. J., Chornock, R., Filippenko, A. V., Sollerman, J., Spyromilio, J., Kirshner, R. P., Wood-Vasey, W. M., Clocchiatti, A., Aguilera, C., Barris, B., Becker, A. C., Challis, P., Covarrubias, R., Davis, T. M., Garnavich, P., Hicken, M., Jha, S., Krisciunas, K., Li, W., Miceli, A., Miknaitis, G., Pignata,

G., Prieto, J. L., Rest, A., Riess, A. G., Salvo, M. E., Schmidt, B. P., Smith, R. C., Stubbs, C. W., & Suntzeff, N. B. 2006. Using Line Profiles to Test the Fraternity of Type Ia Supernovae at High and Low Redshifts. *Astronomical Journal*, **131**(Mar.), 1648–1666.

Bohlin, R. C. 2000. Comparison of White Dwarf Models with STIS Spectrophotometry. *Astronomical Journal*, **120**(July), 437–446.

Bohlin, R. C. 2007 (Apr.). HST Stellar Standards with 1% Accuracy in Absolute Flux. *Pages 315–+ of:* Sterken, C. (ed), *The Future of Photometric, Spectrophotometric and Polarimetric Standardization*. Astronomical Society of the Pacific Conference Series, vol. 364.

Bohlin, R. C., & Gilliland, R. L. 2004. Absolute Flux Distribution of the SDSS Standard BD +17deg4708. *Astronomical Journal*, **128**(Dec.), 3053–3060.

Böhm, A., Ziegler, B. L., Saglia, R. P., Bender, R., Fricke, K. J., Gabasch, A., Heidt, J., Mehlert, D., Noll, S., & Seitz, S. 2004. The Tully-Fisher relation at intermediate redshift. *Astronomy & Astrophysics*, **420**(June), 97–114.

Boulade, O., Charlot, X., Abbon, P., Aune, S., Borgeaud, P., Carton, P.-H., Carty, M., Da Costa, J., Deschamps, H., Desforge, D., Eppellé, D., Gallais, P., Gosset, L., Granelli, R., Gros, M., de Kat, J., Loiseau, D., Ritou, J.-., Roussé, J. Y., Starzynski, P., Vignal, N., & Vigroux, L. G. 2003 (Mar.). MegaCam: the new Canada-France-Hawaii Telescope wide-field imaging camera. *Pages 72–81 of:* Iye, M., & Moorwood, A. F. M. (eds), *Society of Photo-Optical Instrumentation Engineers (SPIE) Conference Series*. Society of Photo-Optical Instrumentation Engineers (SPIE) Conference Series, vol. 4841.

Bronder, T. J., Hook, I. M., Astier, P., Balam, D., Balland, C., Basa, S., Carlberg, R. G., Conley, A., Fouchez, D., Guy, J., Howell, D. A., Neill, J. D., Pain, R., Perrett, K., Pritchet, C. J., Regnault, N., Sullivan, M., Baumont, S., Fabbro, S., Filliol, M., Perlmutter, S., & Ripoche, P. 2008. SNLS spectroscopy: testing for evolution in type Ia supernovae. *Astronomy & Astrophysics*, **477**(Jan.), 717–734.

Cardelli, J. A., Clayton, G. C., & Mathis, J. S. 1989. The relationship between infrared, optical, and ultraviolet extinction. *APJ*, **345**(Oct.), 245–256.

Casertano, S., & van Gorkom, J. H. 1991. Declining rotation curves - The end of a conspiracy? *Astronomical Journal*, **101**(Apr.), 1231–1241.

Chiu, K., Bamford, S. P., & Bunker, A. 2008. Tully-Fisher relation of DEEP2 galaxies (Chiu+, 2007). *VizieR Online Data Catalog*, **837**(Mar.), 70806–+.

Chwolson, O. 1924. Über eine mögliche Form fiktiver Doppelsterne. *Astronomische Nachrichten*, **221**(July), 329–+.

Clayton, D. D. 1974. Line 57 CO Gamma Rays: New Diagnostic of Supernova Structure. *Astrophysical Journal*, **188**(Feb.), 155–158.

Clocchiatti, A., Schmidt, B. P., Filippenko, A. V., Challis, P., Coil, A. L., Covarrubias, R., Diercks, A., Garnavich, P., Germany, L., Gilliland, R., Hogan, C., Jha, S., Kirshner, R. P., Leibundgut, B., Leonard, D., Li, W., Matheson, T., Phillips, M. M., Prieto, J. L., Reiss, D., Riess, A. G., Schommer, R., Smith, R. C., Soderberg, A., Spyromilio, J., Stubbs, C., Suntzeff, N. B., Tonry, J. L., & Woudt, P. 2006. Hubble Space Telescope and Ground-based Observations of Type Ia Supernovae at Redshift 0.5: Cosmological Implications. *Astrophysical Journal*, **642**(May), 1–21.

Coc, A., Vangioni-Flam, E., Descouvemont, P., Adahchour, A., & Angulo, C. 2004. Updated Big Bang Nucleosynthesis Compared with Wilkinson Microwave Anisotropy Probe Observations and the Abundance of Light Elements. *Astrophysical Journal*, **600**(Jan.), 544–552.

Cole, S., Percival, W. J., Peacock, J. A., Norberg, P., Baugh, C. M., Frenk, C. S., Baldry, I., Bland-Hawthorn, J., Bridges, T., Cannon, R., Colless, M., Collins, C., Couch, W., Cross, N. J. G., Dalton, G., Eke, V. R., De Propris, R., Driver, S. P., Efstathiou, G., Ellis, R. S., Glazebrook, K., Jackson, C., Jenkins, A., Lahav, O., Lewis, I., Lumsden, S., Maddox, S., Madgwick, D., Peterson, B. A., Sutherland, W., & Taylor, K. 2005. The 2dF Galaxy Redshift Survey: power-spectrum analysis of the final data set and cosmological implications. *Monthly Notices of the Royal Astronomical Society*, **362**(Sept.), 505–534.

Colgate, S. A., & McKee, C. 1969. Early Supernova Luminosity. *Astrophysical Journal*, **157**(Aug.), 623–+.

Colless, M., Dalton, G., Maddox, S., Sutherland, W., Norberg, P., Cole, S., Bland-Hawthorn, J., Bridges, T., Cannon, R., Collins, C., Couch, W., Cross, N., Deeley, K., de Propris, R., Driver, S. P., Efstathiou, G., Ellis, R. S., Frenk, C. S., Glazebrook, K., Jackson, C., Lahav, O., Lewis, I., Lumsden, S., Madgwick, D., Peacock, J. A., Peterson, B. A., Price, I., Seaborne, M., & Taylor, K. 2003. The 2dF Galaxy Redshift Survey 100k Data Release (2dFGRS Team, 2001). *VizieR Online Data Catalog*, **7226**(June), 0–+.

Conley, A., Carlberg, R. G., Guy, J., Howell, D. A., Jha, S., Riess, A. G., & Sullivan, M. 2007. Is There Evidence for a Hubble Bubble? The Nature of Type Ia Supernova Colors and Dust in External Galaxies. *Astrophysical Journal Letters*, **664**(July), L13–L16.

Conley, A., Sullivan, M., Hsiao, E. Y., Guy, J., Astier, P., Balam, D., Balland, C., Basa, S., Carlberg, R. G., Fouchez, D., Hardin, D., Howell, D. A., Hook, I. M., Pain, R., Perrett, K., Pritchet, C. J., & Regnault, N. 2008. SiFTO: An Empirical Method for Fitting SN Ia Light Curves. *Astrophysical Journal*, **681**(July), 482–498.

Davis, M., Faber, S. M., Newman, J., Phillips, A. C., Ellis, R. S., Steidel, C. C., Conselice, C., Coil, A. L., Finkbeiner, D. P., Koo, D. C., Guhathakurta, P., Weiner, B., Schiavon, R., Willmer, C., Kaiser, N., Luppino, G. A., Wirth, G., Connolly, A., Eisenhardt, P., Cooper, M., & Gerke, B. 2003 (Feb.). Science Objectives and Early Results of the DEEP2 Redshift Survey. *Pages 161–172 of:* Guhathakurta, P. (ed), *Society of Photo-Optical Instrumentation Engineers (SPIE) Conference Series*. Society of Photo-Optical Instrumentation Engineers (SPIE) Conference Series, vol. 4834.

Davis, M., Guhathakurta, P., Konidaris, N. P., Newman, J. A., Ashby, M. L. N., Biggs, A. D., Barmby, P., Bundy, K., Chapman, S. C., Coil, A. L., Conselice, C. J., Cooper, M. C., Croton, D. J., Eisenhardt, P. R. M., Ellis, R. S., Faber, S. M., Fang, T., Fazio, G. G., Georgakakis, A., Gerke, B. F.,

Goss, W. M., Gwyn, S., Harker, J., Hopkins, A. M., Huang, J.-S., Ivison, R. J., Kassin, S. A., Kirby, E. N., Koekemoer, A. M., Koo, D. C., Laird, E. S., Le Floc'h, E., Lin, L., Lotz, J. M., Marshall, P. J., Martin, D. C., Metevier, A. J., Moustakas, L. A., Nandra, K., Noeske, K. G., Papovich, C., Phillips, A. C., Rich, R. M., Rieke, G. H., Rigopoulou, D., Salim, S., Schiminovich, D., Simard, L., Smail, I., Small, T. A., Weiner, B. J., Willmer, C. N. A., Willner, S. P., Wilson, G., Wright, E. L., & Yan, R. 2007. The All-Wavelength Extended Groth Strip International Survey (AEGIS) Data Sets. *Astrophysical Journal Letters*, **660**(May), L1–L6.

Davis, R. J., Harmer, D. S., & Neely, F. H. 1969. Solar Neutrinos. *Pages 287–+ of:* Douglas, K. N., Robinson, I., Schild, A., Schucking, E. L., Wheeler, J. A., & Woolf, N. J. (eds), *Quasars and high-energy astronomy*.

Dunkley, J., Komatsu, E., Nolta, M. R., Spergel, D. N., Larson, D., Hinshaw, G., Page, L., Bennett, C. L., Gold, B., Jarosik, N., Weiland, J. L., Halpern, M., Hill, R. S., Kogut, A., Limon, M., Meyer, S. S., Tucker, G. S., Wollack, E., & Wright, E. L. 2009. Five-Year Wilkinson Microwave Anisotropy Probe Observations: Likelihoods and Parameters from the WMAP Data. *Astrophysical Journal Supplement Series*, **180**(Feb.), 306–329.

Eddington, A. S. 1919. The total eclipse of 1919 May 29 and the influence of gravitation on light. *The Observatory*, **42**(Mar.), 119–122.

Einstein, A. 1916. Die Grundlage der allgemeinen Relativitätstheorie. *Annalen der Physik*, **354**, 769–822.

Einstein, A. 1936. Lens-Like Action of a Star by the Deviation of Light in the Gravitational Field. *Science*, **84**(Dec.), 506–507.

Eisenstein, D. J., Zehavi, I., Hogg, D. W., Scoccimarro, R., Blanton, M. R., Nichol, R. C., Scranton, R., Seo, H.-J., Tegmark, M., Zheng, Z., Anderson, S. F., Annis, J., Bahcall, N., Brinkmann, J., Burles, S., Castander, F. J., Connolly, A., Csabai, I., Doi, M., Fukugita, M., Frieman, J. A., Glazebrook, K., Gunn, J. E., Hendry, J. S., Hennessy, G., Ivezić, Z., Kent, S., Knapp, G. R., Lin, H., Loh, Y.-S., Lupton, R. H., Margon, B., McKay, T. A., Meiksin, A., Munn, J. A., Pope, A., Richmond, M. W., Schlegel, D., Schneider, D. P., Shimasaku, K., Stoughton, C., Strauss, M. A., SubbaRao, M., Szalay, A. S., Szapudi, I., Tucker, D. L., Yanny, B., & York, D. G. 2005. Detection of the Baryon Acoustic Peak in the Large-Scale Correlation Function of SDSS Luminous Red Galaxies. *Astrophysical Journal*, **633**(Nov.), 560–574.

Fabbro, S. 2001. *Photométrie de supernovae de type Ia et implications cosmologiques*. Ph.D. thesis, Université Denis Diderot, Paris.

Faber, S. M., & Jackson, R. E. 1976. Velocity dispersions and mass-to-light ratios for elliptical galaxies. *Lick Observatory Bulletin*, **714**, 1–+.

Filippenko, A. V. 1997. Optical Spectra of Supernovae. *Annual Review of Astronomy & Astrophysics*, **35**, 309–355.

Fioc, M., & Rocca-Volmerange, B. 1999. PEGASE.2, a metallicity-consistent spectral evolution model of galaxies: the documentation and the code. *ArXiv Astrophysics e-prints*, Dec.

Fish, R. A. 1964. A Mass-Potential Relationship in Elliptical Galaxies and Some Inferences Concerning the Formation and Evolution of Galaxies. *Astrophysical Journal*, **139**(Jan.), 284–+.

Franx, M. 1993. Constraining galaxy evolution and cosmology from galaxy kinematics - First observations at Z = 0.18. *Publications of the Astronomical Society of the Pacific*, **105**(Sept.), 1058–1062.

Gallagher, J. S., Garnavich, P. M., Berlind, P., Challis, P., Jha, S., & Kirshner, R. P. 2005. Chemistry and Star Formation in the Host Galaxies of Type Ia Supernovae. *Astrophysical Journal*, **634**(Nov.), 210–226.

Gallagher, J. S., Garnavich, P. M., Caldwell, N., Kirshner, R. P., Jha, S. W., Li, W., Ganeshalingam, M., & Filippenko, A. V. 2008. Supernovae in Early-Type Galaxies: Directly Connecting Age and Metallicity with Type Ia Luminosity. *Astrophysical Journal*, **685**(Oct.), 752–766.

Garnavich, P. M., Kirshner, R. P., Challis, P., Tonry, J., Gilliland, R. L., Smith, R. C., Clocchiatti, A., Diercks, A., Filippenko, A. V., Hamuy, M., Hogan, C. J., Leibundgut, B., Phillips, M. M., Reiss, D., Riess, A. G., Schmidt, B. P., Schommer, R. A., Spyromilio, J., Stubbs, C., Suntzeff, N. B., & Wells, L. 1998. Constraints on Cosmological Models from Hubble Space Telescope Observations of High-z Supernovae. *Astrophysical Journal Letters*, **493**(Feb.), L53+.

Goldhaber, G., Groom, D. E., Kim, A., Aldering, G., Astier, P., Conley, A., Deustua, S. E., Ellis, R., Fabbro, S., Fruchter, A. S., Goobar, A., Hook, I., Irwin, M., Kim, M., Knop, R. A., Lidman, C., McMahon, R., Nugent, P. E., Pain, R., Panagia, N., Pennypacker, C. R., Perlmutter, S., Ruiz-Lapuente, P., Schaefer, B., Walton, N. A., & York, T. 2001. Timescale Stretch Parameterization of Type Ia Supernova B-Band Light Curves. *Astrophysical Journal*, **558**(Sept.), 359–368.

Goobar, A., Mörtsell, E., Amanullah, R., Goliath, M., Bergström, L., & Dahlén, T. 2002. SNOC: A Monte-Carlo simulation package for high-z supernova observations. *Astronomy & Astrophysics*, **392**(Sept.), 757–771.

Goobar, A., Hannestad, S., Mörtsell, E., & Tu, H. 2006. The neutrino mass bound from WMAP 3 year data, the baryon acoustic peak, the SNLS supernovae and the Lyman-α forest. *Journal of Cosmology and Astro-Particle Physics*, **6**(June), 19–+.

Guide, D. 2005. *Détermination des paramétres cosmologiques à l'aide de supernovae de type Ia à grands décalages vers le rouge*. Ph.D. thesis, Université Paris 6.

Gunnarsson, C. 2004. Q-LET quick lensing estimation tool: an application to SN2003es. *Journal of Cosmology and Astro-Particle Physics*, **3**(Mar.), 2–+.

Gunnarsson, C., Dahlén, T., Goobar, A., Jönsson, J., & Mörtsell, E. 2006. Corrections for Gravitational Lensing of Supernovae: Better than Average? *Astrophysical Journal*, **640**(Mar.), 417–427.

Guth, A. H. 1981. Inflationary universe: A possible solution to the horizon and flatness problems. *Physical Review D*, **23**(Jan.), 347–356.

Guy, J., Astier, P., Nobili, S., Regnault, N., & Pain, R. 2005. A Spectral Adaptive Lightcurve Template for fitting SN Ia lightcurve templates. *Astronomy & Astrophysics(in press)*.

Guy, J., Astier, P., Baumont, S., Hardin, D., Pain, R., Regnault, N., Basa, S., Carlberg, R. G., Conley, A., Fabbro, S., Fouchez, D., Hook, I. M., Howell, D. A., Perrett, K., Pritchet, C. J., Rich, J., Sullivan, M., Antilogus, P., Aubourg, E., Bazin, G., Bronder, J., Filiol, M., Palanque-Delabrouille, N., Ripoche, P., & Ruhlmann-Kleider, V. 2007. SALT2: using distant supernovae to improve the use of type Ia supernovae as distance indicators. *Astronomy & Astrophysics*, **466**(Apr.), 11–21.

Hamuy, M., Phillips, M. M., Maza, J., Suntzeff, N. B., Schommer, R. A., & Aviles, R. 1995. A Hubble diagram of distant type IA supernovae. *Astronomical Journal*, **109**(Jan.), 1–13.

Hamuy, M., Phillips, M. M., Suntzeff, N. B., Schommer, R. A., Maza, J., & Aviles, R. 1996. The Absolute Luminosities of the Calan/Tololo Type IA Supernovae. *Astronomical Journal*, **112**(Dec.), 2391–+.

Hamuy, M., Trager, S. C., Pinto, P. A., Phillips, M. M., Schommer, R. A., Ivanov, V., & Suntzeff, N. B. 2000. A Search for Environmental Effects on Type IA Supernovae. *Astronomical Journal*, **120**(Sept.), 1479–1486.

Hannestad, S., & Raffelt, G. G. 2006. Neutrino masses and cosmic radiation density: combined analysis. *Journal of Cosmology and Astro-Particle Physics*, **11**(Nov.), 16–+.

Haynes, M. P., Giovanelli, R., Chamaraux, P., da Costa, L. N., Freudling, W., Salzer, J. J., & Wegner, G. 1999. The I-Band Tully-Fisher Relation for SC Galaxies: 21 Centimeter H I Line Data. *Astronomical Journal*, **117**(May), 2039–2051.

Hillebrandt, W., & Niemeyer, J. C. 2000. Type IA Supernova Explosion Models. *Annual Review of Astronomy & Astrophysics*, **38**, 191–230.

Hinshaw, G., Weiland, J. L., Hill, R. S., Odegard, N., Larson, D., Bennett, C. L., Dunkley, J., Gold, B., Greason, M. R., Jarosik, N., Komatsu, E., Nolta, M. R., Page, L., Spergel, D. N., Wollack, E., Halpern, M., Kogut, A., Limon, M., Meyer, S. S., Tucker, G. S., & Wright, E. L. 2009. Five-Year Wilkinson Microwave Anisotropy Probe Observations: Data Processing, Sky Maps, and Basic Results. *Astrophysical Journal Supplement Series*, **180**(Feb.), 225–245.

Hirata, K. S., Inoue, K., Ishida, T., Kajita, T., Kihara, K., Nakahata, M., Nakamura, K., Ohara, S., Sakai, A., Sato, N., Suzuki, Y., Totsuka, Y., Yaginuma, Y., Mori, M., Oyama, Y., Suzuki, A., Takahashi, K., Yamada, M., Koshiba, M., Nishijima, K., Kajimura, T., Suda, T., Tajima, T., Miyano, K., Miyata, H., Takei, H., Fukuda, Y., Kodera, E., Nagashima, Y., Takita, M., Yokoyama, H., Kaneyuki, K., Takeuchi, Y., Tanimori, T., Beier, E. W., Frank, E. D., Frati, W., Kim, S. B., Mann, A. K., Newcomer, F. M., van Berg, R., & Zhang, W. 1992. Observation of a small atmospheric ν_μ/ν_e ratio in Kamiokande. *Physics Letters B*, **280**(Apr.), 146–152.

Hoekstra, H., Yee, H. K. C., & Gladders, M. D. 2004. Properties of Galaxy Dark Matter Halos from Weak Lensing. *Astrophysical Journal*, **606**(May), 67–77.

Hoekstra, H., Hsieh, B. C., Yee, H. K. C., Lin, H., & Gladders, M. D. 2005. Virial Masses and the Baryon Fraction in Galaxies. *Astrophysical Journal*, **635**(Dec.), 73–85.

Hogg, D. W., Baldry, I. K., Blanton, M. R., & Eisenstein, D. J. 2002. The K correction. *ArXiv Astrophysics e-prints*, Oct.

Holtzman, J. A., Marriner, J., Kessler, R., Sako, M., Dilday, B., Frieman, J. A., Schneider, D. P., Bassett, B., Becker, A., Cinabro, D., DeJongh, F., Depoy, D. L., Doi, M., Garnavich, P. M., Hogan, C. J., Jha, S., Konishi, K., Lampeitl, H., Marshall, J. L., McGinnis, D., Miknaitis, G., Nichol, R. C., Prieto, J. L., Riess, A. G., Richmond, M. W., Romani, R., Smith, M., Takanashi, N., Tokita, K., van der Heyden, K., Yasuda, N., & Zheng, C. 2008. The Sloan Digital Sky Survey-II: Photometry and Supernova IA Light Curves from the 2005 Data. *Astronomical Journal*, **136**(Dec.), 2306–2320.

Holz, D. E., & Linder, E. V. 2005. Safety in Numbers: Gravitational Lensing Degradation of the Luminosity Distance-Redshift Relation. *Astrophysical Journal*, **631**(Oct.), 678–688.

Howell, D. A., Sullivan, M., Perret, K., Bronder, T.J., Hook, I. M., & Astier, P. 2005a. Gemini spectroscopy of supernovae from SNLS: improving high redshift SN selection and classification. *Astrophysical Journal in press*.

Howell, D. A., Sullivan, M., Perrett, K., Bronder, T. J., Hook, I. M., Astier, P., Aubourg, E., Balam, D., Basa, S., Carlberg, R. G., Fabbro, S., Fouchez, D., Guy, J., Lafoux, H., Neill, J. D., Pain, R., Palanque-Delabrouille, N., Pritchet, C. J., Regnault, N., Rich, J., Taillet, R., Knop, R., McMahon, R. G., Perlmutter, S., & Walton, N. A. 2005b. Gemini Spectroscopy of Supernovae from the Supernova Legacy Survey: Improving High-Redshift Supernova Selection and Classification. *Astrophysical Journal*, **634**(Dec.), 1190–1201.

Hubble, E. 1929. A Relation between Distance and Radial Velocity among Extra-Galactic Nebulae. *Proceedings of the National Academy of Science*, **15**(Mar.), 168–173.

Ichikawa, K., Fukugita, M., & Kawasaki, M. 2005. Constraining neutrino masses by CMB experiments alone. *Physical Review D*, **71**(4), 043001–+.

Ilbert, O., Arnouts, S., McCracken, H. J., Bolzonella, M., Bertin, E., Le Fèvre, O., Mellier, Y., Zamorani, G., Pellò, R., Iovino, A., Tresse, L., Le Brun, V., Bottini, D., Garilli, B., Maccagni, D., Picat, J. P., Scaramella, R., Scodeggio, M., Vettolani, G., Zanichelli, A., Adami, C., Bardelli, S., Cappi, A., Charlot, S., Ciliegi, P., Contini, T., Cucciati, O., Foucaud, S., Franzetti, P., Gavignaud, I., Guzzo, L., Marano, B., Marinoni, C., Mazure, A., Meneux, B., Merighi, R., Paltani, S., Pollo, A., Pozzetti, L., Radovich, M., Zucca, E., Bondi, M., Bongiorno, A., Busarello, G., de La Torre, S., Gregorini, L., Lamareille, F., Mathez, G., Merluzzi, P., Ripepi, V., Rizzo, D., & Vergani, D. 2006. Accurate photometric redshifts for the CFHT legacy survey calibrated using the VIMOS VLT deep survey. *Astronomy & Astrophysics*, **457**(Oct.), 841–856.

Ilbert, O., Capak, P., Salvato, M., Aussel, H., McCracken, H. J., Sanders, D. B., Scoville, N., Karaltepe, J., Arnouts, S., LeFloc'h, E., Mobasher, B., Taniguchi, Y., Lamareille, F., Leauthaud, A., Sasaki, S., Thompson, D., Zamojski, M., Zamorani, G., Bardelli, S., Bolzonella, M., Bongiorno, A., Brusa, M., Caputi, K. I., Carollo, C. M., Contini, T., Cook, R., Coppa, G., Cucciati, O., de la Torre, S., de Ravel, L., Franzetti, P., Garilli, B., Hasinger, G., Iovino, A., Kampczyk, P., Kneib, J.-P., Knobel, C., Kovac, K., LeBorgne, J. F., LeBrun, V., LeFèvre, O., Lilly, S., Looper, D., Maier, C., Mainieri, V., Mellier, Y., Mignoli, M., Murayama, T., Pellò, R., Peng, Y., Pérez-Montero, E., Renzini, A., Ricciardelli, E., Schiminovich, D., Scodeggio, M., Shioya, Y., Silverman, J., Surace, J., Tanaka, M., Tasca, L., Tresse, L., Vergani, D., & Zucca, E. 2009. Cosmos Photometric Redshifts with 30-BANDS for 2-deg^2. *Astrophysical Journal*, **690**(Jan.), 1236–1249.

Jha, S., Riess, A. G., & Kirshner, R. P. 2007. Improved Distances to Type Ia Supernovae with Multicolor Light-Curve Shapes: MLCS2k2. *Astrophysical Journal*, **659**(Apr.), 122–148.

Jönsson, J., Dahlén, T., Goobar, A., Gunnarsson, C., Mörtsell, E., & Lee, K. 2006. Lensing Magnification of Supernovae in the GOODS Fields. *Astrophysical Journal*, **639**(Mar.), 991–998.

Jonsson, J., Dahlen, T., Goobar, A., Mortsell, E., & Riess, A. 2006. Tentative detection of the gravitational magnification of type Ia supernovae. *ArXiv Astrophysics e-prints*, Dec.

Jönsson, J., Kronborg, T., Mörtsell, E., & Sollerman, J. 2008. Prospects and pitfalls of gravitational lensing in large supernova surveys. *Astronomy & Astrophysics*, **487**(Aug.), 467–473.

Kaiser, N., Wilson, G., & Luppino, G. A. 2000. Large-Scale Cosmic Shear Measurements. *ArXiv Astrophysics e-prints*, Mar.

Kamionkowski, M. 1998. Possible Relics from New Physics in the Early Universe: Inflation, the Cosmic Microwave Background, and Particle Dark Matter. *ArXiv Astrophysics e-prints*, Sept.

Kasen, D., Woosley, S., Nugent, P., & Röpke, F. 2007. The light curves and spectra of supernova explosions: multi-dimensional time-dependent Monte Carlo radiative transfer calculations. *Journal of Physics Conference Series*, **78**(1), 012037–+.

Kasen, D., Thomas, R. C., Röpke, F., & Woosley, S. E. 2008. Multidimensional radiative transfer calculations of the light curves and spectra of Type Ia supernovae. *Journal of Physics Conference Series*, **125**(1), 012007–+.

Kasen, D., Roepke, F., & Woosley, S. E. 2009. The Diversity of Type Ia Supernovae from Broken Symmetries. *ArXiv e-prints*, July.

Kleinheinrich, M., Schneider, P., Rix, H. ., Erben, T., Wolf, C., Schirmer, M., Meisenheimer, K., Borch, A., Dye, S., Kovacs, Z., & Wisotzki, L. 2004. Weak lensing measurements of dark matter halos of galaxies from COMBO-17. *ArXiv Astrophysics e-prints*, Dec.

Kleinheinrich, M., Rix, H.-W., Erben, T., Schneider, P., Wolf, C., Schirmer, M., Meisenheimer, K., Borch, A., Dye, S., Kovacs, Z., & Wisotzki, L. 2005. The influence of redshift information on galaxy-galaxy lensing measurements. *Astronomy & Astrophysics*, **439**(Aug.), 513–520.

Knop, R. A., Aldering, G., Amanullah, R., Astier, P., Blanc, G., Burns, M. S., Conley, A., Deustua, S. E., Doi, M., Ellis, R., Fabbro, S., Folatelli, G., Fruchter, A. S., Garavini, G., Garmond, S., Garton, K., Gibbons, R., Goldhaber, G., Goobar, A., Groom, D. E., Hardin, D., Hook, I., Howell, D. A., Kim, A. G., Lee, B. C., Lidman, C., Mendez, J., Nobili, S., Nugent, P. E., Pain, R., Panagia, N., Pennypacker, C. R., Perlmutter, S., Quimby, R., Raux, J., Regnault, N., Ruiz-Lapuente, P., Sainton, G., Schaefer, B., Schahmaneche, K., Smith, E., Spadafora, A. L., Stanishev, V., Sullivan, M., Walton, N. A., Wang, L., Wood-Vasey, W. M., & Yasuda, N. 2003. New Constraints on Ω_M, Ω_Λ, and w from an Independent Set of 11 High-Redshift Supernovae Observed with the Hubble Space Telescope. *Astrophysical Journal*, **598**(Nov.), 102–137.

Kochanek, C. S. 1994. The dynamics of luminous galaxies in isothermal halos. *Astrophysical Journal*, **436**(Nov.), 56–66.

Komatsu, E. 2003. Wilkinson Microwave Anisotropy Probe constraints on non-Gaussianity. *New Astronomy Review*, **47**(Nov.), 797–803.

Komatsu, E., Dunkley, J., Nolta, M. R., Bennett, C. L., Gold, B., Hinshaw, G., Jarosik, N., Larson, D., Limon, M., Page, L., Spergel, D. N., Halpern, M., Hill, R. S., Kogut, A., Meyer, S. S., Tucker, G. S., Weiland, J. L., Wollack, E., & Wright, E. L. 2009. Five-Year Wilkinson Microwave Anisotropy Probe Observations: Cosmological Interpretation. *Astrophysical Journal Supplement Series*, **180**(Feb.), 330–376.

Koopmans, L. V. E., Treu, T., Bolton, A. S., Burles, S., & Moustakas, L. A. 2006. The Sloan Lens ACS Survey. III. The Structure and Formation of Early-Type Galaxies and Their Evolution since z ˜ 1. *Astrophysical Journal*, **649**(Oct.), 599–615.

Koopmans, L. V. E., Bolton, A., Treu, T., Czoske, O., Auger, M., Barnabe, M., Vegetti, S., Gavazzi, R., Moustakas, L., & Burles, S. 2009. The Structure and Dynamics of Massive Early-type Galaxies: On Homology, Isothermality and Isotropy inside one Effective Radius. *ArXiv e-prints*, June.

Kowalski, M., Rubin, D., Aldering, G., Agostinho, R. J., Amadon, A., Amanullah, R., Balland, C., Barbary, K., Blanc, G., Challis, P. J., Conley, A., Connolly, N. V., Covarrubias, R., Dawson, K. S., Deustua, S. E., Ellis, R., Fabbro, S., Fadeyev, V., Fan, X., Farris, B., Folatelli, G., Frye, B. L., Garavini, G., Gates, E. L., Germany, L., Goldhaber, G., Goldman, B., Goobar, A., Groom, D. E., Haissinski, J., Hardin, D., Hook, I., Kent, S., Kim, A. G., Knop, R. A., Lidman, C., Linder, E. V., Mendez, J., Meyers, J., Miller, G. J., Moniez, M., Mourão, A. M., Newberg, H., Nobili, S., Nugent, P. E., Pain, R., Perdereau, O., Perlmutter, S., Phillips, M. M., Prasad, V., Quimby, R., Regnault, N., Rich, J., Rubenstein, E. P., Ruiz-Lapuente, P., Santos, F. D., Schaefer, B. E., Schommer, R. A., Smith, R. C., Soderberg, A. M., Spadafora, A. L., Strolger, L.-G., Strovink, M., Suntzeff, N. B., Suzuki, N., Thomas, R. C., Walton, N. A., Wang, L., Wood-Vasey, W. M., & Yun, J. L. 2008. Improved Cosmological Constraints from New, Old, and Combined Supernova Data Sets. *Astrophysical Journal*, **686**(Oct.), 749–778.

Krisciunas, K., Phillips, M. M., & Suntzeff, N. B. 2004. Hubble Diagrams of Type Ia Supernovae in the Near-Infrared. *Astrophysical Journal Letters*, **602**(Feb.), L81–L84.

Kuchner, M. J., Kirshner, R. P., Pinto, P. A., & Leibundgut, B. 1994. Evidence for Ni-56 yields Co-56 yields Fe-56 decay in type IA supernovae. *Astrophysical Journal Letters*, **426**(May), L89+.

Landolt, A. U. 1992. UBVRI photometric standard stars in the magnitude range 11.5-16.0 around the celestial equator. *AJ*, **104**(July), 340–371.

Landolt, A. U., & Uomoto, A. K. 2007. Optical Multicolor Photometry of Spectrophotometric Standard Stars. *Astronomical Journal*, **133**(Mar.), 768–790.

Le Fèvre, O., Mellier, Y., McCracken, H. J., Foucaud, S., Gwyn, S., Radovich, M., Dantel-Fort, M., Bertin, E., Moreau, C., Cuillandre, J.-C., Pierre, M., Le Brun, V., Mazure, A., & Tresse, L. 2004. The VIRMOS deep imaging survey. I. Overview, survey strategy, and CFH12K observations. *Astronomy & Astrophysics*, **417**(Apr.), 839–846.

Leibundgut, B. 2001. Cosmological Implications from Observations of Type Ia Supernovae. *Annual Review of Astronomy & Astrophysics*, **39**, 67–98.

Leibundgut, B. 2008. Supernovae and cosmology. *General Relativity and Gravitation*, **40**(Feb.), 221–248.

Linde, A. D. 1982. A new inflationary Universe scenario: a possible solution of the horizon, flatness, homogeneity, isotropy and primordial monopole problems. *Physics Letters B*, **108**, 389–393.

Magnier, E. A., & Cuillandre, J.-C. 2004. The Elixir System: Data Characterization and Calibration at the Canada-France-Hawaii Telescope. *Publications of the Astronomical Society of the Pacific*, **116**(May), 449–464.

Ménard, B., & Dalal, N. 2005. Revisiting the magnification of type Ia supernovae with SDSS. *Monthly Notices of the Royal Astronomical Society*, **358**(Mar.), 101–104.

Milvang-Jensen, B., Aragón-Salamanca, A., Hau, G. K. T., Jørgensen, I., & Hjorth, J. 2003. The Tully-Fisher relation of cluster spirals at z= 0.83. *Monthly Notices of the Royal Astronomical Society*, **339**(Feb.), L1–L5.

Mitchell, J. L., Keeton, C. R., Frieman, J. A., & Sheth, R. K. 2005. Improved Cosmological Constraints from Gravitational Lens Statistics. *Astrophysical Journal*, **622**(Mar.), 81–98.

Narayan, R., & Bartelmann, M. 1996. Lectures on Gravitational Lensing. *ArXiv Astrophysics e-prints*, June.

Navarro, J. F., Frenk, C. S., & White, S. D. M. 1997. A Universal Density Profile from Hierarchical Clustering. *Astrophysical Journal*, **490**(Dec.), 493–+.

Nolta, M. R., Dunkley, J., Hill, R. S., Hinshaw, G., Komatsu, E., Larson, D., Page, L., Spergel, D. N., Bennett, C. L., Gold, B., Jarosik, N., Odegard, N., Weiland, J. L., Wollack, E., Halpern, M., Kogut, A., Limon, M., Meyer, S. S., Tucker, G. S., & Wright, E. L. 2009. Five-Year Wilkinson Microwave Anisotropy Probe Observations: Angular Power Spectra. *Astrophysical Journal Supplement Series*, **180**(Feb.), 296–305.

Nugent, P., Kim, A., & Perlmutter, S. 2002. K-Corrections and Extinction Corrections for Type Ia Supernovae. *Publications of the Astronomical Society of the Pacific*, **114**(Aug.), 803–819.

Parker, L. C., Hudson, M. J., Carlberg, R. G., & Hoekstra, H. 2005. Mass-to-Light Ratios of Galaxy Groups from Weak Lensing. *Astrophysical Journal*, **634**(Dec.), 806–812.

Parker, L. C., Hoekstra, H., Hudson, M. J., van Waerbeke, L., & Mellier, Y. 2007. The Masses and Shapes of Dark Matter Halos from Galaxy-Galaxy Lensing in the CFHT Legacy Survey. *Astrophysical Journal*, **669**(Nov.), 21–31.

Peiris, H. V., Komatsu, E., Verde, L., Spergel, D. N., Bennett, C. L., Halpern, M., Hinshaw, G., Jarosik, N., Kogut, A., Limon, M., Meyer, S. S., Page, L., Tucker, G. S., Wollack, E., & Wright, E. L. 2003. First-Year Wilkinson Microwave Anisotropy Probe (WMAP) Observations: Implications For Inflation. *Astrophysical Journal Supplement Series*, **148**(Sept.), 213–231.

Penzias, A. A., & Wilson, R. W. 1965. A Measurement of Excess Antenna Temperature at 4080 Mc/s. *Astrophysical Journal*, **142**(July), 419–421.

Percival, W. J., Nichol, R. C., Eisenstein, D. J., Weinberg, D. H., Fukugita, M., Pope, A. C., Schneider, D. P., Szalay, A. S., Vogeley, M. S., Zehavi, I., Bahcall, N. A., Brinkmann, J., Connolly, A. J., Loveday, J., & Meiksin, A. 2007. Measuring the Matter Density Using Baryon Oscillations in the SDSS. *Astrophysical Journal*, **657**(Mar.), 51–55.

Percival, W. J., Reid, B. A., Eisenstein, D. J., Bahcall, N. A., Budavari, T., Fukugita, M., Gunn, J. E., Ivezic, Z., Knapp, G. R., Kron, R. G., Loveday, J., Lupton, R. H., McKay, T. A., Meiksin, A., Nichol, R. C., Pope, A. C., Schlegel, D. J., Schneider, D. P., Spergel, D. N., Stoughton, C., Strauss, M. A., Szalay, A. S., Tegmark, M., Weinberg, D. H., York, D. G., & Zehavi, I. 2009. Baryon Acoustic Oscillations in the Sloan Digital Sky Survey Data Release 7 Galaxy Sample. *ArXiv e-prints*, July.

Perlmutter, S., Deustua, S., Gabi, S., Goldhaber, G., Groom, D., Hook, I., Kim, A., Kim, M., Pennypacker, C., Goobar, A., Pain, R., Ellis, R., McMahon, R., Boyle, B., Bunclark, P., Carter, D., Irwin, M., Filippenko, A. V., Matheson, T., Glazebrook, K., Dopita, M., Mould, J., Couch, W., & The Supernova Cosmology Project. 1995 (Dec.). Cosmology from 7 High-Redshift Supernovae: Type IA Homogeneity at Z ˜ 0.4 and the Measurement of q_0. *Pages 1413–+ of: Bulletin of the American Astronomical Society*. Bulletin of the American Astronomical Society, vol. 27.

Perlmutter, S., Gabi, S., Goldhaber, G., Goobar, A., Groom, D. E., Hook, I. M., Kim, A. G., Kim, M. Y., Lee, J. C., Pain, R., Pennypacker, C. R., Small, I. A., Ellis, R. S., McMahon, R. G., Boyle, B. J., Bunclark, P. S., Carter, D., Irwin, M. J., Glazebrook, K., Newberg, H. J. M., Filippenko, A. V., Matheson, T., Dopita, M., Couch, W. J., & The Supernova Cosmology Project. 1997a. Measurements of the Cosmological Parameters Omega and Lambda from the First Seven Supernovae at Z >= 0.35. *Astrophysical Journal*, **483**(July), 565–+.

Perlmutter, S., Gabi, S., Goldhaber, G., Goobar, A., Groom, D. E., Hook, I. M., Kim, A. G., Kim, M. Y., Lee, J. C., Pain, R., Pennypacker, C. R., Small, I. A., Ellis, R. S., McMahon, R. G., Boyle, B. J., Bunclark, P. S., Carter, D., Irwin, M. J., Glazebrook, K., Newberg, H. J. M., Filippenko, A. V., Matheson, T., Dopita, M., Couch, W. J., & The Supernova Cosmology Project. 1997b. Measurements of the Cosmological Parameters Omega and Lambda from the First Seven Supernovae at Z >= 0.35. *Astrophysical Journal*, **483**(July), 565–+.

Perlmutter, S., Aldering, G., della Valle, M., Deustua, S., Ellis, R. S., Fabbro, S., Fruchter, A., Goldhaber, G., Groom, D. E., Hook, I. M., Kim, A. G., Kim, M. Y., Knop, R. A., Lidman, C., McMahon, R. G., Nugent, P., Pain, R., Panagia, N., Pennypacker, C. R., Ruiz-Lapuente, P., Schaefer, B., & Walton, N. 1998. Discovery of a supernova explosion at half the age of the universe. *Nature*, **391**(Jan.), 51–+.

Perlmutter, S., Aldering, G., Goldhaber, G., Knop, R. A., Nugent, P., Castro, P. G., Deustua, S., Fabbro, S., Goobar, A., Groom, D. E., Hook, I. M., Kim, A. G., Kim, M. Y., Lee, J. C., Nunes, N. J., Pain, R., Pennypacker, C. R., Quimby, R., Lidman, C., Ellis, R. S., Irwin, M., McMahon, R. G., Ruiz-Lapuente, P., Walton, N., Schaefer, B., Boyle, B. J., Filippenko, A. V., Matheson, T., Fruchter, A. S., Panagia, N., Newberg, H. J. M., Couch, W. J., & The Supernova Cosmology Project. 1999. Measurements of Omega and Lambda from 42 High-Redshift Supernovae. *Astrophysical Journal*, **517**(June), 565–586.

Persic, M., & Salucci, P. 1991. The universal galaxy rotation curve. *Astrophysical Journal*, **368**(Feb.), 60–65.

Persic, M., Salucci, P., & Stel, F. 1996. Rotation curves of 967 spiral galaxies: implications for dark matter. *Astrophysical Letters Communications*, **33**(Feb.), 205–211.

Pettini, M., Zych, B. J., Murphy, M. T., Lewis, A., & Steidel, C. C. 2008. Deuterium abundance in the most metal-poor damped Lyman alpha system: converging on $\Omega_{b,0}h^2$. *Monthly Notices of the Royal Astronomical Society*, **391**(Dec.), 1499–1510.

Phillips, M. M. 1993. The absolute magnitudes of Type IA supernovae. *Astrophysical Journal Letters*, **413**(Aug.), L105–L108.

Pierce, M. J., & Tully, R. B. 1992. Luminosity-line width relations and the extragalactic distance scale. I - Absolute calibration. *Astrophysical Journal*, **387**(Mar.), 47–55.

Poveda, A. 1961. A Mass-Luminosity Relation for Dust-Poor Stellar Systems. *Astrophysical Journal*, **134**(Nov.), 910–+.

Prugniel, P., & Simien, F. 1996. The fundamental plane of early-type galaxies: stellar populations and mass-to-light ratio. *Astronomy & Astrophysics*, **309**(May), 749–759.

Rana, N. C., & Basu, S. 1992. Derivation of the age-metallicity relation and initial mass function of stars in the solar neighbourhood. *Astronomy & Astrophysics*, **265**(Nov.), 499–503.

Raux, J. 2003. *Photométrie différentielle de supernovae de type Ia lointaines ($0.5 < z < 1.2$) mesurées avec le télescope spatial Hubble et estimation des paramètres cosmologiques*. Ph.D. thesis, Université Paris-Sud.

Regnault, N., Conley, A., Guy, J., Sullivan, M., Cuillandre, J. C., Astier, P., Balland, C., Basa, S., Carlberg, R. G., Fouchez, D., Hardin, D., Hook, I. M., Howell, D. A., Pain, R., Perrett, K., & Pritchet, C. J. 2009. Photometric Calibration of the SuperNova Legacy Survey Fields.

Riess, A. G., Press, W. H., & Kirshner, R. P. 1996. A Precise Distance Indicator: Type IA Supernova Multicolor Light-Curve Shapes. *Astrophysical Journal*, **473**(Dec.), 88–+.

Riess, A. G., Filippenko, A. V., Challis, P., Clocchiatti, A., Diercks, A., Garnavich, P. M., Gilliland, R. L., Hogan, C. J., Jha, S., Kirshner, R. P., Leibundgut, B., Phillips, M. M., Reiss, D., Schmidt, B. P., Schommer, R. A., Smith, R. C., Spyromilio, J., Stubbs, C., Suntzeff, N. B., & Tonry, J. 1998. Observational Evidence from Supernovae for an Accelerating Universe and a Cosmological Constant. *Astronomical Journal*, **116**(Sept.), 1009–1038.

Riess, A. G., Filippenko, A. V., Li, W., & Schmidt, B. P. 1999. Is there an Indication of Evolution of Type IA Supernovae from their Rise Times? *Astronomical Journal*, **118**(Dec.), 2668–2674.

Riess, A. G., Filippenko, A. V., Liu, M. C., Challis, P., Clocchiatti, A., Diercks, A., Garnavich, P. M., Hogan, C. J., Jha, S., Kirshner, R. P., Leibundgut, B., Phillips, M. M., Reiss, D., Schmidt, B. P., Schommer, R. A., Smith, R. C., Spyromilio, J., Stubbs, C., Suntzeff, N. B., Tonry, J., Woudt, P., Brunner, R. J., Dey, A., Gal, R., Graham, J., Larkin, J., Odewahn, S. C., & Oppenheimer, B. 2000. Tests of the Accelerating Universe with Near-Infrared Observations of a High-Redshift Type IA Supernova. *Astrophysical Journal*, **536**(June), 62–67.

Riess, A. G., Strolger, L., Tonry, J., Casertano, S., Ferguson, H. C., Mobasher, B., Challis, P., Filippenko, A. V., Jha, S., Li, W., Chornock, R., Kirshner, R. P., Leibundgut, B., Dickinson, M., Livio, M., Giavalisco, M., Steidel, C. C., Benítez, T., & Tsvetanov, Z. 2004. Type Ia Supernova Discoveries at z ¿ 1 from the Hubble Space Telescope: Evidence for Past Deceleration and Constraints on Dark Energy Evolution. *Astrophysical Journal*, **607**(June), 665–687.

Riess, A. G., Strolger, L.-G., Casertano, S., Ferguson, H. C., Mobasher, B., Gold, B., Challis, P. J., Filippenko, A. V., Jha, S., Li, W., Tonry, J., Foley, R., Kirshner, R. P., Dickinson, M., MacDonald, E., Eisenstein, D., Livio, M., Younger, J., Xu, C., Dahlén, T., & Stern, D. 2007. New Hubble Space Telescope Discoveries of Type Ia Supernovae at z >= 1: Narrowing Constraints on the Early Behavior of Dark Energy. *Astrophysical Journal*, **659**(Apr.), 98–121.

Roberts, M. S., & Rots, A. H. 1973. Comparison of Rotation Curves of Different Galaxy Types. *Astronomy & Astrophysics*, **26**(Aug.), 483–+.

Rubin, V. C., & Ford, W. K. J. 1970. Rotation of the Andromeda Nebula from a Spectroscopic Survey of Emission Regions. *Astrophysical Journal*, **159**(Feb.), 379–+.

Sarkar, D., Amblard, A., Holz, D. E., & Cooray, A. 2008. Lensing and Supernovae: Quantifying the Bias on the Dark Energy Equation of State. *Astrophysical Journal*, **678**(May), 1–5.

Schmidt, B. P., Suntzeff, N. B., Phillips, M. M., Schommer, R. A., Clocchiatti, A., Kirshner, R. P., Garnavich, P., Challis, P., Leibundgut, B., Spyromilio, J., Riess, A. G., Filippenko, A. V., Hamuy, M., Smith, R. C., Hogan, C., Stubbs, C., Diercks, A., Reiss, D., Gilliland, R., Tonry, J., Maza, J., Dressler, A., Walsh, J., & Ciardullo, R. 1998. The High-Z Supernova Search: Measuring Cosmic Deceleration and Global Curvature of the Universe Using Type IA Supernovae. *Astrophysical Journal*, **507**(Nov.), 46–63.

Seljak, U., Slosar, A., & McDonald, P. 2006. Cosmological parameters from combining the Lyman-α forest with CMB, galaxy clustering and SN constraints. *Journal of Cosmology and Astro-Particle Physics*, **10**(Oct.), 14–+.

Sheth, R. K., Bernardi, M., Schechter, P. L., Burles, S., Eisenstein, D. J., Finkbeiner, D. P., Frieman, J., Lupton, R. H., Schlegel, D. J., Subbarao, M., Shimasaku, K., Bahcall, N. A., Brinkmann, J., & Ivezić, Ž. 2003. The Velocity Dispersion Function of Early-Type Galaxies. *Astrophysical Journal*, **594**(Sept.), 225–231.

Spergel, D. N., & Zaldarriaga, M. 1997. Cosmic Microwave Background Polarization as a Direct Test of Inflation. *Physical Review Letters*, **79**(Sept.), 2180–2183.

Spergel, D. N., Verde, L., Peiris, H. V., Komatsu, E., Nolta, M. R., Bennett, C. L., Halpern, M., Hinshaw, G., Jarosik, N., Kogut, A., Limon, M., Meyer, S. S., Page, L., Tucker, G. S., Weiland, J. L., Wollack, E., & Wright, E. L. 2003. First-Year Wilkinson Microwave Anisotropy Probe (WMAP) Observations: Determination of Cosmological Parameters. *Astrophysical Journal Supplement Series*, **148**(Sept.), 175–194.

Spergel, D. N., Bean, R., Doré, O., Nolta, M. R., Bennett, C. L., Dunkley, J., Hinshaw, G., Jarosik, N., Komatsu, E., Page, L., Peiris, H. V., Verde, L., Halpern, M., Hill, R. S., Kogut, A., Limon,

M., Meyer, S. S., Odegard, N., Tucker, G. S., Weiland, J. L., Wollack, E., & Wright, E. L. 2007. Three-Year Wilkinson Microwave Anisotropy Probe (WMAP) Observations: Implications for Cosmology. *Astrophysical Journal Supplement Series*, **170**(June), 377–408.

Starobinskii, A. A. 1979. Spectrum of relict gravitational radiation and the early state of the universe. *ZhETF Pis ma Redaktsiiu*, **30**(Dec.), 719–723.

Stritzinger, M., Hamuy, M., Suntzeff, N. B., Smith, R. C., Phillips, M. M., Maza, J., Strolger, L.-G., Antezana, R., González, L., Wischnjewsky, M., Candia, P., Espinoza, J., González, D., Stubbs, C., Becker, A. C., Rubenstein, E. P., & Galaz, G. 2002. Optical Photometry of the Type Ia Supernova 1999ee and the Type Ib/c Supernova 1999ex in IC 5179. *Astronomical Journal*, **124**(Oct.), 2100–2117.

Sullivan, M., & The Supernova Legacy Survey Collaboration. 2005 (Dec.). The Supernova Legacy Survey. *Pages 466–+ of:* Turatto, M., Benetti, S., Zampieri, L., & Shea, W. (eds), *1604-2004: Supernovae as Cosmological Lighthouses*. Astronomical Society of the Pacific Conference Series, vol. 342.

Sullivan, M., Howell, D. A., Perrett, K., Nugent, P. E., Astier, P., Aubourg, E., Balam, D., Basa, S., Carlberg, R. G., Conley, A., Fabbro, S., Fouchez, D., Guy, J., Hook, I., Lafoux, H., Neill, J. D., Pain, R., Palanque-Delabrouille, N., Pritchet, C. J., Regnault, N., Rich, J., Taillet, R., Aldering, G., Baumont, S., Bronder, J., Filiol, M., Knop, R. A., Perlmutter, S., & Tao, C. 2006a. Photometric Selection of High-Redshift Type Ia Supernova Candidates. *Astronomical Journal*, **131**(Feb.), 960–972.

Sullivan, M., Le Borgne, D., Pritchet, C. J., Hodsman, A., Neill, J. D., Howell, D. A., Carlberg, R. G., Astier, P., Aubourg, E., Balam, D., Basa, S., Conley, A., Fabbro, S., Fouchez, D., Guy, J., Hook, I., Pain, R., Palanque-Delabrouille, N., Perrett, K., Regnault, N., Rich, J., Taillet, R., Baumont, S., Bronder, J., Ellis, R. S., Filiol, M., Lusset, V., Perlmutter, S., Ripoche, P., & Tao, C. 2006b. Rates and Properties of Type Ia Supernovae as a Function of Mass and Star Formation in Their Host Galaxies. *Astrophysical Journal*, **648**(Sept.), 868–883.

Sullivan, M., Ellis, R. S., Howell, D. A., Riess, A., Nugent, P. E., & Gal-Yam, A. 2009. The Mean Type Ia Supernova Spectrum Over the Past Nine Gigayears. *Astrophysical Journal Letters*, **693**(Mar.), L76–L80.

Timmes, F. X., Brown, E. F., & Truran, J. W. 2003. On Variations in the Peak Luminosity of Type Ia Supernovae. *Astrophysical Journal Letters*, **590**(June), L83–L86.

Tonry, J. L., Schmidt, B. P., Barris, B., Candia, P., Challis, P., Clocchiatti, A., Coil, A. L., Filippenko, A. V., Garnavich, P., Hogan, C., Holland, S. T., Jha, S., Kirshner, R. P., Krisciunas, K., Leibundgut, B., Li, W., Matheson, T., Phillips, M. M., Riess, A. G., Schommer, R., Smith, R. C., Sollerman, J., Spyromilio, J., Stubbs, C. W., & Suntzeff, N. B. 2003. Cosmological Results from High-z Supernovae. *Astrophysical Journal*, **594**(Sept.), 1–24.

Treu, T., Koopmans, L. V., Bolton, A. S., Burles, S., & Moustakas, L. A. 2006. The Sloan Lens ACS Survey. II. Stellar Populations and Internal Structure of Early-Type Lens Galaxies. *Astrophysical Journal*, **640**(Apr.), 662–672.

Tripp, R. 1998. A two-parameter luminosity correction for Type IA supernovae. *Astronomy & Astrophysics*, **331**(Mar.), 815–820.

Tully, R. B., & Fisher, J. R. 1977. A new method of determining distances to galaxies. *Astronomy & Astrophysics*, **54**(Feb.), 661–673.

Turatto, M. 2003. Supernova Spectra. *ArXiv Astrophysics e-prints*, Oct.

Van Waerbeke, L., Mellier, Y., Erben, T., Cuillandre, J. C., Bernardeau, F., Maoli, R., Bertin, E., Mc Cracken, H. J., Le Fèvre, O., Fort, B., Dantel-Fort, M., Jain, B., & Schneider, P. 2000. Detection of correlated galaxy ellipticities from CFHT data: first evidence for gravitational lensing by large-scale structures. *Astronomy & Astrophysics*, **358**(June), 30–44.

Verheijen, M. A. W. 2001. The Ursa Major Cluster of Galaxies. V. H I Rotation Curve Shapes and the Tully-Fisher Relations. *Astrophysical Journal*, **563**(Dec.), 694–715.

Wang, Y. 2005. Observational signatures of the weak lensing magnification of supernovae. *Journal of Cosmology and Astro-Particle Physics*, **3**(Mar.), 5–+.

Williams, L. L. R., & Song, J. 2004. Weak lensing of the high-redshift SNIa sample. *Monthly Notices of the Royal Astronomical Society*, **351**(July), 1387–1394.

Wittman, D. M., Tyson, J. A., Kirkman, D., Dell'Antonio, I., & Bernstein, G. 2000. Detection of weak gravitational lensing distortions of distant galaxies by cosmic dark matter at large scales. *Nature*, **405**(May), 143–148.

Wood-Vasey, W. M., Miknaitis, G., Stubbs, C. W., Jha, S., Riess, A. G., Garnavich, P. M., Kirshner, R. P., Aguilera, C., Becker, A. C., Blackman, J. W., Blondin, S., Challis, P., Clocchiatti, A., Conley, A., Covarrubias, R., Davis, T. M., Filippenko, A. V., Foley, R. J., Garg, A., Hicken, M., Krisciunas, K., Leibundgut, B., Li, W., Matheson, T., Miceli, A., Narayan, G., Pignata, G., Prieto, J. L., Rest, A., Salvo, M. E., Schmidt, B. P., Smith, R. C., Sollerman, J., Spyromilio, J., Tonry, J. L., Suntzeff, N. B., & Zenteno, A. 2007. Observational Constraints on the Nature of Dark Energy: First Cosmological Results from the ESSENCE Supernova Survey. *Astrophysical Journal*, **666**(Sept.), 694–715.

Woosley, S. E., Kasen, D., Blinnikov, S., & Sorokina, E. 2007. Type Ia Supernova Light Curves. *Astrophysical Journal*, **662**(June), 487–503.

Wright, C. O., & Brainerd, T. G. 2000. Gravitational Lensing by NFW Halos. *Astrophysical Journal*, **534**(May), 34–40.

Yadav, J., Bharadwaj, S., Pandey, B., & Seshadri, T. R. 2005. Testing homogeneity on large scales in the Sloan Digital Sky Survey Data Release One. *Monthly Notices of the Royal Astronomical Society*, **364**(Dec.), 601–606.

Zwicky, F. 1933. Die Rotverschiebung von extragalaktischen Nebeln. *Helvetica Physica Acta*, **6**, 110–127.

Zwicky, F. 1937. Nebulae as Gravitational Lenses. *Phys. Rev.*, **51**(4), 290.